The Journal of Gemmology

2012 / Volume 33 / Nos. 1/4

The Gemmological Association of Great Britain

The Gemmological Association of Great Britain

27 Greville Street, London EC1N 8TN, UK
T: +44 (0)20 7404 3334 **F:** +44 (0)20 7404 8843
E: information@gem-a.com **W:** www.gem-a.com

Registered Charity No. 1109555
Registered office: Palladium House, 1–4 Argyll Street, London W1F 7LD

The Journal of Gemmology

The Editor is glad to consider original articles shedding new light on subjects of gemmological interest for publication in *The Journal of Gemmology*. A guide to the preparation of typescripts for publication in *The Journal* is given on our website, or contact the Production Editor at the Gemmological Association of Great Britain.

Any opinions expressed in *The Journal of Gemmology* are understood to be the views of the contributors and not necessarily of the publishers.

Determining the geographical origins of natural emeralds through nondestructive chemical fingerprinting

D.P. Cronin and A.M. Rendle

Abstract: Analytical methods capable of differentiating trace elements in natural emerald may enable their geographical point of origin (GPO) to be elucidated. Emeralds were sampled from six distinct GPOs and the elemental composition of each sample was obtained nondestructively using energy dispersive X-ray spectroscopy (EDX). EDX results were chemometrically assessed for compositional differences and the results reveal that emeralds from the six GPOs possess a chemical identity that is statistically heterogeneous between GPOs, with the chromophores V, Ni and Mg being the most important trace elements for elucidating GPOs.

Keywords: chemometrics, chromophore, emerald, energy dispersive X-ray spectroscopy, precipitation model

Introduction

Evidenced from the earliest remnants of human civilization, minerals have always been important natural resources intimately linked to distinct cultural attributes such as personal adornment, religious and secular customs, wealth and trade, and the arts. Determining the geographical point of origin of minerals and other gems from antiquity required little more than a qualitative understanding of cultural anthropology, geographically specific artisanship, traditional trade routes, and/or mining regions consistent with the age-specific attributes of the artefact. But with advances in geophysical surveying and increased global trade throughout the past century — coupled with a combination of corporatized, indigenous and illegal mining operations — elucidating the point of origin of any gem material from qualitative analyses alone would be irresponsible. The pursuit of scientific certainty relevant to mineral origin has greatly advanced in the past decade and continues to take monumental strides towards a unified body of science.

This research began towards identifying and relating trace elemental differences in emeralds from the Cordillera Oriental in Colombia, differences which had arisen as a result of interstitial fluid migration prior to precipitation. Although the more subtle processes that link geochemical interactions to the precise incorporation of trace elements remains poorly understood, this research revealed that the chemical composition of emeralds — particularly the chromophores — from mining locations separated by only a few kilometres (e.g. the Muzo and Cosquez mining localities of Colombia) are distinctively different. Hence, even within one basic precipitation model for fluid processes culminating within a single geological formation there exist a range of even more subtle precipitation mechanisms and fluid dynamics leading to chemical heterogeneity between emerald points of origin.

The initial data that emerged changed the course of the research when it was recognized that within-site chemical homogeneity and between-sites chemical heterogeneity was contingent on the chromophore concentrations in the crystal structure. This unanticipated result during the course of investigating the chemistry of interstitial fluids during

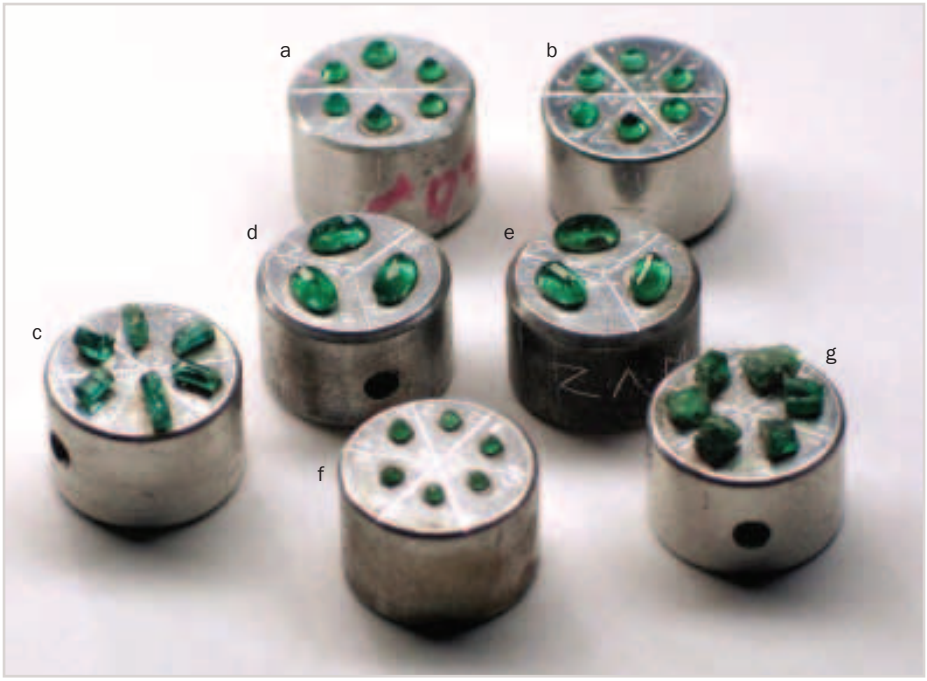

Figure 1: Each of the 36 emerald samples was mounted on an aluminium stud with silver conductive paint for SEM-EDX analysis. The studs were etched with numbered pie-shaped sectors for identification during SEM-EDX analysis and each stud was drilled for use with a positioning and removal tool to prevent contamination. (a) CZC, (b) MZC, (c) CVC, (d) ZAM, (e) ZAM, (f) GOB and (g) CFB. Photo by D. P. Cronin.

tectonic precipitation dynamics in the Cordillera Oriental quickly led to this research evolving to determine if chemical heterogeneity between emerald mining localities was chemometrically unique and statistically significant based on chromophore constituents alone. To test this assertion, three additional sites (two in Brazil and one in Zambia) were sampled and assessed for their architectural chemistries and chromophore constituents.

Natural emeralds

Emerald is the richly coloured green variety of the mineral species beryl. As an allochromatic mineral species that is colourless and transparent in its purest state (var. goshenite), beryl does not meet the defined characteristics of emerald unless the requisite chromophore elements are properly incorporated into the six-member cyclosilicate crystal structure. Furthermore, chromophore incorporation must occur in the proper quantity and configuration within the crystal structure to result in the characteristic visible absorption that transmits the distinctive green hue and treasured chroma that defines the emerald variety. Because beryllium and the primary chromophores necessary for emerald precipitation, chromium and vanadium, are not normally in close association in Nature, the rarity of this geochemical concurrence is the reason for the scarcity of emerald occurrences worldwide (Schwarz and Giuliani, 2001).

The selective substitution of metal cations in the beryl crystal structure, such as the incorporation of chromium ions (Cr^{3+}) in octahedral sites that would otherwise host the framework aluminium ion (Al^{3+}) (Hasan, Keany and Manson, 1986; Parikh *et al.,* 2003; Acharya *et al.,* 2000; Kim *et al.,* 2000; Nassau, 1978), produces the defining hue of emerald (Kleiðmantas and Skridlaitë, 2004). Emeralds with characteristically low chromium content often contain the trivalent primary chromophore vanadium (V^{3+}), approximately 0.3% by weight in the Al^{3+} sites (Moroz *et al.,* 2000). While it was once believed that the Al^{3+} site was the only location in which the primary chromophore Cr^{3+} could reside (Edgar and Hutton, 1978), it has since been suggested that Cr^{3+} in a coupled substitution with a monovalent cation may occupy tetravalent sites normally containing the framework silicon ion (Si^{4+}) (Parikh *et al.,* 2003).

Whereas the primary chromophore(s) in the chemical framework give emeralds their distinctive green colour, it is the incorporation of secondary chromophores (i.e. Fe^{2+}, Fe^{3+}, Ni^{2+}) that alter the chroma of emeralds and lead to their wide-range of visible chromaticity. Much of the chromaticity dynamics results from secondary chromophores competing for the Cr^{3+} and V^{3+} sites, thereby depleting concentrations of Cr^{3+} and V^{3+} (Platonov, Taran and Balitsky, 1984). More importantly, secondary chromophores are polyvalent ions that act as electron withdrawing groups. Their incorporation into the crystal structure imparts an effect on the visible spectrum that shifts the Cr^{3+} and V^{3+} absorption bands towards longer wavelengths. For example, Al^{3+} can be substituted with ferric iron (Fe^{3+}) or with magnesium (Mg^{2+}), the latter requiring a coupled substitution with a monovalent cation (Acharya *et al.,* 2000; Parikh *et al.,* 2003), leading to red-shifting in the absorption bands. With a lack of d-electrons and no electronic transitions in the visible region, Mg^{2+} would normally not be considered to be a secondary chromophore, but its presence can shift absorption bands and alter the colour of an emerald. In addition to Fe^{3+} and Mg^{2+} placement into Al^{3+} sites, Fe^{3+}, Mg^{2+} and divalent ferrous iron (Fe^{2+}) ions can each occupy the divalent beryllium (Be^{2+}) tetrahedral sites (Braga *et al.,* 2002); again, red-shifting the chromium and vanadium absorption bands and changing the hue and chroma of emerald.

In addition to the primary and secondary chromophore elements, emeralds also contain other trace elements that reflect the localized geology and fluid-rock interaction dynamics that exist during precipitation. For each of the six site-specific emerald occurrences the following aspects were considered in this study: the influence of the host rock chemistry on skeletal

crystal architecture, the occurrence of trace elements that link emeralds to their point of origin, the subsurface geology, fluid-rock interactions and the geochemical processes leading to emerald precipitation. By measuring the contents of framework elements, chromophore elements (both primary and secondary), and other trace chemical impurities in emeralds with EDX technologies and evaluating the results with a custom analysis of variance (ANOVA) program code for emerald chemical constituents both among and between known sample points of origin, we aimed to establish the chemical 'fingerprint' of emerald from six different geographical points of origin and test whether they can be chemically distinguishable from one another.

Materials and methods

For this work, 36 emeralds were randomly sampled (six individual samples from each of six commercial emerald-producing mines). Sampling procedure for both sites and specimens was executed in alignment with research sampling protocols set forth by ASTM International (formerly known as the American Society for Testing and Materials (ASTM)), and the mining localities were selectively chosen based on the merits of their geological and geographical similarities and differences, their importance in the international emerald market, and our ability to ensure that the collected samples originated from the mines in which sample acquisition was to occur. The 36 emerald samples acquired for this research originated from: (1) Guali, Colombia (CVC), (2) Cosquez, Colombia (CZC), (3) Muzo, Colombia (MZC), (4) Campo Verdes, Brazil (GOB), (5) Carnaíba, Brazil (CFB), and (6) Chantete, Zambia (ZAM). The gem quality emerald samples, as shown in *Figure 1*, include anhedral crystals (those from CFB), euhedral crystals (those from CVC), round brilliant cuts (those from CZC, MZC and GOB), and oval brilliant cuts (those from ZAM). Sample sizes were kept to a minimum (0.01 ct – 0.26 ct) to maximize the quantity of emeralds mounted on each stud for analysis in the scanning electron microscope (SEM). By maximizing the number of samples per stud, any contamination from successive openings of the chamber door of the SEM during data acquisition is minimized.

Sample preparation and analytical equipment

The emerald samples were mounted on cylindrical SEM studs custom crafted for this research from 6061-T6 aluminium to a diameter of 15 mm and a depth of 10 mm. The studs were soaked overnight in optical grade methanol and rinsed afterwards with fresh methanol to remove trace impurities on the stud surface. Emerald specimens were surface cleaned with a polishing cloth (3M High-Performance Polishing Cloth) and rinsed in methanol to remove epidermis oils, aerosols, residues of filling resins and any other extraneous particulates capable of altering the accuracy of chemical analysis. Following sample preparation, all emerald samples were immediately affixed to the aluminium studs using BUSCH Silber Leitlack silver conductive paint to ensure electrical contact with the SEM stage and to minimize sample charging. To optimize the validity of the elemental analysis results, sputter coating was not employed.

Elemental analysis was performed using an Amray (Bedford, Massachusetts) scanning electron microscope (SEM) coupled to an EDAX (Mahwah, New Jersey) CDU Leap Detector (model AMR-1200B) energy dispersive X-ray spectrometer (EDX). Initial calibration of the energy scale of the EDAX unit was performed using an uncoated piece of sheet copper over approximately one-half of the underlying aluminium stud (Cu-Al stud) and cross checked with a stud-mounted bead of casting alloy (Stuller, Inc.), also uncoated, composed of precise amounts of Ag, Cu, Zn, B and Si. Calibration was continuously performed throughout the research, using the standardized Cu-Al stud. For analysis using SEM-EDAX, the emerald sample studs were pressure mounted to the SEM stage with carbon adhesive tape (SPI Supplies, Inc.), tilted 30° with respect to the horizontal, and the sample stage was clamped to reduce vibration. The EDX detector was positioned at a working distance of 4.5 cm and the electron beam was rastered across the sample to average out any point-to-point chemical zoning or any variation resulting from inclusions, organic fracture filling, and/or surface contamination. The size of the raster field was adjusted to subtend a maximal surface area across only the emerald surface. The EDX was operated at an acceleration voltage of 30 kV, which produced an average of 2000 counts per second (cps) during a 200s acquisition interval; average dead time was between 10% and 15%. The electron beam spot size and acquisition times were periodically adjusted to maintain 2000 cps between samples in order to avoid morphology-induced intensity fluctuations that might alter the signal to noise ratio between experimental runs across the 36 emerald samples. To minimize drift, calibration was performed between all subsequent chamber evacuations using the standardized Cu-Al stud by adjusting the gain and zero offset controls to 8.038 keV for Cu and 1.485 keV for Al.

SEM-EDX, as is clearly relayed by Walzak, Davidson, and Biesinger (1998), "is the workhorse of many analyses because of the power inherent in being able to provide a pictorial representation combined with an elemental analysis" (p.

317). The pictorial representation of the sample through SEM methods allowed the emerald's morphology, surface matrix, and any inclusions to be chemically evaluated using point analysis prior to rastering the sample surface. In conjunction with SEM, EDX analysis provides a sensitive platform for reliable elemental analysis down to 0.01% by atomic weight (Chattopadhyay, Galeska, and Papadimitrakopoulos, 2002).

Quantification of X-ray data

Chemical interpretation of the EDX data was performed using the PC-based EDAX International DX-4:Edx-Zaf analysis software. The analytical software identifies peaks by evaluating spectral regions in comparison to the mean baseline. Energy emissions less than 0.266 keV are not detected due to the beryllium window in the EDAX, although beryllium windows provide more robust count rates by eliminating pile-up effects. Elemental abundances were normalized and reported by the software in both weight and atomic percentages (at.%) — the percentage of any one type of atom with respect to the total number of atoms that compose the mass. Preliminary analysis of the atomic percentages for all 36 emerald samples revealed that the composition of all emerald samples is fully described by 24 elements. Because some samples contained fewer elements, each of the 144 spectra were re-quantified and normalized to include all 24 elements; a group that ranged from carbon at 0.28 keV to mercury at 9.03 keV (see *Figure 2*).

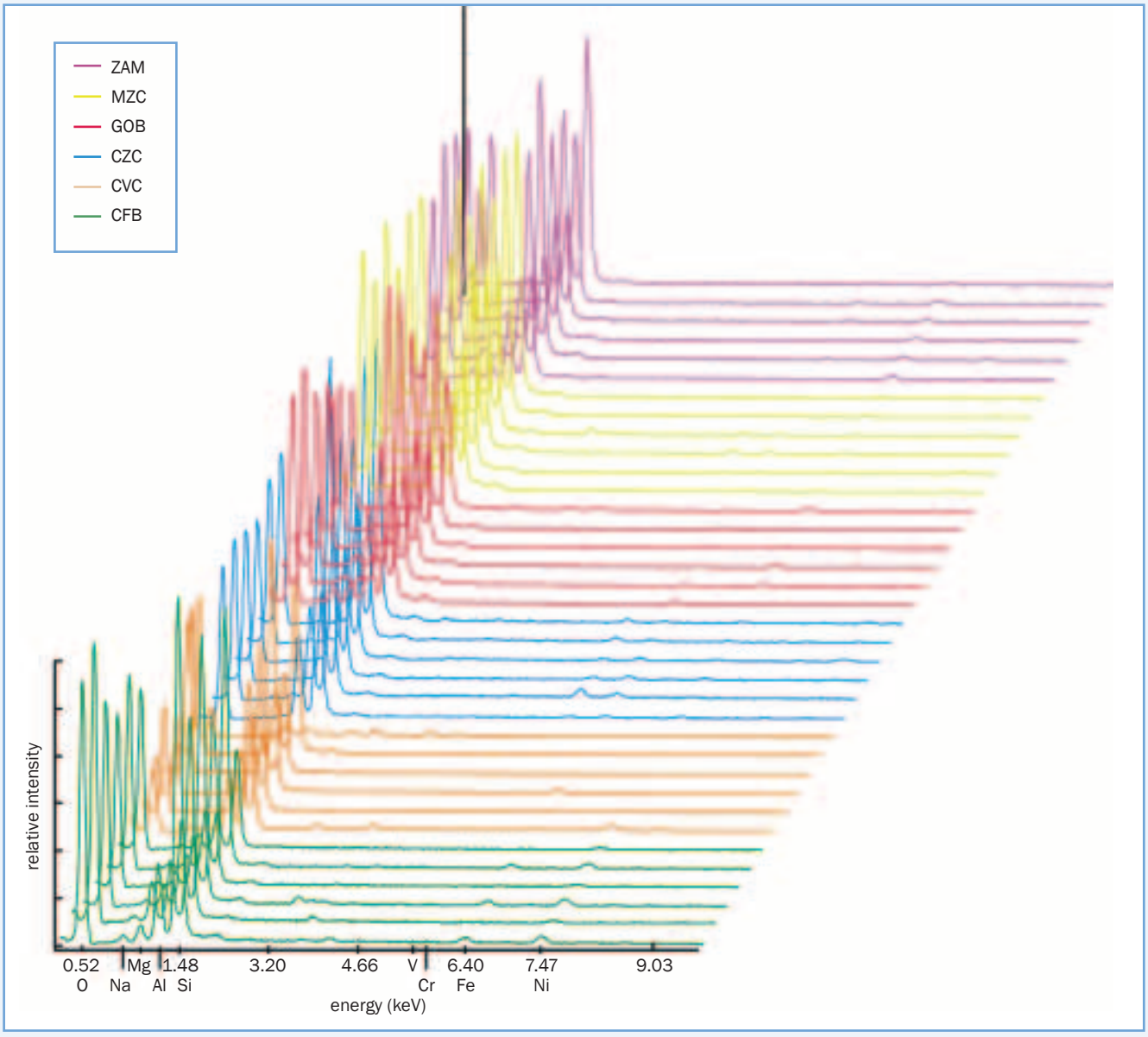

Figure 2: EDX spectra for all emerald samples showing the relative intensity of the individual elements by increasing energy level, from carbon to mercury, within each raster scan. The graphic is only intended to show minor changes in elemental trends for within sites and between sites.

Analysis of variance (ANOVA)

While many statistical procedures exist for scientific research, choosing the correct procedure is the most important component of any work and the correct choice lends validity and reliability to the results. Analysis of variance (ANOVA)* was employed to evaluate whether emeralds grouped according to geographical point of origin are statistically distinguishable based on their chemical signature. In setting out to show chemical homogeneity within sites and chemical heterogeneity between sites, the null hypothesis — that all emeralds have similar chemical compositions regardless of their geographical point of origin — was tested using original software written in MATLAB 5.3.0 (The MathWorks, Inc.). By demonstrating that the null hypothesis is not statistically supported, it can be concluded that the research hypothesis has merit (a high probability of being true). Applied to this work, this means that chemical heterogeneity exists between natural emerald points of origin which is sufficiently different to enable distinction of any of the six emerald mining localities from any of the remaining five. A null hypothesis is an opposing statement to the research hypothesis that can never be proven true but can be scientifically proven false. A null hypothesis is an important scientific component anytime the methods are designed to test the significance of differences between data sets. The MATLAB source code was written and employed to be an expeditious data analysis tool. The source code automatically imported the DX-4 eDX ZAF data acquired through EDX analysis, performed 1536 single factorial ANOVA tests and calculated the corresponding Fisher scores (F-scores)† for each ANOVA.

For the six emerald mining localities in this study, 64 site combinations (2^6) are possible, as can be viewed on the left graphic of *Figure 3*. However, seven site combinations have fewer than two sites represented and are empirically meaningless for this work. Consequently, the MATLAB source code performed 1368 meaningful ANOVA tests. Each of the 57 meaningful site combinations was evaluated 24 times, once each for the 24 elements quantified and normalized for each sample. The precision of the MATLAB source code algorithm was confirmed following the research and determined to be better than 10^{-5} and its accuracy was validated to the hundredths place by comparing a random subset of F-score results to those calculated using the SAS Institute, Inc. SAS 9.1.3 statistical analysis software.

Due to the site- and sample-specific variations in the number of sites during data analysis and the number of ANOVA tests performed, the degrees of freedom from test-to-test were in constant flux. Within the MATLAB source code the degrees of freedom for each ANOVA, which are used to determine the critical value and F-score, were calculated in accord with standard ANOVA execution as:

$$df_b = k-1 \quad (1)$$

and

$$df_w = k(n-1) \quad (2)$$

where df_b is the degrees of freedom between groups, df_w is the degrees of freedom within groups, k is the number of mining localities in each meaningful site combination (2 to 6) and n is the number of emeralds sampled from each mining locality (n=6). Hence, when evaluating the site combination that includes all six sites, the obtained F-score (F_{obt}) is compared against an F distribution based on 5 (df_b= 6-1) and 30 (df_w= 6(6-1)) degrees of freedom ($F_{5,30}$).

Critical values of the F distribution were obtained using the conventional significance value of 0.05 (α=0.05) (Howell, 2002; Kanji, 1993; Rohlf and Sokal, 1994), which corresponds to a probability (P) of less than or equal to 5% (P≤0.05) of making a Type I error. A Type I error is when the statistical results erroneously reject a null hypothesis that is actually true. To insure the ANOVA results are as robust as possible, the data were also evaluated at the scrutiny of α=0.025 (P≤0.025) and α=0.01 (P≤0.01) in order to identify the trace elements most responsible for distinguishing between emerald points of origin based on chemical signature. All ANOVA F-scores that exceed their corresponding critical value are considered statistically significant and their null hypothesis is rejected. Hence, F-scores larger than their corresponding critical values represent emerald mining sites that yield distinct emerald chemical signatures that exhibit a statistically significant difference in the atomic percentage of

* ANOVA is used to determine and evaluate how much of the variation in element-specific atomic percentages and element-combined atomic percentages can be attributed to variation between the mining sites sampled and how much can be attributed to factors other than those being explored. This within-site variation is considered in one category as error because the research makes no attempt to identify those factors responsible for the variation.

† The F-score is a point on a positively skewed F distribution matrix that enables the researchers to determine if a null hypothesis should be rejected based on a given statistical probability determined before research is performed. By selecting a statistical probability criterion for rejection prior to beginning the research, a critical value under the F distribution is assigned based on the degrees of freedom. If the F-score calculated by the ANOVA is greater than the critical value, the null hypothesis is rejected and the research hypothesis accepted. The greater the difference between the F-score and the critical value, the more reliable the statistical results are.

the element being evaluated compared to the remaining five emerald sampling sites included in this work. In total, 1425 meaningful null hypotheses are defined within the framework of this research. These null hypotheses correspond to 57 site combinations evaluated for 24 elements (1368 element-wise ANOVAs), and 57 summary comparisons that consider whether at least one element exerts a distinguishing effect for each site combination.

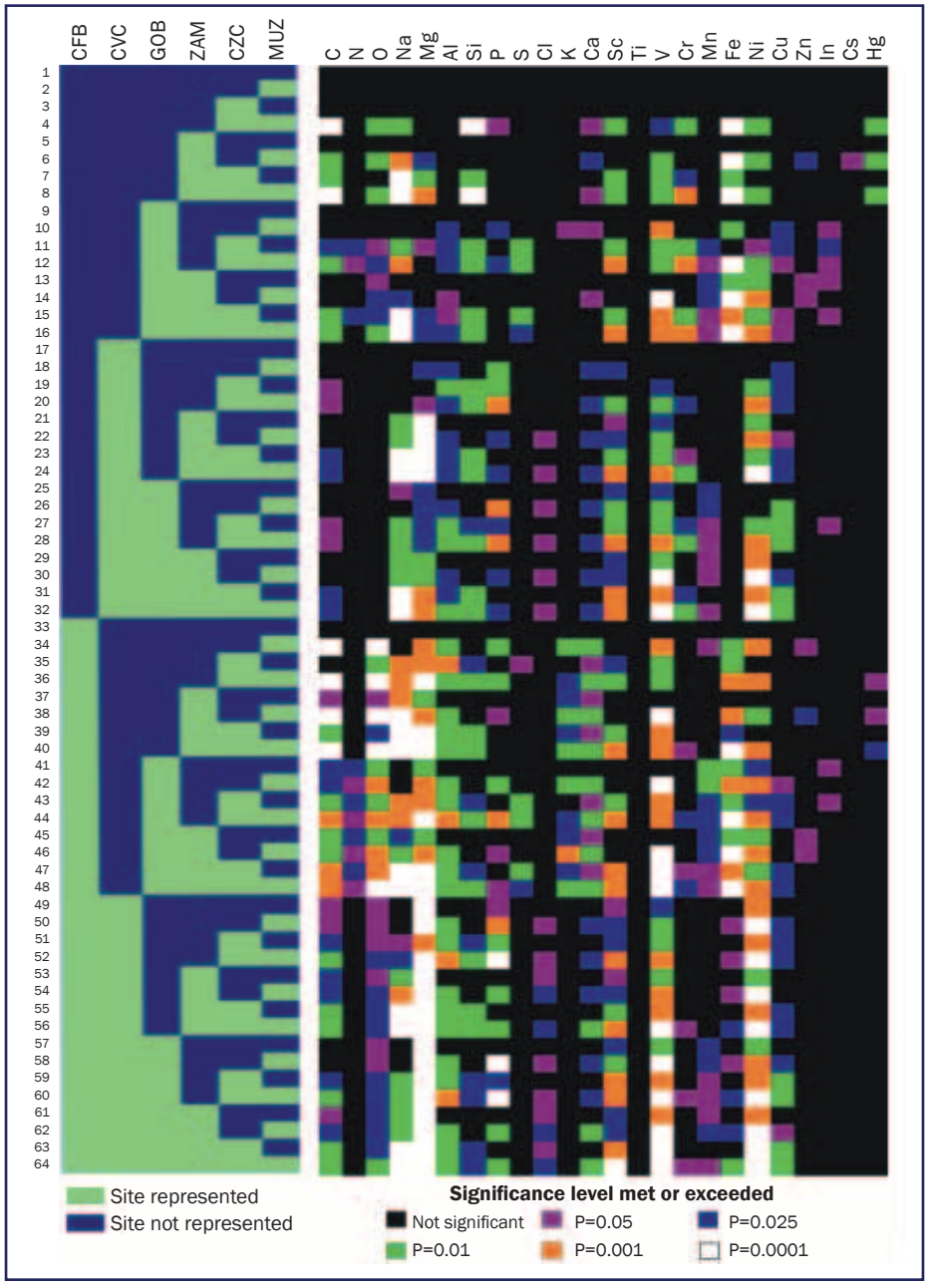

Figure 3: Graphical representation of both the site combination matrix used in each ANOVA analysis and the statistical results for each of the 24 elements included in the site combination ANOVA (site combinations and ANOVA results share the same row). Because the research only looked for statistically significant results, those elements that failed to have F-scores exceeding their critical value are blacked out. There are 64 rows (reading from the top) and those that are not meaningful have rows that are completely blacked out. The most important result for this work is the bottom row where all six sites included in this research are compared to each other for all 24 elements. In this row the most significant discriminatory elements (colourless) are Na, Mg, Sc, V and Ni.

Results and discussion

The hypothesis of primary importance for this work is that each of the six emerald mining sites produces emeralds having chemical signatures statistically distinguishable from all other research samples included in this work through EDX and chemometrics. In comparing the 24 elements for all six sites, 16 elements differed in their abundances at a traditional significance value of P≤=0.05 (see *Table I*). Since more than one element exhibited between site heterogeneity at the significance value of P≤=0.05, we employed successively

Table I: The 16 most important emerald constituents for revealing between site chemical heterogeneity (ANOVA critical value: $F_{0.05(5,30)}$=2.53).

Element	F score	P
Mg	16.0068	<0.0001
V	10.4929	<0.0001
Ni	10.1714	<0.0001
Na	9.6558	<0.0001
Sc	7.5607	0.0001
Al	5.5040	0.0010
C	4.3288	0.0044
Cu	4.2459	0.0049
P	3.9598	0.0071
Ca	3.9000	0.0077
Fe	3.8869	0.0078
O	3.8040	0.0087
Si	3.5507	0.0122
Cl	3.2157	0.0192
Cr	3.0286	0.0249
Mn	2.6262	0.0438

NB: While one or more of the elements may provide statistical distinction between all six points of origin, each element and combination of sites must be examined to determine if statistical significance continues to exist when the degrees of freedom are affected.

Determining the geographical origins of natural emeralds through nondestructive chemical fingerprinting

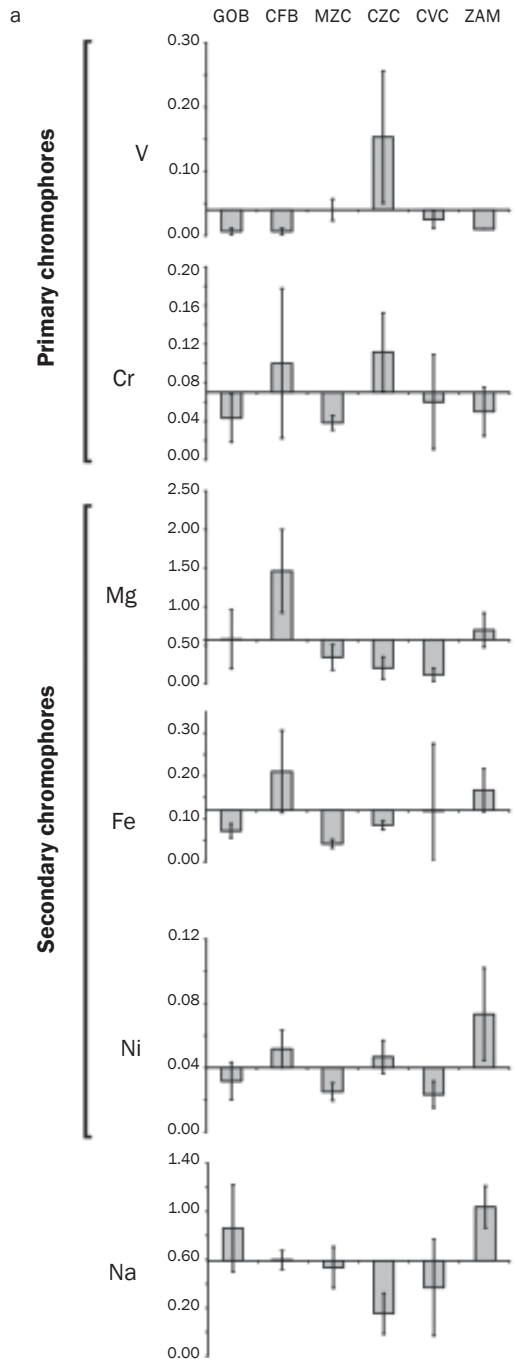

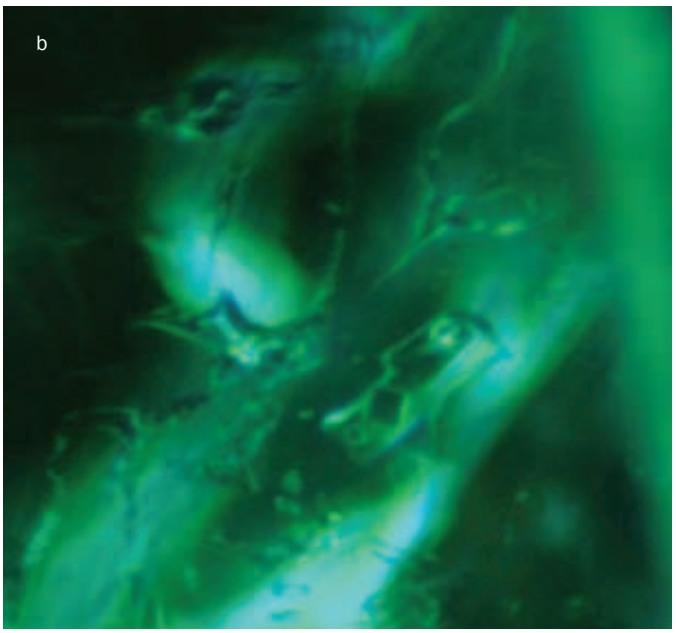

Figure 4: (a) The graphic shows site-specific trends in chromophore and sodium content among all the sampling sites. For each element, the horizontal line represents the mean atomic percentage for all sites while individual site means are represented by the parallel line capping each shaded box; coupled with vertical standard deviation whiskers. Sodium was an important aspect of a parallel piece of research given the brine solution that is the liquid component of both two- and three-phase inclusions and the sodium chloride crystals that are a common constituent in Colombian three-phase inclusions.
(b) Three-phase inclusion in a sample stone from Chivor. Photo D.P. Cronin.

smaller significance values in order to estimate which elements are the most statistically significant in indicating these differences. At the more conservative significance value of P≤=0.025, 15 elements exhibited chemical contents that are statistically distinguishable and at P≤=0.01, 12 elements continue to exhibit between site heterogeneity. As a result of these analyses, it is concluded that element-based heterogeneity does exist between the six emerald mining sites in this study. Consequently, natural emeralds originating from any one site are distinguishable from emeralds originating from any of the remaining five. Thus, through the employment of EDX in the acquisition of chemical data, statistically significant chemical heterogeneity between sites has been revealed by means of a technique that is non-destructive and preserves the integrity of the sample.

The ANOVA results provide a statistically robust estimate of whether or not differences exist among combinations of sites in a combinatorial matrix. *Figure 3* presents a graphical representation showing statistical trends by both element and site combination. As mining sites are added or removed from the matrix, consequent changes in the number of degrees of freedom result in variability among the F-scores and their corresponding significance levels for heterogeneity assessments. This variability makes pinpointing the

elements of greatest significance for additional site combinations much more complex than simply reviewing the ANOVA results for all sampling sites. In countering this tendency, *Figure 4* shows how site-specific trends in the elemental compositions are analyzed for use in conjunction with the statistical results.

As the calculated F-score (F_{obt}) for a given site combination increases, so does the probability (P) that the sampling sites differ. In other words, larger F-scores indicate a lower probability that a null hypothesis addressing a specific site sample's chemical signature was erroneously rejected. Towards ascertaining probability through as robust a modelling procedure as possible, subsequent analysis was performed for the four most important elements leading to the rejection of the combined-element null hypothesis for the summary comparison. All sites and samples remained represented and the four most important elements were identified as magnesium (F_{obt} = 16.0068; P<0.0001), vanadium (F_{obt} = 10.4929; P<0.0001), nickel (F_{obt} = 10.1714; P<0.0001) and sodium (F_{obt} = 9.6558; P<0.0001). Two other elements important to this research, the iron (F_{obt} = 3.8869; P=0.0078) and chromium (F_{obt} = 3.0286; P=0.0249) chromophores, both displayed statistically significant results as well. Furthermore, vanadium and magnesium, alone, are capable of differentiating the geographic point of origin of an emerald for 56 of the 57 relevant site combinations. By extending the analysis to include an additional secondary chromophore, nickel or iron, all 57 site combinations can in fact be distinguished. Because these chromophore elements are responsible for an emerald's visible colour — keeping in mind the role of Mg^{2+} that, as discussed, acts as a secondary chromophore through its ability to shift absorption spectra in emeralds — we believe that high-resolution visible absorption spectroscopy could be performed on natural emeralds in place of EDX in the future.

In addition to the primary goal of finding which elements in natural emeralds of known origins were useful in statistically establishing between-site chemical heterogeneity, the question of whether emeralds from mining locations in close proximity to one another exhibited geologically-based chemical heterogeneity was also addressed. By performing ANOVA on the chemical signatures of emeralds from the Brazilian sites, for example, we have discovered site-specific chemical differences that are consistent with the fluid-rock interactions that led to emerald precipitation. Within the context of discussing both geographically- and geologically-based chemical heterogeneity between mining locations, within-site chemical homogeneity of the six sampling sites and their chemometric results are presented according to geopolitical boundaries.

Colombia

Three of the emerald mining sites included in this research, Muzo, Guali and Cosquez, are located along the outer fringes of the traditional emerald zone of the Cordillera Oriental of Colombia. While the emerald zone of the Cordillera Oriental was once well-known for its emerald production, the zone currently has no emerald production and is better known today as the site of 'potatoes and coal'. Modern production actually occurs in two belts along the zone. Muzo and Cosquez lie in the Muzo Belt (the 1226 area) trending NNE along the western fringe of the emerald zone while Guali is a few kilometres east of Chivor in the Chivor Belt (the 1228 area) trending NE along the southeastern fringe. By performing ANOVA element-wise for each of the three Colombian sampling sites, 11 elements exhibited statistically significant differences in their elemental abundances (see *Table II*). The four most significant of the 11 elements are nickel (F_{obt} = 15.0000; P=0.0003), phosphorus (F_{obt} = 12.3774; P=0.0007), silicon (F_{obt} = 8.1434; P=0.004) and vanadium (F_{obt} = 8.0148; P=0.0043), each being well below the traditional significance level of α=0.05. Of primary interest were two of the most highly prized Colombian emerald mining localities, Muzo and Cosquez, located only 10.4 km apart. Chemical and chemometric analyses of the samples collected from the two locations unveiled statistically meaningful differences for 12 elements (see *Table III*). The four most significant of these are carbon (F_{obt} = 72.4751; P<0.0001), iron (F_{obt} = 54.5161; P<0.0001), silicon (F_{obt} = 37.2153; P=0.0001) and oxygen (F_{obt} = 20.9163; P=0.0001); with the latter two being basic framework constituents of the six-member cyclosilicate emerald crystal structure.

Table II: The 11 statistically significant elements revealing chemical heterogeneity between three Colombian emerald localities (ANOVA critical value: $F_{0.05(2,15)}$=3.68).

Element	F score	P
Ni	15.0000	0.0003
P	12.3774	0.0007
Si	8.1434	0.0040
V	8.0148	0.0043
Sc	7.4706	0.0056
Cr	6.2115	0.0108
Al	5.9548	0.0125
Ca	5.1033	0.0204
Cu	4.8995	0.0230
C	4.7375	0.0254
Mg	4.2431	0.0346

Table III. Twelve elements in Muzo and Cosquez emeralds showing statistically significant difference (ANOVA critical value: $F_{0.05(1,10)}$=4.97).

Element	F score	P
C	72.4751	<0.0001
Fe	54.5161	<0.0001
Si	37.2153	0.0001
O	20.9163	0.0001
Ni	20.6098	0.0011
Cr	18.8327	0.0015
Na	15.2731	0.0029
Sc	13.0000	0.0048
Hg	10.9459	0.0079
V	7.0920	0.0238
Ca	5.9756	0.0346
P	5.5479	0.0403

The results of chemometric analysis of Muzo and Cosquez samples raises

an important question addressing the cause of statistically significant chemical heterogeneity between emeralds drawn from localities in such close proximity to one another. Work published in references quoted above indicates that the emeralds of Colombia and the Cordillera Oriental region are the result of tectonic-hydrothermal precipitation in which emerald precipitation is generally linked to major faults or shear zones in basic and ultrabasic schistose rocks and crystal development is isolated to the fluid-rock interaction zone (see also the precipitation mechanics of emeralds in the southeast Yukon (Canada) described by Marshall *et al.,* 2003). The emeralds of the Cordillera are hosted within and around organic black shales in the western 1226 area (Guavio-Macanal) and carbonaceous black shales with intercalated dolomitic limestone in the eastern 1228 area (Rosablanca formation and Paja formation) (Cheilletz and Giuliani, 1996; Giuliani *et al.,* 1993; Banks *et al.,* 2000; Webster and Anderson, 1983). Due to the characteristically low chromium content of the organic sedimentary shale host rock of the Cordillera Oriental, the primary chromophore of the Colombian emeralds is not chromium but vanadium (Kleiðmantas and Skridlaitë, 2004).

Our results, reported in atomic percentage (at.%), reveal that the emeralds of Muzo have an average (μ) chromium content of 0.038 at.% (s.d.=0.007) that is only slightly less than their average vanadium content 0.040 at.% (s.d.=0.017), where s.d. is the standard deviation. While the vanadium content is consistent with the content average for all emerald samples included in this research (μ=0.040 at.%), the chromium content is just over one-half the content average of all samples (μ=0.067 at.%). Continued chemometric analysis of the secondary chromophore content averages revealed that magnesium (μ=0.343 at.%; s.d.=0.163) and iron (μ=0.041 at.%; s.d.=0.009) are significantly less than the magnesium (μ=0.567 at.%) and iron (μ=0.115 at.%) content averages for all other sites. Similar to the emeralds of Muzo, the Cosquez emerald samples have an average chromium content of 0.112 at.% (s.d.=0.041) that is lower in concentration than their average vanadium content of 0.150 at.% (s.d.=0.103). The secondary chromophores, again similar to the emeralds of Muzo, have magnesium contents (μ=0.205 at.%; s.d.=0.145) and iron contents (μ=0.085 at.%; s.d.=0.010) well below the content averages for all emerald samples in this research. However, unlike the Muzo emerald samples, the average vanadium content of the Cosquez emerald samples is nearly four times the average vanadium content of all samples (μ=0.040 at.%) and the chromium content is nearly twice that of all samples included in this work (μ=0.067 at.%).

While the contents of primary and secondary chromophores are invaluable in acquiring statistical knowledge that helps to separate the point of origin of emeralds, their position and concentration within the crystal structure help explain the prized colour of emeralds from in and around the Cordillera Oriental. The elevated concentration of vanadium in comparison to chromium, in comparison to chromium (11.6×10^{-24} cm^3), results in a stable spectral identity from the primary chromophores and a near absence of red-shifting due to the low concentration of secondary chromophores.

In stark contrast to the emeralds of Muzo and Cosquez, the average chromium content of Guali emeralds is 0.060 at.% (s.d.=0.049), 2.5× their vanadium content average of 0.025 at.% (s.d.=0.014) and 0.625× the average vanadium content of all samples included in this research (μ=0.040 at.%); having a chromium content similar to the average chromium content of all samples (μ=0.067 at.%). Analysis of the secondary chromophore content averages reveals that while magnesium's content average of 0.118 at.% (s.d.=0.083) is only one-fifth the magnesium content average of all samples (μ=0.567 at.%), iron (μ=0.118 at.%; s.d.=0.157) is nearly identical to the mean atomic percentage of iron (μ=0.115 at.%) for all samples included in this work. Although the Guali emerald samples, similar to Muzo emeralds, have a lower concentration of primary chromophores compared to the other mining localities, the relatively low concentration of secondary chromophores has resulted in absorption band stability and their richer hue and chroma.

Consistent with the research of Kleiðmantas and Skridlaië (2004), our results indicate a greater concentration of vanadium in the crystal structure of natural emeralds from the Cordillera Oriental. Their formation stems from the movement of Be-enriched hydrothermal fluids directed by tectonic events that concentrates fluid circulation along post-tectonic structures. Fluid inclusion research of minerals from rocks in the Cordillera has revealed that the mineral-forming hydrothermal fluids are of magmatic origins west of the Cordillera and of mixed magmatic/meteoric origins east of the Cordillera, with beryllium acquisition occurring during saline brine migration (Giuliani *et al.,* 2000; Schwarz and Giuliani, 2001). The consequential fluid-rock dynamics leading to metasomatic alteration of the sedimentary series incorporates the primary chromophore vanadium from the V-rich organic and carbonaceous shales of the Cordillera (Schwarz and Giuliani, 2001; Cheilletz and Giuliani, 1996; Giuliani *et al.,* 1993). The heightened concentration of vanadium in comparison to chromium primary chromophore leads to the characteristic green colour of the emeralds from Muzo and Cosquez. In contrast, the concentration ratio of chromium/vanadium (24:10) in the Guali emeralds indicates that chromium is the primary chromophore. Collectively, the emeralds of Colombia owe their colour not only to the contents of the primary chromophores, but also to the relatively depleted atomic percentage of secondary chromophores that would normally compete for similar positions in the crystal structure. The lack of secondary chromophore accumulation lends stability to the absorption bands created by the primary chromophores, thereby providing a rich chroma to an unaltered visible hue (Platonov, Taran and Balitsky, 1984; Braga *et al.,* 2002). As a consequence of

Table IV: Eight elements revealing chemical heterogeneity between the emeralds of Campos Verde and Carnaíba, Brazil at a critical value of 4.97 ($F_{0.05(1,10)}$=4.97).

Element	F score	P
O	15.8013	0.0026
Mn	14.4118	0.0035
Fe	12.1413	0.0059
Mg	10.7379	0.0083
N	9.2813	0.0123
Ni	8.7805	0.0142
C	7.9807	0.0180
In	5.2941	0.0442

the temperature and pressure reductions experienced by migrating hydrothermal fluids, emerald was co-precipitated with fluorite in pyritic, albitic and calcitic veins, fissures and vugs within brecciated black organic shales and sedimentary calcium-carbonate formations (Giuliani *et al.,* 2000; Banks *et al.,* 2000; Cheilletz *et al.,* 1994). The order of precipitation depleted secondary chromophores in solution prior to emerald precipitation; this is most apparent at Muzo where a distinct Fe depletion occurs due to pyritic precipitation prior to emerald formation.

Chemical heterogeneity between the organic sedimentary shales hosting emerald both west and east of the Cordillera Oriental, along with the widely proposed thermochemical reduction of evaporitic sulphate brines and the oxidation of organic matter originating in the black shale, account for the compositional differences of emeralds originating on opposing sides of the Cordillera (Giuliani *et al.,* 2000). What is not as clear is the cause of chemical heterogeneity between the two closely situated emerald occurrences west of the Cordillera in the Guavio-Macanal formation (Muzo mine and Cosquez mine). Banks *et al.* (2000) discovered that although Muzo and Cosquez are the result of the same subsurface fluid-host rock interaction, the intrinsic permeability, and consequently the hydraulic conductivity of the formations, was altered during a continuous stage of faulting and deformation during tectonic activity. As a result, migrating hydrothermal fluid dynamics were affected and multiple paths of fluid migration through the subsurface occurred in a way that allowed each path to acquire its own chemical identity. Thus, it is likely that the changing chemistry of the hydrothermal fluids during migration, along with the late stage precipitation of emerald crystals at Cosquez, are responsible for the compositional differences of emeralds originating at the neighbouring mines of Muzo and Cosquez in the 1226 area.

Brazil

Of the ANOVAs performed for the compositions of emeralds from the two Brazilian mines Campos Verdes and Carnaíba (line 41 of the combinatorial matrix in *Figure 3*), eight elements were found to be significant at P≤=0.05 (see *Table IV*). Of these, the four most significant elements are oxygen (F_{obt} = 15.8013; P=0.0026), manganese (F_{obt} = 14.4118; P=0.0035), iron (F_{obt} = 12.1413; P=0.0059) and magnesium (F_{obt} = 10.7379; P=0.0083), which are the only elements to remain significant at P=0.01. Although the secondary chromophores, iron and magnesium, are statistically important in differentiating the Brazilian mines at P=0.01, the concentrations of the primary chromophores (vanadium and chromium) are insignificant; a stark contrast to the chemical results for emeralds sampled from Colombia.

In comparing Campos Verdes and Carnaíba emeralds, vanadium yields an F-score of 0.00 (P=1.0) while chromium yields an F-score of 2.89 (P=0.12). Vanadium's probability of 1.0 (P=1.0) indicates a 100% chance of making a Type I error for the null hypothesis that the vanadium content of emeralds originating from Campos Verdes and Carnaíba are the same. This result reflects the near absence of vanadium in the Carnaíba and Campos Verdes samples. Our results, reported in atomic percentage, reveal that the emeralds of Campos Verdes have an average chromium content of 0.043 at.% (s.d.=0.025) six times greater than their average vanadium content of 0.007 at.% (s.d.=0.005) and the Carnaíba emeralds have an average chromium content of 0.100 at.% (s.d.=0.078) that is 15 times greater than their vanadium content of 0.007 at.% (s.d.=0.005). Overall, the Brazilian emeralds have a much higher chromium-vanadium content ratio than the Colombian emeralds, ranging from 64:10 for Campos Verdes to 151:10 for Carnaíba.

Analysis of the secondary chromophore content averages for Carnaíba reveals that the magnesium content average of 1.462 at.% (s.d.=0.538) and iron content average of 0.210 at.% (s.d.=0.096) are 2.57× and 1.90×, respectively, more than the content averages of magnesium (μ=0.567 at.%) and iron (μ=0.115 at.%) for all sites sampled for this work. In contrast, Campos Verdes emerald samples have a magnesium content average of 0.578 at.% (s.d.=0.382) and iron content average of 0.072 at.% (s.d.=0.016) that are 1.02× and 0.62× the content averages for all samples. While the primary chromophore concentration of the Brazilian sampling sites are elevated compared to the other sites sampled, the higher concentrations of secondary chromophores lead to increased red-shifting and a green hue that is not as saturated or distinct as that in their Colombian counterparts.

Examination of the emerald precipitation models for the Brazilian sites uncovers some of the causative differences between the chromophore concentrations in Colombian and Brazilian emeralds while lending insight into the unique chemical signatures of the samples from each of the Brazilian mining locations. The emeralds of Campos Verdes are best explained by the tectonic-hydrothermal precipitation model while the Carnaíba emeralds are more consistent with the magmatic associations model. The events leading to emerald precipitation at Carnaíba began with the intrusion of Be-rich granitic fluids through Archean rock (Campo Formosa ultramafic complex, Mundo Novo Greenstone belt and gneissic-migmatitic basement rock) and the Serra da Jacobina volcanic-sedimentary series (Cruz das

Almas, Rio do Ouro and Serra do Córrego formations) (Giuliani *et al.,* 1990; Webster and Anderson, 1983). Fluid migration was catalysed with the formation of fracture zones and faults resulting from tectonic deformation. Hydrothermal fluid ultimately migrated through the labyrinth of natural conduits created by the faults and fracture zones and metasomatically altered and broke down the mineral components of the schistose rock through deuteric reactions and other fluid-rock reactions. Fluid-rock interactions led to the progression of element enrichment of the hydrothermal solution preceding emerald precipitation in the peripheral veins of the pegmatite and metasomatically developed alteration haloes (Marshall *et al.,* 2003; Schwarz and Giuliani, 2001; Istituto di Geoscienze e Georisorse Sezione di Roma-Consiglio Nazionale delle Ricerche, 2005). As one might expect, the chemistry of the Carnaíba emeralds reflects the chemistry of the Serra da Jacobina rocks metasomatically altered to Mg-, C-, Ca- and Fe-rich biotite, carbonate-biotite and carbonate-biotite-talc schists (Giuliani *et al.,* 1990; Webster and Anderson, 1983). The lack of vanadium in the emeralds of Carnaíba is not completely understood but generally thought to be a consequence of the lack of organic complexes and the scarce association of vanadium-bearing mafic rocks with beryllium during metamorphic chemical exchange resulting from post-tectonic events.

Research of the sub-surface dynamics of the Campos Verdes region has shown distinct similarities to the emerald formation of the Colombian sample sites. Formation of the emeralds is consistent with the tectonic-hydrothermal precipitation model and results from tectonic fracture zones and faulting that catalysed Be-rich hydrothermal fluid migration through the host Santa Terezinha sequence. The metasedimentary formations of the Santa Terezinha sequence, greenstone schist and intercalated country rock (talc schist, carbonate-talc schist, chlorite-talc schist, biotite schist and dolomite schist) resulted from polyphase tectonic deformation (dip and rotation) and thrust faults (Kleiðmantas and Skridlaitë, 2004; Biondi, 1990; D'el-Rey Silva and de Souza Barros Neto, 2002). Hydrothermal fluid movement through the C-, K-, Cr- and Fe-rich metasedimentary formations led to metasomatism in which the fluid acquired chromophores and other trace elements prior to precipitating in alteration haloes and veins (D'el-Rey Silva and de Souza Barros Neto, 2002; Biondi, 1990).

Zambia

Although located more than 5000 miles across the Atlantic Ocean from Carnaíba, within Sub-Saharan Africa, the emeralds of the Chantete mine have also been shown to have resulted from the magmatic association precipitation model.

An examination of the atomic percentages for Chantete emeralds reveals that the content averages of magnesium (μ=0.697 at.%), nickel (μ=0.073 at.%), sodium (μ=1.036 at.%) and iron (μ=0.167 at.%) exceed the content averages of magnesium (μ=0.541 at.%), nickel (μ=0.073 at.%), sodium (μ=0.502 at.%), and iron (μ=0.105 at.%) for the samples from all remaining sites by 1.28× to 2.06×; in contrast, the vanadium content average of 0.01 at.% is extremely low and only approximately one-fifth the vanadium content average of 0.046 at.% for all remaining sites in this research. Chromium is the dominant primary chromophore, but in the emerald spectra, the Cr peaks show significant red shifts due to secondary chromophores.

The Chantete mine is located in the Ndola Rural Protected Area of the Lufwanyama district in the Copperbelt Province of Zambia. The Ndola region consists of a complex series of pegmatite dykes that penetrate thin zones of the meta-sedimentary Muva supergroup (biotite-phlogopite schist around talc-magnetite schist and tremolite-chlorite-magnetite schist) (Coakley, 2001). In the Chantete magmatic association precipitation model, metamorphism prior to emerald mineralization results from beryllium-laden granitic fluid intruding the chromium-vanadium rich basic-ultrabasic schistose host rock (Sinkankas and Read, 1986; Giuliani *et al.,* 1997; Coakley, 2001; Kleiðmantas and Skridlaitë, 2004; Zwaan *et al.,* 2005). Fluid migration occurs discordantly through the basement supergroup (granitic gneiss and migmatite) and Muva supergroup (Coakley, 2001; Zambian Ministry of Mines and Minerals Development, 2006) with quartz and tourmaline commonly precipitated first in the veins. Emerald precipitation occurs within the resultant alteration haloes and veins at the pegmatite-schist contact which cross-cuts the biotite-phlogopite schist that developed as a result of metasomatic alteration of the talc-magnetite schist formation (Coakley, 2001; Laurs, 2004; Zwaan *et al.,* 2005; Marshall *et al.,* 2003).

Conclusions

Initial investigations concerned interstitial fluid migration and tectonic precipitation dynamics of natural emeralds in and around the Cordillera Oriental, Colombia. Chemical and chemometric analyses of trace elements in the emeralds revealed that the chromophore constituents are the most statistically significant in evaluating chemical heterogeneity between the mining localities. In response to this unexpected twist, the research expanded to include three additional sites beyond the geopolitical boundary of Colombia — mining localities in Brazil and Zambia — towards determining whether chromophore constituents would remain statistically significant and useful in describing between site chemical heterogeneity. The results of this work reveal that chemical heterogeneity does statistically exist between natural emeralds and that vanadium, nickel and magnesium are site-specific elements capable of being used in a statistically significant way to distinguish the source locality of a natural emerald randomly chosen from any of the six emerald origins included in this work.

However, the results of this research are just a first step. Whereas this study has revealed the extent of chemical heterogeneity between six sites of gemmological importance, it has not assessed the compositions of all historical

and modern emeralds. But chemical links between emeralds, site heterogeneity and chromophores have been established, and this research opens up a whole new realm of possibility for determining the point of origin for natural emeralds, and perhaps other mineral species and varieties. Furthermore, because the three most important elements in site-specific chemical heterogeneity are vanadium and nickel, both chromophores and magnesium, which acts like a secondary chromophore by red-shifting the absorption bands, we believe that high-resolution visible absorption spectroscopy could be performed on natural emeralds in place of EDX. Visible absorption spectroscopy, similar to EDX, is a nondestructive analytical technique that can yield a quantitative assessment of an emerald's defined colour; an optical property measured subjectively within conventional emerald valuation processes. When this information is linked to the chemical signature of specific geographical points of origin, visible absorption spectroscopy could be used to discern the geographic origins of an emerald sample in a much more efficient and expeditious manner. We hope to both add to the growing foundation of emerald chemistries in the future through continued sampling and, in conjunction with our growing database, use chromophore data and high-resolution visible absorption spectroscopy to reveal how spectral analysis of natural emeralds may be used to determine the point of origin for samples with unknown provenance.

Acknowledgements

The authors are grateful to several individuals for lending their time and expertise to this work. We thank Jim Barker of the Cleveland State University Fenn College of Engineering for his assistance and guidance in procuring SEM-EDX data. We are indebted to Dr John F. Turner II for all his time, support, and guidance leading to this work. In addition, Dr Turner played an integral role in creating the source code enabling hundreds of analysis of variance to be performed in an expeditious manner; generating the hundreds of statistical results used in this work.

References

Acharya, R.N., Mondal, R.K., Burte, P.P., Nair, A.G.C., Reddy, N.B.Y., Reddy, L.K., Reddy, A.V.R., and Manohar, S.B., 2000. Multi-element analysis of emeralds and associated rocks by ko neutron activation analysis. *Applied Radiation and Isotopes,* **53**, 981–6

Banks, D.A., Giuliani, G., Yardley, B.W.D., and Cheilletz, A., 2000. Emerald mineralisation in Colombia: fluid chemistry and the role of brine mixing. *Mineralium Deposita,* **35**, 699–713

Biondi, J. C., 1990. Depósitos de esmeralda de Santa Terezinha (GO). *Revista Brasileira de Geociências*, **20**, 7–24

Braga, G.C.B., Garg, V.K., De Oliveira, A.C., Freitas, Jr., J.A., Kuzmann, E., and Garg, R., 2002. Optical and Mossbauer study of Brazilian emeralds. *Physica Status Solidi,* **194**, 36–46

Chattopadhyay, D., Galeska, I., and Papadimitrakopoulos, F., 2002. Complete elimination of metal catalysts from single wall carbon nanotubes. *Carbon,* **40**(7), 985–8

Cheilletz, A., Feraud, G., Giuliani, G. and Rodriguez, C.T., 1994. Time pressure-temperature constraints on the formation of Colombian emeralds: an 40Ar/39Ar laser-probe and fluid inclusions study. *Economic Geologist,* **89**, 362–80

Cheilletz, A., and Giuliani, G., 1996. The genesis of Colombian emeralds: a restatement. *Mineralium Deposita,* **31**, 359–64

Coakley, G.J. 2001. The mineral industry of Zambia. United States Geological Survey, Reston, VA

D'el-Rey Silva, L.J.H., and de Souza Barros Neto, L., 2002. The Santa Terezinha-Campos Verdes emerald district, central Brazil: structural and Sm-Nd data to constrain the tectonic evolution of the Neoproterozoic Brasilia belt. *Journal of South American Earth Sciences,* **15,** 693–708

Edgar, A., and Hutton, D.R., 1978. Exchange-coupled pairs of Cr^{3+} ions in emeralds. *Journal of Physics C: Solid State Physics,* **11**, 5051–63

Giuliani, G., Cheilletz, A., Sheppard, S.M.F., and Arboleda, C., 1993. Geochemistry and origin of the emerald deposits of Colombia. In: H.A. Fenoll and G. Torres-Ruiz, eds, 1993. *Current research in geology applied to ore deposits.* Balkema, Rotterdam, pp. 105–8

Giuliani, G., France-Lenord, C., Cheilletz, A., Coget, P., Branquet, Y., and Laumomnier, B., 2000. Sulfate reduction by organic matter in Colombian emerald deposits; chemical and stable isotope (C, O, H) evidence. *Economic Geology,* **95**, 1129–54

Giuliani, G., France-Lanord, C., Zimmerman, J.L., Cheilletz, A., Arboleda, C., Charoy, B., Coget, P., Fontan, F., and Giard, D., 1997. Composition of fluids, δD of channel H_2O and $\delta^{18}O$ of lattice oxygen in beryls: genetic implications for Brazilian, Colombian and Afghanistani emerald deposits. *International Geology Review,* **39**, 400–24

Giuliani, G., Silva, L., and Couto, P., 1990. Origin of emerald deposits of Brazil. *Mineralium Deposita*, **25**, 57–64

Hasan, Z., Keany, S.T., and Manson, N.B., 1986. Spectral energy transfer and fluorescence line narrowing in emerald. *Journal of Physics C: Solid State Physics,* **19**, 6381–7

Howell, D.C., 2002. *Statistical methods for psychology (5th edn).* Duxbury, Pacific Grove, CA

Kanji, G.K., 1993. *100 statistical tests.* Sage Publications, Newbury Park, CA

Kim, I.G., Yeom, T.H., Choh, S.H., Hong, K.S., Yu, Y.M., and Choi, E.S., 2000. ^{27}Al NMR relaxation studies of an emerald single crystal. *Solid State Communication,* **114**, 311–14

Kleiðmantas, A., and Skridlaitë, G., 2004. Emerald and chromaquamarine colour and chemistry dependence on their origin. *Geologija,* **48**, 15–21

Marshall, D., Groat, L., Giuliani, G., Murphy, D., Mattey, D., Ercit, T.S., Wise, M.A., Wengzynowski, W., and Eaton, W.D., 2003. Pressure, temperature and fluid inclusions during emerald precipitation, southeastern Yukon, Canada: fluid inclusions and stable isotope evidence. *Chemical Geology,* **194**, 187–99

Moroz, I., Roth, M., Boudeulle, M., and Panczer, G., 2000. Raman microspectroscopy and fluorescence of emeralds from various deposits. *Journal of Raman Spectroscopy,* **31**, 485–90

Nassau, K., 1978. The origins of colour in minerals. *American Mineralogist,* **63**, 219–29

Parikh, P., Saini, H.L., Dalela, S., Bhardwaj, D.M., Fernandes, S., Gupta, R.P., and Garg, K.B., 2003. Using XAFS, EDAX and AFM in comparative study of various natural and synthetic emeralds. *Nuclear Instruments and Methods in Physics Research B,* **199**, 489–93

Platonov, A.N., Taran, M.N., and Balitsky, V.S., 1984. *Nature of gem colouring.* Nedra, Moscow

Rohlf, F.J., and Sokal, R.R., 1994. *Statistical tables. 3rd edn.* W.H. Freeman, New York

Schwarz, D., and Giuliani, G., 2001. Emerald deposits-a review. *Australian Gemmologist,* **21**, 17–23

Sinkankas, J., and Read, P.G., 1986. *Beryl.* Butterworth and Co., London

Walzak, M.J., Davidson, R., and Biesinger, M., 1998. The use of XPS, FTIR, SEM/EDX, contact angle, and AFM in the characterization of coatings. *Journal of Material Engineering and Performance,* **7**(3), 317–23

Webster, R., and Anderson, B.W., 1983. *Gems: their sources, descriptions and identification, 4th edn.* Butterworth and Co., Boston, MA

Zwaan, J.C., Seifert, A., Vrána, S., Laurs, B.M., Anckar, B., Simmons, W.B., Falster, A., Lustenhouwer, W., Muhlmeister, S., Koivula, J.I., and Garcia-Guillerminet, H., 2005. Emeralds from the Kafubu area, Zambia. *Gems & Gemology,* **41**(2), 116–48

Web list

Istituto di Geoscienze e Georisorse Sezione di Roma-Consiglio Nazionale delle Ricerche (CNR), 2005. Emerald database [online]. Available at: < http://w3.uniroma1.it/ centricnr-cseqmr/emeralds/BRAgeo.htm> [Accessed 27 October 2009]

Laurs, B. (ed.), 2004. Update on gem localities in Zambia and Malawi, Gems & Gemology [online] Available at http://www.gia.edu/gemsandgemology [Accessed 03 August 2010]

Zambian Ministry of Mines and Minerals Development, 2006. Mining in Zambia: Gemstones. [online] Available at <http://www.zambiamining.co.zm> [Accessed March 4, 2008]

The Authors

D.P. Cronin
Cleveland State University, 2121 Euclid Avenue, Cleveland, Ohio, U.S.A. 44115
Email: d.patrick.cronin@gmail.com

A.M. Rendle
1800EMERALD/Rio Verde Group, P.O. Box 31029, Victoria BC Canada V8N 6J3
Email: andy@1800EMERALD.ca

Gem-A Multi-Tester

Capable of testing for all diamond simulants including synthetic moissanite.

- LED colour and audible sound sequence for easy to see and hear test results.
- Metal detector
- Portable — battery operated and comes with carry case
- Can be used with transformer (not supplied)
- Loose metal stone holder

Price: £125.00

plus VAT, postage and packing

DIT0016

A 10% discount is given on all instruments ordered by Gem-A members and Gem-A registered students.

MONTHLY SPECIALS
on books and instruments. Log on to the Gem-A website at www.gem-a.com to discover what is on offer.

To order your Multi Tester from the Gem-A shop go to www.gem-a.com/shop.aspx or contact Alan Clark on +44 (0)20 7404 3334, email shop@gem-a.com

Gem-A
THE GEMMOLOGICAL ASSOCIATION OF GREAT BRITAIN

Morphological and gemmological features of gem-quality spinel from the Goron deposit, southwestern Pamirs, Tajikistan

S.A. Ananyev and S.I. Konovalenko

Abstract: Spinel of gem quality from the Goron deposit, Shakhdarinsky Ridge, southwestern Pamirs, Tajikistan, is described. Its source is an essentially bimineralic spinel-chlorite rock with up to 54% by weight of spinel. Many euhedral crystals have stepped tabular growth surfaces and are up to 20 mm across. Colour is generally homogeneous and may be pink or violet. Ferrous iron is the dominant chromophore, and most crystals are distinctly more violet in daylight and pinker in incandescent light.

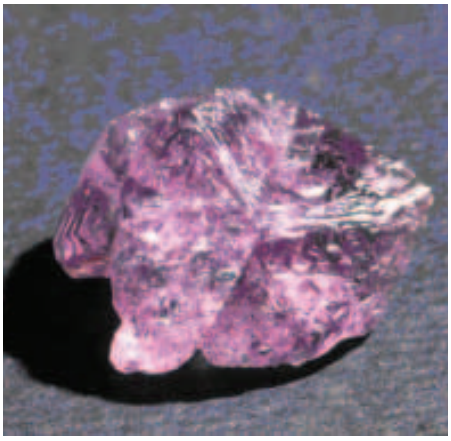

Keywords: colour change, gem-quality spinel, Goron, Pamir mountains, Tajikistan

1. Introduction

In summer 1989 the authors discovered spinel of gem quality in the upper reaches of the Goron River, a left-hand tributary of the Badomdara River which is a left-hand tributary of the Shakhdara River in the Shakhdarinsky Ridge area of the southwestern Pamir Mountains *(Figure 1)*. The locality has the coordinates 37° 05' 22.4" N and 71° 44' 32.7" E at a height of about 5000 m. Exposure is sporadic and depends on snow/ice levels. The geology of this area was described by Konovalenko *et al.* (1991) but gemmological features of the spinels were not included and it is the purpose of this paper to fill this gap. Gem-quality spinel is also known in this general area from Kuh-i-lal which is approximately 30 km distant to the northwest.

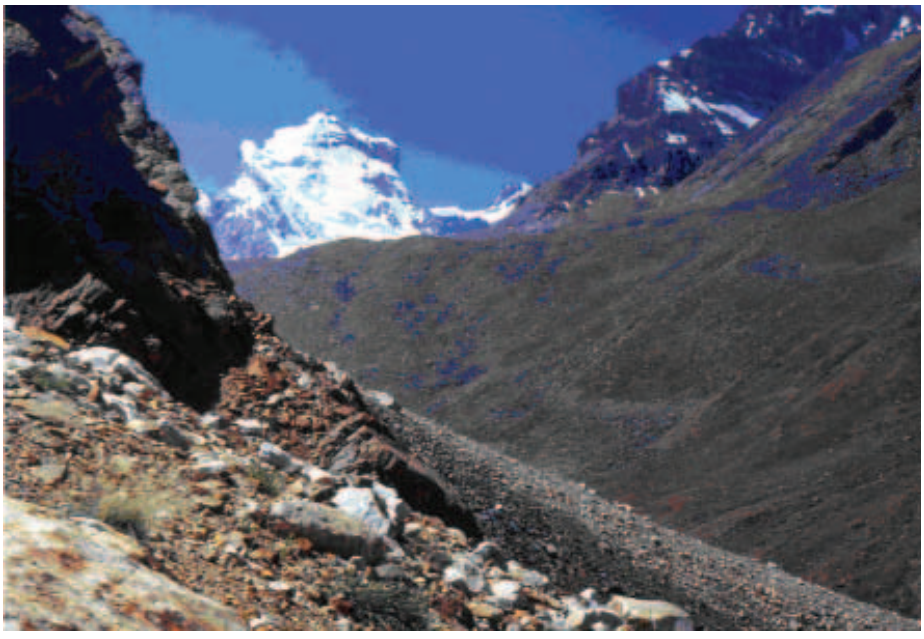

Figure 1: Screes containing rock fragments with gem-quality spinel in the Goron River Valley, southwestern Pamir mountains, Tajikistan. In the distance is the peak Shpil, SW of the spinel locality.

2. Geological background

The Goron spinels occur at the base of the Vakhanskaya horizon in the upper part of the Archaean Goran Series (Konovalenko *et al*., 1991). This horizon consists of pale grey gneiss and migmatite with intercalated thick and extensive calcite-dolomite, dolomite, and dolomite-magnesite marbles, which themselves are the hosts to skarns. The alteration processes in these skarns have produced mineral assemblages consisting of spinel, forsterite, phlogopite and enstatite. In turn and in places, these have suffered further alteration to talc, serpentine and chlorite. The gem-quality spinel is associated with altered forsterite and almost all is now found in bi-mineralic chlorite-spinel pockets and filled cavities or in veins several metres long and up to 0.2 m thick *(Figure 2)*.

By volume the grey-green chlorite (clinochlore) marginally exceeds that of spinel, but by weight, spinel forms about 54% of the rock, with about 1% accessory minerals. Of the latter, the commonest is orange clinohumite which can be present as much-fractured concretions up to 5 cm across. Very much rarer are columnar crystals up to 1 mm across of black ilmenite and, in pockets, a range of low-temperature hydrothermal minerals including aragonite, hydrotalcite and manasseite. At their contacts, some spinel-chlorite clusters can merge into massive green to black-green serpentine rock.

3. Spinel

(a) Morphology

Spinel crystals are commonly octahedral or show twins on (111) planes and have stepped-tabular patterns or structures on their crystal faces; other crystals may be complex aggregates, and many may show traces of partial dissolution (see *Figures 3, 4*). All these habits are strongly idiomorphic to the co-existing chlorite in the rock, and the flakes of chlorite are adjusted to the adjacent spinel plane surfaces with their basal planes oriented along them. This makes the spinel-chlorite assemblage easily processable. Spinel crystals can be manually extracted from the softer chlorite host, leaving 'faceted nests' with complex patterns of imprinted octahedral planes on the walls. Some spinel crystals have narrow, crack-like dips on their surfaces which are filled with chlorite; these are the result of partial dissolution along composition planes or aggregate boundaries. But fractures are rare in the

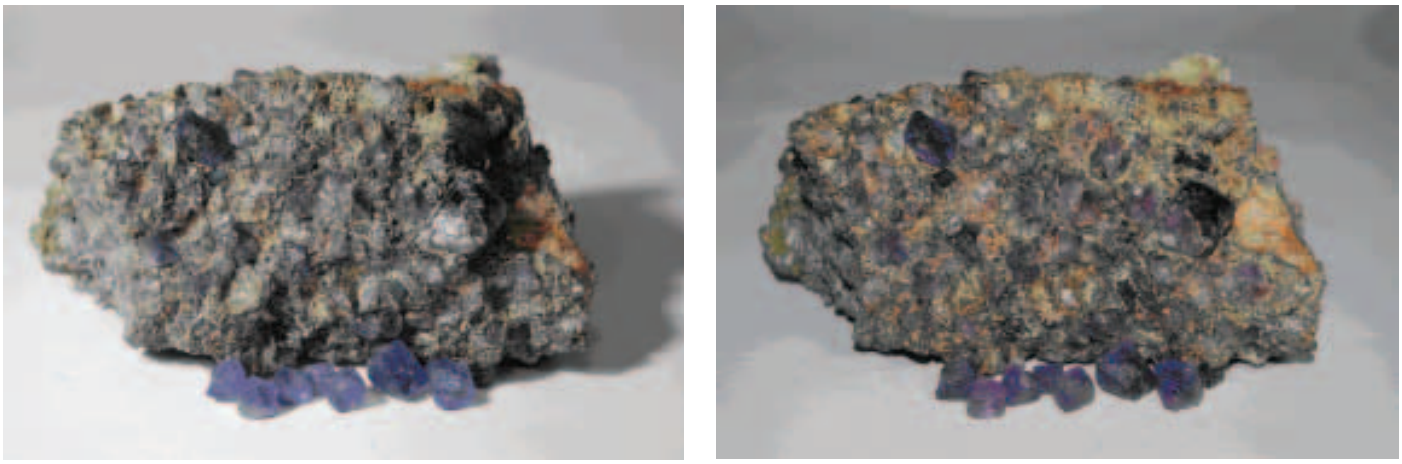

Figure 2: Spinel-chlorite aggregate with some minor clinohumite behind spinel crystals recovered from nearby rocks; the aggregate measures 14×8×7 cm. Photographed in daylight, left, and in incandescent light, right.

Figure 3: Spinels with stepped tabular crystal surfaces.

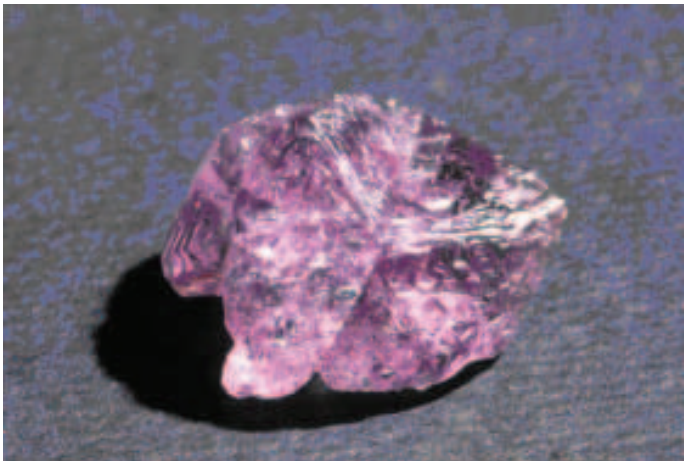

Figure 4: Spinel aggregate showing (111) twin plane and stepped octahedral faces.

Table I: Morphological and weight analysis of spinels from Goron deposit.

Type no.	Morphological types of crystals		Average size mm	Number of crystals	Content of crystals	Weight of crystals	Weight %
1	Octahedrons and octahedron fragments with at least four faces		7–12	11	1.37	16.60	7.89
			5–7	53	6.58	23.68	11.25
			3–5	120	14.91	22.86	10.86
Sub-total:				184	22.96	63.14	29.99
2	Crystal aggregates	Twins	7–15	26	3.23	28.11	13.35
			5–7	45	5.59	20.87	9.91
			3–5	201	24.97	41.74	19.83
		Three individuals	3–10	13	1.61	3.74	1.78
		Four individuals	3–7	2	0.25	0.81	0.38
Sub-total:				287	35.65	95.27	45.25
3	Shapeless crystals		5–10	96	11.93	29.63	14.07
			1.5–5	238	29.57	22.48	10.68
Sub-total:				334	41.49	52.11	24.76
Total:				**805**	**100.00**	**210.52**	**100.00**

spinel crystals and chlorite has not been found as an inclusion.

A sample of typical spinels weighing 210.52 g recovered from 389.85 g of rock from the Goron deposit in 1989 is categorized in *Table I*.

From *Table I* it is clear that in this sample, aggregates and shapeless crystals of spinel predominate. However, approximately a quarter are of gem quality, weighing between 1.5 and 11 ct. The average yield of cut stones from the gem-quality rough is about 20%, but recovery from some larger crystals can reach 40–50%.

(b) Gemmology

The size of the gem-quality spinel crystals ranges from 3 to 20 mm and they are consistently transparent. Their refractive index (RI) is 1.732 ± 0.002 and specific gravity (SG) 3.592. The average of three electron microprobe analyses is as follows:

	Wt.% oxide
TiO_2	0.10
Al_2O_3	71.26
Cr_2O_3	0.01
FeO	2.29
MgO	26.31
MnO_2	0.02
Total	99.99

This corresponds to the formula $(Mg_{.933}Fe_{.044})_{.977}(Al_{2.012}Ti_{.002})O_{3.997}$. The Mossbauer spectrum confirmed that the iron is present as ferrous iron.

The colours of the spinel crystals range from pink to violet and optical spectra obtained using the UMSP-50 spectrophotometer manufactured by Optan (Germany) indicate the presence of two main absorption bands: a narrow weak band at 459 nm and broader band centred at 560 nm. Any possible peaks attributable to Ti, Cr or Mn were not detected. However, a moderately intense emission band at 520–540 nm in the X-ray emission spectrum is attributed to Mn. This emission also occurs in the cathodoluminescence of spinel which glows green.

Many Goron spinels also show an alexandrite effect *(Figure 2)*. In daylight they are violet-blue but in incandescent light they show a distinct red component – making them violet-pink and more attractive as an 'evening stone'. Although rare, similar spinels are known from Tanzania, Sri Lanka and Madagascar (e.g. see *Modern Jeweler*).

The gem-quality spinels are generally free of inclusions but some contain tiny round grains which appear to be spinel rather than zircon or forsterite. Others can contain probable cavities that are at the centre of clusters of thin radial channels *(Figure 5)* which can reach the surfaces of some crystals and terminate in pyramidal-shaped depressions. The channels could have been formed by dissolution along dislocations in the crystal structure, and this kind of feature has been reported in diamond (Orlov, 1984).

4. Comparison with spinels from Kuh-i-lal

The host rocks of the spinels at both Goron and Kuh-i-lal are forsterite-bearing skarns but while the Goron rocks contain abundant chlorite and some clinohumite which is not of gem quality, any chlorite at Kuh-i-lal has been replaced by snow-white aggregates of lizardite serpentine,

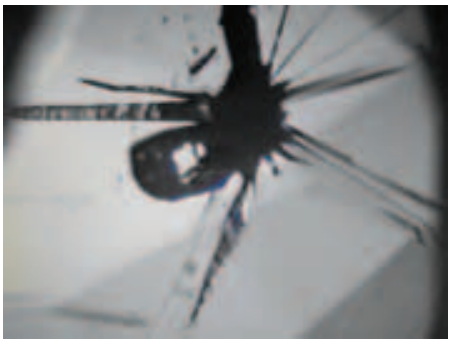

Figure 5: Inclusion typical of spinel from this locality in which a probable cavity is at the centre of a radial array of empty channels. The width of the field of view is 3 mm.

Figure 6: Spinel crystal flanked by a round-cut spinel of 4.61 ct with 73 facets (left) and a modified triangular-cut spinel of 3.12 ct (right).

Figure 7: Necklace pendant and earrings set with Volyn topaz from the Ukraine, spinel from Goron and brilliant-cut diamonds.

hydrotalcite and manasseite. Also at Kuh-i-lal, low temperature alteration processes seem to have involved intense dissolution of the surfaces of gem-quality varieties of spinel, forsterite and clinohumite .

5. Conclusion

Two cut spinels from Goron flanking a crystal from that deposit are shown in *Figure 6*, and similar stones set in jewellery are shown in *Figure 7*. The spinels are generally very homogeneous in colour and take a good polish. They also show good transparency and only rarely contain clusters of radial channels or barely-visible twin planes. The stones shown were cut from our collection and, so far as we know, inaccessibility of the site and lack of infrastructure in the area has precluded any commercial development.

References

Konovalenko S.I., Ananyev S.A., Vasilyev E.R., Garanin V.K., and Kudryavtseva G.P., 1991. Finding chlorite rocks with noble spinel in magnesian skarns (Southwestern Pamirs). *Geology of Ore Deposits,* **6**, 100–3

Orlov Yu.L., 1984. *Diamond mineralogy.* 2nd edn. Nauka, Moscow. p.170

Web list

http://www.modernjeweler.com/online/gemProfile.jsp. Click on August 2009 article by D. Federman entitled Color-change spinel; accessed June 2012

All photographs by S.A. Ananyev.

The Authors

S.A. Ananyev
Mining, Geology and Geotechnology Institute, Siberian Federal University, Krasnoyarsk, Russia
Email: sananiev@mail.ru

S.I. Konovalenko
Tomsk State University, Tomsk, Russia
Email: konov@ggf.ru

Orangey-red to orangey-pink gem spinels from a new deposit at Lang Chap (Tan Huong-Truc Lau), Vietnam

A.-K. Malsy, S. Karampelas, D. Schwarz, L. Klemm, T. Armbruster and D.A. Tuan

Abstract: Gem spinels from a new source at Lang Chap, Vietnam, have been investigated for their gemmological, spectroscopic and chemical characteristics. The Lang Chap mining site produces spinels of orangey-red colour with inclusions and chemical composition which closely resemble similar coloured spinels from Myanmar. Experimental heat treatment at 850°C of one test sample resulted in reduction of the orange component of its colour. XRD, Raman and PL spectra indicate some disorder in the spinel structure after heating.

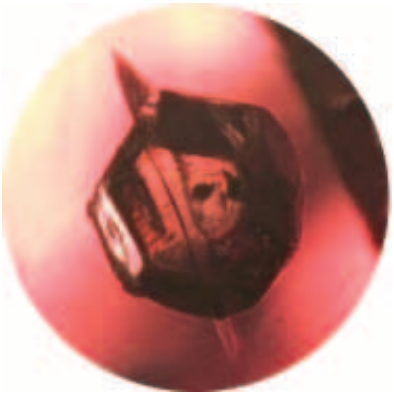

Keywords: colour, heat treatment, Lang Chap, photoluminescence, Raman, spinel, UV-Vis-NIR, Vietnam

Introduction

In the gem market, spinels have 'recovered' and become more popular during the last decade. The vast majority of gem-quality spinels have a composition of spinel *sensu stricto*, i.e. magnesium-aluminium spinel ($MgAl_2O_4$). Among the most popular are those in the red to pink range. In Nature, they are commonly associated with rubies and occur in metamorphic rocks such as gneisses, marbles or calc-silicates. Most gem spinels available on today's market have been mined from primary and secondary deposits in Sri Lanka, Myanmar (Mogok and Namya), Vietnam (Luc Yen area), Madagascar (Ilakaka region), Tajikistan (Pamir Mountains: Kuh-i-Lal) and Tanzania (Morogoro and Mahenge) as stated by Shigley *et al.*, 2010 (see also references therein).

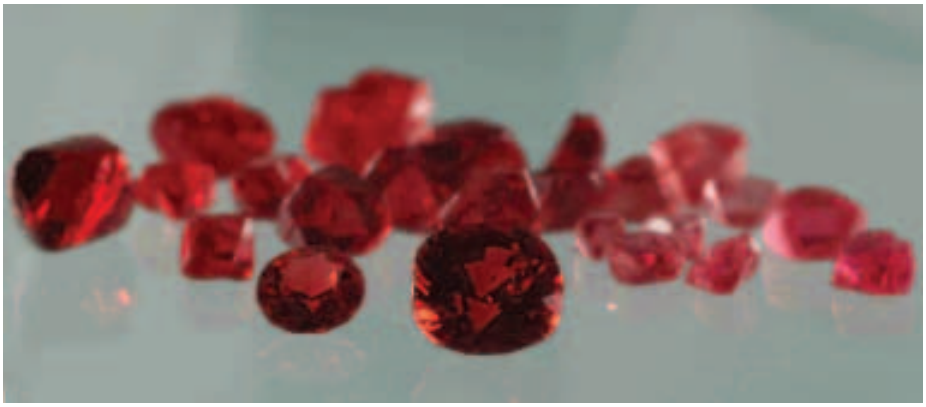

Figure 1: Spinels from the new Lang Chap mine in Vietnam, varying in colour from orangey-red to orangey-pink. The two faceted stones at the front weigh 0.4 and 1.3 ct and represent typical colours of spinels from this mine.

Some orangey-red to orangey-pink spinels *(Figure 1)* from a new alluvial deposit in Northern Vietnam have recently reached the market (Blauwet, 2010). The new deposit is situated at Lang Chap (22° 05' 86" N, 104° 34' 83" E), in the northern part of Yen Bai Province *(Figure 2)* and was discovered around April 2010 (Blauwet, 2011). The mining is on a small scale, operated by locals using primitive equipment, and a detailed description of the mining site is given by Blauwet

Orangey-red to orangey-pink gem spinels from a new deposit at Lang Chap (Tan Huong-Truc Lau), Vietnam

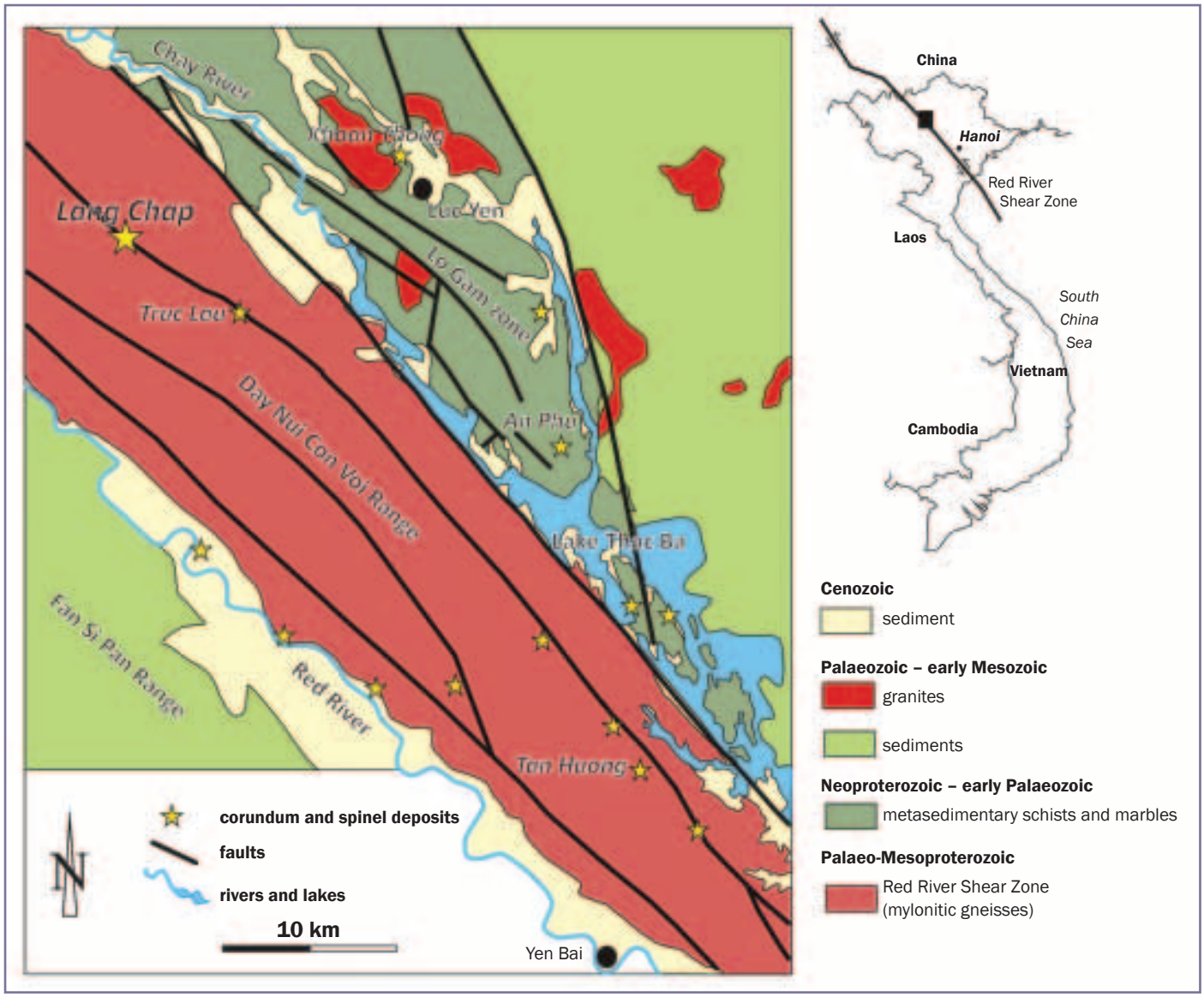

Figure 2: Geological sketch map showing the major tectonic units north of Yen Bai and location of corundum and/or spinel deposits (modified after Garnier et al.*, 2005, and Khoi* et al.*, 2011).*

(2010). In October 2010, when some areas around the mining region were visited by one of the authors (SK), less than 50 people were mining there. The mine sporadically produces spinels of excellent red colour.

In northern Yen Bai province *(Figure 2)*, the Chay River runs (NNW-SSE) through the Luc Yen district; primary and secondary deposits of gem quality corundum and spinel have been found on both sides of the river (Khoi *et al.*, 2011). The first deposits on the east side of the river were discovered in the eighties (Khoan Thong-An Phu mining regions); deposits on the west side (Tan Huong-Truc Lau mining regions) were discovered in the mid-nineties. The latest discovery of spinels described above is situated NW of Truc Lau, at Lang Chap.

The Khoan Thong-An Phu deposits are located on the eastern side of the Red River shear zone, within the Lo Gam tectonic zone (see again *Figure 2*) which consists of moderately to highly metamorphosed (amphibolite-facies) schists, gneisses and marbles (Phan Trong and Hoáng Quang, 1997). Primary spinel together with ruby occurs within marbles (Van Long *et al.*, 2004). The Tan Huong-Truc Lau mining region is situated within the Dai Nui Con Voi range consisting of high-grade (amphibolite-facies) metamorphic rocks with sillimanite-biotite-garnet gneisses and schists with local successions of marbles and amphibolites (Van Long *et al.*, 2004). The mountain range is bordered by large-scale lateral strike-slip faults forming the Red River shear zone.

Since their discovery there have been recurrent market rumours saying that Lang Chap spinels have been misleadingly identified as spinels from Myanmar. So, the present study was carried out to establish the chemical and spectroscopic characteristics of orangey-red to orangey-pink spinels from the new deposit at Lang Chap, and compare them with those previously reported by Malsy and Klemm (2010) on similarly coloured spinels

Table I: List of samples investigated.

Sample name		Colour	Weight [ct]	Condition
SPVNNM1		orangey-red	0.4	faceted
SPVNNM3		orangey-red	1.3	faceted
SPVNNM2/4		orangey-red	2.3/1.6	polished
SPVNL39–51		orangey-red	0.3–2.2	polished
SPVNL52–59		orangey-red	0.7–2.1	polished
SPVNL60		purple-red	4.6	polished
SPVNL61		purplish-red	3.5	polished
SPVNL62		pinkish-orangey-red	1.8	polished
SPVNL70	unheated	orangey-red	1.9	polished
	heated	red	1.8	
SPVNL66		orangey-pink	1.0	polished

from the Himalayan belt, i.e. Myanmar (Mogok), Vietnam (Luc Yen: Koan Thong-An Phu) and Tajikistan (Kuh-i-Lal). Some additional samples from Namya (Myanmar) have also been included in this study for comparison.

Moreover, heat treatment has been performed on one sample to examine its effect on the spinel's colour, transparency, spectral and structural features.

Materials and methods

For the present study, Dr Havy Le Thi-Thu Huong of the Vietnam National University, Hanoi, and Vietphuong/VPGemstones Co. Ltd. (Vietnamese mining company with retail shops in Hanoi and Bangkok) provided 30 spinels, which were stated to be from Lang Chap. Most samples are of gem quality, weighing from 0.3 to 22 ct in a wide range of colours from orangey-red to orangey-pink, although two have a purple component in their colour (see *Table I*). One homogeneously coloured orangey-red spinel (SPVNL 70) was cut in half: one part was heat treated, and the other was kept as the non-heated reference stone (see below for information on the heat treatment conditions).

Standard gemmological instruments were used to observe long- and short-wave UV fluorescence (365 and 254 nm wavelength, respectively), and to measure refractive indices (RIs) and birefringence. Specific gravity (SG) was determined using the hydrostatic method with an electronic balance. The internal structures and inclusions of the samples were studied with various gemmological microscopes. Inclusion microphotographs were taken with a Keyence VHX-500F digital microscope at the Institute of Geological Sciences of the University of Bern, Switzerland (IGSUB).

Absorption spectra in the 200–900 nm range were recorded at the Gübelin Gem Lab (GGL, Lucerne, Switzerland) on eight natural colour spinels and one heat-treated sample, with a Cary 5000 Ultra-Violet-Visible-Near Infrared (UV-Vis-NIR) spectrometer. The data sampling interval (DI) and spectral bandwidth (SBW) of each measurement were 0.7 nm; the scan rate was 60 nm/min.

Raman spectra were acquired on all spinels as well as on their inclusions, wherever accessible, using a Renishaw Raman 1000 spectrometer coupled with a Leica DMLM optical microscope at GGL. All spectra were recorded using an excitation wavelength of 514 nm emitted by an argon ion laser (Ar^+) and most were taken using standard mode (with ×50 magnification); however, confocal mode (with ×100 magnification) was used on some inclusions. Raman spectra were acquired from 200 to 2000 cm^{-1} using a power of 5 mW on the sample, with an acquisition time of 60 seconds (3 cycles) and about 1.5 cm^{-1} resolution. Rayleigh scattering was blocked by a holographic notch filter, the backscattered light was dispersed on an 1800 grooves/mm holographic grating and the slit was set at 50 µm. For the identification of mineral inclusions the spectra were compared with those from the GGL database as well as with spectra available from RRUFF (www.rruff.info). Photoluminescence (PL) spectra (laser induced) from 600 to 800 nm were acquired using the same instrument (×50 magnification) on all samples, most using a power of 1 mW and the remainder using 0.1 mW and 1 second acquisition time; spectral resolution is 0.1 nm.

Minor and trace elements of all the samples were measured by laser ablation inductively coupled plasma mass spectrometry (LA-ICP-MS). All analyses were performed at GGL on a Perkin Elmer ELAN DRC-e single collector quadrupole mass spectrometer combined with a 213 nm CETAC LSX-213 Nd:YAG laser ablation system. A set of four single-spot analyses (100 μm diameter) was collected on each sample with a laser frequency of 10 Hz. Multi-element glass standard reference material NIST610 was used for external standardization; internal standardization was done by normalizing to 100% cations of stoichiometric spinel. Detailed information on the instrument setting and data processing has been described by Malsy and Klemm, 2010. Mineral inclusions, which intersected the sample surface, were also identified using this method.

A chamber furnace (VMK 250 by Linn High Therm Gmbh) at IGSUB, Switzerland, was used for the heat treatment of one sample (SPVNL 70) in an oxidizing atmosphere. The sample was cut in two halves; one was kept as reference and the heat-treatment was applied to the other half. The oven temperature was raised (heating rate 3.5–4.2°C/min) to 850°C, kept at this temperature for 56 hours, and subsequently cooled to ambient temperature at a rate of 1.7°C/min. Unit cell dimensions and crystal structure parameters were determined on both heated and unheated halves of the sample with an Enraf-Nonius CAD4 single-crystal diffractometer using Mo$K\alpha_1$ radiation (λ = 0.70930 Å) at IGSUB.

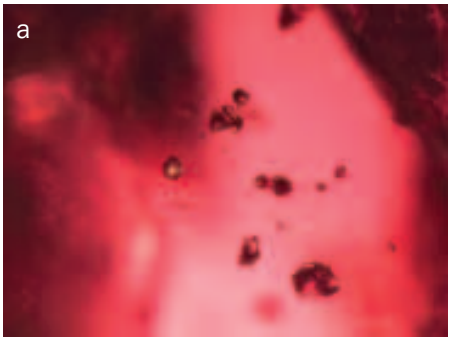

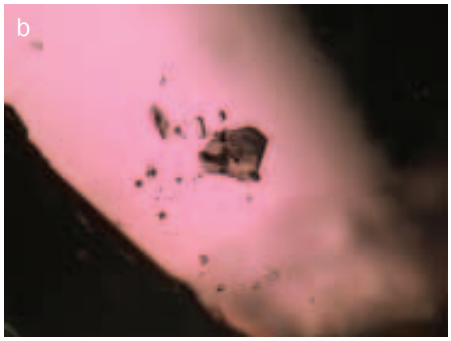

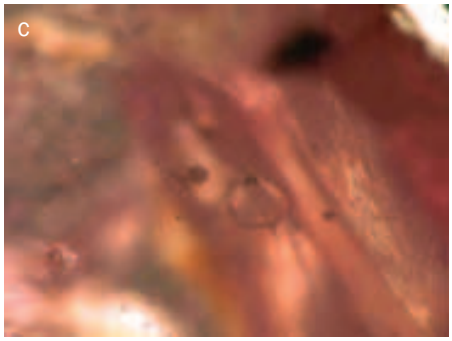

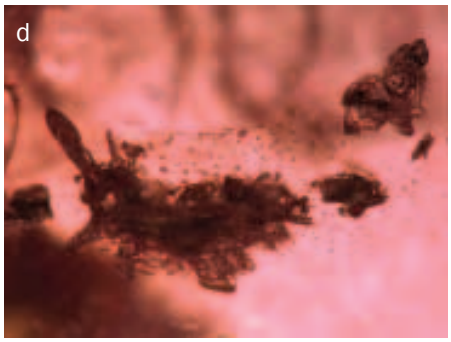

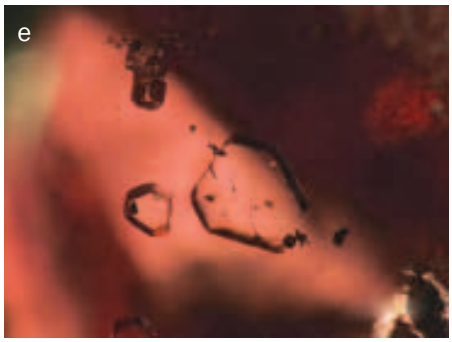

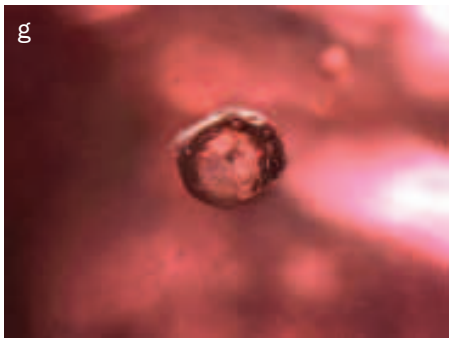

Figure 3: (a) Negative crystals of octahedral shape, which are partly filled with either dolomite or dolomite and calcite. Field of view width about 1.2 mm.
(b) Cluster of small rounded to prismatic transparent dolomite inclusions and a cavity which is filled with dolomite plus calcite. Field of view width about 1.3 mm.
(c) Rounded to nearly spherical calcite inclusion with an 'attached' black graphite platelet. Field of view width about 1.5 mm.
(d) Cavities associated with healed fissures with small fluid inclusions. Field of view width about 1.5 mm.
(e) Group of transparent tabular phlogopite inclusions. These are accompanied by 'attached' black hexagonal or irregularly shaped graphite platelets. Field of view width about 1 mm.
(f and g) Chondrodite inclusion with well-developed crystal faces and accompanied by a perfectly equatorial tension disc (f). The dark area in the central part of the crystal has been identified as mix of carbonate inclusions. Rounded chondrodite inclusion with a dark spot within the crystal (g). Field of view width about 1.3 mm (f) and 1.1 mm (g).

Results

Gemmological and internal features

Table II summarizes our recording of the gemmological and internal features of spinels from Lang Chap. The RI, SG and fluorescence reactions are consistent with those already reported for gem spinels (see, for example, Malsy and Klemm, 2010).

Internal features characteristic of Lang Chap spinels are shown in *Figure 3a–f*. Carbonate-filled negative crystals of octahedral or strongly distorted octahedral shapes of varying size are the most common inclusion feature (see *Figure 3a*). These were found to be filled with magnesite, dolomite or calcite (or a combination of these minerals), presenting a whitish, turbid or 'frosted' aspect. Rarely, dolomite occurs next to apatite. Negative crystals are commonly surrounded by tiny stress fissures giving them a 'frayed' aspect. Dolomite inclusions may also be present in a variety of other habits ranging from prismatic to substantially rounded *(Figure 3b)*. Calcite inclusions are common as transparent rounded grains *(Figure 3c)* and rare as euhedral crystals. Cavities and negative crystals are associated with healed fissures which contain isolated fluid inclusions *(Figure 3d)*. Healed fissures have poorly developed texture in the sense that network-like or fingerprint patterns are not developed. Few samples revealed healed fissures with fluid inclusions arranged on straight or curved lines. Phlogopite is typically present as colourless, pseudohexagonal platy to tabular crystals, with no preferential

Table II: Summary of gemmological properties of Lang Chap spinels.

Colour	orangey-red to orangey-pink
RI	1.718 ± 0.02
SG	3.58 ± 0.02
UV fluorescence long wave short wave	 weak to medium; red inert to faint; red
Mineral inclusions[1]	dolomite
	calcite
	magnesite
	graphite
	phlogopite
	chondrodite
	apatite

[1] Mineral inclusions identified by Raman spectroscopy and/or LA-ICP-MS.

Figure 4: (a) Group of negative crystals. (b) Reflective tension cracks have been induced by the heating process (similar position to 4a). (c) Graphite platelet surrounded by a discoidal tension crack indicating a thermal treatment. Field of view widths: (a) and (b) about 1.1 mm; (c) about 1.3 mm.

orientation relative to the host spinel structure *(Figure 3e)*. The phlogopite crystals show wide variation in size and are commonly accompanied by graphite platelets. Generally, irregularly shaped to well-developed hexagonal, black graphite platelets are present either isolated or in contact with other mineral inclusions *(Figures 3c* and *e)*. Inclusions of chondrodite (a member of the humite-group of minerals), with the general formula $(Mg,Fe^{2+})_5(SiO_4)_2(F,OH)_2$, are present in one third of the spinels studied; some are euhedral and others are rounded *(Figure 3f)*. Many have a dark spot near their centres, identified as carbonate in some, but as yet unidentified in others.

In the heat-treated spinel sample, microscopic observation of the same inclusion scene, before and after treatment *(Figure 4a–b)* clearly indicates alterations caused by the heating process: some mineral inclusions turned white and hazy, there are additional reflective tension fissures, and a graphite inclusion is surrounded by a discoidal tension crack *(Figure 4c)*.

UV-Vis-NIR, XRD, Raman and PL spectroscopy

Figure 5 shows the UV-Vis-NIR spectra of natural coloured orangey-red (SPVNL 43) and orangey-pink (SPVNL 66) spinels in the range from 250 to 900 nm. Absorption bands are present in the violet-blue and green regions of the electromagnetic spectrum, at about 400 nm and 550 nm, respectively. They are present in both samples, and are responsible for the colour. Both absorption bands are superimposed on a continuous absorption which increases from the near-infrared (NIR) region through the visible range to a complete cut-off below 300 nm (UV region). These characteristics are the same as in similar-coloured spinel from Myanmar *(Figure 5)*.

In *Figure 6*, the UV-Vis-NIR spectra of the one spinel that was subjected to heat treatment (SPVNL 70) are shown. After heating, a slight decrease and shift of the continuous absorption as well as a slight shift of the band from about 540 nm to 550 nm is visible in the red spectrum.

Raman spectra of the unheated and heated specimens are shown in *Figure 7*. The main band at about 405 cm^{-1} and the less intense bands at about 310, 665 and 765 cm^{-1} are present in both samples. All untreated spinels examined in this study presented similar spectra. In the

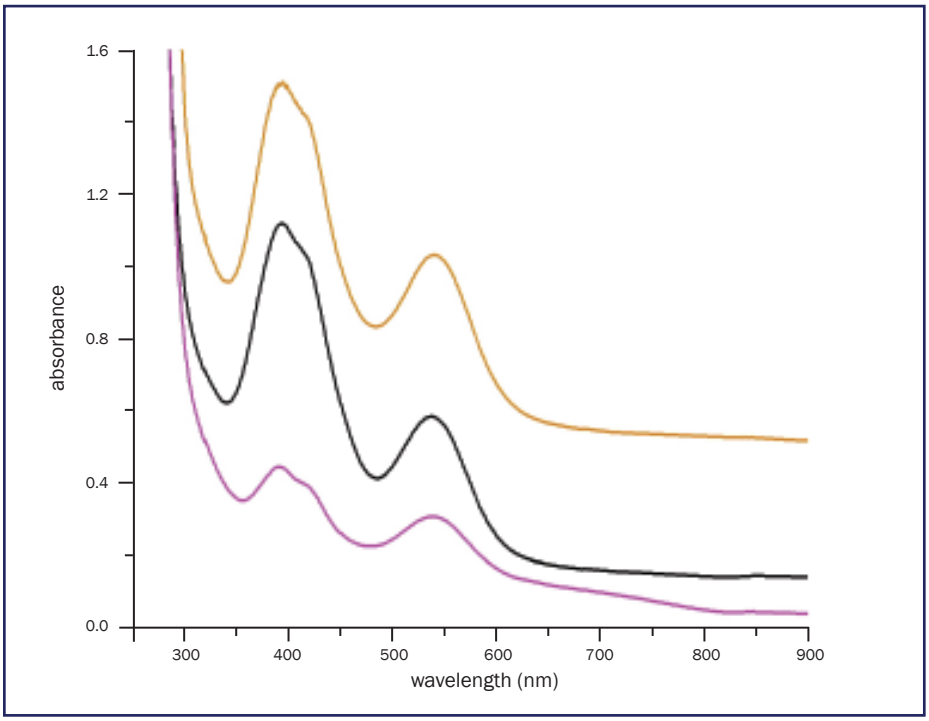

Figure 5: UV-Vis-NIR spectra from 250 to 900 nm of a natural-colour orangey-pink (SPVNL 66; purple line — V_2O_3: 0.23 wt%, Cr_2O_3: 0.20 wt%, Fe_2O_3: 0.38 wt%), an orangey-red spinel from Lang Chap (SPVNL 43; black line — V_2O_3: 0.61 wt%, Cr_2O_3: 0.47 wt%, Fe_2O_3: 0.37 wt%) and an orangey-red spinel from Mogok (orange line — V_2O_3: 0.60 wt%, Cr_2O_3: 0.46 wt%, Fe_2O_3: 0.35 wt%). An absorption band centred at about 400 nm (with two apparent maxima at about 390 and 410 nm) and one centred at about 550 nm are present in all three spectra. Continuous absorption increases steadily from 900 nm to a cut-off below 300 nm. All absorption features are less intense for the orangey-pink compared to the two orangey-red samples. The spectra have been corrected to compensate for differences in sample thickness. The top spectrum is shifted about 1 and the middle spectrum 0.2 absorbance units for convenience.

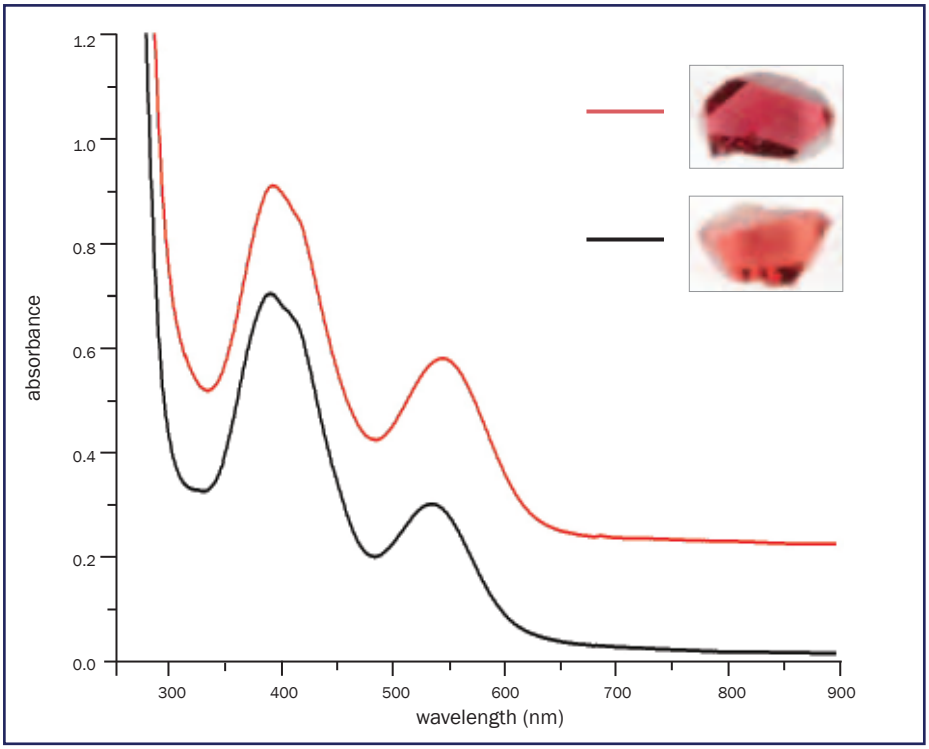

Figure 6: UV-Vis-NIR spectra from 250 to 900 nm of spinel SPVNL 70; unheated part (black line) and heated (red line). A slight decrease and shift of the continuous absorption and a slight shift of the band at about 540 nm to 550 nm after heating are visible. To validate comparison, the spectra are normalized to compensate for any difference in path length of light through the samples. The spectrum of the heated sample is shifted 0.2 absorbance units upwards to avoid overlap.

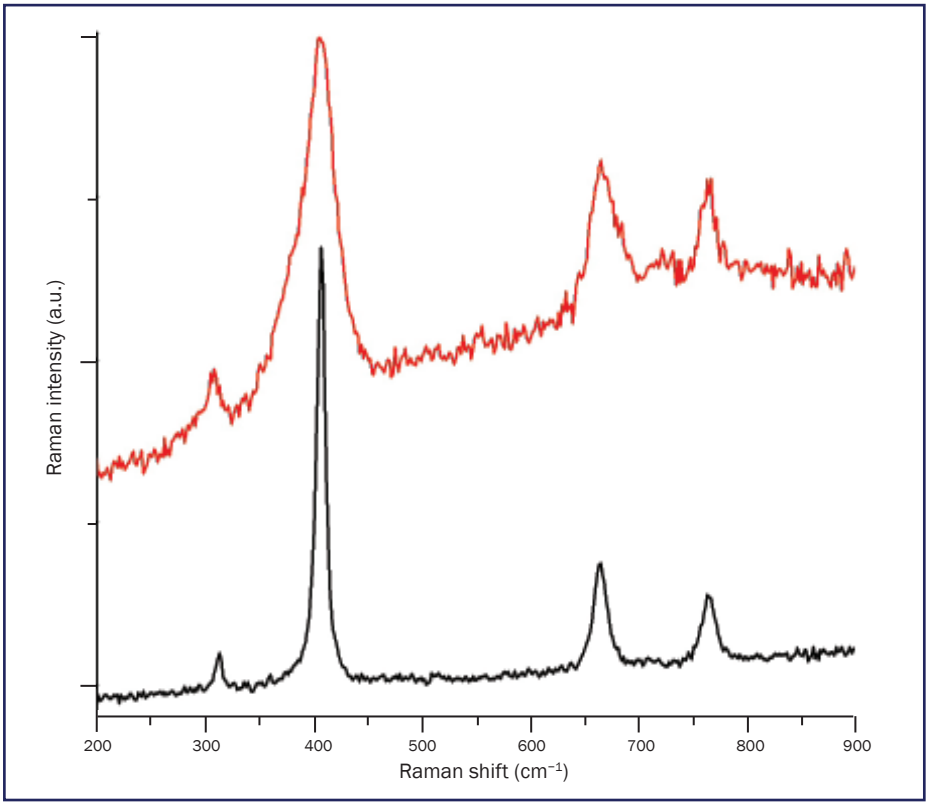

Figure 7: Raman spectra from 200 to 900 cm^{-1} of spinel SPVNL 70; unheated part (black line) and heated (red line). The Raman bands are wider after heating. Intensities of the spectra are normalized to the main band. The upper spectrum is shifted upwards for convenience.

heat-treated sample the Raman bands are slightly wider (i.e. larger full width at half maximum (FWHM)) and some bands (e.g. at 405 cm^{-1}) seem to consist of more than one component. Photoluminescence (PL) spectra of the stones *(Figure 8)* show a principal peak at about 685 nm and some less intense side bands. On heat treatment, the narrow bands in the black spectrum visibly broaden to those in the red spectrum and the largest peak shows a slight shift of centre to 688 nm.

An X-ray single crystal study of the unheated sample yielded a cell dimension a = 8.0902(2) Å, which, on heat treatment, decreased to a = 8.0891(2) Å. Also, more significantly the oxygen parameter u = 0.26342(6) changed to 0.26218(6).

Chemical composition

LA-ICP-MS data for selected elements, given as ranges, mean values and standard deviations are shown in *Table III*. The elements V, Cr, Fe and Zn are present in concentrations from 0.1 to a maximum of 0.7 wt% oxides, whereas Ga and Ti contents are significantly lower. With the exception of Ti, the homogeneity of these elements within all individual samples is quite high (variation <15%). Elements such as Li, Be, Mn, Co, Ni, Cu and Sn were detected as traces (<100 ppmw) only, but Ge, Zr, Sr, Nb, Mo and Pb were below the detection limit of the method.

Discussion

Characteristics of Lang Chap spinels

From our 30 samples and from other stones seen on the gem market in Luc Yen by one author (DS), it can be concluded that the Lang Chap mines principally produce strongly saturated 'blazing' orangey-red to orangey-pink spinels. Lang Chap spinels host a large variety of mineral inclusions and those identified in this study include phlogopite, graphite, dolomite, calcite, magnesite, apatite and chondrodite. These inclusions strongly indicate these spinels to originate from a marble host rock.

Observed absorption features in the UV-Vis-NIR range can be attributed to

V^{3+} (apparent maxima at about 390 and 560 nm) and to Cr^{3+} (apparent maxima at about 410 and 540 nm), both at octahedral sites (Schmetzer *et al.*, 1989). Orangey-red spinels from Lang Chap characteristically contain higher V_2O_3 than Cr_2O_3 (V_2O_3/Cr_2O_3 up to 3.5). Spinels of this colour type have been also described from Mogok (Schmetzer *et al.*, 1989) and Namya (Peretti and Günther, 2003), Myanmar.

Comparison with spinels from other deposits

Spinels from Lang Chap differ in many aspects from those described from mines around Luc Yen (Koan Thong-An Phu mining regions). Inclusion features typically observed in 'Luc Yen spinels', such as dislocation channels and 'blades' of högbomite (see Gübelin and Koivula, 2005, pp. 662–714), zircon and titanite (Malsy and Klemm, 2010), have not been found in our 30 samples. On the other hand, chondrodite and phlogopite inclusions have not been found as inclusions in 'Luc Yen spinels'. Spinels from Tajikistan (Kuh-i-Lal) are generally poorly included, but they do contain some cavities of octahedral shape which look different from Lang Chap inclusions, rarely zircon inclusions and tabular to prismatic colourless mineral inclusions, as yet unidentified (Malsy and Klemm, 2010). Internal features of spinels from Mogok may look very similar to those in Lang Chap spinels, and calcite, dolomite, magnesite, phlogopite and chondrodite may be present in samples originating from both sources. 'Belly button' inclusions, which describe the appearance of a rounded apatite 'decorated' with black graphite or ilmenite (Gübelin and Koivula, 2005), have hitherto been considered as diagnostic for spinel from Mogok *(Figure 9)*, but some inclusions (calcite but not apatite) with attached graphite contained in Lang Chap spinels (e.g. *Figure 3c*) look quite similar and can be confused with those observed in the Mogok spinels. For Namya spinels, octahedral negative crystals, transparent rounded mineral inclusions, and particles or needles have been described (Peretti and Günther, 2003).

Based on their minor element contents, Lang Chap spinels can be distinguished from Luc Yen spinels by their lower Fe contents *(Figure 10)* and lower Li, Be, Mn, ± Co, ± Ni. Spinels from Tajikistan characteristically have slightly higher Fe/Sn ratios and lower Ni contents compared to Lang Chap spinels. However, values of these elements in spinels from Myanmar (Mogok and Namya) widely overlap those of Lang Chap spinels (see again *Figure 10*). Moreover, an overlap is also observed for all other elements and their ratios.

Table III: Minor and trace element contents of Lang Chap spinels obtained using LA-ICP-MS and given as ranges, mean values (Mean) and standard deviations (Sdev).

wt.%	Range	Mean + Sdev
V_2O_3	0.213 – 0.700	0.505 ± 0.136
Cr_2O_3	0.142 – 0.688	0.362 ± 0.148
Fe_2O_3	0.103 – 0.410	0.237 ± 0.095
ZnO	0.103 – 0.522	0.268 ± 0.097
ppmw		
Li	0.50 – 17	4.2 ± 3.5
Be	1.34 – 12	3.7 ± 1.8
Ti	40 – 350	155 ± 57
Mn	4.0 – 14	5.8 ± 1.8
Co	0.23 – 2.7	1.2 ± 0.66
Ni	<0.49 – 64	5.3 ± 9.2
Cu	<0.16 – 2.3	0.46 ± 1.1
Ga	87 – 339	188 ± 46
Sn	0.21 – 1.8	0.77 ± 0.40

Notes: ppmw = parts per million by weight; < = value below the detection limit.

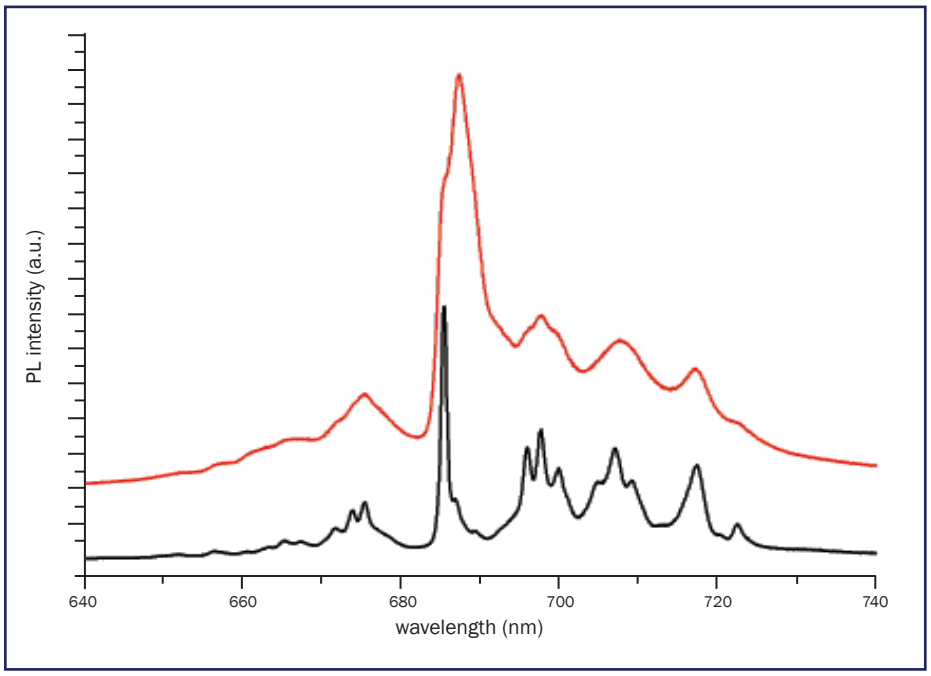

Figure 8: Photoluminescence (PL) spectra from 640 to 740 nm of Lang Chap spinel; unheated part (black line) and heated (red line). The PL pattern in the black spectrum with a main band at about 685 nm and numerous less intense side bands is characteristic for spinels which contain Cr^{3+}. On heating, all bands are broader and the main band shows a slight shift to about 688 nm. The upper spectrum is moved upwards for clarity.

Effects and detection of heat treatment

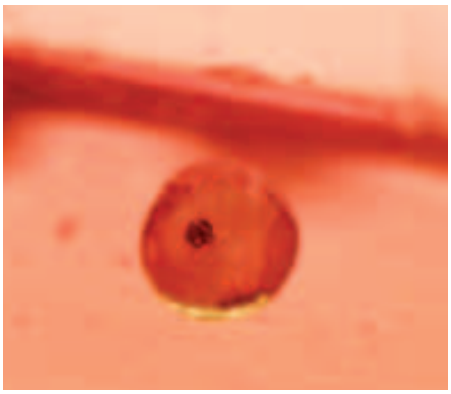

Figure 9: Typical 'belly button' inclusion in a spinel from Mogok, Myanmar. The central rounded crystal is apatite with small black graphite. See also Figure 3c for comparison. Field of view width about 0.3 mm.

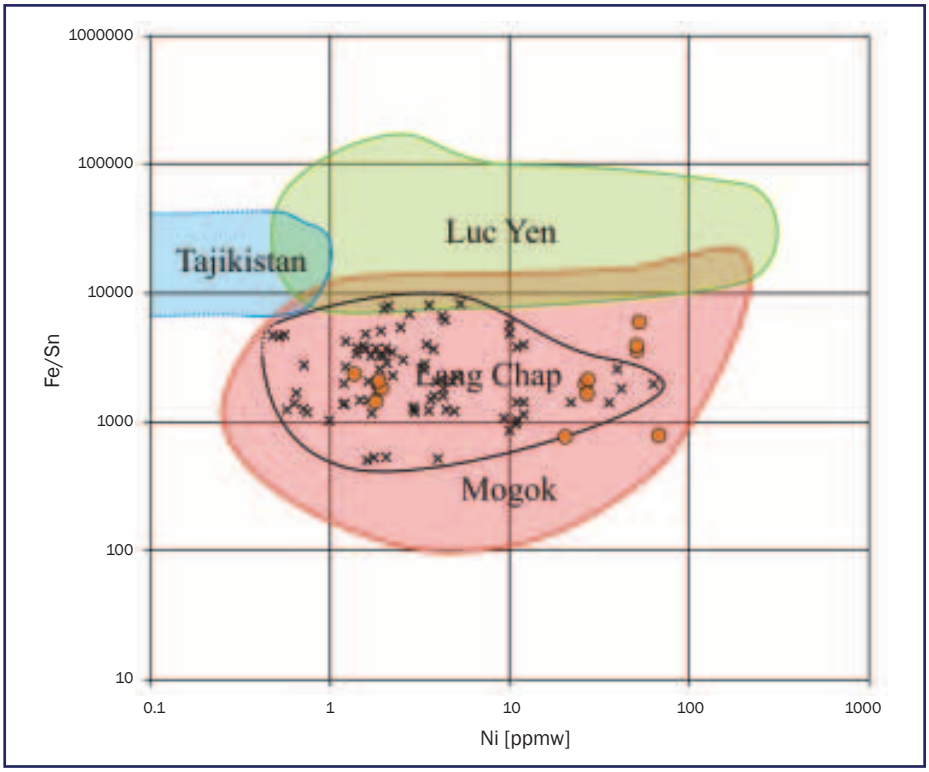

Figure 10: Plot of Ni [ppmw] versus the Fe/Sn ratio from LA-ICP-MS data, adapted from Malsy and Klemm (2010). Dotted lines represent values at the detection limit for the corresponding measurement. Lang Chap spinels differ from other Vietnamese spinels from Luc Yen in having lower Fe/Sn ratios; only a slight overlapping of the two clouds is visible. However, Lang Chap spinels have Ni contents and Fe/Sn ratios similar to those in Mogok and Namya (orange circles), Myanmar, stones.

The heat treatment of spinel from Lang Chap at 850°C in an oxidizing atmosphere caused colour alteration mainly observable as a decrease of orange hue. The observed differences in comparative UV-Vis-NIR spectra (see *Figure 5*) are in accordance with the macroscopic observations. The shift of the absorption band on heating from 540 nm to a longer wavelength and the unchanged position of the absorption at about 400 nm are in accordance with previous findings by Hoang *et al.* (2001). Microscopic examination of inclusions can yield conspicuous signs of heat treatment such as tension cracks often in a 'halo' formation surrounding an inclusion (see, for example, corundum described by Themelis (2003)). These features are generally accepted as strong indicators for heat treatment, but if a gem such as spinel contains very few inclusions, additional criteria for the detection of heat treatment are needed.

The relatively wide Raman bands in the heat-treated spinel spectrum in *Figure 7* are clearly visible. FWHM of the main band at 405 cm^{-1} broadened from about 10 to 30 cm^{-1} after the heating process. Similar observations in Raman spectra have been reported for heat-treated and synthetic high-temperature spinel by Cynn *et al.* (1992), Lazzeri and Thibaudeau (2006) and Saeseaw *et al.* (2009). The latter authors attributed these broadened bands to disorder in the spinel structure caused by the heating process or by high temperature synthesis.

All the PL bands are broader in the spectrum of the heated spinel in *Figure 8*. Moreover, the centre of the most intense band shifts from about 685 nm to about 688 nm and the side band becomes more intense compared with the main band. These changes suggest that the spinel has a more disordered structure after heating (Wood *et al.*, 1968; Tijero and Ibarra, 1993; Mohler and White, 1995). Similar PL observations have been reported for heat-treated and synthetic spinel (see some examples described by Notari and Grobon (2003) and by Saeseaw *et al.* (2009)). The exact position and shape of these Cr^{3+}-related PL bands change when measured at low temperature (Fritsch *et al.*, 2012). Additional confirmation for structural alteration of the spinel by a heating process was obtained from X-ray single-crystal structure analysis of the heated SPVNL 70 using the oxygen parameter u. It seems that during heat treatment the normal spinel structure where Mg has tetrahedral and Al has octahedral coordination ($Mg^{IV}Al^{VI}_2O_4$) transforms or readjusts towards an inverse spinel $Al^{IV}(MgAl)^{VI}O_4$. This is in accordance with previous work on the subject (see for example Preisinger, 1983; Lucchesi and Della Giusta, 1997; Andreozzi *et al.*, 2000).

Conclusions

Spinels from Lang Chap do differ microscopically and chemically from those found at other Vietnamese occurrences in the Koan Thong-An Phu mining regions. However, the Lang Chap samples examined for this study do microscopically and chemically resemble spinels from Myanmar (Mogok and Namya). It seems that the distinction of these spinels is only sometimes possible after careful examination of inclusion features and trace element chemistry.

The heat treatment experiment at 850°C of one Lang Chap sample showed that it is possible to reduce the orange colour component of these spinels. However, although the direct cause for this change is not yet completely understood, detection of any thermal treatment of such natural spinels can be done using Raman and photoluminescence spectroscopy: in both techniques, the spectral peaks of heated natural spinels are broader than their unheated equivalents. Our research team is currently working on the effect and detection of low temperature heat-treatment (i.e. below 850°C) on such coloured spinels.

Acknowledgements

Vladimir Malogajski (Mineralogical Crystallography, University of Bern, Switzerland) is thanked for his assistance to take photomicrographs with the

Keyence digital microscope. Dr Havy Le Thi-Thu Huong (Vietnam National University, Hanoi) and Vietphuong/VPGemstones Co. Ltd. (Hanoi and Bangkok) are thanked for supplying us with sample material and additional information.

References

Andreozzi, G.B., Princivalle, F., Skogby, H., and Della Giusta, A., 2000. Cation ordering and structural variations with temperature in $MgAl_2O_4$ spinel: An X-ray single-crystal study. *Am. Mineral.,* **85**, 1164–71

Blauwet, D., 2010. La mine de spinelle de Lang Chap, au Nord du Vietnam. *Revue de Gemmologie,* 170, 11–15

Blauwet, D., 2011. Spinel from northern Vietnam, including a new mine at Lang Chap. *Gems & Gemol.,* **47**(1), 60–1

Cynn, H., Sharma, S.K., Cooney, T.F., and Nicol, M., 1992. High-temperature Raman investigation of order-disorder behavior in the $MgAl_2O_4$ spinel. *Phys. Rev. D.,* **45**(1), 500–2

Farrugia, L.J., 1999. WinGX suite for small-molecule single-crystal crystallography. *J. Appl. Crystallogr.,* **32**, 837–8

Fristch, E., Rondeau, B., Hainschwang, T., and Karampelas, S., 2012. Raman spectroscopy applied to gemmology. pp. 453– 88. In: *Applications of Raman Spectroscopy to Earth Sciences and Cultural Heritage* (J. Dubessy, F. Rull and M.-C. Caumon, eds). EMU Notes in Mineralogy, **12**. European Mineralogical Union and The Mineralogical Society of Great Britain & Ireland

Garnier, V., Ohnenstetter, D., Giuliani, G., Maluski, H., Deloule, E., Pham Trong, T., Pham Van, L., and Hoáng Quang, V., 2005. Age and significance of ruby-bearing marble from the Red River Shear Zone, Northern Vietnam. *Can. Mineral.,* **43**, 1315–29

Gübelin, E.J., and Koivula, J.I., 2005. *Photoatlas of inclusions in gemstones, Vol. 2*. Opinio Verlag, Basel. pp 662–714

Hoang, L.H., Khoi, N.T., Quang, V.X., Minh, N.V., and Jaing, C.C., 2001. Some optical properties of Vietnam natural spinel. Proceedings of the International Workshop on Material Characterisation by Solid State Spectroscopy: Gems and Minerals of Vietnam, Hanoi, 200–9

Khoi, N.N., Sutthirat, C., Tuan, D. A., Nam, N.V., Thuyet, N.T.M., and Nhung N.T., 2011. Ruby and sapphire from the Tan Huong-Truc Lau area, Yen Bai province, northern Vietnam. *Gems & Gemol.,* **47**(3), 182–95

Lazzeri, M., and Thibaudeau, P., 2006. *Ab initio* Raman spectrum of the normal and disordered $MgAl_2O_4$ spinel. *Phys. Rev. B,* **74**(14), 140301(4)

Lucchesi, S., and Della Giusta, A., 1997. Crystal chemistry of a highly disordered Mg-Al natural spinel. *Miner. Petrol.,* **59**, 91–9

Malsy, A.-K., and Klemm, L., 2010. Distinction of gem spinels from the Himalayan mountain belt. *Chimia*, **64**(10), 741–6

Mohler, R.L., and White, W.B., 1995. Influence of structural order on the luminescence of oxide spinels: Cr^{3+} — activated spinels. *Electrochem. Soc.,* **142**(11), 3923–7

Notari, F., and Grobon, C., 2003. Spectrométrie de fluorescence du chrome dans les spinelles. *Revue de Gemmologie*, 147, 24–30

Peretti, A, and Günther, D., 2003. Spinel from Namya. *Contrib.to Gemol.,* **2**, 15–18

Phan Trong, T., and Hoáng Quang, V., 1997. *So Dô Kiên Tao Vunh Luc Yên*. Geological map of Luc Yen, scale 1:200,000. Institute of Geological Sciences, Hanoi

Preisinger A., 1983. Realbau von spinellen. *Fortschr. Miner.,* **61**(1), 153–67

Schmetzer, K., Haxel, C., and Amthauer, G., 1989. Colour of natural spinels, gahnospinels and gahnites. *Neues Jb. Miner. Abh.,* **160**(2), 159–80

Shigley, J.E., Laurs, B.M., Janse (Bram), A.J.A., Elen, S., and Dirlam, D.M., 2010. Gem localities of the 2000s. *Gems & Gemol.,* **46**(3), 188–216

Themelis, T., 2003. *Be-treated rubies and sapphires*. A&T Pub., Los Angeles. 48 pp

Tijero, J.M.G., and Ibarra, A., 1993. Use of luminescence of Mn^{2+} and Cr^{3+} in probing the disordering process in $MgAl_2O_4$ spinels. *J. Phys. Chem. Solids,* **54**(2), 203–7

Van Long, P., Quang Vinh, H., Garnier, V., Giuliani, G., Ohnenstetter, D., Lhomme, T., Schwarz, D., Fallick, A., Dubessy, J., and Trong Trinh, P., 2004. Gem corundum deposits in Vietnam. *Journal of Gemmology,* **29**(3), 129–47

Wood, D.L., Imbusch, G.F., Macfarlane, R.M., Kisliuk, P., and Larkin, D.M., 1968. Optical spectrum of Cr^{3+} ions in spinels. *J. Chem. Phys.,* **48**(11), 5255–63

Web list

RRUFF Raman spectra database. www.rruff.info

Saeseaw, S., Wang, W., Scarratt, K., Emmett, J.L., Douthit, T.R., 2009. Distinguishing heated spinels from unheated natural spinels and from synthetic spinels: A short review of on-going research. Seen on: http://www.giathai.net/pdf/Heated_spinel_Identification_at_April_02_2009.pdf

The Authors

A.-K. Malsy[1,2]*, S. Karampelas[1]*, D. Schwarz[1], L. Klemm[1], T. Armbruster[2], D.A. Tuan[3]

1. Gübelin Gem Lab Ltd., Maihofstrasse 102, 6006 Lucerne, Switzerland
2. Mineralogical Crystallography, Institute of Geological Sciences, Freiestrasse 3, University of Bern, CH-3012 Bern, Switzerland
3. DOJI Group, Level 9 and 10 Ruby Plaza, 44 Le Ngoc Han Street, Hai Ba Trung, Hanoi, Vietnam

* Corresponding authors: a.malsy@gubelingemlab.ch and s.karampelas@gubelingemlab.ch

The Gem-A Conference

Goldsmiths' Hall, Foster Lane, London EC2V 6BN

Saturday 2 and Sunday 3 November 2013

Celebrating 100 years of the Gemmology Diploma and 50 years of the Diamond Diploma

Save the date ...

Review of some current coloured quartz varieties

Ulrich Henn and Rainer Schultz-Güttler

Abstract: Gemstones of the quartz group display a wide spectrum of colours, both natural and those colours produced by artificial enhancement. Colour modification methods such as heat-treatment and irradiation or a combination of these processes used on macro-crystalline quartz lead to an interesting colour palette for the jewellery trade. Characteristics of these materials are outlined and testing methods for gemmological distinction between naturally coloured and artificially enhanced quartz are described. In the context of the different types of colour centres, the quartz gems are considered in three groups: iron-bearing quartz, quartz containing mainly aluminium and quartz with high water content. In particular, optical absorption spectra are used in the characterization of different colour varieties of quartz. In addition FTIR-spectra in the near-infrared range as well as the observation of pleochroism, presence of Brazil-law twinning and reaction under the Chelsea Colour Filter may be helpful for the determination of particular quartz types.

Keywords: quartz, causes of colour, colour modifications, heat-treatment, irradiation, optical absorption spectra, amethyst, citrine, prasiolite, 'blueberry quartz', bleached quartz, bi-coloured quartz, smoky quartz, 'lemon quartz', green quartz, rose quartz

Introduction

Quartz perhaps shows a surprising variety among gemstones in terms of its macro-crystalline specimens, its micro- to crypto-crystalline structures, and particularly its wide range of colours.

General causes for the varieties of colour in quartz generally can be divided into three groups:

1. colour centres
2. optical effects
3. inclusions

In macro-crystalline quartz *(Figure 1)* colour is most commonly due to colour centres, which are associated with foreign ions in the structural framework of quartz. Of these, the commonest are iron and aluminium and for this reason the colour-centre mechanisms are discussed under the sub-headings iron-bearing and aluminium-bearing quartz. Comprehensive descriptions of the colours of quartz have been published by Lehmann and Bambauer (1973) and Rossman (1994).

This paper concentrates on colour centres rather than optical effects and inclusions and presents an outline of the commercially important colours and colour modifications of macro-crystalline quartz rather than the finer-grained varieties. The currently known mechanisms responsible for each colour variety are described in summary form, and further details may be found in the indicated references. Recent work (Henn and Schultz-Güttler) is augmented with

Figure 1: Some colour varieties of quartz: from left to right — amethyst, prasiolite, citrine (yellow-brown) and smoky quartz. Photo by Rainer Schultz-Güttler.

more illustrations and outlines of possible defects and their interactions (see Box A).

Crystal structure and morphology

The structure of quartz (SiO_2) is represented by a trigonal trapezohedral lattice *(Figure 2)*. Each silicon atom is coordinated with four oxygen atoms and constitutes SiO_4-tetrahedra. These tetrahedra are helically arranged and form a three-dimensional network of helical chains which are aligned in the direction of the *c*-axis. They are linked in such a way that six-sided channels are formed, and within these channels there are vacant interstitial (I) sites which can offer both tetrahedral (I_4) and octahedral (I_6) coordination to possible foreign elements or ions.

Box A: Defects in quartz related to colour varieties

The illustration shows in a schematic way some possible defect centres in natural quartz.

Quartz has a very simple chemical formula SiO_2, and may be considered as a quite perfect substance. But as shown by innumerable investigations (Salh, 2011), quartz can contain large number of defects involving substitutional and interstitial ions, hydroxyl and molecular water, besides such growth defects as spiral growth, small angle boundaries and twinning. The basic structural unit is the AO_4-tetrahedron [AO_4], whereby A is mainly Si, but can be substituted by Al, Fe and (4 H). Where charges need to be balanced, the coupled ions, occupying interstitial positions, are shown nearby the tetrahedron as Li, Na, Fe^{2+} and OH. This scheme leads to the notation [AO_4/M] used in the text and illustrations to explain the modifications of colours by irradiation and heat treatment. Each [AO_4/M] unit may be neutral (º), positively (+) or negatively (-) charged, depending on the addition or removal of electrons. Shown also is molecular water (H_2O), which may

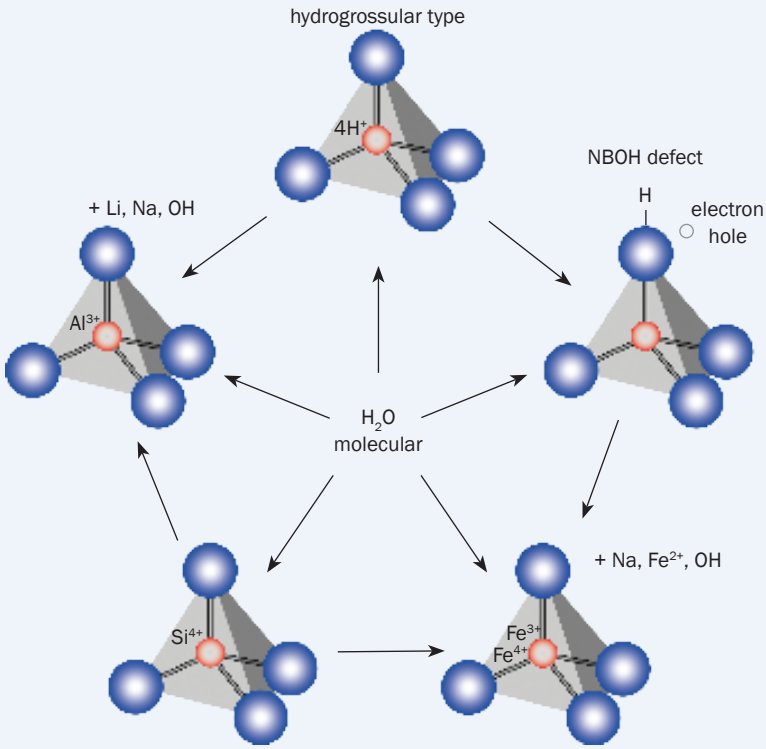

interact with all defects shown; its location is not at structural sites but in the channels of the quartz structure or along grain boundaries, twin planes and micro-structural growth defects of the crystals. From these considerations it is clear that a multitude of combinations of defects in natural quartz can exist, any one combination being a reflection of its geological history.

Review of some current coloured quartz varieties

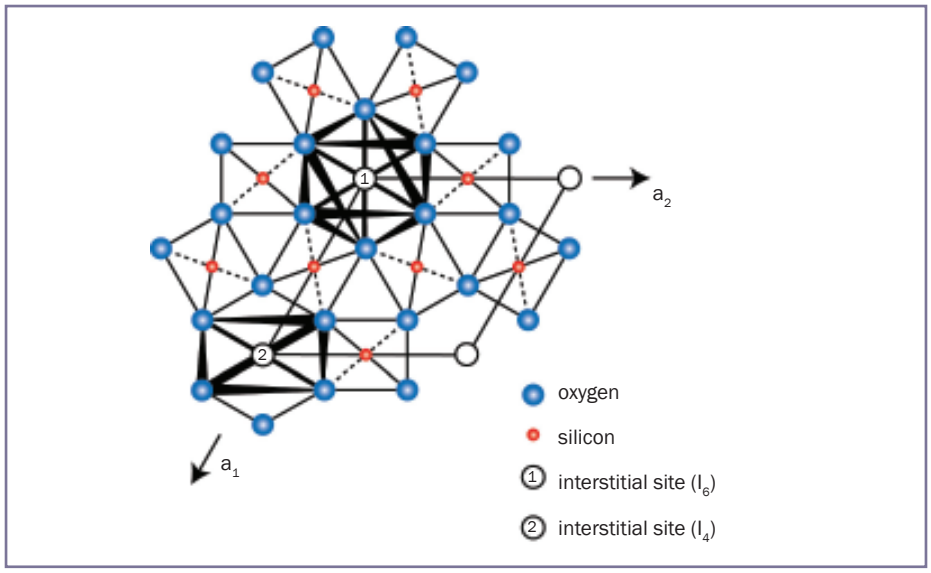

Figure 2: Crystal structure of quartz illustrating the Si sites and the interstitial sites of distorted octahedral (I_6) and tetrahedral (I_4) coordination (after Lehmann and Bambauer, 1973); a1 and a2 are unit cell parameters.

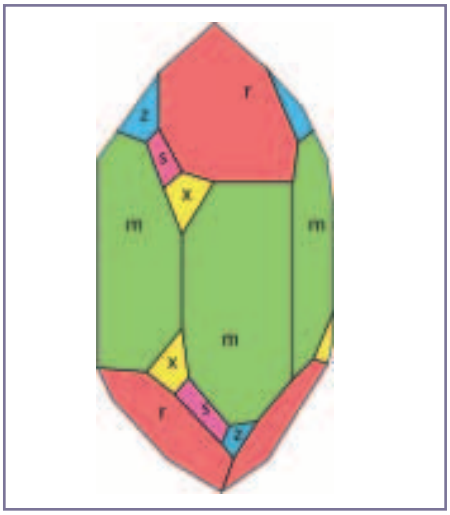

Figure 3: Morphology of a crystal with doubly terminated prismatic form. Perfect examples are rarely found in nature due to frequent twinning and growth defects. Diagram by German Gemmological Association.

Silicon atoms can be replaced by foreign ions. In the case of tetravalent ions such lattice sites are labelled S. If tetravalent Si is replaced by an ion of lower valency, this would lead to the need for charge balancing by alkali ions (e.g. lithium) or protons, and the lattice sites occupied in such a mechanism are labelled S_1 and S_2 respectively.

The helical arrangement of the SiO_4-tetrahedrons parallel to the *c*-axis is responsible for the development of right-handed and left-handed crystals with mirror-image symmetry. The crystal morphology of quartz *(Figure 3)* is dominated by rhombohedral and prismatic faces. The common crystal form is a prism with hexagonal-prismatic habit. The main crystal faces are the first order hexagonal prism **m** $(10\bar{1}0)$, positive and negative rhombohedron **r** $(10\bar{1}1)$ and **z** $(01\bar{1}1)$, second order dipyramid right-hand **s`** $(11\bar{2}1)$ and left-hand **`s** $(2\bar{1}\bar{1}1)$ and trapezohedra right-hand **x`** $(51\bar{6}1)$ and left-hand **`x** $(6\bar{1}\bar{5}1)$.

Iron-bearing quartz

In the crystal structure of quartz, iron can be present in both substitutional S sites and interstitial I sites. However, the replacement is limited because of differences in valency and ionic radii. Iron contents of 10 to 350 ppm were indicated for amethyst and citrine by Lehmann and Bambauer (1973). The first electron transition band of Fe^{3+} is located at about 210 nm in the UV, so does not absorb in the visible range and consequently no colour is produced. Those Fe^{3+} ions occupy both substitutional S_1 sites and interstitial I_4 sites and are considered as precursors of the colour centres in amethyst (Lehmann, 1967; Lehmann and Bambauer, 1973).

Colour causes and modifications of iron-bearing quartz are shown in *Figure 4*. Characteristics and distinguishing features are summarized in *Table I*.

Table I: Characteristics of iron-bearing quartz.

Type	UV/VIS/NIR absorption spectrum	Pleochroism	Brazil law twinning	Infrared spectrum	Upper temperature limit of colour stability; °C
Amethyst	bands at 545 and 357 nm as well as 950 nm	reddish-violet to bluish-violet	present	n.d.	350–450
Citrine: heated amethyst	continuous increase towards UV	none	present	n.d.	400–600
Prasiolite: heated amethyst	broad band maximum at 720 nm	weak in shades of pale green	present	weak H_2O and Si-OH bands	500–600
'Blueberry quartz': irradiated and heated prasiolite	band at 545 nm and shoulder at 720 nm	violetish-blue to reddish-orange	present	n.d.	350–400
'Neon quartz': heated amethyst	shoulders at 545 and 357 nm	-	present	n.d.	approx. 400

NB: n.d. = not diagnostic

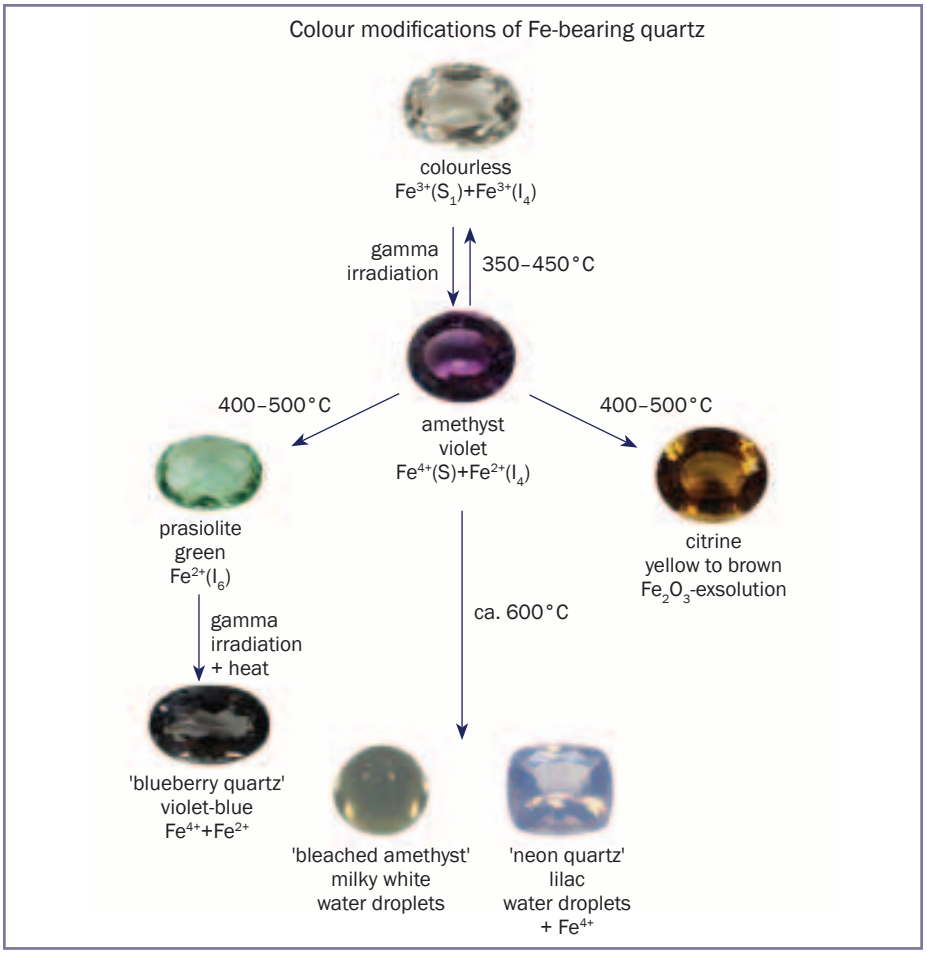

Figure 4: Colour causes and modifications of iron-bearing quartz. The possible ways of changing colours are indicated as are the causes. Photo by German Gemmological Association.

Figure 5: Rough amethyst crystals of different colour intensities; some show distinct colour zoning (for example, centre bottom) due to changing growth conditions. Size of specimens from 2 to 4 cm. Photo by Rainer-Schultz-Güttler.

Amethyst

The iron-related colour centres which are responsible for the violet colour of amethyst have been described by several authors (e.g. Lehmann, 1967; Lehmann and Bambauer, 1973; Cohen, 1985; Rossman, 1994). Following Lehmann and Bambauer (1973) the formation of the iron centres relevant to the violet colour of amethyst (*Figure 5*) can be characterized by the following formula:

$Fe^{3+}(S_1) + Fe^{3+}(I_4) \leftrightarrow Fe^{4+}(S) + Fe^{2+}(I_4)$

The mechanism is due to an electron transition caused by gamma irradiation: an electron is impelled or released from a substitutional Fe^{3+} and trapped by an interstitial Fe^{3+}. Consequently, by losing the negative electron, the substitutional Fe^{3+} is oxidized to an Fe^{4+} centre, while the interstitial Fe^{3+} is reduced to Fe^{2+}. This electron transition process is reversible by heat treatment. The stability limit of the amethyst centre is approximately 350-450°C. Exceeding that temperature the amethyst colour starts to bleach. The structural position of the Fe^{4+} centre and the exact mechanism of colour formation is still a matter for discussion. Cohen (1985) described irradiation-related Fe^{4+} centres, but located on interstitial rather than substitutional sites. Dedushenko *et al.* (2004) confirmed the model of Lehmann and Bambauer (1973) by Mössbauer spectroscopy, but Burkov *et al.* (2005) and SivaRamaiah *et al.* (2011) stress the influence of ferrous iron in amethyst.

In quartz generally, the concentration and distribution of trace elements is related to the growth sectors of the crystal. Generally, concentrations are highest at the positive rhombohedron and reduce at the negative rhombohedron and are lowest at the prism sectors. In amethyst, the violet colour is concentrated in the rhombohedral sectors, with the positive one possessing the deepest colour *(Figure 6)*, while the prismatic sectors are colourless or white *(Figure 7)*.

A diagnostic feature for natural (as opposed to synthetic) amethyst is the presence of Brazil-law twinning. This is due to polysynthetic twinning in the growth sectors of the positive rhombohedron **r** *(Figure 8)*. Twinning of

Review of some current coloured quartz varieties

*Figure 6: Two amethyst cross sections indicating different colour intensity in different growth sectors. Sectors of the positive rhombohedron **r** possess more intense violet colours compared to sectors of the negative rhombohedron **z**. Size of specimens 2.5 and 2 cm. Photo by German Gemmological Association.*

Figure 7: Group of crystals extracted from an amethyst geode from Brazil. The rhombohedral growth sectors show amethyst colour, while the prism sectors are colourless to white. Size of specimen 6.5 cm. Photo by German Gemmological Association.

Figure 8: Unusually large macroscopic Brazil twin in an amethyst from Bahia, Brazil. Most examples of this type of twin are seen under the microscope. 4 cm length. Photo by Rainer Schultz-Güttler.

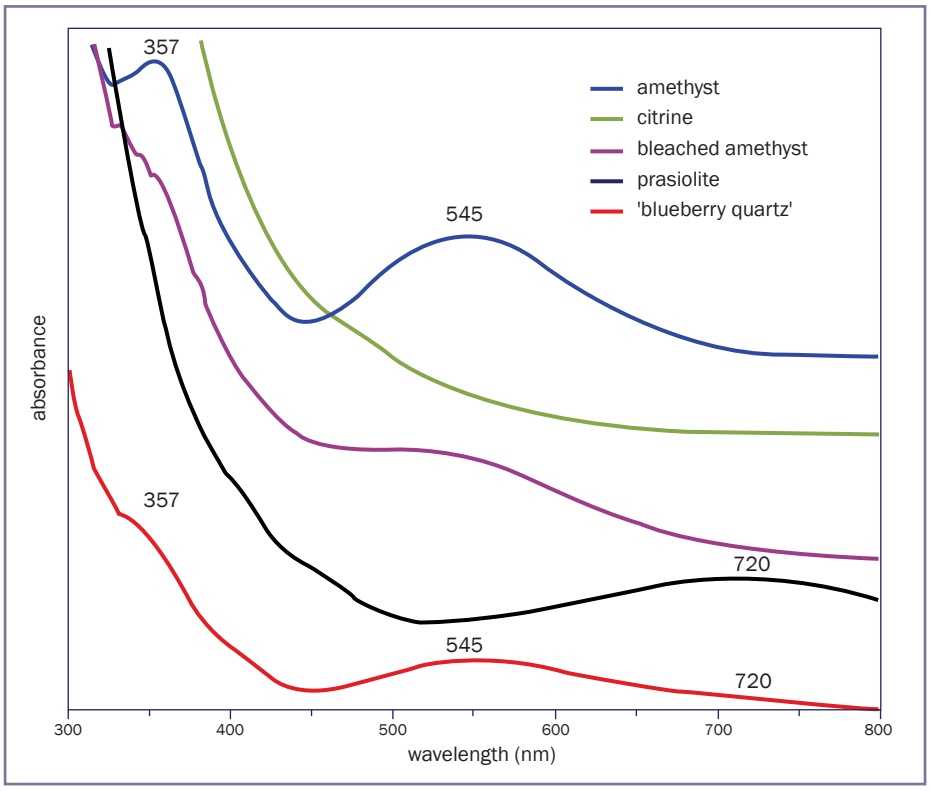

Figure 9: Unpolarized absorption spectra of different colour varieties of iron-bearing quartz. The spectra are displaced on the absorption scale for clarity.

this type also is visible in treated amethyst varieties, in particular in citrine, prasiolite, 'blueberry quartz' and bleached quartz.

The visible range absorption spectrum *(Figure 9)* of amethyst is characterized by a broad absorption band in the yellow-green, which is responsible for the violet colour (Neumann and Schmetzer, 1984). The maximum is located at 545 nm and is only weakly pleochroic (Rossman, 1994), the reddish-violet to bluish-violet change being caused by varying iron entrapment at crystallographically equivalent Si sites (Neumann and Schmetzer, 1984). Cox (1977) described this phenomenon as an anomalous trichroism. Outside the visible range, a second absorption band of Fe^{4+} is situated in the UV at 357 nm and is clearly pleochroic; a further band lies in the NIR with a maximum at 950 nm.

Citrine

Most citrines on the gemstone market are heat-treated amethysts. At temperatures of about 350 to 450°C amethyst bleaches to colourless or pale yellow and the concentration of the provisional iron centres $Fe^{3+}(S_1)$ and $Fe^{3+}(I_4)$ accumulates (Stock and Lehmann, 1977). Coincidently, the formation of iron particles derived from iron originating from these centres starts and the colour develops from yellow to brown. The particles consist of hematite (Fe_2O_3) with an approximate size of 100 nm. Because the distribution of the hematite particles is dispersed, random and relatively homogeneous, the coloration is isotropic and no pleochroism exists. The higher the temperatures are raised during the heat treatment the stronger becomes the brown

Figure 10: Citrine (heat-treated amethyst) of various yellow to brownish-orange colours: pale yellow, yellow, golden citrine, Palmeira citrine, Madeira citrine (from left to right). Weight of the specimens 7.43 to 10.85 ct. Photo by German Gemmological Association.

Figure 11: Amethyst (centre), heat-treated prasiolite (green) and irradiated and heat-treated 'blueberry quartz' from Montezuma, MG, Brazil. Size of amethyst 5 cm long, blueberry quartz 1.5 to 2.5 cm and prasiolite 0.8 to 1.5 cm. Photo by Rainer Schultz-Güttler.

Figure 12: Faceted prasiolite (heat-treated amethyst) from Montezuma, Brazil (6 ct). This colour is stable to light and heat up to 500–600 °C. Photo by Rainer Schultz-Güttler.

Figure 13: Faceted 'blueberry quartz', i.e. gamma-irradiated and heat-treated prasiolite (4 ct). This colour resembles that of much tanzanite. Photo by Rainer Schultz-Güttler.

to orange hue *(Figure 10)*. The optical spectrum *(Figure 9)* shows a continuous increase of absorption towards the UV (Neumann and Schmetzer, 1984).

In the gem trade, golden-yellow material is called golden citrine; more brownish-orange to orange stones are called Madeira citrine; the name Palmeira citrine describes stones from the Palmeira amethyst mine which provides amethyst suitable for heat treatment to citrine of fine quality, so these particular stones have a Brazilian origin.

Prasiolite

Certain amethysts can turn green on heat treatment (*Figures 11* and *12*). The so-called natural prasiolite is very rare and in Nature it has probably formed as a result of heating from nearby volcanic activities (Schultz-Güttler *et al*., 2008).

The prasiolite offered on the gemstone market nowadays is heat-treated amethyst, much of it probably coming from the Montezuma mine in Minas Gerais, Brazil. The mechanism of the colour modification is a valency change of the amethyst iron centres. As in the heating process used to produce yellow citrine colours the iron centres $Fe^{4+}(S)$ and $Fe^{2+}(I_4)$ are transformed into the provisional centres $Fe^{3+}(S_1)$ and $Fe^{3+}(I_4)$ of the colourless state. Subsequently, a green colour is produced by heat treatment at 400–500°C when the interstitial $Fe^{3+}(I_4)$ changes to Fe^{2+} which is in octahedral coordination (I_6) (see again *Figure 4*). The colour is stable up to temperatures of 500 to 600°C.

Its visible range absorption spectrum *(Figure 9)* is characterized by a broad band with a maximum at 720 nm. Where there is a yellow component in the colour, as in yellow-green to champagne-coloured material, there is a distinct increase of absorption towards the UV (Schultz-Güttler *et al.,* 2008).

'Blueberry quartz'

Gamma irradiation and heat treatment of prasiolite produces violet, violet-blue to dark blue colours (Schultz-Güttler, 2006; Schultz-Güttler and Kohigashi, 2006). The violet-blue to blue material is called 'blueberry quartz' in the gem trade (*Figures 11* and *13*).

The absorption spectrum *(Figure 9)* is characterized by a broad band with a maximum at 545 nm which is caused by the amethyst iron centre Fe^{4+}. Contrary to amethyst, which shows large transmission between 600 and 800 nm, in blueberry quartz a further absorption continues with a shoulder at 720 nm and this is due to Fe^{2+} as in prasiolite. It is this feature which absorbs much of the red wavelength and produces the blue colour. It may be noted that the typical amethyst colour basically is a fine compromise of blue and red components producing lilac. Compared with amethyst the absorption minimum is located at a longer wavelength: at 465 nm rather than the 444 nm of amethyst. That phenomenon is caused by a prior increase of the absorption towards the shoulder in the UV at 357 nm.

Bleached quartz

Heat treatment of amethyst at temperatures above 500°C develops a slightly milky turbidity and bleaching of the violet colour, and some stones of this type have been called 'neon quartz' in the gem trade *(Figure 14)*. At higher temperatures of about 600°C the milky turbidity develops much more strongly and the violet to lilac colour completely disappears. What happens is that silanol (-Si-OH) groups bound in the quartz structure react to the heat by releasing the –OH as tiny water droplets which cause the light scattering and milky turbidity. The resulting appearance resembles adularescent gem materials and such stones are used as moonstone imitations.

The absorption spectrum *(Figure 9)* indicates the presence of amethyst iron centres, but in comparison with the amethyst spectrum, the Fe^{4+} absorption bands possess lower intensity and are less distinctly developed as shoulders.

Bi-coloured quartz

The best-known bi-coloured quartz is ametrine *(Figure 15)* and, as the name accurately implies, the stones consist of amethyst and citrine colour zones. The prime natural source of these stones is the Anahí mine, Bolivia (Vasconcelas *et al*., 1994). The violet amethyst colour is found in the sectors of the positive rhombohedron **r** and is caused by Fe^{4+} centres. The sectors of the negative rhombohedron **z** are yellow. Aines and Rossman (1986) described that phenomenon as follows: the rhombohedral **z** sectors contain higher water contents; natural ionizing radiation results in radiolysis, i.e. a breakdown of water into H_2 and O_2 (see also Hashimoto *et al.,* 2001); and the presence of hydrogen prevents the formation of Fe^{4+} amethyst centres, so there is no violet coloration.

Colour-zoned amethyst from both Bolivia and Brazil (Marabá/Pará or Brejinho das Ametistas/Bahia) can be heat treated to yellow/colourless stones *(Figure 16)* which are sometimes named 'Lunasol' in the trade. In heat treatment at about 475°C the sectors of the positive rhombohedron **r** can change to colourless ($Fe^{4+} \rightarrow Fe^{3+}$) while the sectors of the negative rhombohedron **z** turn yellow (due to precipitation of Fe_2O_3). The process is partially reversible by irradiation, i.e. the sectors of the positive rhombohedron **r** can be returned to violet (Nassau, 1981).

Quartz containing mainly aluminium

Independently or accompanying iron, aluminium is the other main trace element that can replace silicon in the crystal structure on tetrahedral lattice sites (substitution). The radii of aluminium ions are smaller than those of iron at equivalent sites, so substitution of larger quantities is easier and generally the concentration of aluminium is much higher than that of iron (hundreds to thousands of ppm). The difference in charge produced by the substitution of Si^{4+} with Al^{3+} in the structure is compensated for by the presence of alkali ions such as sodium, potassium, lithium, or the hydronium ion (H_3O^+) or a proton. These ions occupy interstitial sites or reside in the channels of the crystal structure. In quartz, as shown above, there are two types of channel parallel to the *c*-axis, one with a trigonal cross-section of smaller diameter and one with a distorted hexagonal cross section of larger diameter; in addition there are channels perpendicular to the rhombohedral faces and inclined to the *c*-axis whose influence on distributions of substitutional ions have not yet been clarified.

Therefore, there is a number of different sites for the compensating ions to occupy to achieve charge balance, with the result that a number of different configurations of colour centres may be present.

The causes of colour and processes of change of colour in aluminium-containing quartz are shown in *Figure 17*, and characteristics and distinguishing features are shown in *Table II*.

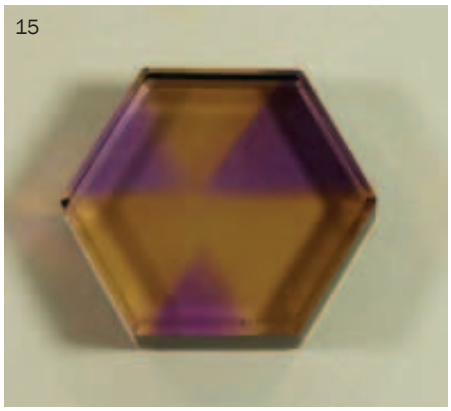

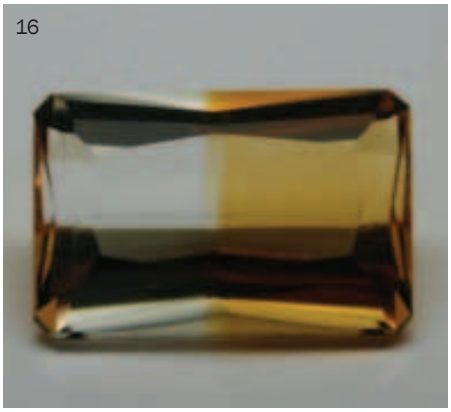

Figure 14: Faceted 'neon quartz', i.e. bleached amethyst. The milky appearance is produced by microscopic fluid inclusions, formed due to heat treatment. Weight of the specimen 4.84 ct. Photo by German Gemmological Association.

Figure 15: Ametrine from Bolivia. The violet amethyst colour is concentrated at the growth sector of the positive rhombohedron ***r****, while the yellow citrine colour is limited to the sectors of the negative rhombohedron* ***z****. Size of the specimen 4.6 cm. Photo by German Gemmological Association.*

Figure 16: Bi-coloured colourless/yellow quartz obtained by heat treatment of colour-zoned amethyst. Weight of the faceted stone 6.23 ct. Photo by German Gemmological Association.

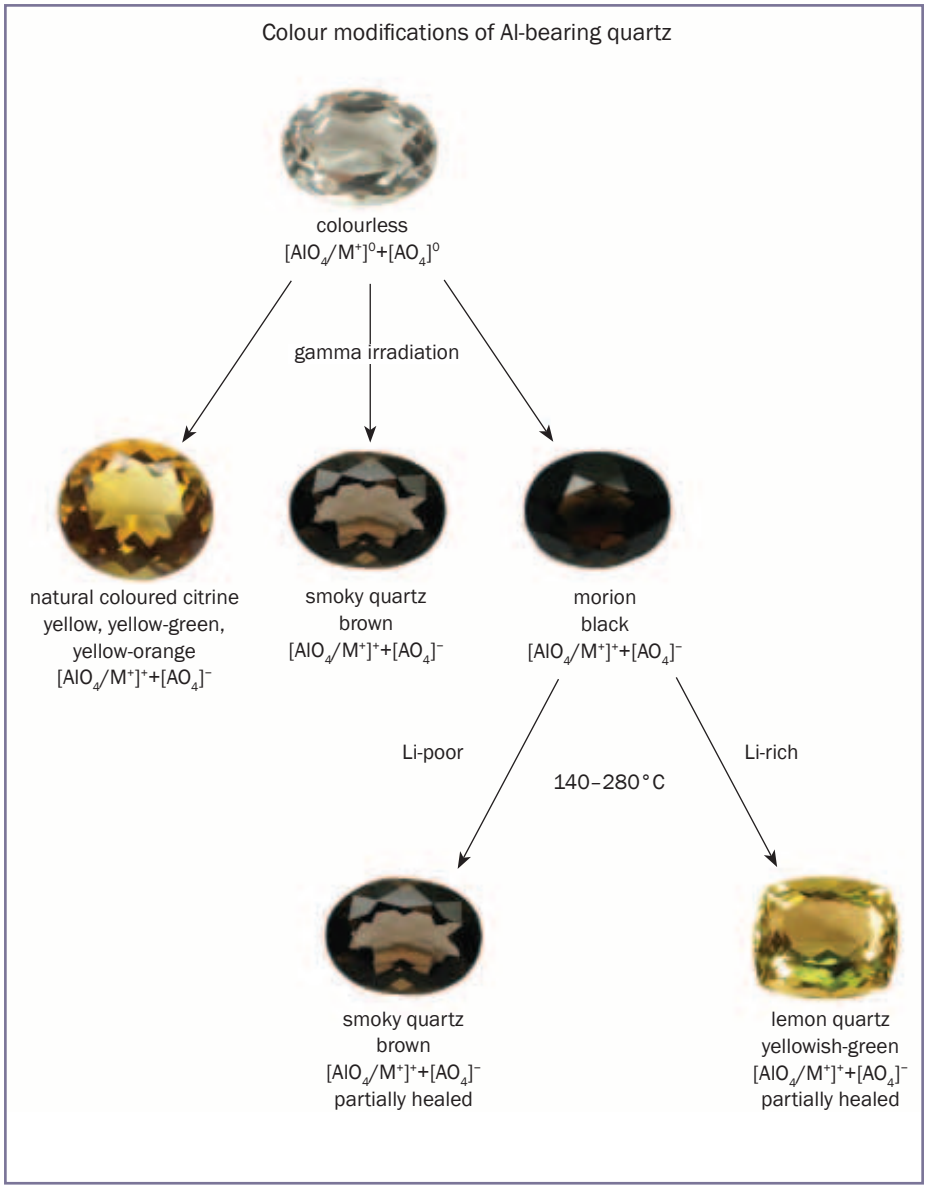

Figure 17: Colour causes and modifications of aluminium-bearing quartz. The colour-forming complexes are shown and the ways to change colour are indicated. Photos by German Gemmological Association.

Table II: Characteristics of aluminium-bearing quartz.

Type	UV/VIS/NIR absorption spectrum	Pleochroism	Brazil law twinning	Infrared spectrum	Upper temperature limit of colour stability, °C
Citrine	shoulder at 400 nm	light yellow to intense yellow	absent	n.d.	200–300
Smoky quartz	bands at 427, 486 and 670 nm	brown to reddish-brown	absent	weak Li-band	200–300
Lemon quartz	bands at 400 and 650 nm	yellow to yellow-green	absent	distinct Li-band (3483 cm^{-1})	200–300

NB: n.d. = not diagnostic

Citrine and smoky quartz

The main colours of this aluminium bearing quartz are all shades of lime green, yellow to yellow-orange (citrine in the real sense with natural colour, *Figures 18* and *19*) and all shades in brown to black, where the range grades into the greyer smoky quartz (*Figures 18* and *20*) and the opaque black variety called morion.

Some crystals contain a wide range of shades of yellow, indicating changing conditions of incorporation of trace elements with changing growth conditions and /or changes in the chemistry of mineral-forming fluids. As Rossman (1994) pointed out, the details of the natures of colour centres in this Al dominated quartz are not yet fully understood. Taking into account the above-mentioned variety of valence-balancing ions which can be incorporated in the quartz structure and more recent work — see for example Götze (2009) and Stevens-Kalceff (2009) — this statement is readily understandable.

The absorption spectra of Al-dominated colour varieties typically contain five bands (after Nassau and Prescott, 1975 and 1977) and the hue and colour depth are determined by their relative intensities. They have their maxima at 670 nm (A1), 486 nm (A2), 427 nm (A3), 314 nm (B) and 270 nm (C). The relative intensity of each absorption band in a spectrum determines the shade of yellow, orange, brown or almost black in that stone. It is outside the scope of this work to discuss further the possible allocation of individual bands to certain defects derived from the general case $[AlO_4/ M]$, whereby M represents a Na, K, Li, or hydronium ion or a missing electron in an orbital, i.e. a hole. However, it is worth stating that the presence of hydroxyl or hydronium ions will reduce the intensities of any yellow and brown colours (Guzzo *et al.*, 1997).

Thus, as was discussed above for iron, radiation is necessary for the creation of colour centres and therefore for colour in quartz with Al as the main impurity. Natural disintegration of radioactive elements in the quartz veins,

Review of some current coloured quartz varieties

Figure 18: An extensive range of natural-coloured citrine and smoky quartz from Santo Sé, Bahia, Brazil. This locality has recently furnished nearly all natural citrine-related quartz in Brazil. Size of specimens from 3 to 6.5 cm in diameter. Photo by Rainer Schultz-Güttler.

Figure 19a and b: Citrines of natural colour from Zambia. Weight of the faceted stones 7.21 and 8.93 ct. Photo by German Gemmological Association.

Fig ure 20: Smoky quartz from Brazil. Weight of the faceted stone 9.72 ct. Photo by German Gemmological Association.

for example, or in surrounding granites or pegmatites can irradiate quartz which, although maybe in small doses, over long geological time can accumulate and produce the colours found in natural material. In the laboratory, however, very high doses of irradiation, mostly gamma-rays, can produce in much shorter times the desired colour(s). It may be worthwhile to stress that irradiation be it natural or applied at the irradiation facility will turn all material nearly black and the described colours are the product of additional heating.

Heat, either through metasomatic or metamorphic processes in a geological setting or by heating under controlled conditions in the laboratory, increases the electron mobility in the quartz, thus counteracting the intensity of the formed colour centres. By careful observation

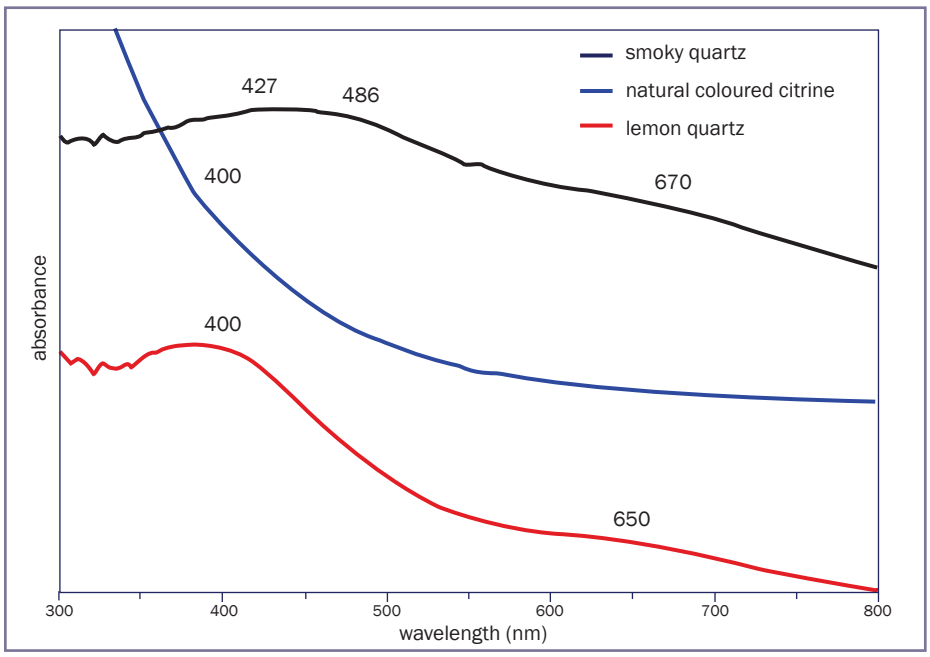

Figure 21: Absorption spectra of aluminium-bearing quartz. The typical absorption peaks for each variety are indicated.

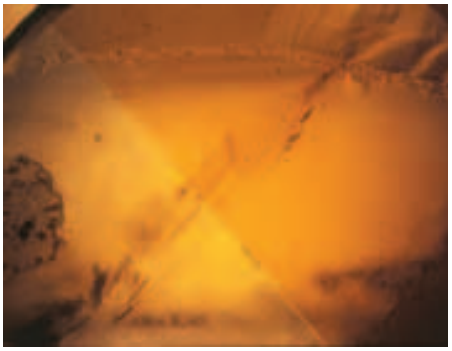

Figure 22: Pleochroism of natural-coloured citrine from Zambia. This is a strong colour difference seldom seen in citrine samples. Photo by German Gemmological Association.

Table III: Differentiation between natural-coloured citrine, citrine obtained by heat treatment of amethyst and lemon quartz.

	Citrine, natural colour	Citrine, heat treated amethyst	Lemon quartz, Heat-treated smoky quartz
Pleochroism	pale to intense yellow	none	yellow to yellow-green
Absorption spectrum	shoulder at 400 nm	continuous increase towards UV	peaks centred at 400 and 650 nm
FTIR spectrum	n.d.	n.d.	Li-band at 3483 cm^{-1}
Brazil law twinning	none	present	none

NB: n.d. = not diagnostic

under controlled heating any one of the commercial colours can be produced.

With appropriate heat treatment, all colours can be reduced and even completely bleached at temperatures of about 210 to 280°C and over periods of 60 to 360 minutes (Barbosa, 2009).

The absorption spectrum of smoky quartz *(Figure 21)* has a wide band with maximum centred about 427 nm and shoulders about 486 and 670 nm. Greenish-yellow, yellow and yellow-orange aluminium-containing crystals (citrine in the traditional sense or so-called 'citrine of natural colour') show a continuous increase in their absorption spectra from red to the ultraviolet with a more or less clearly defined shoulder or absorption band at 400 nm *(Figure 21)*. In contrast to the citrine created by heat treatment of amethyst, natural citrine possesses distinct pleochroism *(Figure 22)*, but no twin intergrowth according to the Brazil law.

Lemon quartz ('green gold')

Even though this variety is one of the above mentioned citrines, its economic importance justifies particular attention. In the gem trade, this quartz is known as 'lemon quartz' or 'green gold' *(Figure 23)*.

The colour is similar to the colour of the best chrysoberyls, a 'chartreuse', a yellow with a distinct touch of green. Only in a few quartz deposits in Brazil or the rest of the world can this attractive quartz be found. Previous studies (Nunes *et al.*, 2009; Trabulsi, 2010; Favacho Silva, 2000) indicate that this colour can only be found in quartz with a high lithium content. The absorption spectrum *(Figure 21)* of such quartz shows a well defined band centred at 400 nm, and one less pronounced at about 650 nm. The degree of intensity of the band at 650 nm relates to strength of the green component in the colour. The source of colour in this case is the molecule $[AlO_4/ Li, H]^0$, which releases an electron by irradiation and forms the colour centre. It should be mentioned that the intensity of the green component is reduced in the presence of a proton or of a hydronium ion.

The distinguishing features of 'lemon quartz', citrine of natural colour and citrine obtained by heat-treatment of amethyst are summarized in *Table III*.

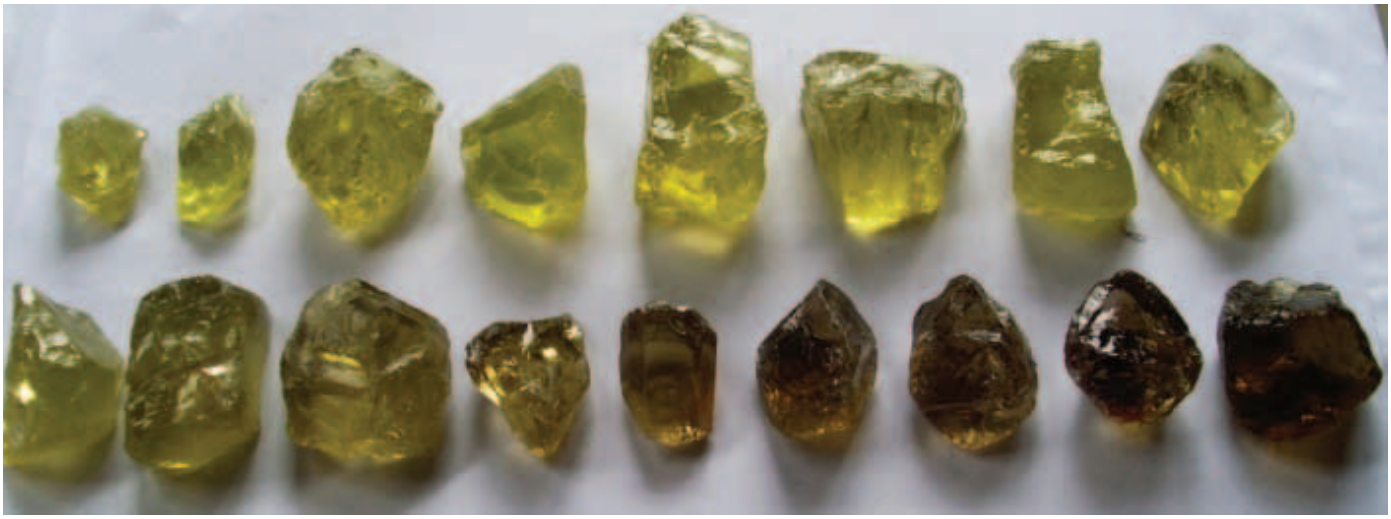

Figure 23: Range of colours of 'lemon quartz' and citrine from Pará, Brazil. They form a colour gradation from near-colourless to dark olive green brown. Sizes from 2 to 6 cm in diameter. Photo by Rainer Schultz-Güttler.

Quartz with high water content

In the last few years a new, green variety of quartz has appeared *(Figure 24)*. In the gem trade, it is sold under the pseudonym 'green amethyst' or 'greened amethyst' or it can be offered as prasiolite. Most of the raw material of this variety comes from the geode-bearing basalts in the south and southwest of Brazil, i.e. from the states of Rio Grande do Sul, Paraná and southwest Minas Gerais. It has been shown that this colour variety is different from the prasiolite obtained from amethyst (Schultz-Güttler *et al*., 2008), and each variety can be distinguished easily using a Chelsea Colour Filter: the prasiolite derived by heat treatment of amethyst from the Montezuma deposit, will show green and this new green variety will show red *(Table IV)*.

Optical spectroscopy and infrared studies have shown that this and similar quartz has a very high content (up to 5000 ppm, Iwasaki and Iwasaki, 1993; Hebert and Rossman, 2008) of molecular water and silanol, or Si-OH groups *(Figure 25)*. Other trace elements such as Fe, Al or Li are very low or are in the range of normal natural quartz as ongoing investigations showed (Guttler *et al*., 2009). So the trace elements in prasiolite and this new green quartz are quite different and the causes of their colours are based on completely different mechanisms.

Macroscopic examination of the original material shows a certain peculiar aspect of its appearance that can best be described as an 'greasy lustre'; this is certainly connected with the high water content of this type of quartz.

On heat treatment to temperatures higher than 500°C, the crystals show a milky, cloudy opalescence, due to water being exsolved as fine microscopic fluid inclusions, similar to the above-mentioned opalescent quartz (Iwasaki, 1980). Comparing the spectra of quartz of pegmatitic origin with those of quartz with the greasy lustre from geodes *(Figure*

Table IV: Distinguishing features of prasiolite and green quartz with high water content.

	Prasiolite	'Wet quartz' irradiated to result in green quartz
Main absorption peak in visible range spectrum	720 nm	610 nm
FTIR spectrum	weak H_2O and Si-OH bands	H_2O band at 1900 cm^{-1} Si-OH bands at 1400 and 2200–2400 cm^{-1}
Colour under Chelsea Colour Filter	green	red

Figure 24: Gamma-irradiated green quartz from Rio Grande do Sul, Brazil. Although the irradiation dose is the same, the difference in colour of the crystals from pale green in the lower left to dark green in the upper right is clearly visible. Size of specimens from 1.5 to 4.6 cm. Photo by Rainer Schultz-Güttler.

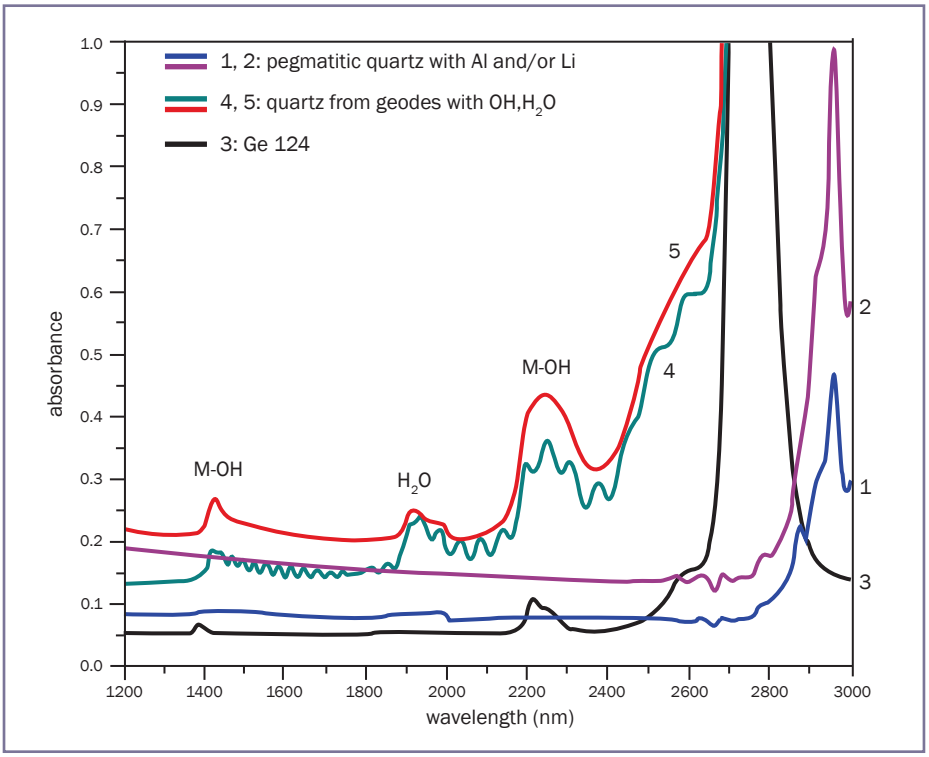

Figure 25: NIR-spectra of different types of quartz. Spectra 1 and 2 are from pegmatitic quartz with contents of Li and Al but no water or OH groups (labelled H_2O and M-OH respectively). Spectra 4 and 5 are from 'wet quartz' from geodes in Rio Grande do Sul, Brazil, and their H_2O and OH peaks are clearly visible. The wavy appearance of spectrum 4 is due to internal reflection of the light beam. The presence of silanol groups is made clear by comparison with spectrum 3, an ultrapure General Electric standard glass, GE 124 with < 5ppm OH.

Review of some current coloured quartz varieties

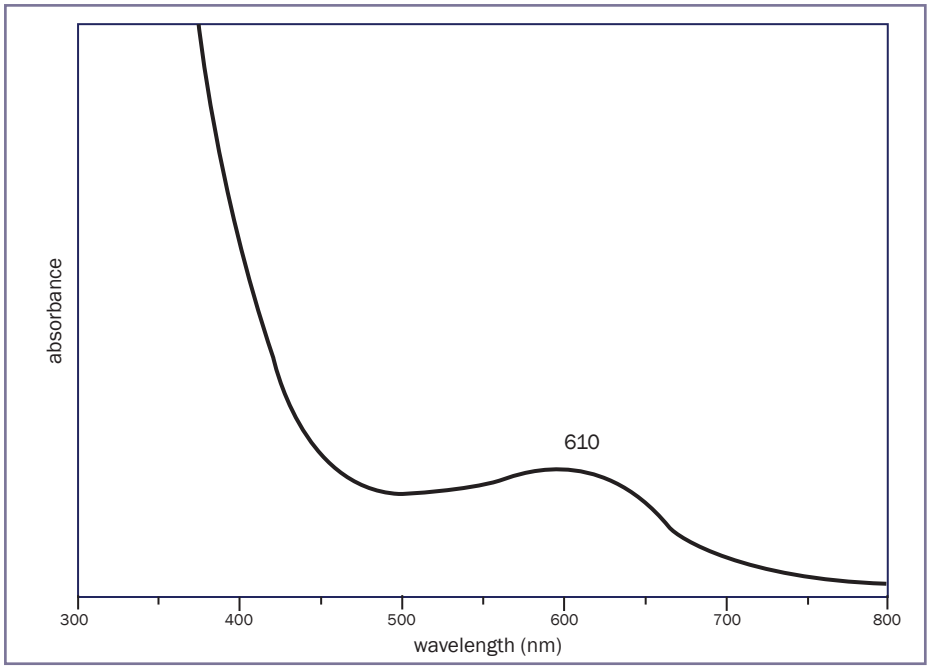

Figure 26: Absorption spectrum of gamma-irradiated green quartz from Rio Grande do Sul, Brazil. This absorption peak has long been specific for non-bonding oxygen hole (NBOH) defects in silica and glass, and more recently in quartz.

25), the intensities of the water and OH absorption bands are clearly higher in the latter. This type of quartz with high water content should therefore be called 'wet quartz' and its spectral characteristics resemble those of chalcedony as shown by Graetsch *et al.,* 1985.

The presence of molecular water and silanol quenches all tendency towards the formation of colour centres based on Al or Fe. Therefore, geodes commonly contain amethyst crystals of very pale colour even though their contents of Fe are comparable with those in quartz of intense amethyst colour which has come from other sources.

Since only irradiation produces this green colour one has to assume that gamma radiation interacts with water to form oxygen and hydrogen and that the groups Si-OH and Si-O already present as point or line defects along twin planes or growth defects will be split forming respectively hydrogen and oxygen (Hashimoto *et al.,* 2001). This Si-O group is now electronically active to form colour centres that produce a band at 590 to 620 nm in the visible absorption spectrum *(Figure 26)* and a strong absorption at 220–260 nm in the UV. This centre is called the 'non-bonding oxygen hole centre' (NBOHC) and occurs in various types of silica, both crystalline and amorphous. The two absorption bands effectively form a transmission window at about 490 to 540 nm which produces the green colour *(Figure 27)*.

Figure 27: Untreated and gamma-irradiated wet quartz crystals. The same dose of irradiation produces different intensities of colour. Size of specimens between 2 and 4 cm. Photo by Rainer Schultz-Güttler.

These NBOHC defects are quite different from the Fe or Al substitutions described above. Rather, they find themselves on dislocations in the crystal structure with no direct bonding to neighbouring SiO_4 tetrahedra, or they exist in regions with highly strained bonds, such as twin lines, growth defects, spiral growth hillocks, step growth defects and so on. As such, they can be linked to a range of growth features in different crystals (Hosaka *et al.*, 1986; Stevens-Kalceff, 2009).

Perfection of growth in quartz depends strongly on growth velocity and suitability of solution chemistry. Quartz grown rapidly shows striations and the amount and thickness of these is a function of the growth rate. Higher growth rate will produce finer striations, whereas quartz grown slowly, fractions of mm a day, will show hardly any growth defects. In examining green quartzes, one can always find fine striations parallel to the rhombohedral faces —which may be produced by Brazil twins or growth defects.

It must then be concluded that this kind of 'wet quartz' grew rapidly. Since the growth of a crystal is a very local event, e.g. in geodes, it is understandable that there can be several generations of quartz in the same geode, each with certain specific growth features. Crystals which grew slowly can show intense

Figure 28: Bi-coloured quartz with an amethystine core and a green outer layer from Rio Grande do Sul, Brazil, probably reflecting different growth rates in different growth solutions. Crystals with green cores and amethystine layers can also be found. Size 8.3 cm. Photo by Rainer Schultz-Güttler.

amethyst colour and have a relatively low water content, while 'wet quartz' with its rapid growth will be colourless, even though it may have high amounts of iron and/or aluminium.

Sometimes the growth rate may vary and this can affect the number of defects in a single crystal. If initial growth is slow and later growth is fast, quartz can be produced which has a core with amethyst colour *(Figure 28)*, but which is green in the outer layers.

Studies of the colour stability of this green variety of quartz have shown that temperatures of 150°C are enough to bleach the quartz within one to two hours (Clerici, 2010), and its behaviour and stability under UV radiation and sunlight are currently being examined.

Rose quartz

Most pink quartz is found in massive compact form, only rarely as smaller euhedral crystals, and has a cloudy or translucent rather than transparent appearance *(Figure 29)*. A wide band with maximum at about 500 nm in the absorption spectrum *(Figure 30)* is characteristic. Lehmann and Bambauer (1973) ascribed this band to Ti^{3+} on substitutional sites of the crystal structure. The cause of the cloudy appearance is probably a light scattering process from tiny fibrous inclusions: Ignatov *et al.* (1990) and Goreva *et al.* (2001) found

Figure 29: Massive rose quartz. The cloudy appearance is typical and is probably due to an intergrowth of quartz with dumortierite. Weight of the faceted stone 8.76 ct. Photo by German Gemmological Association.

pink-coloured dumortierite in quartz and attributed the absorption band to Fe^{2+}-Ti^{4+}electron charge transfer. The pink single crystals are intrinsically different from massive rose quartz. In their absorption spectrum they have bands at 338 and 524 nm which have been attributed by Rossman (1994) to an Al O^{-}-P-associated complex forming a colour centre. The use of gamma irradiation intensifies the colour of these single-crystal rose quartzes *(Figure 31)*.

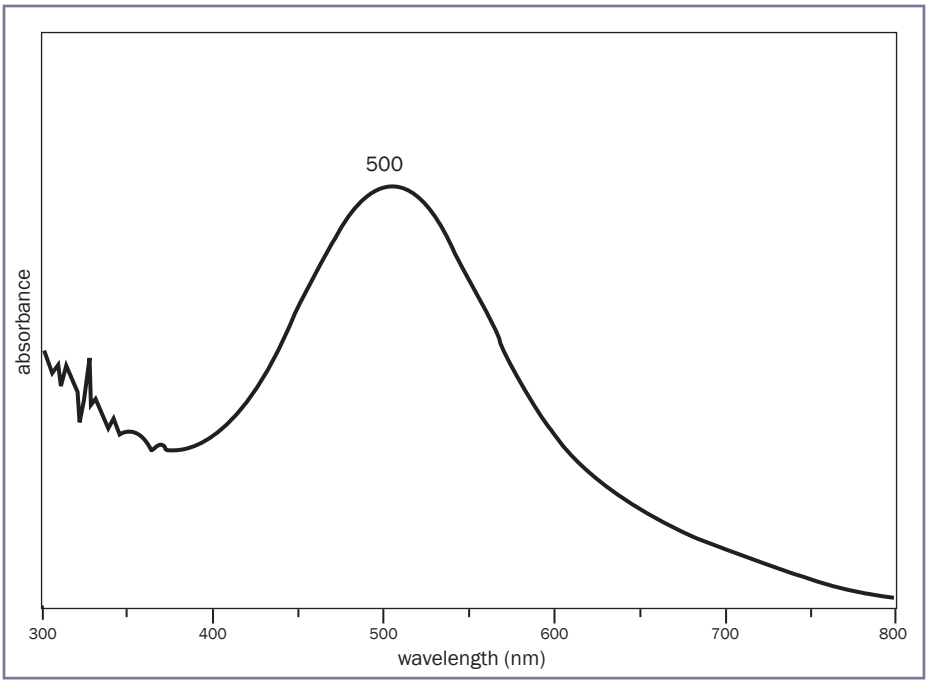

Figure 30: Visible range absorption spectrum of massive rose quartz, with a broad peak centred at about 500 nm.

Figure 31: Euhedral rose quartz crystal cluster: pale colour and irradiated sample with strong pink colour, which is quite stable to light. This sample is from Galileia, Minas Gerais; size 5 and 7 cm for each cluster. Photo by Rainer Schultz-Güttler.

Conclusions

Quartz, generally thought of as a gemstone with only a few colour varieties, such as amethyst, citrine and smoky quartz, has a more extensive range of colours, some of them induced by treatments. Heat and irradiation in particular have opened the way to increasing the range and availability of gem materials and to increasing their economic importance. So there is no need to search for deposits of these varieties, since so much colourless quartz with appropriate trace impurities can be found not only in Brazil but also in other parts of the world. The search for criteria to distinguish quartz susceptible to treatment is an ongoing task, since complex natural conditions of growth, as shown in this work, can influence and often determine the resulting colour of quartz.

However, the spectra and comparison tables presented here indicate some criteria that can already be used to identify the different kinds of quartz. Using spectroscopy, wet, hydrothermal quartz can be distinguished from quartz with very little water; using pleochroism and twinning, citrine and smoky quartz can be distinguished.

Besides this it is also important to know whether the colour of a gemstone is natural or induced by means of treatments. From the data discussed in this work it is clear that much has still to be done to decipher all the factors determining each type of colour. But what is now established is that it is easy to separate the two types of green quartz, prasiolite and green quartz by means of use of the Chelsea Colour Filter, and to recognize the colour of 'green gold' as a product of irradiation and heat treatment. The temperatures discussed in the text and on the charts also indicate that jewellers should take special care when using heat in repairing any jewellery that contains coloured varieties of quartz.

References

Aines, R.D., and Rossman, G.R., 1986. Relationships between radiation damage and trace water in zircon, quartz and topaz. *Am. Mineral.*, **71**, 1186–93

Barbosa, C.T., 2009. A cor do citrino: Efeito de irradiação e tratamento térmico. TCC-State University of São Paulo, UNESP, 77pp

Burkov, V.I., Egorisheva, A.V., Kargin, Yu F., Mar'in, A.A., and Fedotov, E.V., 2005. Circular dichroism Spectra of synthetic amethyst crystals. *Crystallography Reports,* **50**(3) 461–4

Clerici, G., 2010. Quartzo verde e Ametista: Formação de Cor e Estabilidade Térmica. Trabalho de Formatura 50p. Universidade de São Paulo. 50 pp

Cohen, A.J., 1985. Amethyst color in quartz, the result of radiation protection involving iron. *Am. Miner.,* **70**, 1180–5

Cox, R.T., 1977. Optical absorption of the d4 ion Fe^{4+} in pleochroic amethyst quartz. *J. Phys. C. Solid State Phys.,* **10**, 4631–43

Dedushenko, S.K., Makhina, I.B., Mar'in, A.A., Mukhanov, V.A., and Perfiliev, Yu D., 2004. What oxidation state of iron determines the Amethyst colour. *Hyperfine Interactions,* **156/157**, 417–22

Favacho-Silva, M., 2000. Variedades gemológicas de quartzo em Minas Gerais : Geologia, mineralogia, causas de cor, técnicas de tratamento e aspectos econômicos. *Dissertação de Mestrado,* UFMG, 182 pp

Goreva J.S., Ma, C., and Rossman, G.R., 2001. Fibrous nanoinclusions in massive rose quartz: The origin of rose coloration. *American Mineralogist,* **86**, 466–72

Götze, J., 2009. Chemistry, textures and physical properties of quartz — geological interpretation and technical application. *Mineral. Mag.,* **73**(4), 645–71

Graetsch, H., Flörke, O.W., and Miehe, G., 1985. The nature of water in chalcedony and opal-C from Brazilian agate Geodes. *Phys. Chem. Min.,* **12**, 300–6

Guttler, R.A.S., Enokihara, C.T., and Rela, P.R., 2009. Characterization of color centers in quartz induced by gamma irradiation. *INAC, International Nuclear Atlantic Conference, 2009,* Rio de Janeiro

Guzzo, P.L., Iwasaki, F., and Iwasaki, H., 1997. Al-related centres in relation to gamma-irradiation. Response in natural quartz. *Phys. Chem. Min.,* **24**, 254–63

Hashimoto, T., Fujita, H., and Hase, H., 2001. Effects of atomic hydrogen and annealing temperatures on some radiation-induced phenomena in differently originated quartz. *Radiation Measurements,* **33**, 431–7

Hebert, L.B., and Rossman, G., 2008. Greenish quartz from the Thunder Bay Amethyst Mine Panorama, Thunder Bay, Ontario, Canada. *Canadian Mineralogist,* **46**, 61–74

Henn, U., and Schultz-Güttler, R., 2011. Das Farbenspektrum der Quarze. *Z. Dt. Gemmol. Ges.,* **60**(3/4), 63–86

Hosaka, M., Miyata, T., and Taki, S., 1986. Observations of striations on hydrothermally-grown prism faces of quartz. *Journal of Crystal Growth,* **75**, 473–80

Ignatov, S.I., Platonov, A.N., Sedenko, V.S., and Taran, M.N., 1990. Rose colour of quartz caused by dumortierite micro inclusions. *Dop. Akad. Nauk Ukrain.,* RSR B7, 23–7

Iwasaki, F., 1980. Hydrogen bonded OH in synthetic quartz. *Japanese Journal of Applied Physics,* **19**, 1247–56

Iwasaki, F., and Iwasaki, H., 1993. Impurity species in synthetic and Brazilian natural quartz. *Japanese Journal Appl. Phys.,* **32**, 893–907

Lehmann, G., 1967. Farbzentrum des Eisens als Ursache der Farbe von Amethyst. *Z. Naturforschung,* **22**, 2080–5

Lehmann, G., and Bambauer, H.U., 1973. Quarzkristalle und ihre Farben. *Angew. Chem.,* **85**, 281–9

Nassau, K., 1981. Artificially induced color in amethyst-citrine quartz. *Gems & Gemology,* **17**, 37–9

Nassau, K., and Prescott, B.E., 1975. A reinterpretation of smoky quartz. *Phys. Stat. Solid.,* **29**, 659–63

Nassau, K., and Prescott, B.E., 1977. Smoky, blue, greenish yellow, and other irradiation-related colors in quartz. *Min. Mag.,* **41**, 301–12

Neumann, E., and Schmetzer, K., 1984. Farbe, Farbursachen und Mechanismen der Farbumwandlung von Amethyst. *Z. Dt. Gemmol. Ges.,* **33**, 35–42

Nunes, E.H.M., Melo, V., Lameiras, F., Liz, O., Pinheiro, A., Machado, G., and Vasconcelos, W., 2009. Determination of the potential for extrinsic color development in natural colorless quartz. *Am. Mineral.,* **94**, 935–41

Rossman, G.R., 1994. Colored varieties of the silica minerals. *Reviews in Mineralogy and Geochemistry,* **29**, 433–63

Salh, R., 2011. Defect related luminescence in silicon dioxide network: a review. In: *Crystalline Silicon — Properties and Uses,* Basu, S. (Ed.), p. 135–72. InTech, Rijeka, Croatia

Schultz-Güttler, R., 2006. Blau-Quarz aus Minas Gerais, Brasilien. *Z. Dt. Gemmol. Ges.,* **55**, 135–6

Schultz-Güttler, R., and Kohigashi, H.C., 2006. Treated violetish blue to violet quartz from Brazil. *Gems & Gemology,* **42**, 285–6

Schultz-Güttler, R., Henn, U., and Milisenda, C.C., 2008. Grüne Quarze – Farbursachen und Behandlung. *Z. Dt. Gemmol. Ges.,* **57**, 61–72

SivaRamaiah, G., Lin, J.R., and Pan, Y.M., 2011. Electron paramagnetic resonance spectroscopy of Fe ions in amethyst: Thermodynamic potentials and magnetic susceptibility. *Physics and Chemistry of Minerals,* **38**(2), 159–67

Stevens-Kalceff, M.A., 2009. Cathodoluminscence micro-characterization of point defects in α-quartz. *Mineral. Mag.,* **73**(4), 585–605

Stock, H.D., and Lehmann, G., 1977. Phenomena associated with diffusion of trivalent iron in amethyst quartz. *J. Phys. Chem. Solids,* **38**, 243–6

Trabulsi, M., 2010. Quartzo fumé, Citrino e Greengold: Formação da Cor e estabilidade térmica. Bsc Thesis USP, São Paulo, 52 pp

Vasconcelos, P.M., Wenk, H.-R., and Rossman, G.R., 1994. The Anahí ametrine mine, Bolivia. *Gems & Gemology,* **30**, 4–23

The Authors

Dr Ulrich Henn
German Gemmological Association, Prof.-Schlossmacher-Str. 1, D-55743 Idar-Oberstein, Germany
Email: ulihenn@dgemg.com

Prof. Dr Rainer Schultz-Güttler
Instituto de Geociencias-USP, Rua do Lago 562, São Paulo, Brasil
Email: rainersg@usp.br

Tanita digital carat scale

- Perfect for accurately weighing diamonds and precious gems
- 100.00 ct portable scale (batteries included)
- Accuracy 0.01 ct; also measures in grams, grains and ounces
- Portable case supplied for protection whilst in transit
- 20 gram calibration weight supplied

Price: £185.00

plus VAT, postage and packing

BAL0026

A 10% discount is given on all instruments ordered by Gem-A members and Gem-A registered students.

MONTHLY SPECIALS
on books and instruments.
Log on to the Gem-A website at www.gem-a.com to discover what is on offer.

Tanita, used worldwide by the jewellery trade, is one of the most respected makers of balances.

To order your Tanita Scale from the Gem-A shop go to www.gem-a.com/shop.aspx or contact Alan Clark on +44 (0)20 7404 3334, email shop@gem-a.com

Gem-A
THE GEMMOLOGICAL ASSOCIATION OF GREAT BRITAIN

The identification features of undisclosed loose and mounted CVD synthetic diamonds which have appeared recently in the NGTC laboratory

Zhonghua Song, Taijin Lu, Yan Lan, Meidong Shen, Jie Ke, Jianhui Liu and Yubing Zhang

Abstract: Since February 2012, undisclosed CVD synthetic diamonds, both loose and mounted, submitted to National Gemstone Testing Centre (NGTC), China, have been examined. It was found that these gem-quality CVD synthetic diamonds, particularly the mounted ones, are difficult to distinguish from natural diamonds using only routine identification techniques and procedure, but they were effectively identified using photoluminescence and DiamondView™ techniques. The 736 nm double lines in the photoluminescence spectra and the layered growth striations observed in DiamondView™ fluorescence images are the two most important characteristics for identification of the CVD synthetic diamonds. The gemmological and spectroscopic properties of the CVD synthetic diamonds identified are reported.

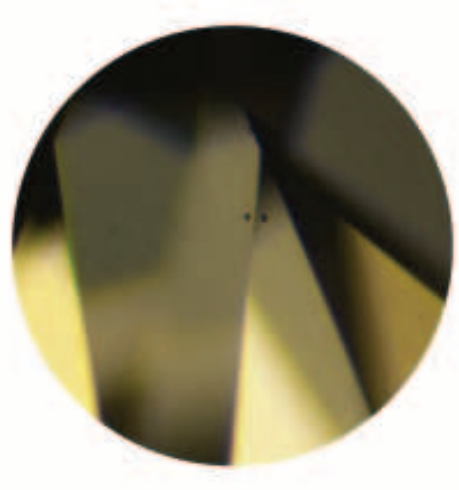

Keywords: CVD synthetic diamond, diamond testing, DiamondView™, fluorescence, internal features, phosphorescence, photoluminescence

Introduction

In recent years, a considerable number of gem-quality synthetic diamonds produced by chemical vapour deposition (CVD) have reached the market. Most of these have come from Apollo Diamond Inc. (Wang *et al.*, 2003). In November 2010, Gemesis Corporation announced plans to market CVD-grown synthetics. In autumn 2011, the GIA laboratory reported the identification characteristics of the CVD synthetic diamonds grown by Gemesis Corporation (Wang and Moses, 2011). Subsequently, this summer, Wang *et al.*, (2012) reported further gemmological and spectroscopic properties of CVD synthetic diamonds from Gemesis Corporation in detail.

In 2012, CVD synthetic diamond has been a subject of concern in the gem market, since the synthetic diamonds now being produced are very similar to natural diamond in visual appearance. It has been reported that undisclosed CVD synthetic diamonds were submitted to the International Gemological Institute (IGI), National Gemstone Testing Centre (NGTC)

Figure 1: Undisclosed loose and mounted CVD synthetic diamonds submitted to NGTC lab. Photograph by Zhixin Wu and Fei Wang.

and Gemological Institute of America (GIA) laboratories as natural diamonds for standard grading reports (DTC, 2012; NGTC, 2012; Even-Zohar, 2012). From February to July 2012, a total of 49 loose and 14 mounted diamonds all undisclosed CVD synthetic diamonds, were submitted to the NGTC — in both the Shenzhen and Beijing laboratories — for identification and grading reports. Here, the gemmological properties, particularly the identification features for these undisclosed CVD synthetic diamonds, are reported and discussed.

Samples and identification techniques

The surfaces and internal features of all 63 stones were examined using a gemmological microscope. Luminescence to ultraviolet radiation and phosphorescence were observed using 254 nm (short-wave) and 365 nm (long-wave) excitation, and also with the DiamondView™ deep-ultraviolet (<230 nm) imaging system.

Infrared absorption spectra were recorded on all the samples covering the mid-infrared range (6000–400 cm^{-1}, 2 cm^{-1} resolution) and near infrared range (12000–4000 cm^{-1}) at room temperature with a Nicolet 6700 Fourier transform infrared (FTIR) spectrometer. A KBr beam splitter was used for the mid-infrared range, and a quartz beam splitter for the near-infrared range. Vis-NIR spectra in the range of 400–1000 nm were collected with the Avantes-2048 system. We recorded photoluminescence spectra with the diamond immersed in liquid nitrogen, using a Renishaw 2000 system with a 514.5 nm Ar ion laser as the light source. Qualitative chemical analyses were obtained using energy-dispersive X-ray fluorescence (EDXRF) with a Thermo Electron Quant'X spectrometer at a voltage of 18 kV and a beam current of 0.3 mA for metallic element detection.

Results

Visual appearance

All the stones are colourless or near-colourless (G–J colour grade) *(Figure 1)*, although some are pale grey; none shows any brown coloration. The loose stones weigh between 0.30 and 0.60 ct, and the size of the mounted stones ranged from an estimated 0.24 to 0.38 ct. All the diamonds are round brilliants and no laser inscriptions were found on the girdles.

Inclusions

A few dark irregular inclusions are visible under magnification *(Figure 2)*,

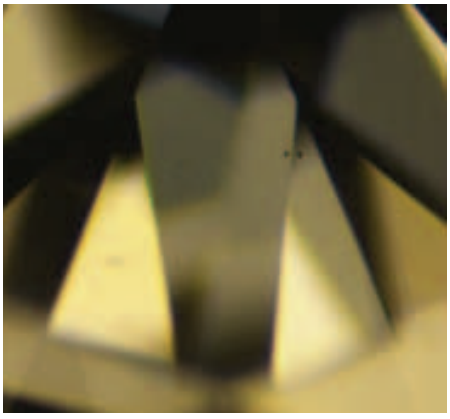

Figure 2: Dark inclusion in a 0.56 ct CVD synthetic diamond, Magnified 50 ×. Photomicrograph by Zhonghua Song and Licong Li.

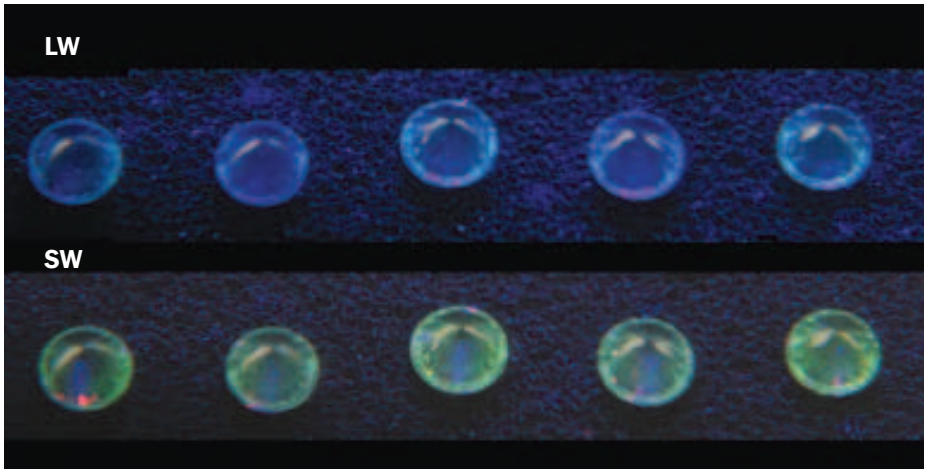

Figure 3: Fluorescence of some CVD synthetic diamonds under long-wave (top) and short-wave (bottom) UV light. Fluorescence under SWUV is stronger than that under LWUV.

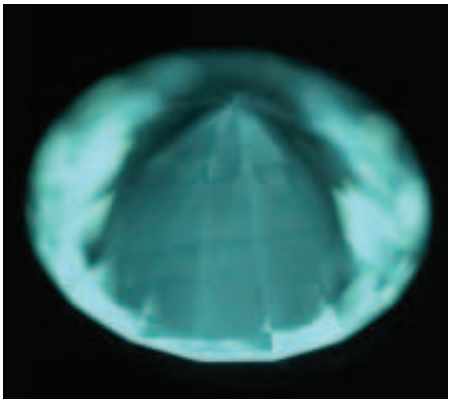

Figure 4: DiamondView™ fluorescence image of a CVD synthetic diamond showing layered growth striations and bluish-green fluorescence.

which are similar to the dark inclusions in natural diamonds. The dark inclusions were believed to be non-diamond carbon by Martineau *et al.* (2004). The clarity grades of these diamonds were equivalent to VS2 or better. When these diamonds are observed between crossed polarizers, they do not show the tatami structure typical of type IIa natural diamond.

Luminescence

When exposed to long-wave UV radiation, some of the stones were inert to UV, while others fluoresced very weak greenish blue. However, almost all showed weak to moderate greenish yellow fluorescence under short-wave UV radiation, and in any one stone, the fluorescence was stronger than under long-wave radiation *(Figure 3)*. No obvious phosphorescence was seen.

When viewed in DiamondView™, the diamonds displayed bluish-green fluorescence and noticeable blue phosphorescence, with characteristic layered growth striations *(Figure 4)*.

Spectra

The infrared absorption spectra in the mid-infrared region showed that these diamonds were all type IIa, with an absence of any absorption bands related to nitrogen and hydrogen. In the near-infrared region, there was no evidence of any H-related absorption.

The Vis-NIR spectrum revealed a smooth, gradual increase in absorption from long wave to short wave, but no distinct absorption lines such as 415 nm lines (found in many natural diamonds) were noted.

All of our CVD samples showed similar photoluminescence (PL) spectra *(Figure 5)*, including moderately strong photoluminescence N-V emission lines at 575 and 637 nm. The relative intensities of these two lines varied, but in general the 637 nm line was more intense. All samples tested had a weak to moderate to strong doublet peak at 736.3 nm and 736.0 nm that is attributed to silicon-vacancy centres (Clark *et al.*, 1995).

Composition

The EDXRF analysis of all the stones did not display any X-ray emission peaks associated with metal elements such as nickel, iron or cobalt, and the stones were not attracted to a magnet.

Discussion

Wang *et al.* (2011) reported on similar products introduced by Florida-based Gemesis Corporation and it was noted that although these CVD synthetic diamonds were more similar in appearance to natural diamonds, they did show differences in their spectra and fluorescence features under the DiamondView™ (Wang *et al.*, 2003; Martineau *et al.*, 2004).

In early 2012, the NGTC laboratory discovered undisclosed CVD synthetic diamonds during routine processing of submitted stones. The main features were found to be extremely similar to those that the GIA laboratory had reported in the autumn of 2011. What calls for special attention is that the undisclosed CVD synthetic diamonds were found mounted in diamond jewellery.

The colour grades of these synthetic diamonds lie in the range G–J. This differs from previously-grown CVD diamonds which generally had a brown tone. So the current CVD diamonds are closer to natural diamonds in visual appearance.

The clarity grades of these samples vary between VS2 and VVS2, and reflect the small quantities of black inclusions; these resemble those in natural diamonds *(Figure 2)*, so they are of no help in distinguishing the stones from natural diamonds.

The blue-green fluorescence and blue phosphorescence colours of the DiamondView™ images *(Figure 4)*

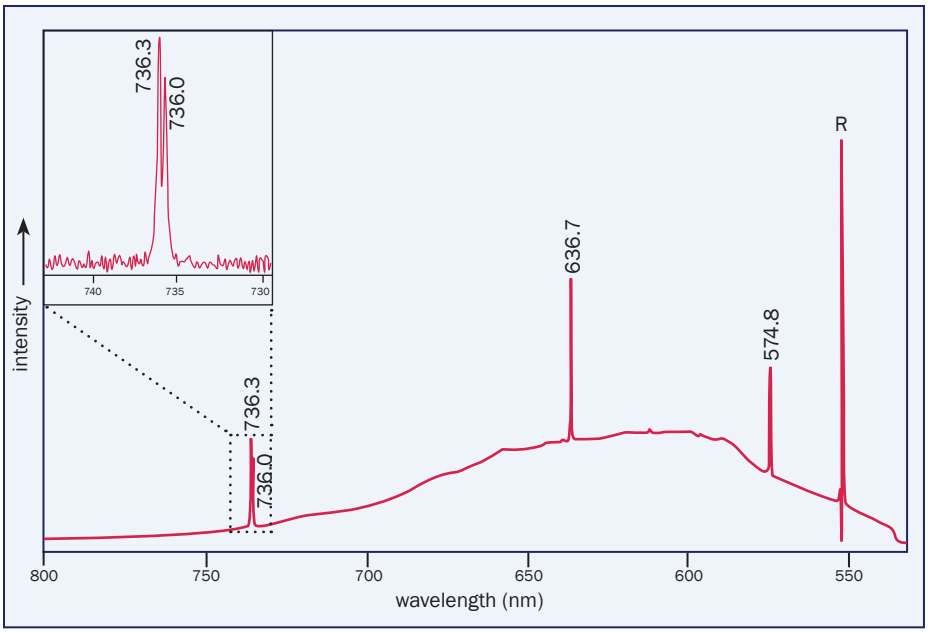

Figure 5: Photoluminescence spectrum of a CVD synthetic diamond, excited at 514.5 nm, recorded with the specimen at 77K. R is produced by first-order Raman scattering, the peaks at 574.8 and 636.7 nm are due to transitions at the neutral and negative N-V centres respectively, and the Si-related peaks at 736.0 nm and 736.3 nm are clearly visible.

described above are quite different from those of the traditional CVD products, which hitherto have been shades of orange. The blue phosphorescence is mainly caused by the boron added during the growth processes (Martineau *et al*., 2004). DiamondView™ images are best obtained from the pavilions of brilliants which reveal typical growth striations of CVD synthetics, but for mounted diamonds, obtaining a view of the pavilion is usually impossible. So the better method for these stones is to use the PL spectrum obtained at the liquid nitrogen temperature. Whether for mounted or loose stones, all display doublet lines at 736.3 and 736.0 nm caused by the Si-V defect lines in the PL spectrum *(Figure 5)*.

Wang *et al*. (2003) reported that Apollo CVD synthetic diamonds have the hydrogen-related absorption lines at 8753 cm^{-1}, 7354 cm^{-1}, 6856 cm^{-1}, 6425 cm^{-1}, 5563 cm^{-1} and 3123 cm^{-1} in the near- and mid-infrared areas, which were only found in CVD synthetic diamonds, not in natural diamonds. However, after high temperature and high pressure treatment, such absorption peaks disappeared and a new absorption peak at 3107 cm^{-1} appeared; unfortunately this peak also occurs in natural diamonds. Our CVD synthetic diamonds do not have any hydrogen-related characteristic absorption peaks in the near- and mid-infrared ranges.

Although these CVD synthetic diamonds were annealed after their growth to improve their colour and transparency (Wang and Moses, 2011; Wang *et al.,* 2012), the Si-V defect (736 nm line) is relatively very stable and is not likely to be destroyed by high temperature (Clark *et al*., 1995). Therefore, PL spectra and fluorescence properties are the key to identifying these recent CVD diamonds.

Summary

Gemmological and spectroscopic properties of loose and mounted diamonds submitted to NGTC laboratories have been identified as CVD synthetics. They are colourless or near-colourless, ranging from G to J, with clarity grades of VVS2 to VS2. Absorption spectra show all samples to be type IIa, and no other defect-related absorption features were detected in the mid- and near-infrared spectral ranges. Photoluminescence spectra were dominated by N-V and $[Si\text{-}V]^-$ centres. PL spectroscopy at low temperature and DiamondView™ fluorescence images are critical in separating these synthetic diamonds from their natural counterparts. For fast identification of mounted synthetic diamonds, PL spectra are more useful because the current DiamondView™ fluorescence imaging system is most effective if there is access to the pavilion of a stone.

Acknowledgements

The authors thank all the members of the NGTC for their great support and valuable comments; and Ning Hu for his skilled picture editing. Also grateful thanks are due to Dr David Fisher, Dr Philip M. Martineau of the DTC research centre and Yang Fan, Forevermark, China, who have all provided useful information about the CVD synthetic diamonds.

References

Clark, C.D., Kanda, H., Kiflawi, I., and Sittas, G., 1995. Silicon defects in diamond. *Physical Review B,* **51**, 16681–8

Diamond Trading Company (DTC), 2012. Undisclosed submissions of CVD synthetics to grading laboratories. See, for example, *Diamond Intelligence Briefs,* **27**(709), 7290

Even-Zohar, C., 2012. Synthetic specifically "made to defraud". *Diamond Intelligence Briefs,* **27**(709), 7281–3

Martineau, P.M., Lawson, S.C., Taylor, A.J., Quinn, S.J., Evans, D.J.F., and Crowder, M.J., 2004. Identification of synthetic diamond grown using chemical vapor deposition (CVD). *Gems & Gemology,* **40**(1), 2–25

National Gemstone Testing Center (NGTC), 2012. Notice of CVD synthetic diamonds found in Chinese market, 2012 June

Wang, W., D'Haenens-Johansson, U.F.S., Johnson P., Moe, K.S., Emerson, E., Newton, M.E., and Moses, T.M., 2012. CVD synthetic diamonds from Gemesis Corp. *Gems & Gemology,* **48**(2), 80–97

Wang, W., and Moses, T.M., 2011. Gem quality CVD synthetic diamonds from Gemesis. *Gems & Gemology,* **47**(3), 227–8

Wang, W., Moses, T.M., Linares, R.C., Shigley, J.E., Hall, M., and Butler, J.E., 2003. Gem-quality synthetic diamonds grown by the Chemical Vapor Deposition (CVD) method. *Gems & Gemology,* **39**(4), 268–83

The Author

Zhonghua Song CGC, NGTC, Beijing, China.
Taijin Lu Ph.D., Chief Researcher, NGTC, Beijing
Yan Lan, Deputy Director, NGTC Shenzhen Laboratory
Meidong Shen, Chief Technology Officer, NGTC, Beijing
Jie Ke, Director, NGTC
Jianhui Liu, Gemologist, NGTC, Beijing
Yubing Zhang CGC, NGTC, Shenzhen

National Gemstone Testing Center (NGTC), Beijing 100013, China

Flux-grown synthetic alexandrites from Creative Crystals Inc.

Dr Karl Schmetzer, Dr Heinz-Jürgen Bernhardt and Thomas Hainschwang

Abstract: Mineralogical and gemmological properties of flux-grown synthetic alexandrites from Creative Crystals Inc. are described. The samples were grown with three different seed orientations parallel to the prism **r** (130), parallel to the pinacoid **b** (010) and parallel to the dipyramid **l** (133). Details of the growth process are indicated by the morphology of rough single crystals and by the internal growth patterns of the rough and faceted alexandrites. The samples were produced in numerous growth cycles in a slow cooling process, which is responsible for the growth of successive alexandrite layers and for distinct colour zoning within each layer. Detailed microprobe scans across several samples indicate that the colour zoning is due to variable chromium and iron contents. Absorption spectra in the visible and infrared ranges are presented. Absorption bands in the visible are assigned to chromium and iron as main colour-causing trace elements, and colour and pleochroism of samples in different orientations is evaluated using colorimetric data. The absorption bands in the infrared are polarized and assigned to structural OH-groups. The properties of the samples are compared with diagnostic features of Russian flux-grown alexandrites.

Keywords: alexandrite, chrysoberyl, chromium, colour zoning, comparison with Russian synthetic alexandrite, Creative Crystals Inc., crystal habit, inclusions, infrared spectra, iron, synthesis, visible spectra

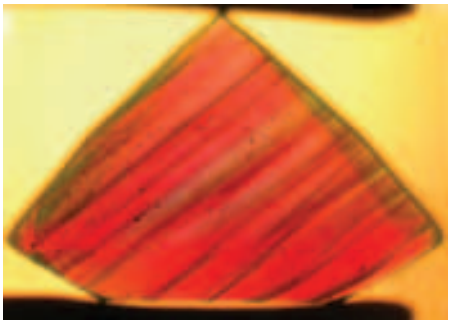

Layered growth zoning associated with an intense colour zoning in a faceted synthetic alexandrite grown by Creative Crystals Inc.; immersion, field of view 5.3 × 4.0 mm. Photo by K. Schmetzer.

Introduction

The first descriptions of flux growth of chrysoberyl date back to the mid-nineteenth century and an overview of this literature is given by Elwell and Scheel (1975). In the twentieth century, modern synthesis of chrysoberyl and chromium-bearing chrysoberyl (alexandrite) started in the 1960s. The first successful crystal growth experiments were conducted in fluxes of PbO, mixtures of PbO and PbF_2 or mixtures of Li_2MoO_4 and MoO_3. In general, the nutrient was added to the solvents (fluxes) and annealed in crucibles for some hours at temperatures between 1400 and 1350 °C. Reducing the temperature at a slow rate of about 12.5°C per hour initiated spontaneous nucleation and crystal growth to a maximum size of 5 mm, but mostly in the range of 1–2 mm in PbO or PbO/PbF_2 fluxes. From Li_2MoO_4/MoO_3 fluxes twinned platelets up to 3 mm were obtained. Seeded growth was also performed successfully (Farrell *et al.*, 1963; Farrell and Fang, 1964). However, using slower cooling rates of 0.5 °C per hour, much larger crystals up to 4.4 cm in diameter were obtained (Bonner and Van Uitert, 1968).

Figure 1: One of the first synthetic alexandrites grown by Creative Crystals Inc. in the early 1970s in daylight (left) and incandescent light (right); diameter of the sample 5.5 mm. Photo by K. Schmetzer.

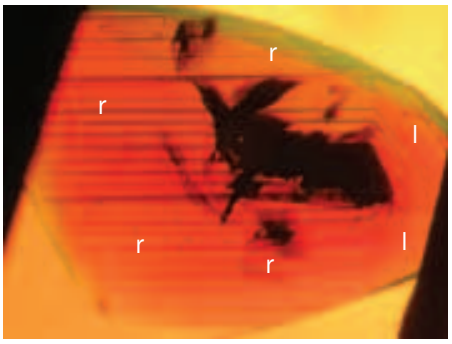

*Figure 2: Layered growth zoning associated with an intense colour zoning in a faceted synthetic alexandrite grown by Creative Crystals Inc.; the seed of the sample was oriented parallel to the **r** prism face, the internal growth pattern consists of layers parallel to the **r** prism and parallel to the **l** dipyramid; immersion, field of view 6.1 × 4.6 mm. Photo by K. Schmetzer.*

In the following decades, several papers about flux growth of synthetic chrysoberyl and alexandrite were published. Until the 1980s, growth was performed using the slow cooling method mentioned above, but experiments were done with different fluxes (see overview by Schmetzer *et al.*, 1996). Further progress in flux growth of chrysoberyl and alexandrite was made by the application of a temperature gradient to different parts of the crucible in specially constructed furnaces. This method, in which the nutrient is kept at a somewhat higher temperature than the growing crystals, was described by Russian and Japanese scientists (see again the summary in Schmetzer *et al.*, 1996). With this technique, crystal growth was performed both by spontaneous nucleation and by seeded growth (Bukin, 1993).

In 1972 the first commercially produced synthetic alexandrites were introduced to the US market by the company Creative Crystals Inc., residing at San Ramon, California *(Figure 1)*. The first descriptions by Liddicoat (1972) and Eppler (1974) indicated a flux growth technique and described various inclusion forms of residual flux as well as metallic particles, the latter most probably derived from the crucible walls. Both authors mentioned distinct growth zoning or growth banding in the faceted samples, a feature also indicated by cathodoluminescence images, and this indicates variable chemical composition within the crystals (Gaal, 1976).

The first faceted samples of Russian flux-grown alexandrite, which were produced from Bi_2O_3- and MoO_3-bearing fluxes at the Institute of Geology and Geophysics, Novosibirsk (Rodionov and Novgorodtseva, 1988; Bukin, 1993), appeared on the market in the mid 1980s and were described in detail in various papers correlating mineralogical and gemmological properties with the growth method used (Trossarelli, 1986; Henn *et al.*, 1988; Henn, 1992, 2000; Schmetzer *et al.*, 1996). In contrast, although a patent by Cline and Patterson assigned to Creative Crystals Inc. was published in 1975 and great quantities of synthetic alexandrites were produced and released to the market in the 1970s to 1980s (see, e.g. Elwell, 1979; Nassau, 1980 a,b), no further detailed studies of the material produced by Creative Crystals Inc., which correlates chemical, physical and microscopic properties with growth conditions were published. In addition, to the knowledge of the present authors, no gemmological data concerning any rough material is publicly available.

The most detailed examination of faceted alexandrites produced by Creative Crystals Inc. is found in an unpublished diploma thesis of Pohl (1989). In addition to the various forms of residual flux and platinum particles which had been mentioned by Liddicoat (1972) and Eppler (1974), she described a shell-like three-dimensional growth structure. Under crossed polarizers, the different growth planes of the successive growth layers show a distinct interference pattern. Furthermore, an angle of 54 ± 2° was found to be common between different dominant growth faces, but the individual faces were not identified.

Although it is generally understood that identification of the alexandrites grown by Creative Crystals Inc. and their distinction from natural alexandrites is straightforward because of the presence of various forms of residual flux and metallic platinum particles, this is not foolproof because faceted samples above 10 ct without any such diagnostic inclusions are available, and, in some slightly included samples, parts of the flux feathers can closely resemble healing feathers in natural alexandrites. So, for stones like these, the internal growth pattern might be the only microscopic feature of diagnostic value — if properly identified and understood.

History of research and challenges

In the process of Pohl's preparation of her diploma thesis in the late 1980s at Heidelberg University, Germany, one of the present authors (KS) had the chance to examine under the microscope her research material, which had been loaned from the collection of H. Bank, Idar-Oberstein. Several microscopic features were not understood in detail and could not be correlated with a specific growth process. In particular, all faceted samples showed a three-dimensional layered growth pattern *(Figure 2)*, occasionally

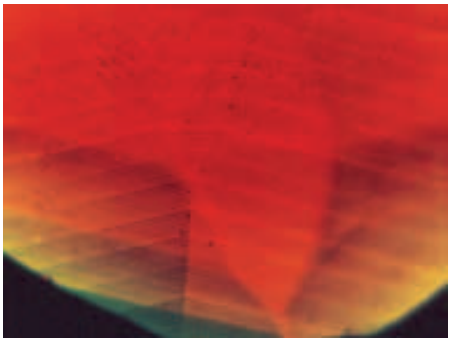

Figure 3: Characteristic interference pattern shown by the layered growth structure of a faceted synthetic alexandrite by Creative Crystals Inc.; immersion, crossed polarizers, field of view 4.1 × 3.1 mm. Photo by K. Schmetzer.

combined with an intense colour zoning. Under crossed polarizers, interference effects were visible at the boundaries of these layers *(Figure 3)*.

Because these interference effects closely resembled the optical impression which is commonly seen at the twin boundaries of alexandrite twins or trillings, the possibility that the different boundaries in the material from Creative Crystals Inc. represented twin boundaries of perhaps a sort of polysynthetic twinning was discussed. In contrast to the twinned components commonly seen in natural alexandrite however, the pleochroic colours of the area on each side of any boundary in a Creative Crystals Inc. alexandrite were always identical.

Having these unresolved problems in mind it was decided to dedicate some time to a new study of synthetic alexandrites grown by Creative Crystals Inc., mainly to understand the observed microscopic structures. With the experience gained from the study of natural alexandrites from different sources (Schmetzer, 2010, 2011), it was considered possible to interpret the internal growth patterns in more detail and to understand the basic growth technology of these samples. Because the faceted alexandrites studied in the late 1980s were no longer available, the authors started with five samples obtained from different collections and from gemmological colleagues.

In this period, with the help of A. Matlins, Woodstock, VT, U.S.A., we were able to contact David Patterson, one of the former owners of Creative Crystals Inc., residing now at San Ramon, CA, U.S.A. From the results obtained from the study of the first five faceted samples and some hints in the US patent by Cline and Patterson (1975), it was concluded that the alexandrites were grown using a process of several successive growth cycles (see below). Mr Patterson confirmed these first conclusions and agreed to help with further samples and information and especially to check if the interpretations obtained were consistent with his detailed knowledge about the general growth process and the variants applied. He also submitted a detailed history of alexandrite synthesis by Creative Crystals Inc., which was summarized for the present paper (see Box A).

Samples

The first faceted samples used for this study came from the personal collections of one author (KS) and gemmological friends and colleagues as well as from the reference and teaching collections of the German Gemmological Society, Idar-Oberstein, and the Swiss Gemmological Institute, Basel. Furthermore, David Patterson provided three rough crystals and five faceted alexandrites *(Figure 4)* from his personal collection, and a list of eight crystals which had been given to private museums and reference collections in the 1970s and 1980s. Finally, we were able to borrow four of these crystals and some additional faceted samples from the GIA collection, Carlsbad, and from the Smithsonian collection, Washington *(Figure 5)*. One additional crystal was submitted from the collection of Kevin Patterson.

D. Patterson (pers. comm., 2012) said that different orientations of the seed were used for crystal growth. After examination of the eight rough crystals available, it was concluded that each was grown on a seed with one of three different seed orientations, namely, parallel to the **r** (130), to the **b** (010) or to the **l** (133) faces of chrysoberyl. Most of the faceted samples in our study were found to belong to the type grown from seeds oriented parallel to the **r** prism. Therefore, in order to improve our representation of the Creative Crystals Inc. production, D. Patterson provided some faceted

Figure 4: Faceted synthetic alexandrites grown by Creative Crystals Inc. in daylight (above) and incandescent light; weight of samples from 0.87 to 1.93 ct, the rectangular sample on the left (1.61 ct) measures 8.5 × 5.2 mm. Photo by K. Schmetzer.

Box A

Alexandrite synthesis by Creative Crystals Inc., a history[1]

By David Patterson

In 1970 I heard of a group, formerly from the Lawrence Radiation Laboratory (LRL), who had synthesized alexandrite and emerald. I contacted them and we started working together. They were then owned by Physics International, a manufacturer of electron accelerators. The group, at that time, consisted of Carl Cline and a very talented technician named Don Kingman. Carl was a theoretical metallurgist and Don was an expert at growing crystals. At that time, they were able to grow spontaneously-nucleated chromium-doped chrysoberyl and had just started looking at seeding. The solubility of the flux had been well established. Carl had accepted a job with Allied Chemical and was scheduled to move to New Jersey in a month.

Physics International approached me to see if I was interested in buying the operation. Creative Crystals Inc. was incorporated and I was made president. Neither Carl Cline nor Don Kingman had seen a fine alexandrite before. I had several of them and some Russian and Rhodesian rough. We ran a wet chemical analysis on rough of both origins and found chromium, iron, and vanadium as most likely involved in the colour change.

We concurrently started studying the chromium-iron relationship and seed orientation. The chromium additive level was about right. We added iron and ran several cycles until we could see what the green was going to be. In each series of cycles we doubled the iron from the previous series of cycles. It took about five of these series before the red started to fade. We then backed off the iron and tried one series with vanadium at about the same concentration as the chromium. That series produced a wonderful green and absolutely no red at all. Thus, we abandoned vanadium, because we had to get into production to bring some cash into the operation and couldn't experiment further. We ran tests on five possible growth planes and found the **r** (130) face to be the best to grow on. It was at the beginning of this process that Carl Cline moved to New Jersey, after which his role consisted of occasional consultations and interfacing with the patent attorney.

In late 1971, early 1972, we were in production. At the time we purchased the crystal growing operation there was one production furnace (12 inch muffle), and two small research furnaces (5 inch muffles). All of the composition and orientation studies were done using the two small research furnaces. We then built three production furnaces (8 inch muffles). Production continued with the large and three medium-sized furnaces until the operation was shut down.

For crystal growth, a seed frame was located in the middle of a platinum crucible. Most flux growing operations use ceramic crucibles with platinum liners at operating temperatures in the neighbourhood of 800°C. At the temperatures we used (1240°C), the platinum liner and the ceramic reacted. Therefore, we had to use freestanding platinum crucibles. A straight cylindrical crucible would sag toward the bottom of the cylindrical surface after some months of use. Accordingly, we had special crucibles manufactured for us with a significantly thicker wall toward the bottom of the cylindrical surface and the bottom itself. This controlled the distortion to an allowable extent.

Each seed was drilled by hand and a platinum wire was inserted through the drilled hole and twisted. Each seed was then individually hung from the seed frame. The crucible was charged with part of the eutectic lithium-molybdate/molybdenum oxide flux and the desired additives. The partly filled crucible was placed in the airlock of the glove box. A previously mixed and blended mixture of beryllium oxide and alumina was put into the crucible and covered with the remaining flux. This procedure avoided any chance of beryllium contamination outside the glove box.

The charged crucible was raised into the furnace, the temperature was brought up to the high of the cycle and the charge of flux was allowed to melt. When all temperatures had equalized at 1240°C, the seed frame was lowered into the crucible. After ageing for about an hour, the downward cycle was started. The cooling rate was 0.5°C per hour for about two hours, at which time it was increased to 1°C per hour. The finishing temperature was 1000°C. The typical cycle was approximately one week.

At the end of the cycle, the crucible, with spent flux, was removed from the furnace and the seed frame was removed. The seeds and seed frame were cleaned by boiling in water. This cleaning was followed by a second cleaning with distilled water and then followed by isopropyl alcohol. If the crystals were large enough, they were harvested. Those that needed more growth were re-hung on the seed frame along with new seeds and returned for the next cycle. This procedure was basically followed from the beginning of production until it was finally shut down.

The first seeds were oriented from diffraction patterns. Since the test was expensive, we based initial seed orientation on the crystal faces we could see in the natural chrysoberyl material. This severely limited the usefulness of the material

1. A more detailed text was originally written for another purpose and condensed by one of the authors (KS) for this paper.

at hand, as most of it was anhedral and had no visible faces. Then it dawned on us that we could put a quantity of natural seed material in a crucible and grow a couple of layers on it. It was then easy to determine the face orientation before we sliced the material into seeds. This was a real breakthrough and gave us the accuracy of orientation we needed without the expense of X-ray diffraction. It also allowed us to sort out the trillings, as they were useless for single crystal seeds. For much of the production, natural chrysoberyl was used as the original seed material. The rough was sawn into seeds about 1.5–2 mm thick, parallel to the desired plane and ground and polished. About five cycles were grown on the seeds. The resulting crystals were sawn into three layers, the middle one being the original seed. The two outside halves were then used as production seeds and the middle seed was used to grow more production seeds. Each seed was hand finished to maintain the desired orientation.

Five seed orientations were originally tried. We settled on the seed orientation parallel to **r** (130) because it seemed to be the best balance between growth-rate and the resulting colour change. It was also a preferred orientation for the table of cut stones. Since the resulting crystals were roughly the profile of a cut stone, cutting yields were excellent. A few crystals were grown with seeds sliced parallel to one of the faces of the synthetic alexandrites oblique to the crystallographic a-, b- and c-axes[2]. These produced a superior colour change but the growth rate was comparatively slow. The fastest growth rates were those grown on the **b** (010) face, but the resulting colour change was not as good. Production with **b** oriented seeds started in 1979 and after 1980, most of the production was grown on the **b** (010) face.

In about 1976 we found it difficult to obtain single-crystal chrysoberyl for seed material, as most of it was twinned. We bought a pulled boule of colourless chrysoberyl, put the boule in our large furnace and grew a couple layers on it, which allowed us to identify the various crystal faces. The boule was cut into about two inch sections and each section was sawn with a wire saw to slices parallel to **r** (130). The wire saw produced a smooth enough surface that we didn't have to finish them by hand. After several growth cycles, to produce additional production seeds, the flux grown synthetic portions of the crystal were separated from the colourless seeds. As a result, there were a few, very few, instances where a small amount of colourless material remained in a production seed and in rare instances in the final product.

David Patterson in his cutting shop in front of a furnace, taken in 2012.

The Creative Crystals Inc. synthetic alexandrite was introduced to the market at the 1972 AGS convention in New Orleans. It created a significant amount of interest. On the basis of that experience and the fact that my stone dealer friends were very enthusiastic about it, I thought we had an easy market. This was certainly not so. The members of the AGS were not the typical jeweller and made up a relatively small market. After a few years of selling synthetic alexandrite, we still found some resistance to the product by the retail jeweller. They wanted a reference stone, but didn't want to stock it. This was before Chatham and other products of flux-grown origin had developed the market. Therefore, we were unable to ride piggyback on what they had done. Emeralds and rubies were well known, but at that time alexandrites were rare and appealed to fewer people than the more well-known gems.

Cost of production was very high. Raising the prices was not an option because they were already higher than those of flux-grown emeralds and rubies. We came to believe the cost of marketing would exceed the size of the market. Therefore, we concluded it was a dead-end project for us. The operation was sold in 1979 to a limited partnership formed for that purpose. The operation and the equipment were moved to other quarters in 1980. By 1982 the furnaces were not properly monitored and the inside of the furnaces melted. The limited partnership continued selling the product in stock, primarily to jewellers.

2. It was established by the present study that these seeds were oriented parallel to the **l** (133) face.

Flux-grown synthetic alexandrites from Creative Crystals Inc.

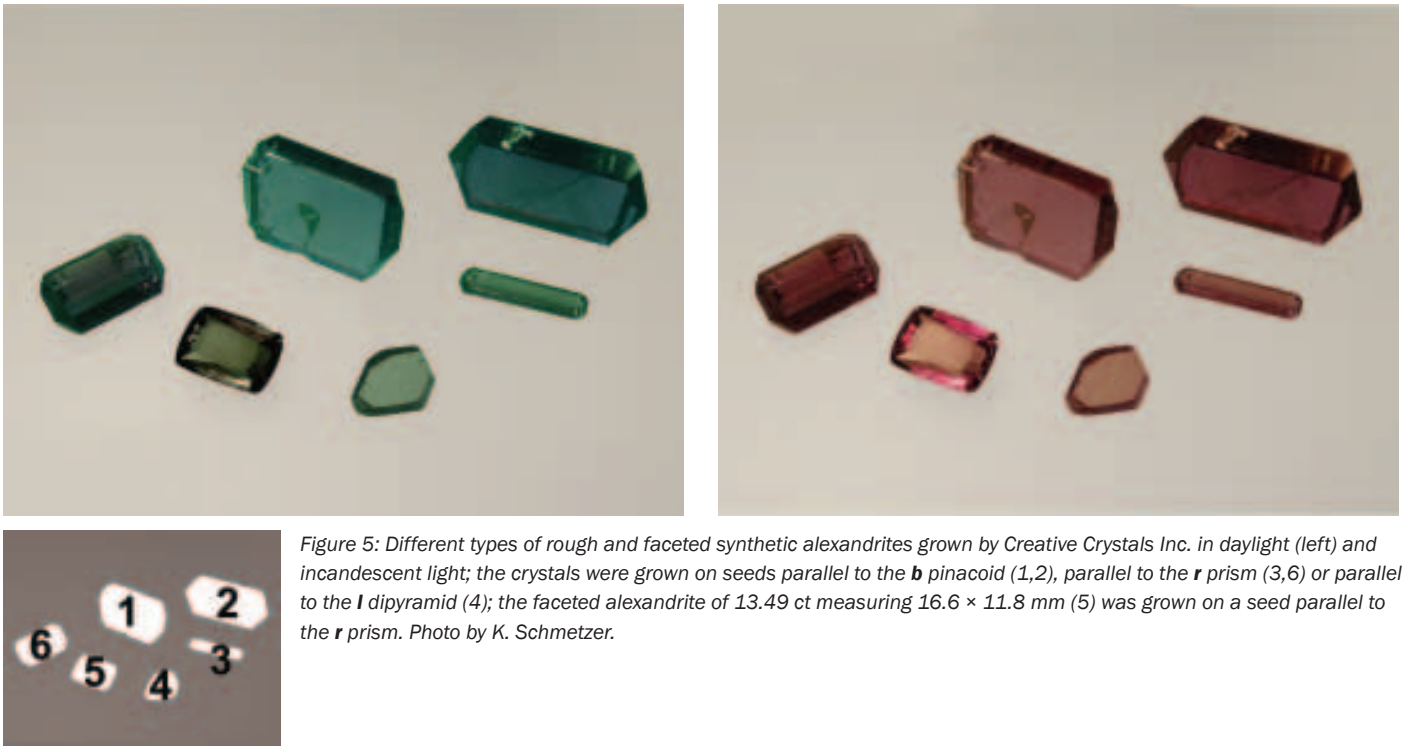

*Figure 5: Different types of rough and faceted synthetic alexandrites grown by Creative Crystals Inc. in daylight (left) and incandescent light; the crystals were grown on seeds parallel to the **b** pinacoid (1,2), parallel to the **r** prism (3,6) or parallel to the **l** dipyramid (4); the faceted alexandrite of 13.49 ct measuring 16.6 × 11.8 mm (5) was grown on a seed parallel to the **r** prism. Photo by K. Schmetzer.*

Table I: Dimensions of eight synthetic alexandrite crystals grown by Creative Crystals Inc.

Sample	Seed orientation parallel r (130)			
	Crystal 1 GIA collection	Crystal 2a K. Patterson collection	Crystal 2 Smithsonian collection	Crystal 3 GIA collection
Weight (ct)	12.38	15.25	20.41	5.12
Habit	tabular parallel **r**	thick tabular parallel **r**	thick tabular parallel **r**	columnar along c-axis
Seed plate	chrysoberyl	alexandrite	alexandrite	alexandrite
Mean thickness perpendicular to the seed plate (mm)	3.7	6.0	7.2	4.4
Dimensions parallel to the seed plate (mm)	∥ c-axis 19.7 ⊥ c-axis 12.8	∥ c-axis 19.4 ⊥ c-axis 11.8	∥ c-axis 21.2 ⊥ c-axis 12.8	∥ c-axis 22.8 ⊥ c-axis 5.2

Sample	Seed orientation parallel b (010)		Seed orientation parallel l (133)	
	Crystal 4 D. Patterson collection	Crystal 5 S. Avery collection	Crystal 6 D. Patterson collection	Crystal 7 D. Patterson collection
Weight (ct)	54.90	78.22	5.15	3.08
Habit	tabular parallel **b**	tabular parallel **b**	tabular parallel **l**	tabular parallel **l**
Seed plate	alexandrite	alexandrite	chrysoberyl/ alexandrite	alexandrite
Mean thickness perpendicular to the seed plate (mm)	4.9	7.8	2.4	1.9
Dimensions parallel to the seed plate (mm)	∥ c-axis 29.8 ∥ a-axis 23.4	∥ c-axis 37.1 ∥ a-axis 17.9	∥ **r** (seed) 15.1 ⊥ **r** (seed) 11.8	∥ **r** (seed) 13.8 ⊥ **r** (seed) 8.6

alexandrites belonging to the two other types (**b**- and **l**-grown samples), which he had kept in his collection since the 1980s or which were faceted from some of his remaining rough for the present study.

In total, in addition to the eight complete rough crystals (from 3 to 78 ct in weight, see *Table I*), this study is based on 17 faceted samples (from 0.75 to 13.49 ct in weight), 11 of them with seeds oriented parallel to **r** (130), four cut from crystals grown with seeds parallel to **b** (010), and two cut from rough grown with seeds parallel to the **l** (133) face. For the study of colour change and pleochroism, a small alexandrite cube with faces exactly perpendicular the crystallographic a-, b- and c-axes of chrysoberyl was prepared. The dimensions of the cube (length of edges) weighing 3.32 ct were 5.9 × 5.8 × 5.8 mm.

Morphology of rough crystals

The dimensions and seed orientations of eight rough crystals are summarized in *Table I.* The faces found in these crystals were the pinacoids **a** and **b**, three prism faces **k**, **m** and **r** and two dipyramids **o** and **l** (*Table II, Figure 6*). Five of these seven forms, namely the pinacoids **a** and **b**, the prisms **m** and **r**, and the dipyramid **o** are forms which are common in natural alexandrites from different localities. The prism **k** is present in chrysoberyl and alexandrite from a limited number of localities, e.g. Sri Lanka, and is a dominant crystal form in Russian flux-grown alexandrites (Schmetzer *et al.*, 1996). The dipyramid **l** has been, to the knowledge of the present authors, only described as an accessory form in one twinned chrysoberyl from Sri Lanka (Goldschmidt and Preiswerk, 1900).

Figure 7 shows an idealized drawing of a crystal with all seven forms. To understand growth features in rough and faceted alexandrites, it is important to realize that the dipyramid **l** is a dominant form. In samples grown with **r** (130) and **b** (010) seeds, the formation of larger **l** faces is a function of all growth parameters and — most probably — strongly influenced by the molybdenum-bearing flux. In crystals grown on **l** (133) seeds, it is clear that the **l** face is dominant. Three different angles are visible between different **l** faces (see *Figure 7*), which are designated as adjacent (with an angle of 56.61°), opposite (with an angle of 39.24°) and diagonal (with an angle of 71.04°).

Although an idealized alexandrite crystal is drawn in *Figure 7*, the synthetic alexandrites grown on seeds with orientations parallel to the **r** and **l** faces form strongly distorted crystals, in contrast to those grown on seeds parallel to the **b** pinacoid (see again *Figure 6*). In **b**-oriented seeds, the seed is chosen parallel to the two existing **b** (010) faces, and no other **b** faces with different sizes can exist or grow according to the symmetry of chrysoberyl. Therefore near-

Table II: Morphological properties of synthetic alexandrites grown by Creative Crystals Inc. Observed crystal forms and designation.

Crystal form	Designation	Miller indices (hkl)*	Number of faces
Pinacoid	a	(100)	2
	b	(010)	2
Prism	k	(021)	4
	m	(110)	4
	r	(130)	4
Dipyramid	o	(111)	8
	l	(133)	8

*Based on a morphological cell with a 4.42, b 9.39, c 5.47
Crystal class 2/m 2/m 2/m = D2h, twinning on (031) and (0$\bar{3}$1) is not present in the samples examined

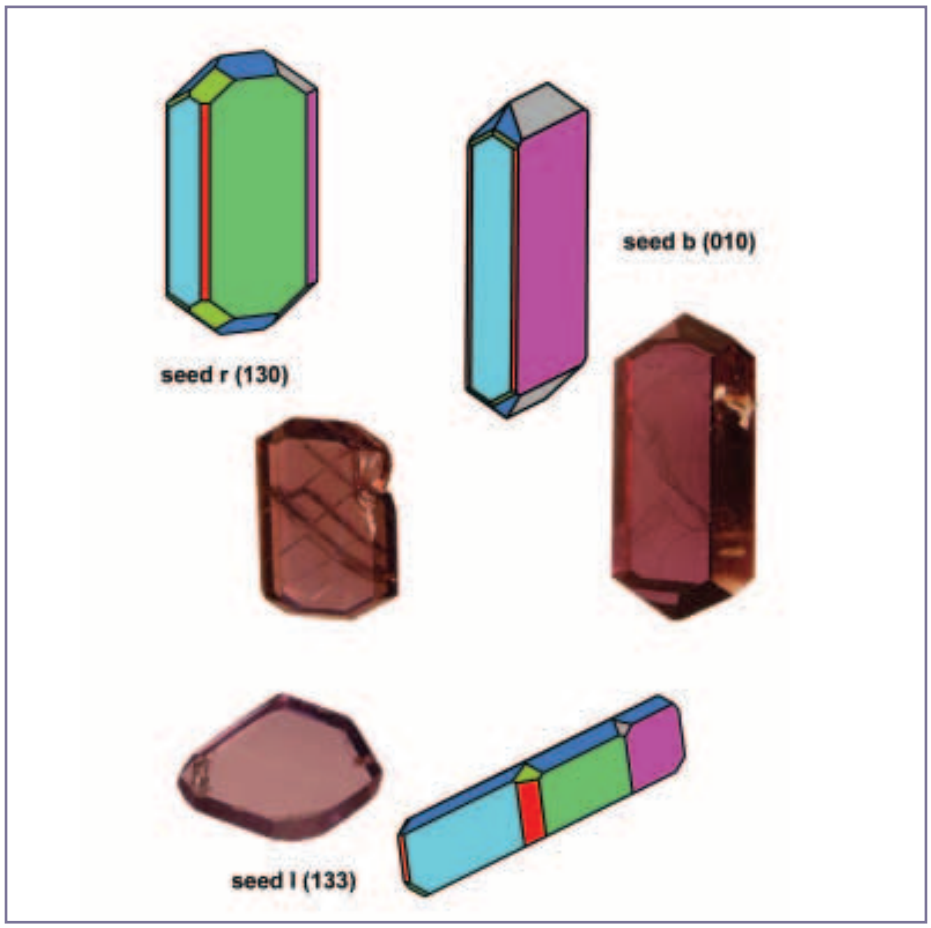

*Figure 6: Crystal drawings and samples of the three different types of synthetic alexandrite grown by Creative Crystals Inc., with seed orientations parallel to the **r**, **b** and **l** faces; crystals pictured in incandescent light, crystal with **r** seed 19.7 × 12.8 mm, crystal with **b** seed 37.1 × 17.9 mm, crystal with **l** seed 15.1 × 11.8 mm (samples not to scale). Photos and crystal drawings by K. Schmetzer.*

Flux-grown synthetic alexandrites from Creative Crystals Inc.

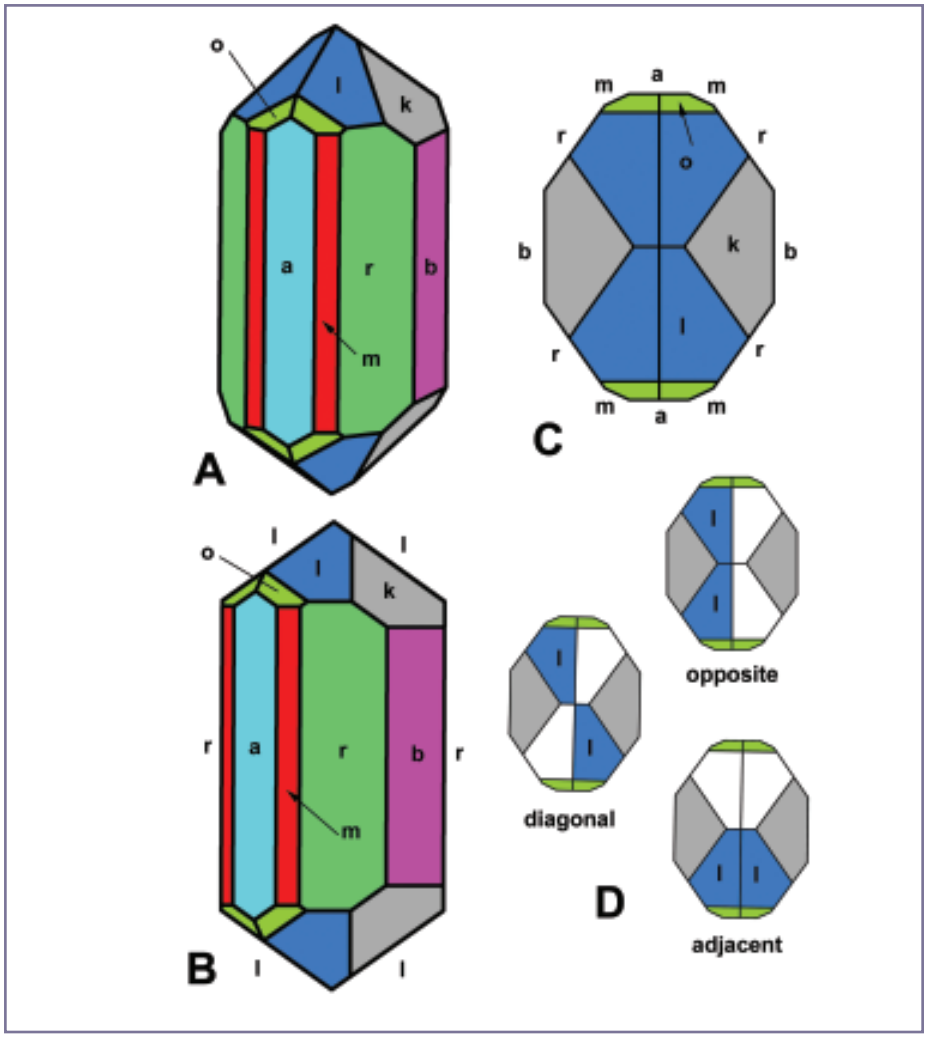

*Figure 7: Idealized drawing of a synthetic alexandrite crystal showing all faces observed in the different types of crystals grown by Creative Crystals Inc., namely the two pinacoids **a** and **b**, the three prisms **m**, **r**, and **k** and the two dipyramids **o** and **l**; (A) clinographic projection, (B) parallel projection of the zone [310] indicating a view perpendicular to the c-axis and parallel to two of the **r** faces, (C) parallel projection in a view parallel to the c-axis, (D) same view as in drawing (C) indicating the three different pairs of **l** dipyramids forming three different angles; in drawing (B) the pair of diagonal **l** faces is depicted forming an interfacial angle of 71°. Crystal drawings by K. Schmetzer.*

ideal undistorted crystals are grown with that seed orientation *(Figure 8)*.

In crystals grown on **r** seeds, in addition to the pair of crystal faces parallel to the seed, another pair of symmetry-equivalent **r** prism faces exists and grows. At the beginning of crystal growth, the two **r** faces parallel to the seed are large and dominant and the other **r** prisms are absent or distinctly smaller. This means that in various stages of crystal growth, the two different pairs of parallel **r** prism faces have different sizes, a feature which is also displayed by some of the other faces, namely the prism **m,** and the dipyramids **l** and **o** *(Figure 9)*. For alexandrites grown on seeds parallel to the **l** dipyramid, four pairs of symmetry equivalent **l** faces grow with different sizes. At the beginning of crystal growth, the two **l** dipyramids parallel to the seed are dominant, and the three other pairs are distinctly smaller. In the course of growth, these four different pairs of **l** faces (and other faces too) grow with different sizes and form strongly distorted crystals *(Figure 10)*.

The two crystals grown with seeds parallel to the **b** pinacoid are close to complete ideal crystals (*Figure 8*, see also *Figure 5*), showing no excessive development of one face over another. The two crystals with seeds parallel to the **l** dipyramid were flat tabular crystals, in which the pair of **l** faces parallel to the chosen seed was still dominant for the complete morphology of the samples

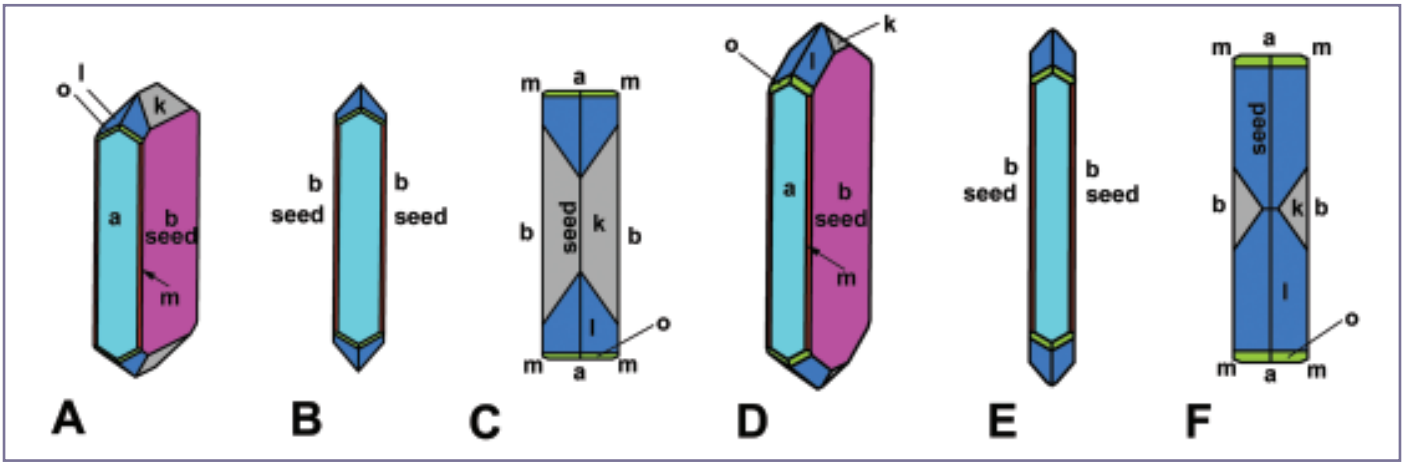

*Figure 8: Morphology of two crystals grown by Creative Crystals Inc. with **b** (010) seed orientation and tabular habit parallel to **b**, with drawings A to C representing crystal 4 and drawings D to F representing crystal 5, both in* Table I; *(A, D) clinographic projections, (B, E) parallel projections in a view along the a-axis, (C, F) parallel projections in a view along the c-axis. Crystal drawings by K. Schmetzer.*

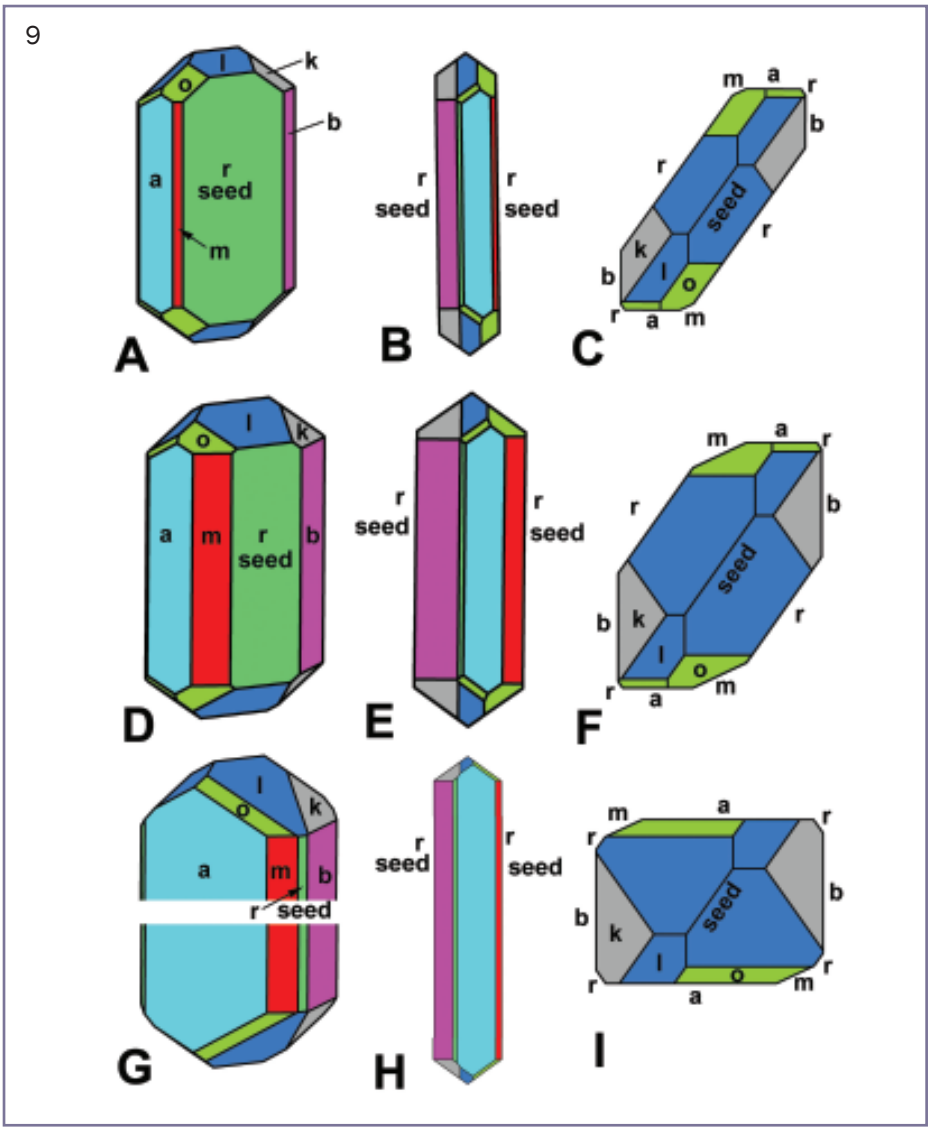

Figure 9: Morphology of three crystals grown by Creative Crystals Inc. with ***r*** *(130) seed orientation, with drawings A to C representing crystal 1, drawings D to F representing sample 2 and drawings D to F representing crystal 3, all in* Table I; *(A, D, G) clinographic projections, (B, E, H) parallel projections in a view parallel to the seed* ***r****, (C, F, I) parallel projections in a view along the c-axis. Crystal 1 shows tabular habit parallel to the seed* ***r****, crystal 2 shows thick tabular habit parallel to the seed, and sample 3 shows a columnar habit parallel to the c-axis. In drawing G the long columnar centre was omitted. Crystal drawings by K. Schmetzer.*

(*Figure 10*, see also *Figure 5*). In contrast, the four crystals grown from **r** seeds showed a wide variation in morphology (*Figures 9, 11 a,b*). In one, the two **r** faces parallel to the seed are much larger than the other **r** faces (*Figures 9 A–C, 11 a,b*). In the second, the crystal had been grown for a longer period resulting in a crystal with smaller **r** faces parallel to the seed (*Figures 9 D–F, 11 a,b*). In the third crystal, the **r** faces parallel to the seed are small and comparable in size with the other two symmetry-equivalent **r** faces present (*Figures 9 G–I, 11a,b*). The last sample, crystal 2a in *Table I*, shows features intermediate between crystals 1 and 2, but very close to sample 2.

Seeding technique

As we shall discuss later in greater detail, the substance between two plane growth boundaries represents one layer of synthetic alexandrite which was produced during a single growth cycle. Each run or growth cycle lasts from five to seven days during which the seed or crystal is immersed in and grows in the flux. After removal from the flux, the crystal is cleaned and placed again in the furnace for the next run.

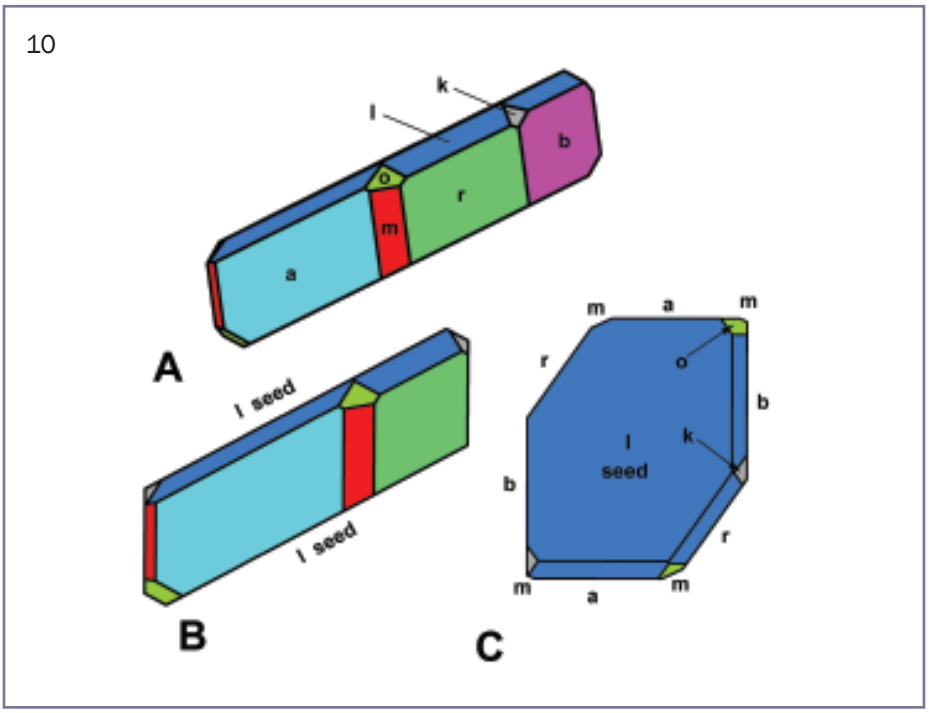

Figure 10: Morphology of one crystal grown by Creative Crystals Inc. with ***l*** *(133) seed orientation, with drawings A to C representing crystal 6 of Table I ; (A) clinographic projection, (B) parallel projection in a view parallel to the seed l, (C) parallel projection in a view along the c-axis. The crystal shows tabular habit parallel to the seed l, in drawing C the differences in size of the four* ***l*** *faces (blue violet) are clear. Crystal drawings by K. Schmetzer.*

Flux-grown synthetic alexandrites from Creative Crystals Inc.

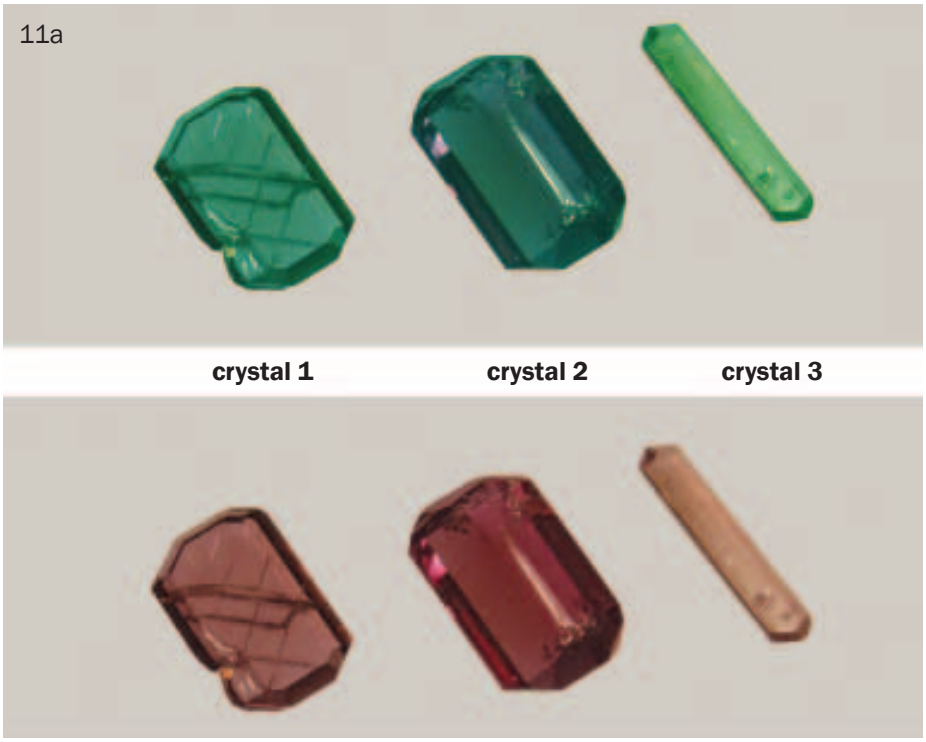

*Figure 11: Morphology of three crystals grown by Creative Crystals Inc. with **r** (130) seed orientation (crystals 1 to 3 of* Table I*). (a) samples in daylight (above) and incandescent light, size of the right columnar crystal 22.8 x 5.2 mm (samples to scale); (b) crystal drawings in parallel projections in views along the c-axis (left column) and photomicrographs of the samples in identical orientations in immersion (right column, samples not to scale). In the sequence of crystal 1 to crystal 3, the way in which the face parallel to the **r** seed grows and becomes gradually smaller with **a**, **b** and **m** faces becoming larger is visible. In crystal 3 the **r** faces parallel to the seed are comparable in size to the **r** faces which are not parallel to the seed. Photos and crystal drawings by K. Schmetzer.*

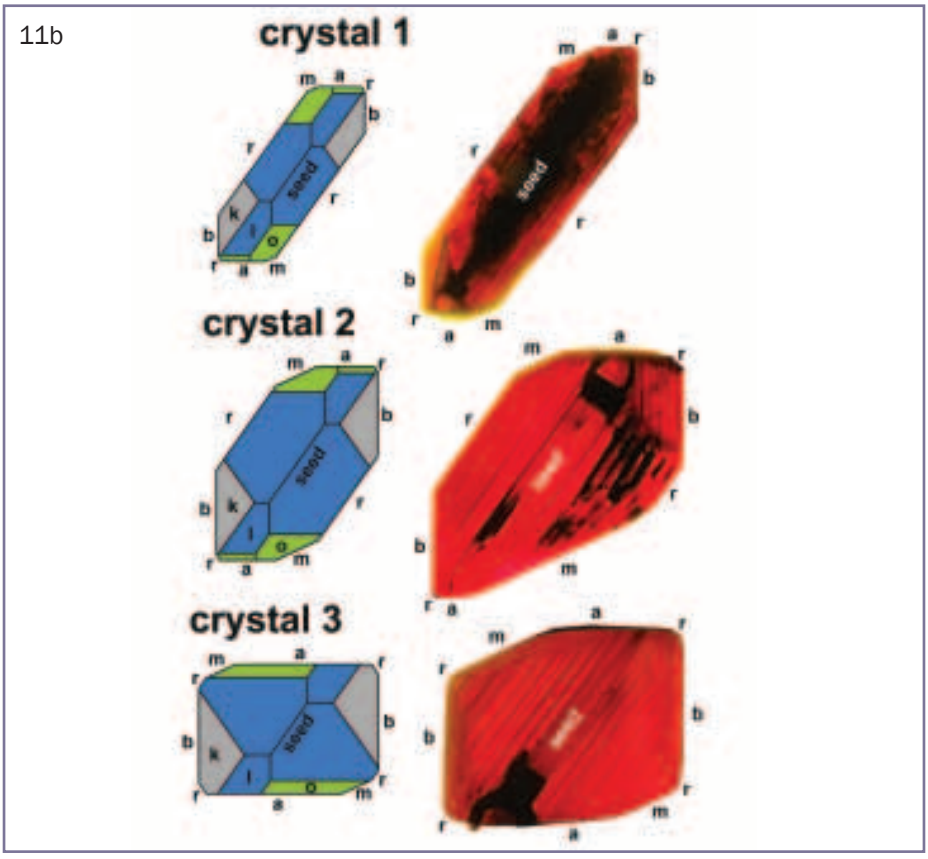

The simplest seeding technique is to cut a colourless or very pale yellow seed plate in the desired orientation from a Czochralski-grown synthetic or from a natural chrysoberyl crystal. Although these seeds have been completely avoided or removed in all the faceted alexandrites that we examined, they may be still present in some of the rough *(Figure 12)*. We shall call this type of rough 'first growth'.

In general, rough crystals which were grown in several growth cycles to a certain thickness, have been cut parallel to the seed orientation and then the resulting synthetic alexandrite plates used as new seeds for subsequent growth. If small and relative thin plates were used for the second growth, the resulting crystal is grown more or less symmetrically, layer by layer, parallel to the seed plate *(Figure 13)*. Depending on the position within the crystal from which the seed plate is sawn, it may consist of layers parallel to its surface *(Figure 13)* or of layers which differ in orientation from the faces of the seed *(Figure 14)*.

In some stones, it is very difficult to locate the boundary between the seed and

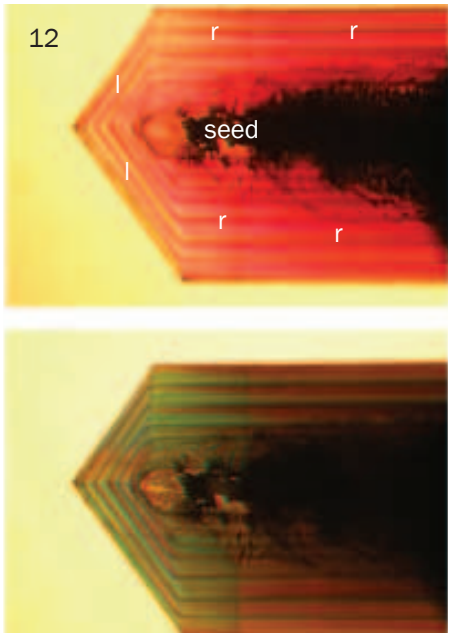

*Figure 12: Pleochroism and growth zoning, associated with colour zoning in r-grown synthetic alexandrite; the slightly yellowish seed is clearly visible in the centre; growth layers parallel to the faces **r** and **l** are indicated. Immersion, plane polarized light, field of view 6.0 x 4.5 mm. Photos by K. Schmetzer.*

Flux-grown synthetic alexandrites from Creative Crystals Inc.

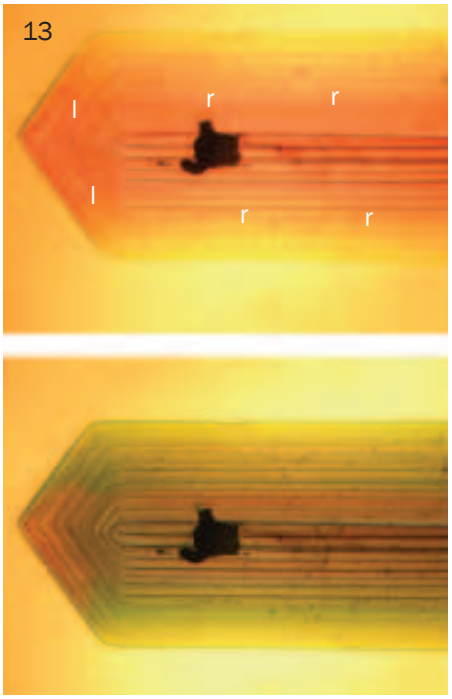

*Figure 13: Pleochroism and growth zoning, associated with colour zoning in r-grown synthetic alexandrite; the thin synthetic alexandrite seed in the centre shows the same coloration and pleochroism as the main crystal; growth layers parallel to the faces **r** and **l** are indicated. Immersion, plane polarized light, field of view 9.5 × 7.2 mm. Photos by K. Schmetzer.*

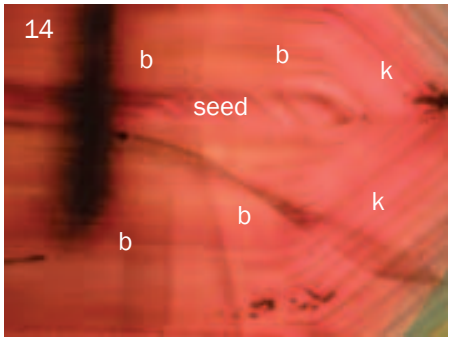

*Figure 14: Growth zoning associated with colour zoning in b-grown synthetic alexandrite; the thin synthetic alexandrite seed in the centre shows identical coloration but somewhat different growth zoning to that of the main crystal; growth layers parallel to the faces **b** and **k** are indicated. Immersion, plane polarized light, field of view 6.0 × 4.5 mm. Photo by K. Schmetzer.*

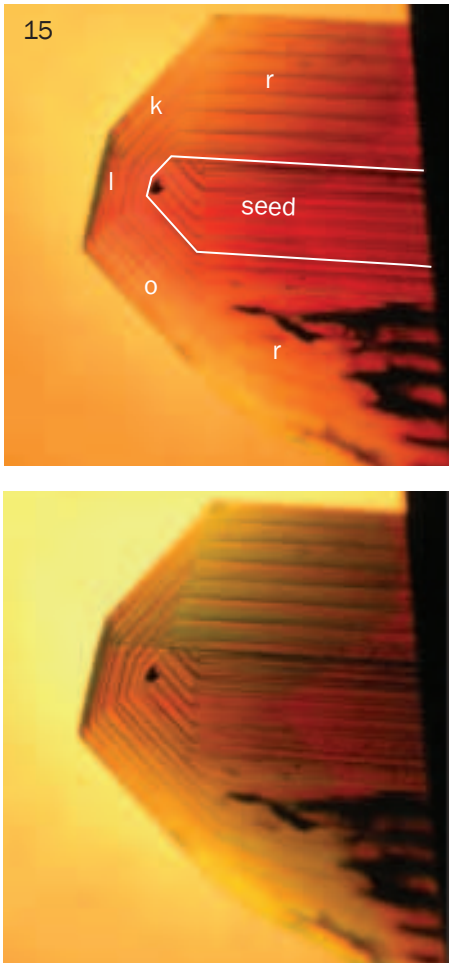

*Figure 15: Pleochroism and growth zoning, associated with colour zoning in r-grown synthetic alexandrite; the thick non-symmetrical synthetic alexandrite seed in the centre shows the same coloration and pleochroism as the main crystal; growth layers parallel to the faces **r**, **o**, **l** and **k** are indicated. Immersion, plane polarized light, field of view 9.5 × 7.2 mm. Photos by K. Schmetzer.*

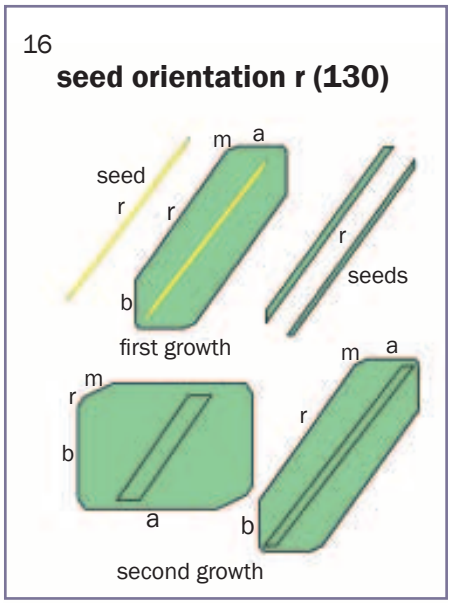

*Figure 16: Seeding technique in r-grown synthetic alexandrite; in the first growth cycle a synthetic colourless or pale yellow natural seed plate cut parallel to the **r** face is used; after this first growth period, synthetic alexandrite seeds were cut from the grown crystal and used as seeds for a second series of growth cycles; the final crystal consists of a synthetic alexandrite seed surrounded by numerous layers of synthetic alexandrite.*

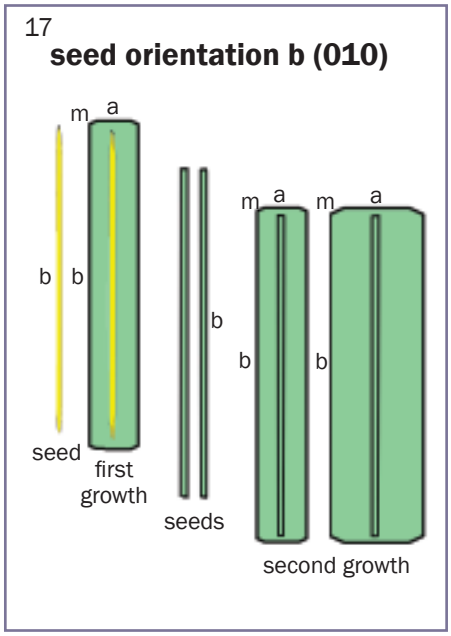

*Figure 17: Seeding technique in b-grown synthetic alexandrite; in the first growth cycle a synthetic colourless or pale yellow natural seed plate cut parallel to the **b** face is used; after this first growth period, synthetic alexandrite seeds were cut from the grown crystal and used as seeds for a second series of growth cycles; the final crystal consists of a synthetic alexandrite seed surrounded by numerous layers of synthetic alexandrite.*

the layers related to the second growth. If the seed is relatively thick and consists of perhaps five to ten layers, subsequent synthetic alexandrite can grow in a non-uniform way around the seed. In such crystals, a real growth inconsistency may be visible in the immersion microscope *(Figure 15)* and the final crystal can show different thicknesses on each side of the seed. A general overview of these different seeding techniques is given for crystals with **r** and **b** seed orientations in *Figures 16* and *17*.

In synthetic alexandrites with seed orientation parallel to the **l** dipyramid, we found that these seeds had been cut from first or second growth crystals which had their seed orientation parallel to **r**. One sample showed a seed with a colourless central layer parallel to **r** and numerous alexandrite layers on both sides (*Figures 18, 19*). This indicates that the plate used for crystal growth had been cut from a complete r-grown crystal parallel to one of the larger **l** faces. In several growth cycles,

Flux-grown synthetic alexandrites from Creative Crystals Inc.

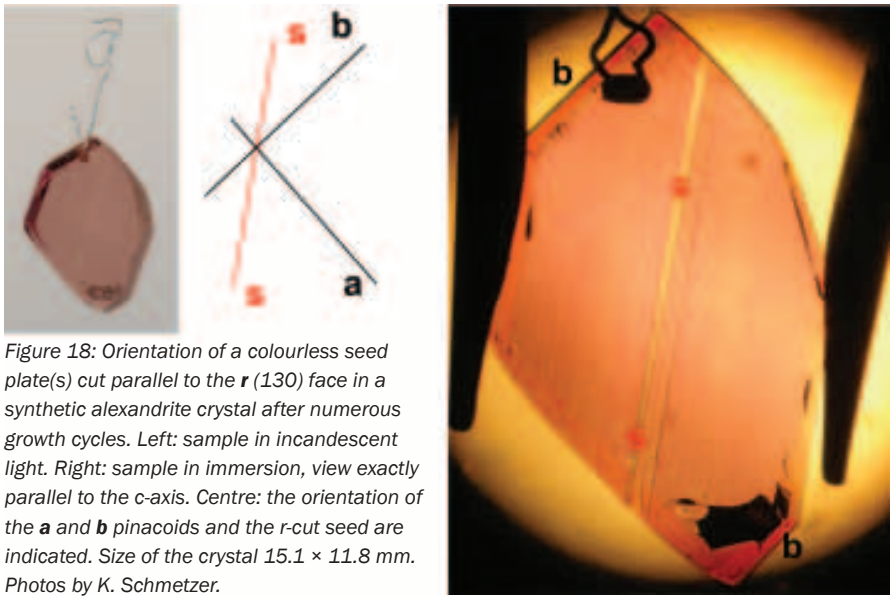

*Figure 18: Orientation of a colourless seed plate(s) cut parallel to the **r** (130) face in a synthetic alexandrite crystal after numerous growth cycles. Left: sample in incandescent light. Right: sample in immersion, view exactly parallel to the c-axis. Centre: the orientation of the **a** and **b** pinacoids and the r-cut seed are indicated. Size of the crystal 15.1 × 11.8 mm. Photos by K. Schmetzer.*

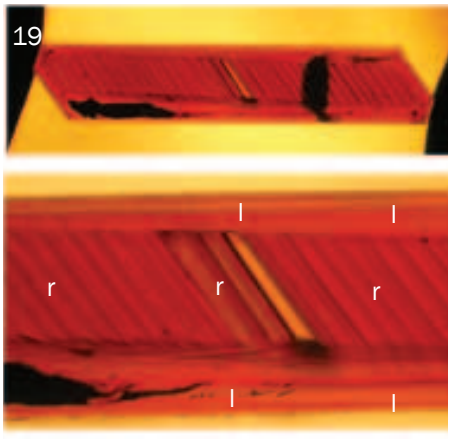

Figure 19: After the first growth cycle the crystal shown in Figure 18 *was sliced parallel to the **l** (133) face and overgrown in several growth cycles with layers of synthetic alexandrite. The seed for the second series of growth cycles consists of one colourless layer with r-cut and several layers of synthetic alexandrite grown with this seed orientation. The complete crystal measures 12.0 × 2.4 mm in this orientation (above); in the detailed picture (below) the **r** and **l** faces are indicated. Both photos by K. Schmetzer, immersion.*

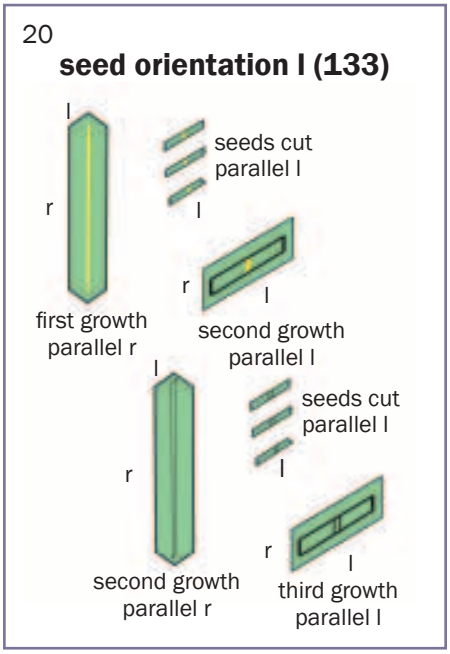

Figure 20: Seeding technique in l-grown synthetic alexandrite:
*Above: in the first growth cycle a synthetic colourless or pale yellow natural seed plate cut parallel to the **r** face is used; after this first growth period, synthetic alexandrite seeds were cut from the grown crystal parallel to an **l** face and used as seeds for a second series of growth cycles; this procedure represents a summary of the different growth steps performed with the crystal pictured in* Figures 18 *and* 19*;*
*Below: the seeds parallel to an **l** dipyramid are sliced from an r-grown synthetic alexandrite with synthetic r-grown seed (see* Figure 16*); these seeds were used for a third series of growth cycles. The final sample consists of a synthetic r-grown alexandrite seed surrounded by numerous l-grown layers.*

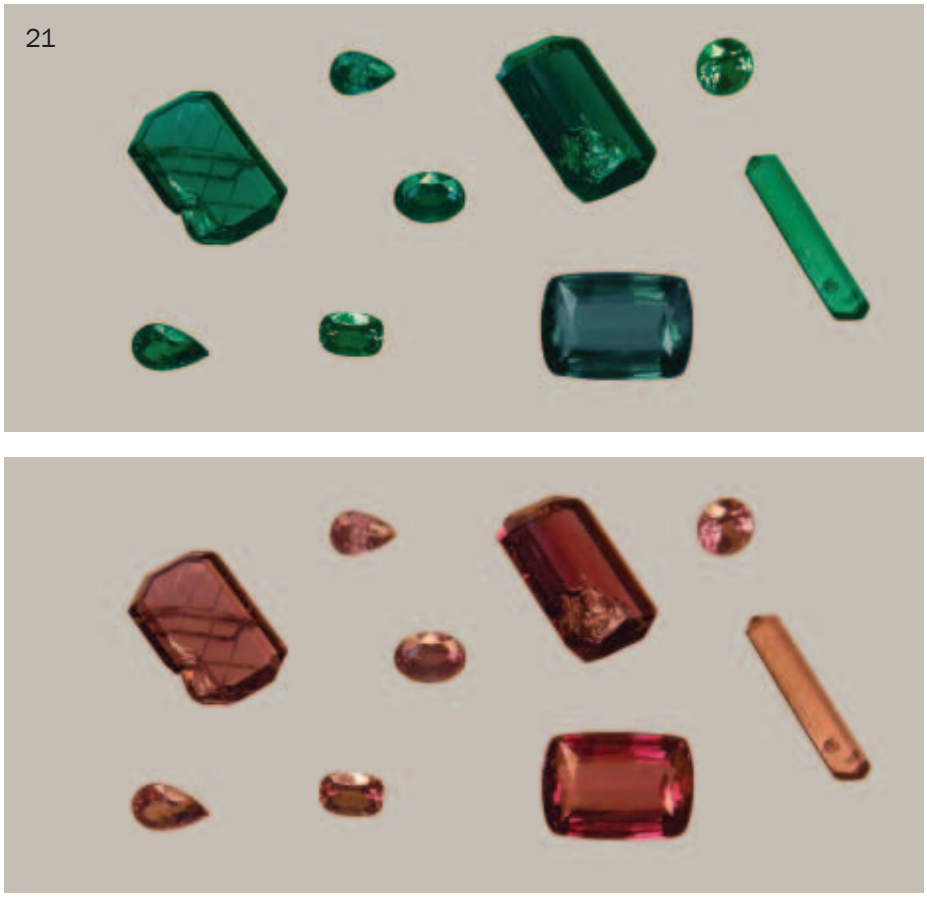

*Figure 21: Rough and faceted synthetic alexandrites grown with seeds which were cut parallel to the **r** (130) prism in daylight (above) and incandescent light (below); the crystals (see* Table I*) weigh 12.38 ct (left), 20.41 ct (centre) and 5.12 ct (right); the largest faceted alexandrite (lower right) of 13.49 ct measures 16.6 × 11.8 mm, the smaller faceted stones weigh from 0.86 to 1.91 ct. Photos by K. Schmetzer.*

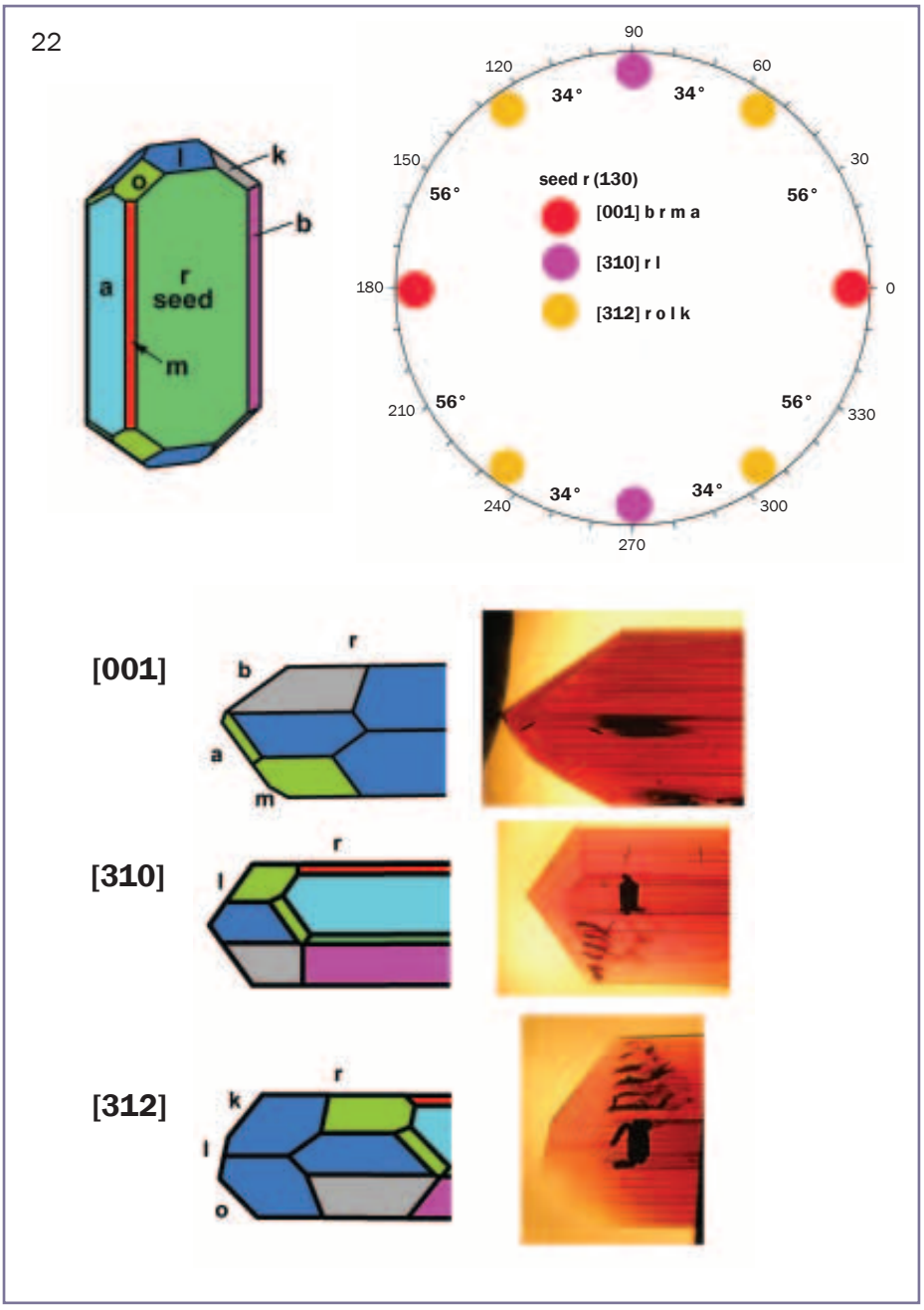

*Figure 22: Upon rotation of a rough alexandrite crystal (upper left) or a faceted alexandrite with seed orientation parallel to the **r** prism, with a rotation axis oriented perpendicular to the seed plate, three different growth zones [001], [310] and [312] are visible with each growth zone consisting of several growth faces. Schematic drawings of the three growth zones are given in the left column, examples are depicted in the right column (all photographed in immersion). The rotation angles which are needed to move from one of these views to the next are schematically plotted on the 360° diagram; according to the symmetry of chrysoberyl, during a full rotation of 360° several growth zones are repeated.*

this plate was 'overgrown' with several new layers of synthetic alexandrite. In another sample, the seed cut parallel to an **l** face consisted only of several **r**-grown layers of synthetic alexandrite. This indicates that this seed was cut from a second growth synthetic alexandrite which had been grown with a seed in **r** orientation. An overview of the seeding technique in **l** orientation is given in *Figure 20*.

Microscopic growth features

Crystals

The internal growth patterns of Creative Crystals Inc. rough and faceted alexandrites closely reflect the chosen seed orientations and their external morphologies. In all samples, a series of dominant internal growth planes runs

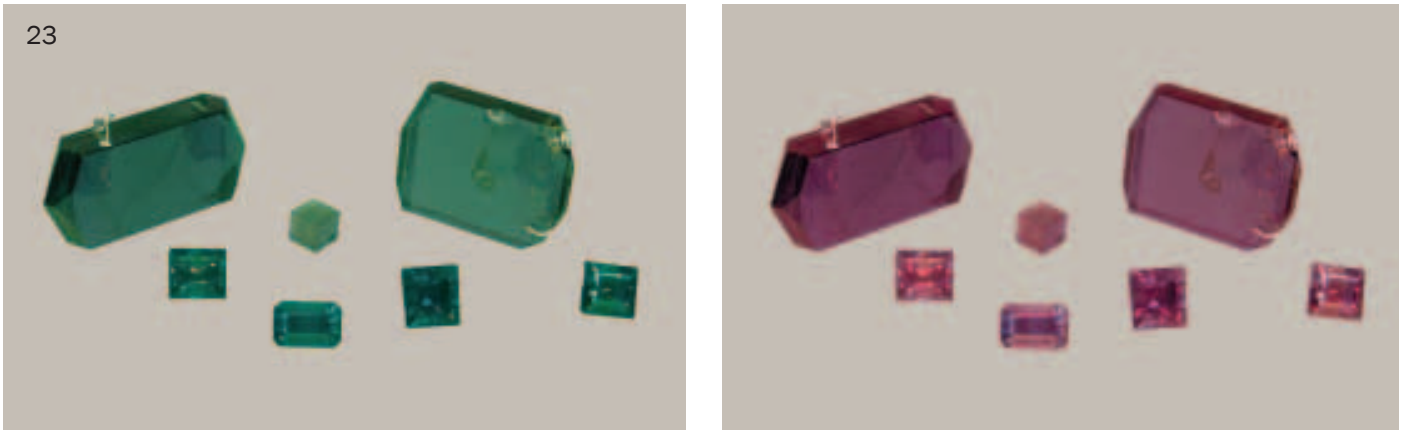

*Figure 23: Rough and faceted synthetic alexandrites grown with seeds which were cut parallel to the **b** (010) prism in daylight (left) and incandescent light; the crystals (see* Table I*) weigh 78.22 ct (left) and 54.90 ct (right); the cube in the centre weighs 3.22 ct and measures 5.8 × 5.8 mm; the faceted stones weigh from 3.22 to 5.84 ct. Photos by K. Schmetzer.*

Flux-grown synthetic alexandrites from Creative Crystals Inc.

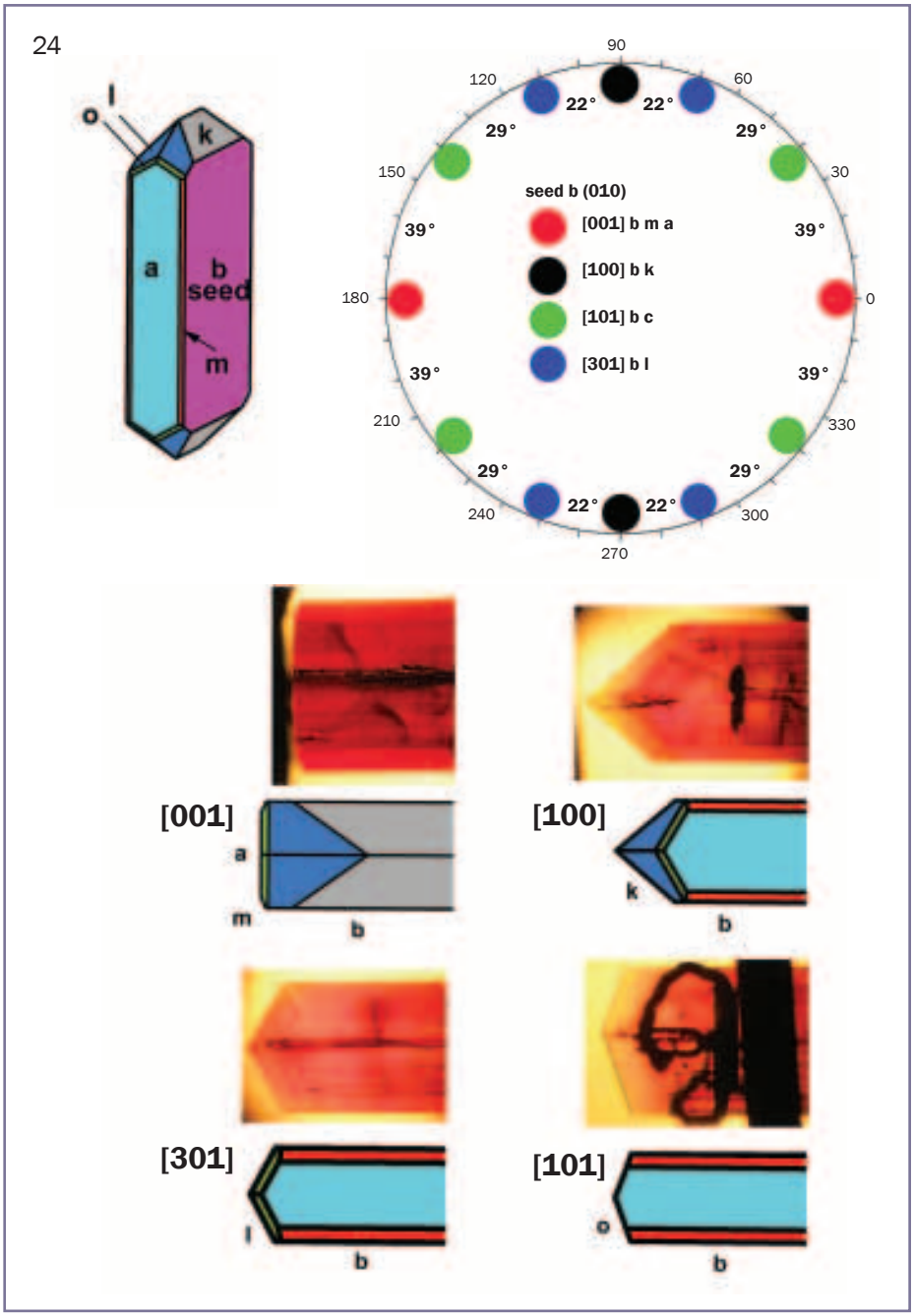

*Figure 24: Upon rotation of a rough alexandrite crystal (upper left) or a faceted alexandrite with seed orientation parallel to the **b** pinacoid, with a rotation axis oriented perpendicular to the seed plate, four different growth zones [001], [301], [100] and [101] are visible with each growth zone consisting of several growth faces. Schematic drawings of the four growth zones are shown, and examples are depicted above each line drawing (all photographed in immersion). The rotation angles which are needed to move from one of these views to the next are schematically plotted on the 360° diagram; according to the symmetry of chrysoberyl, during a full rotation of 360° several growth zones are repeated.*

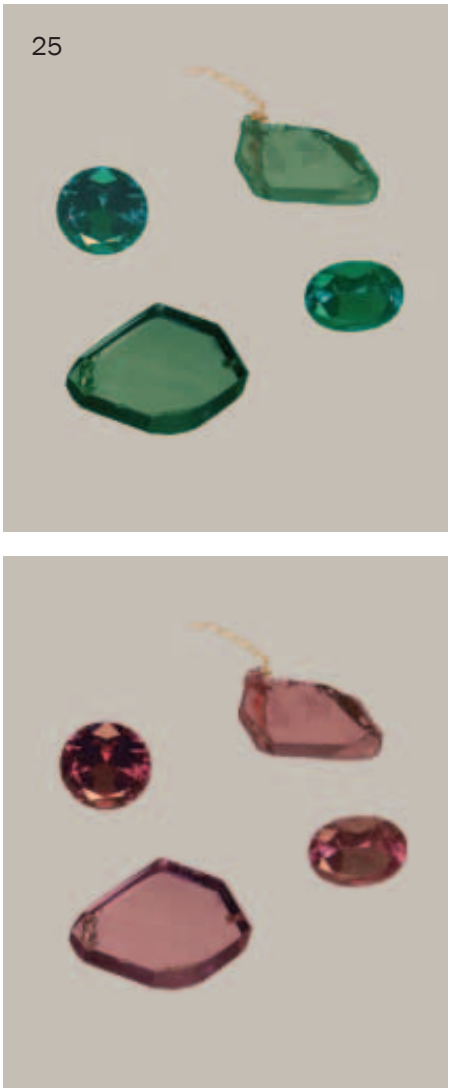

*Figure 25: Rough and faceted synthetic alexandrites grown with seeds which were cut parallel to the **l** (133) prism in daylight (above) and incandescent light (below); the crystals (see Table I) weigh 5.15 ct (lower left) and 3.08 ct (upper right); the faceted stones weigh 2.43 ct (upper left, diameter 8.4 mm) and 1.91 ct. Photos by K. Schmetzer.*

parallel to the seed plane, and in order to determine what other growth planes may be present, the samples were oriented in the sample holder with the dominant growth planes perpendicular to the rotation axes (see Schmetzer, 2011).

Upon rotation of the synthetic alexandrite crystals through 360°, several characteristic growth patterns may be obtained for each seed orientation. For **r**-grown alexandrites (*Figure 21 a,b*), three different zones with distinct growth patterns are visible *(Figure 22)*, and for b- and l-grown samples (*Figures 23 a,b; 25 a,b*), four different growth patterns are always present *(Figures 24, 26)*. The rotation angles between different zones and the angles between different crystal faces within these zones are given in *Table III*. The schematic overviews given in *Figures 22, 24* and *26* also show the rotation angles between different views of characteristic zones and the repetition of these positions according to the orthorhombic symmetry of chrysoberyl.

In **r**-grown crystals *(Figures 21 a,b; 22)*, for example, the three growth zones [001], [310] and [312] are present. The faces seen in these different orientations

Flux-grown synthetic alexandrites from Creative Crystals Inc.

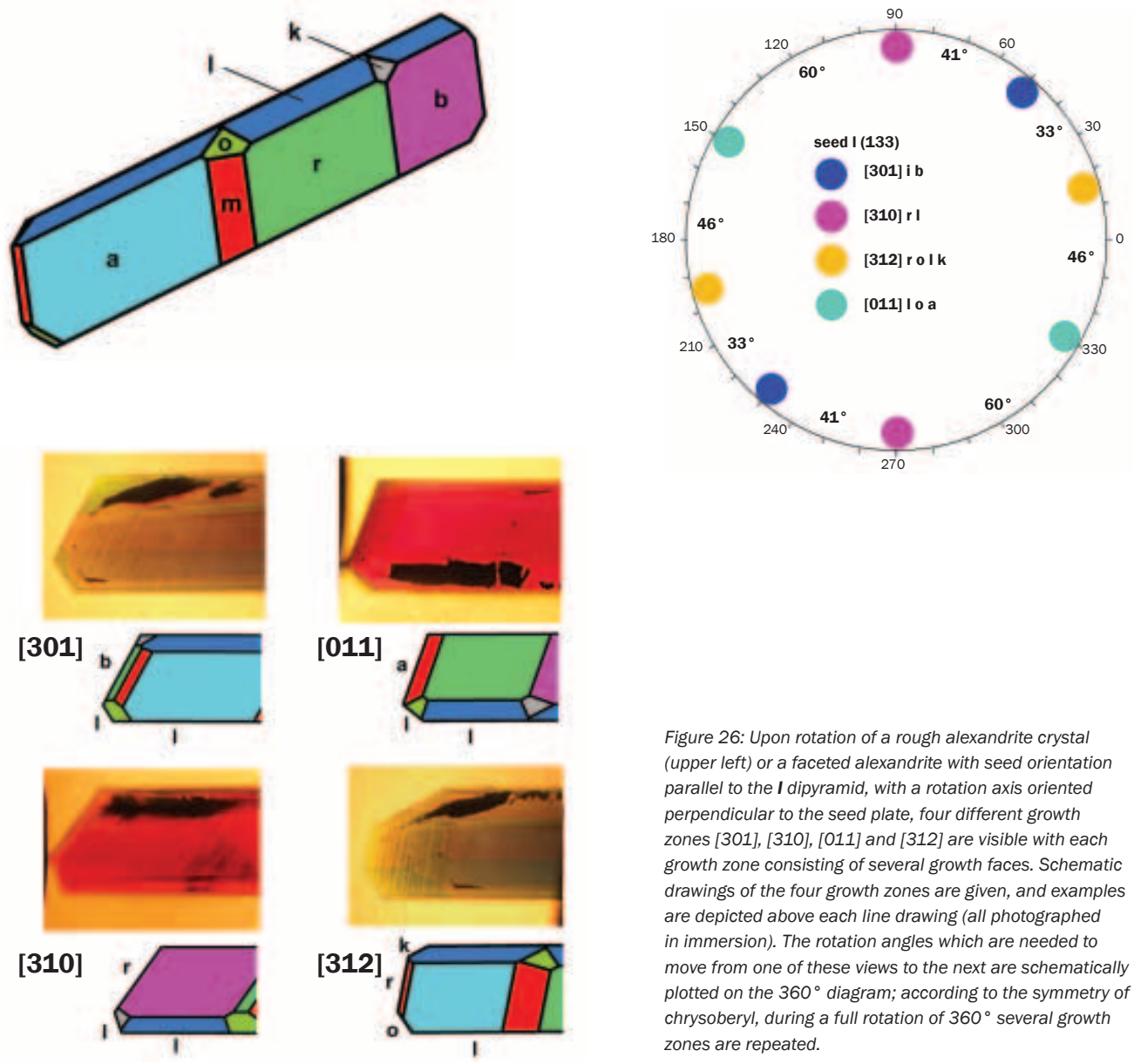

*Figure 26: Upon rotation of a rough alexandrite crystal (upper left) or a faceted alexandrite with seed orientation parallel to the **l** dipyramid, with a rotation axis oriented perpendicular to the seed plate, four different growth zones [301], [310], [011] and [312] are visible with each growth zone consisting of several growth faces. Schematic drawings of the four growth zones are given, and examples are depicted above each line drawing (all photographed in immersion). The rotation angles which are needed to move from one of these views to the next are schematically plotted on the 360° diagram; according to the symmetry of chrysoberyl, during a full rotation of 360° several growth zones are repeated.*

are **b**, **r**, **m** and **a** for zone [001], **r** and **l** for zone [310] and **r**, **o**, **l** and **k** for zone [312]. The rotation angles between the different zones are 34° for a rotation between zones [310] and [312] and 56° for a rotation between zones [001] and [312]. For symmetry reasons, several zones and rotation angles are repeated by full rotation through a circle of 360°. For **b**- and **l**-grown crystals, the schematic overviews in Figures 24 and 26 together with the angles in *Table III* are self explanatory.

In *Figure 27* the commonest growth patterns of rough and faceted alexandrites and the pleochroism in different orientations of the crystals are shown. In **r**-grown samples, growth and colour zoning is common in the three growth zones [001], [310] and [312] *(Figure 27 A–H)*, and for **b**-grown alexandrites growth zoning is visible in the zones [100] and [301] *(Figure 27 I–L)*.

Faceted alexandrites

In faceted samples, the same patterns are observed as have been described for rough crystals. In a few samples cut from the central parts of the rough crystals, only the dominant series of growth planes parallel to the seed was observed (see *Figure 28 A,H,K,* for **r**, ***b*** and **l** seed orientations), but in most samples a more complete picture was seen. Upon rotation of the faceted alexandrites around an axis perpendicular to the dominant **r**, **b** or **l** growth planes (which are parallel to the seed), this procedure generally revealed one or several growth zones with the complete number of faces as given in *Figures 22* to *27*. Some examples are pictured in *Figure 28 B–G* for alexandrites grown with **r** seed orientation, and in *Figure 28 I,J,L* for those with **b** or **l** seed orientation. With this overview it is now

possible to understand the patterns recorded by Pohl (1989). The samples examined at that time were **r**-grown synthetic alexandrites, and they contained patterns which can now be assigned to growth zone [310] with an angle of 55° between **l** and **r** faces and to growth zone [312] with an angle of 52° between **k** and **r** faces.

Colour zoning in crystals and faceted alexandrites and interference effects at growth boundaries

A common type of zoning with numerous lighter and darker layers is shown in *Figures 27* and *28*. A detailed examination showed that each successive growth layer from the centre outwards starts with strongly coloured alexandrite and grades to lighter or sometimes almost colourless material towards the subsequent growth boundary *(Figure 29)*.

Under crossed polarizers, an interference effect is visible at the boundaries between successive growth layers *(Figure 30)* and this pattern closely resembles that seen in many twinned rubies and sapphires. In corundum the cause is polysynthetic twinning, but in our synthetic alexandrites, this cause is most unlikely because the pleochroism in the successive growth layers is identical (in contrast to the varying pleochroic colours across the boundaries in natural alexandrite twins or trillings; see Schmetzer, 2010). This colour zoning and the cause of the interference effects is explained in detail in the chemistry section below.

Surfaces of growth layers

In numerous samples, the successive growth layers are either parallel to each other or are slightly inclined to the former boundary *(Figures 27, 28)*. This effect is due to growth inconsistencies. In some samples, the growth surfaces look like somewhat irregular cobbles *(Figure 31)*. This appearance is due to a dissolution process at the beginning of each growth cycle. The starting temperature for each run was slightly above the crystallization temperature (D. Patterson, pers. comm., 2012), which meant that dissolution occurred for a limited time before the slight cooling enabled new alexandrite material to commence crystallization on the etched surface. This dissolution at the beginning of each growth cycle explains the detailed structure of the growth boundaries. In some samples, numerous small particles of flux or crucible metal are visible close to parts of the growth boundaries *(Figure 31C)*, an indication of some disturbance and instability at the beginning of some growth cycles.

Table III: Characteristic angles of synthetic alexandrite crystals grown by Creative Crystals Inc.

Seed orientation parallel **r** (130)

Rotation through 180°, zone sequence and rotation angles*			↔ [001] 56° ↔ [312] 34° ↔ [310] 34° ↔ [312] 56° ↔ [001]
Zone	[001]	[312]	[310]
View	‖ c-axis	intermediate	⊥ c-axis
Faces	**a b r m**	**r o l k**	**r l**
Interfacial angles (°)	**ab** 90 **br** 35.30 **bm** 64.79 **am** 25.21 **ar** 54.70 **rm** 29.49 **rr** 70.61 **rr** 109.39	**ro** 45.36 **rl** 101.12 **ol** 55.76 **lk** 27.14 **lr** 78.88 **kr** 51.74	**rl** 54.48 **ll** 71.04 (diagonal)

Seed orientation parallel **b** (010)

Rotation through 180°, zone sequence and rotation angles*				↔ [001] 39° ↔ [101] 29° ↔ [301] 22° ↔ [100] 22° ↔ [301] 29° ↔ [101] 39° ↔ [001]
Zone	[001]	[101]	[301]	[100]
View	‖ c-axis	intermediate	intermediate	⊥ c-axis, ‖ a-axis
Faces	**b m a**	**b o**	**b l**	**b k**
Interfacial angles (°)	**ab** 90 **bm** 64.79 **am** 25.21	**bo** 69.89 **oo** 40.22 (adjacent)	**bl** 61.70 **ll** 56.61 (adjacent)	**bk** 40.64 **kk** 98.72

Seed orientation parallel **l** (133)

Rotation through 180°, zone sequence and rotation angles*				↔ [310] 60° ↔ [011] 46° ↔ [312] 33° ↔ [301] 41° ↔ [310]
Zone	[310]	[011]	[312]	[301]
View	⊥ c-axis	intermediate	intermediate	intermediate
Faces	**l r**	**a o l**	**l o r k**	**l b**
Interfacial angles (°)	**rl** 54.48 **ll** 71.04 (diagonal)	**lo** 27.30 **la** 70.38 **ao** 43.08 **ll** 39.24 (opposite)	**lo** 55.76 **or** 45.36 **rk** 51.74 **kl** 27.14	**bl** 61.70 **ll** 56.61 (adjacent)

* rotation axis perpendicular to the seed plate

Flux-grown synthetic alexandrites from Creative Crystals Inc.

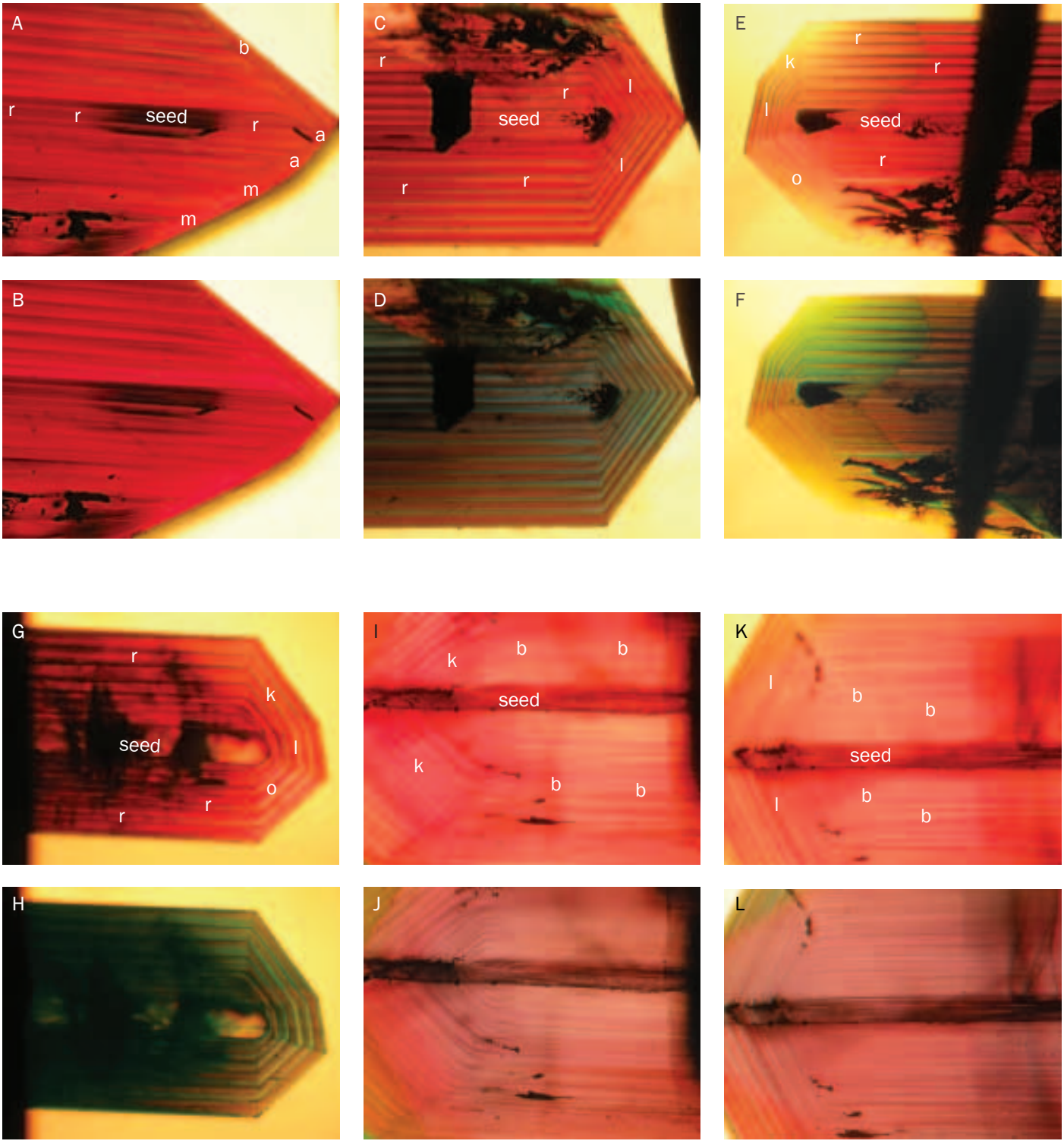

*Figure 27: Pleochroism and growth zoning, associated with colour zoning in synthetic alexandrite crystals grown with different seed orientation: (A–H) seeds parallel to the **r** prism, (A,B) growth zone [001], (C,D) growth zone [310], (E,F) growth zone [312], (G.H) growth zone [312]; (I–L) seeds parallel to the **b** pinacoid, (I,J) growth zone [100], (K,L) growth zone [301]; the position of the seed is indicated, the faces of the different growth zones are labelled.*

Immersion, plane polarized light, field of view (A,B) 6.7 × 5.0 mm, (C,D) 7.8 × 5.9 mm, (E,F) 9.1 × 6.9 mm, (G,H) 6.1 × 4.6 mm, (I,J) 7.6 × 5.7 mm, (K,L) 7.6 × 5.7 mm. Photos by K. Schmetzer.

Flux-grown synthetic alexandrites from Creative Crystals Inc.

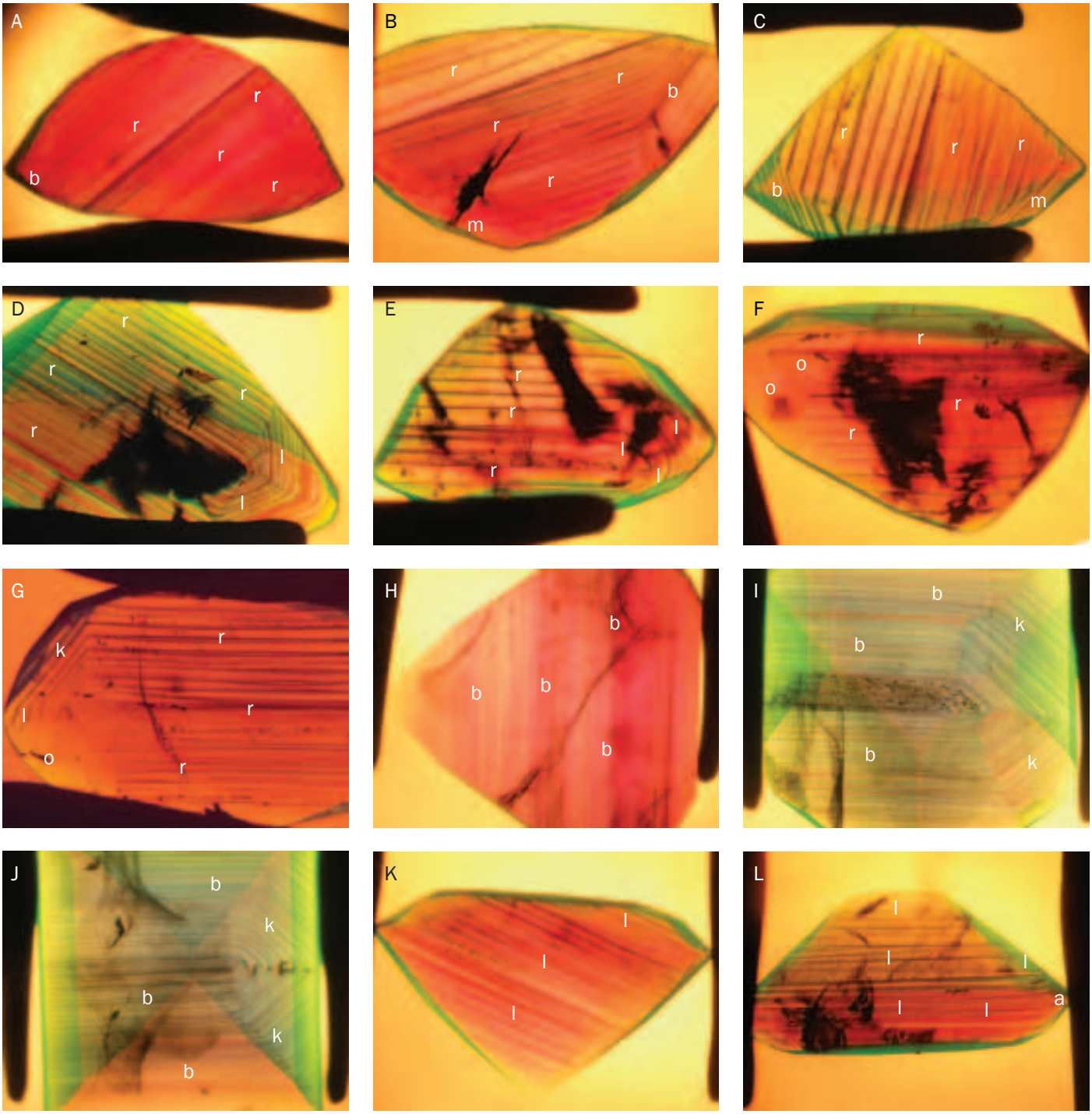

*Figure 28: Growth zoning, associated with colour zoning in faceted synthetic alexandrite grown with different seed orientation: (A–G) seeds parallel to the **r** prism, (A,B,C) growth zone [001], (D,E) growth zone [310], (F,G) growth zone [312]; (H–J) seeds parallel to the **b** pinacoid, (H) growth zone [001], (I,J) growth zone [100]; (K,L) seeds parallel to the **l** dipyramid, (K,L) growth zone [011]; the faces of the different growth zones are labelled.*

Immersion, plane polarized light, field of view (A) 11.5 × 8.7 mm, (B) 6.3 × 4.7 mm, (C) 5.5 × 4.1 mm, (D) 6.5 × 4.9 mm, (E) 5.3 × 4.0 mm, (F) 4.9 × 3.7 mm, (G) 5.6 × 4.2 mm, (H) 8.5 × 6.4 mm, (I) 7.5 × 5.7 mm, (J) 8.8 × 6.6 mm, (K) 8.9 × 6.7 mm, (L) 9.5 × 7.2 mm. Photos by K. Schmetzer.

Flux-grown synthetic alexandrites from Creative Crystals Inc.

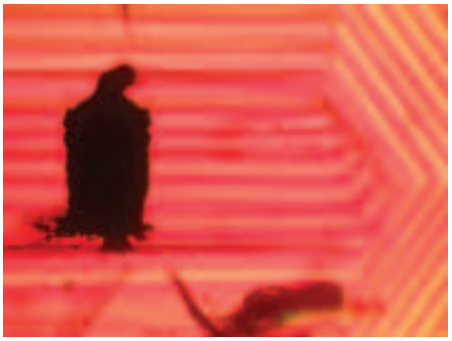

*Figure 29: Growth zoning, associated with colour zoning in a synthetic alexandrite crystal grown with **r** seed orientation, growth zone [310], faces **r** and **l**; from the centre to the rim, each growth layer starts with an intensely coloured area which gradually fades to a paler zone and then to a near-colourless part.*

Immersion, plane polarized light, field of view 4.6 × 3.5 mm. Photo by K. Schmetzer.

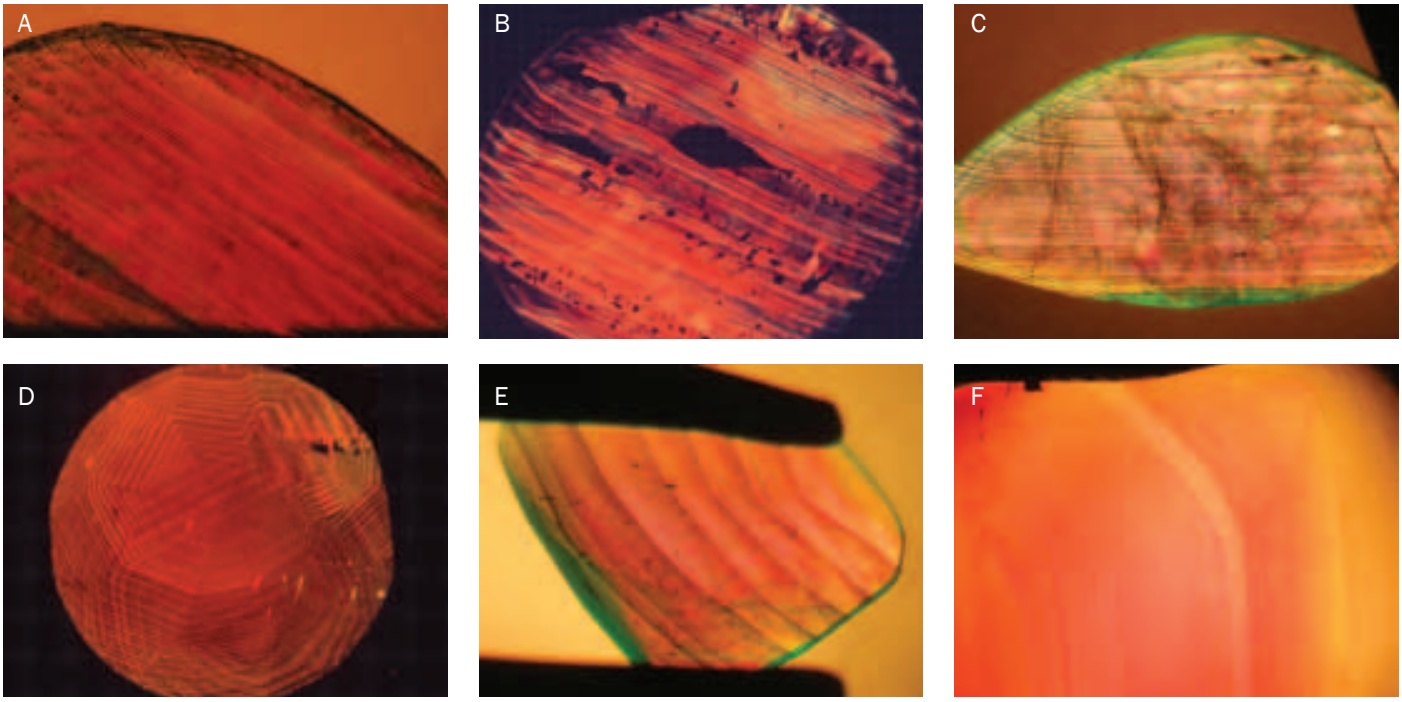

Figure 30: Characteristic interference patterns displayed by the layered growth structures of a faceted synthetic alexandrite.

Immersion, crossed polarizers or slightly uncrossed polarizers (for photography), field of view (A) 4.4 × 3.3 mm, (B) 5.6 × 4.2 mm, (C) 6.9 × 5.2 mm, (D) 10.1 × 7.6 mm, (E) 5.8 × 4.4 mm, (F) 11.9 × 9.0 mm. Photos by K. Schmetzer.

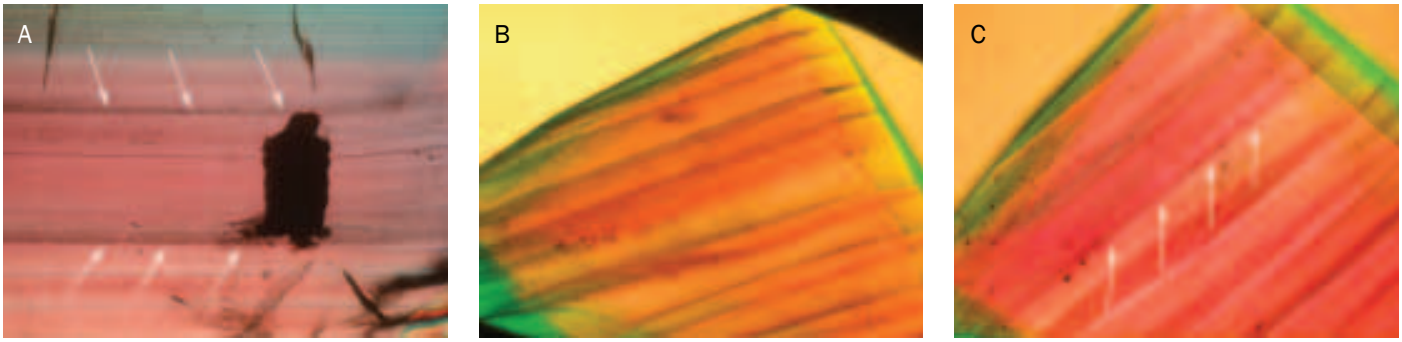

Figure 31: Growth boundaries showing somewhat irregular, 'cobbled' surfaces which are caused by some dissolution at the beginning of each growth cycle; occasionally, numerous small particles (indicated by arrows) are trapped close to some of these irregular surfaces. (A) seed confined to the outer layers by two irregular surfaces, (B) numerous irregular surfaces at successive growth boundaries, (C) numerous irregular surfaces at successive growth boundaries, one of them with a high concentration of trapped particles.

Immersion, plane polarized light, field of view (A) 6.0 × 4.5 mm, (B) 3.8 × 2.9 mm, (C) 3.6 × 2.7 mm. Photos by K. Schmetzer.

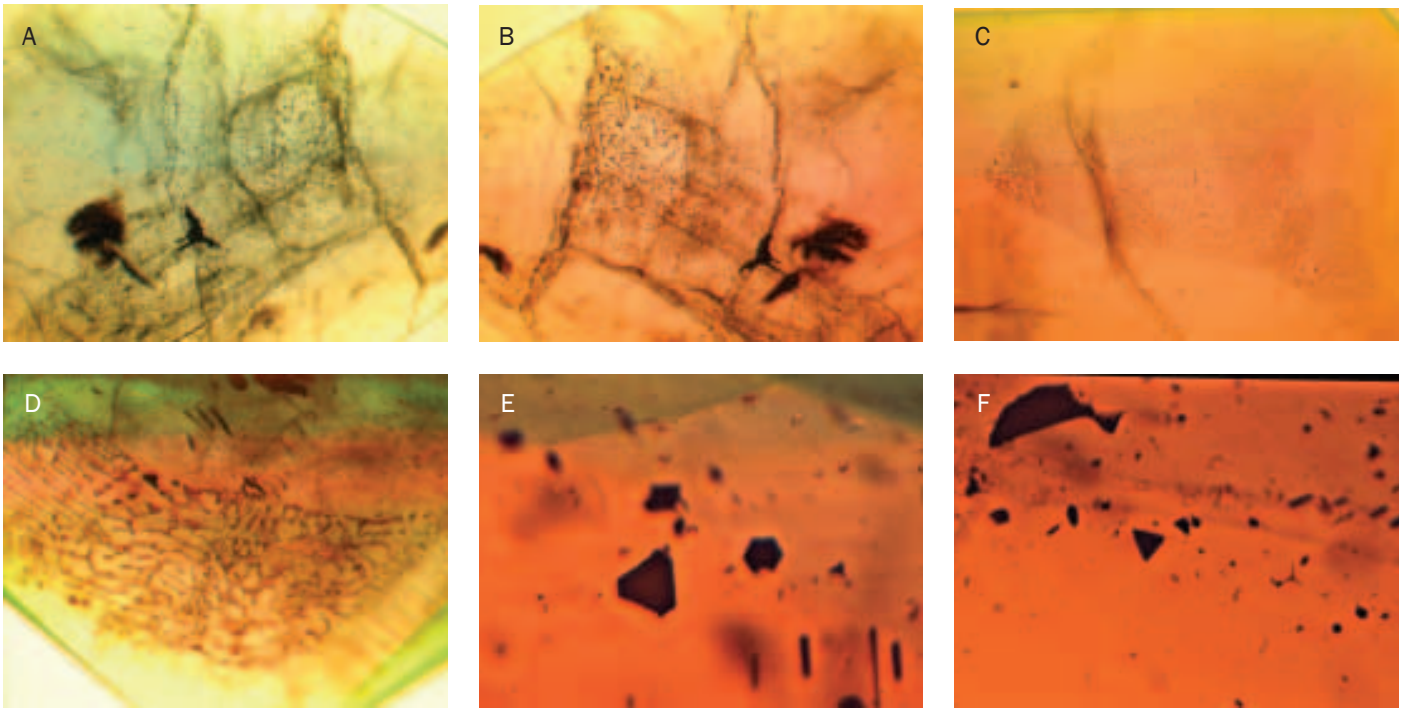

Figure 32: Various forms of residual flux are common (A–D); less common are platinum particles, needles or platelets (E,F). Immersion, plane polarized light, field of view (A,B) 6.0 × 4.5 mm, (C) 7.6 × 5.7 mm, (D) 3.6 × 2.7 mm, (E,F) 1.8 × 1.3 mm. Photos by K. Schmetzer

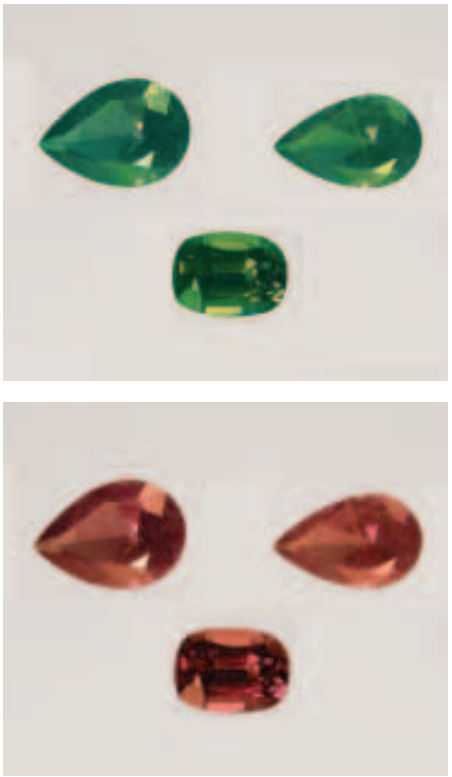

Figure 33: Electron microprobe scans of 9 or 10 analyses points were carried out across the table facets of these three synthetic alexandrites. The samples are shown in daylight (above) and incandescent light (below); their weights vary between 1.49 and 0.98 ct, the cushion-shaped stone measures 7.1 × 5.1 mm. Photo by K. Schmetzer.

Inclusions in rough and faceted alexandrites

Both the rough and faceted alexandrite samples show a range of clarities: some are heavily included, but others are very clean. The largest faceted sample of 13.49 ct, for example, contained neither platinum from the crucible nor any visible residual flux material. In most samples, however, there are variable quantities of residual flux in various forms, ranging from individual droplets to larger twisted veil-like feathers *(Figure 32 A–D)*. Only in a smaller percentage of the faceted samples are needles or triangular to hexagonal platinum platelets present *(Figure 32 E,F)*. In some samples, there are also small particles close to the growth boundaries *(Figure 31C)*.

X-ray fluorescence analysis

The compositions of seven rough crystals and 14 of the faceted samples were determined using X-ray fluorescence (XRF) analysis. Iron and chromium are the main colour-causing trace elements in all samples. In addition, in all heavily included faceted stones and in the more

Table IV: Ranges and average contents of colour-causing trace elements in alexandrites produced by Creative Crystals Inc. (in wt%).

Samples	A (Figure 34a)	B (Figure 34b)	C (Figure 34c)	D (Figure 35, 36)
No. of analyses	10	10	9	402
TiO_2 range	0.0 - 0.03	0.0 – 0.02	0.0– 0.03	0.0– 0.03
mean	0.01	0.01	0.01	0.0
V_2O_3 range	0.0 – 0.02	0.0 – 0.02	0.0 – 0.03	0.0 – 0.03
mean	0.01	0.01	0.01	0.01
Cr_2O_3 range	0.13 – 0.28	0.08 – 0.32	0.22 – 0.30	0.07 – 0.30
mean	0.20	0.20	0.26	0.18
Fe_2O_3 range	0.92 – 1.61	0.76 – 1.50	0.77 – 0.96	0.79 – 1.57
mean	1.14	1.0	0.86	1.05

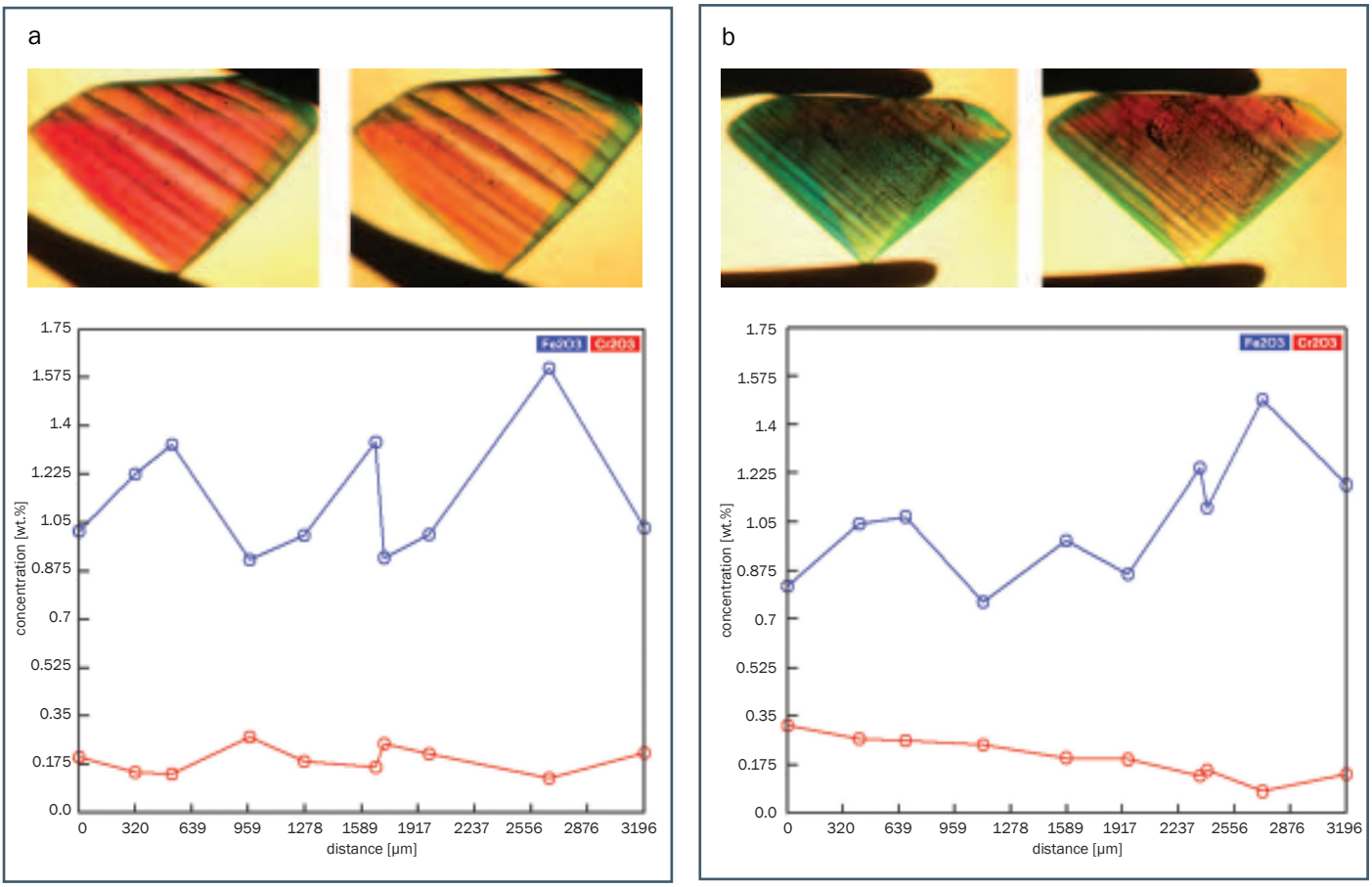

Figure 34 a,b,c: Pleochroism and growth zoning, associated with colour zoning in synthetic alexandrites (above, see also Figure 33*) and plots of chromium and iron concentrations measured by electron microprobe scans across the table facets; the trace element contents show clear variation in different growth layers.*

Sizes and weights of samples (a) 0.97 ct, 7.1 × 5.1 mm, (b) 1.02 ct, 9.1 × 5.6 mm, (c) 1.49 ct, 9.4 × 6.5 mm; all photos in immersion, plane polarized light. Photos by K. Schmetzer.

impure parts of the rough crystals molybdenum was detected and this has been derived from the flux. In some cleaner parts of the rough crystals and in clean or almost clean faceted samples molybdenum was not detected.

Surprisingly, traces of tin are present in all our samples. Upon request we were informed that no tin-bearing compounds were intentionally added to the flux or the nutrient; most probably these tin contents originate from the industrial grade lithium molybdate or the molybdic oxide used as the main components of the flux (D. Patterson, pers. comm., 2012).

Electron microprobe analysis

In most cut samples, the table facet is distinctly inclined to the dominant growth planes (which indicate the orientation of the seed), whereas in the remainder the table facet was almost parallel or only slightly inclined to the main growth layers. We obtained quantitative microprobe analyses for three samples *(Figure 33)*, specifically of two samples with distinct inclination of the main growth layers to the table facets *(Figure 34 a,b)*

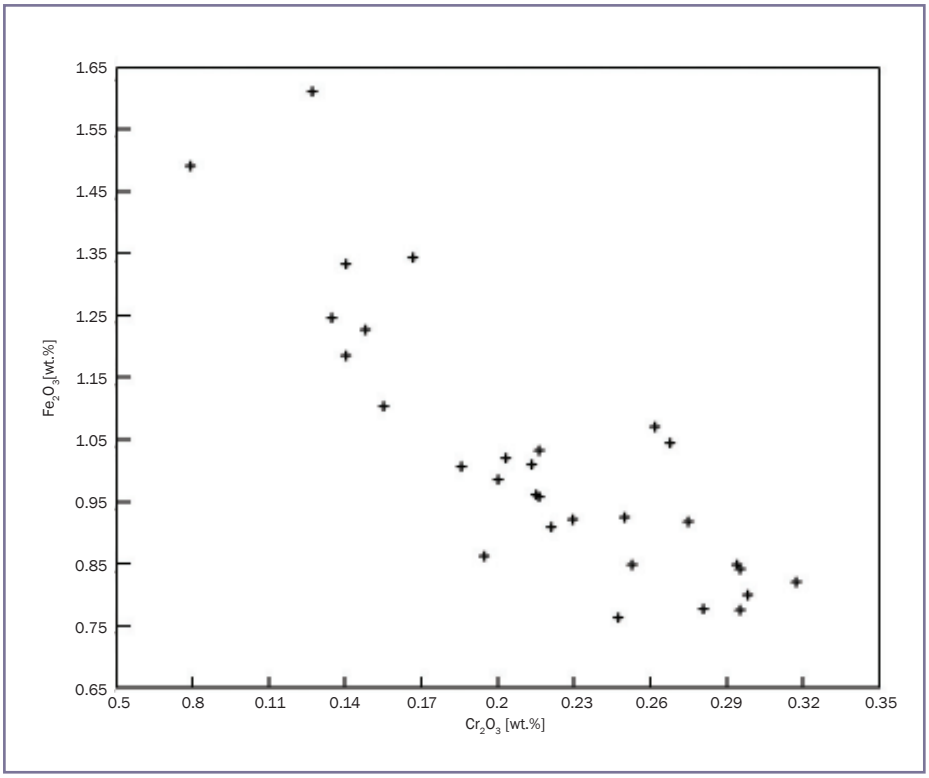

Figure 35: Chromium/iron binary diagram showing the ranges of these trace element contents in three synthetic alexandrites; the data are from microprobe scans (see Figures 33 *and* 34 a,b,c*) and show a negative correlation between the two trace elements, i.e. a decrease of iron with increasing chromium.*

and of one in which the table facet was slightly inclined *(Figure 34c)*. For all three of these **r**-grown samples, traverses with nine or ten point analyses each were measured across the table facets. The results are summarized in *Table IV*.

The main colour-causing trace elements, iron and chromium, show distinct zoning and extremely variable concentrations within the different growth layers. The iron contents ranged from 0.76 to 1.61 wt.% Fe_2O_3 and chromium contents ranged from 0.08 to 0.32 wt.% Cr_2O_3. In the first two samples (see *Figure 33 a,b*) it is clear that the ten analyses originate from eight to ten growth layers exposed at the table facets. In the third sample, only two growth layers are exposed at the table facet *(Figure 34c)*. The chemical data show a first zone with gradually increasing iron contents and gradually decreasing chromium contents (six analyses) and a second zone with similar iron and chromium variation (three analyses). An inconsistency between two analyses (Nos. 6 and 7) of this series indicates the transition between the two subsequent growth layers exposed at the table facet of this alexandrite. A plot of the analyses from these three samples (iron versus chromium contents) shows a clear negative correlation between both colour-causing trace elements, i.e. with increasing chromium content there is a decrease in iron *(Figure 35)*.

Detailed investigation of chemical zoning

For a more detailed examination of chemical zoning, one faceted sample was cut perpendicular to the table facet. The microscopic examination *(Figure 36A)* showed the sample to consist of seven somewhat broader central layers and one narrower layer on each side of this central area. Grown on each of these two small layers are two somewhat broader layers in the direction of the table facet and one broad layer in the direction of the culet. In a view perpendicular to this direction, an inconsistency in the internal growth pattern is present between the second broad layer (starting from the table facet) and the underlying narrower layer. The main growth boundary is oriented parallel to **r** indicating crystal growth with the most commonly observed **r** seed orientation.

A detailed microprobe scan was performed across the sample in a direction perpendicular to the table facet. This scan of about 2.3 mm in length crossed all the layers described above and consisted of 402 quantitative point analyses with point distances of about 6 µm each. Remarkable chemical zoning was recorded with iron contents between 0.79 and 1.57 wt.% Fe_2O_3 and chromium contents between 0.07 and 0.29 wt.% Cr_2O_3 *(Table IV, Figure 36A)*. These ranges are consistent with those measured for the other three alexandrites *(Figure 34 a,b,c)*.

A correlation of chemical data with the visually observed layer structure *(Figure 36B)* shows that the chromium content continuously decreases from the first to the second boundary of a specific layer, while the iron content continuously increases. This sequence is consistent in both the two smaller layers (marked 1 and 9 in *Figure 36B*) and the seven broader layers of the central area (marked 2 to 8). Subsequent to layers 1 and 9, a change of zoning of chromium and iron is present in the two layers towards the table (marked 10 and 11 in *Figure 36B*), but no change is apparent in the last broad layer towards the culet at the bottom (layer 10).

From these observations, the history of the sample is deduced as follows:

a) Synthetic alexandrite was grown in an unknown number of growth cycles on a seed cut parallel to the **r** prism of chrysoberyl.
b) From this crystal a section was cut which contained nine growth layers. After cutting and polishing this slab consisted of seven thicker layers in the centre and one thinner layer on each side of the central part.
c) This slab was used as seed for subsequent growth cycles. Towards the bottom, the growth direction was identical with the former growth direction of the central part, but towards the later table facet, growth was in the opposite direction (see the

Flux-grown synthetic alexandrites from Creative Crystals Inc.

A

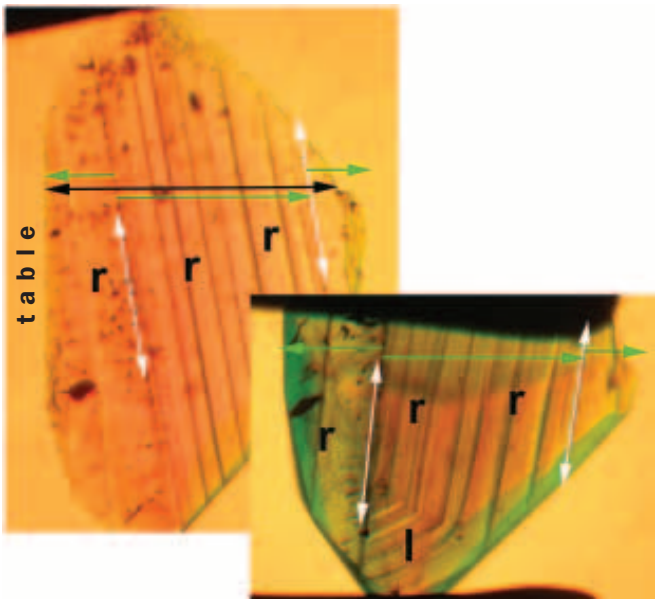

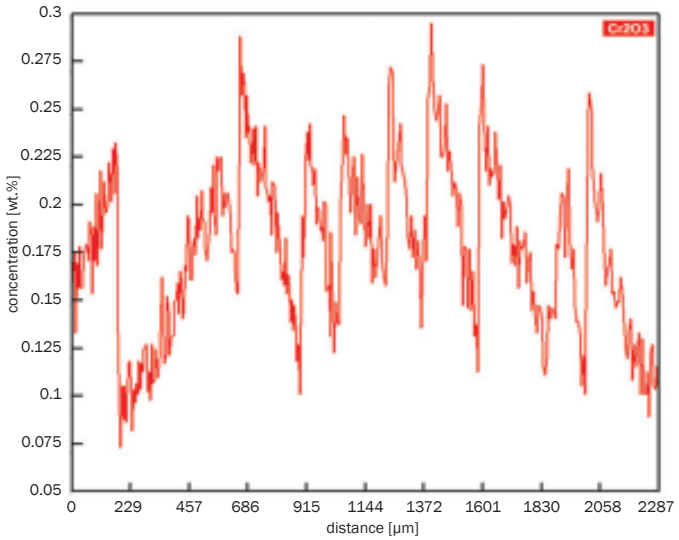

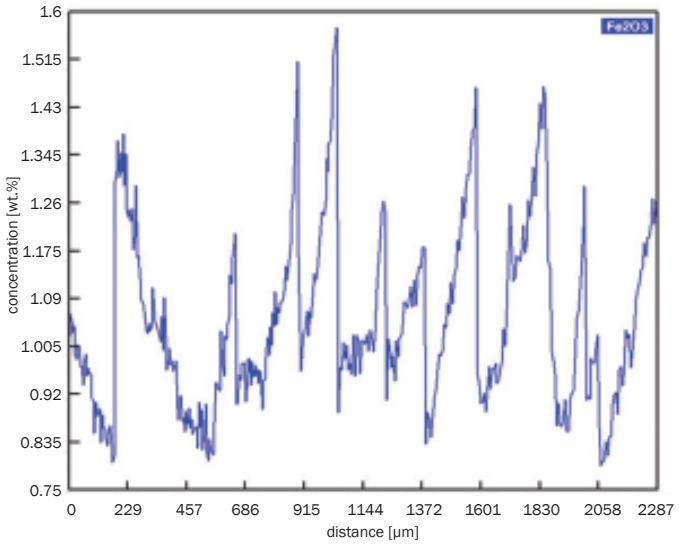

Figure 36A: Growth zoning, associated with colour zoning in synthetic alexandrite (above, photos of the same sample in two different orientations) and plots of chromium and iron concentration measured by an electron microprobe scan, about 2.3 mm long, consisting of 402 analysis points (black arrow). The alexandrite consists of a core which was overgrown after cutting and polishing; the boundaries between the core and the layers of the overgrowth are indicated by white arrows; the growth directions of the different layers of the core and the layers of the overgrowth are indicated by green arrows. The variation of trace element contents in each growth layer is clear; the plots of chromium (red) and iron contents (blue, below) and the patterns indicate a negative correlation.

Figure 36B: The Cr and Fe trace element contents are correlated with growth and colour zones in the alexandrite. This consists of a core with seven broader layers (labelled 2 to 8), two narrower layers (labelled 1 and 9) and an overgrowth of several layers on both sides of the core (labelled 10 and 11); the boundaries between the core and the layers of the overgrowth are indicated by white arrows; the growth directions of the different layers of the core and the layers of the overgrowth are indicated by green arrows.

At the beginning of each growth cycle, relatively high chromium contents and relatively low iron contents are incorporated into the growing alexandrite crystal; within each growth cycle, the chromium contents decrease and the iron contents increase. This variation in each growth cycle is the cause of the strong colour zoning (see Figures 27, 28 *and* 29*).*

B

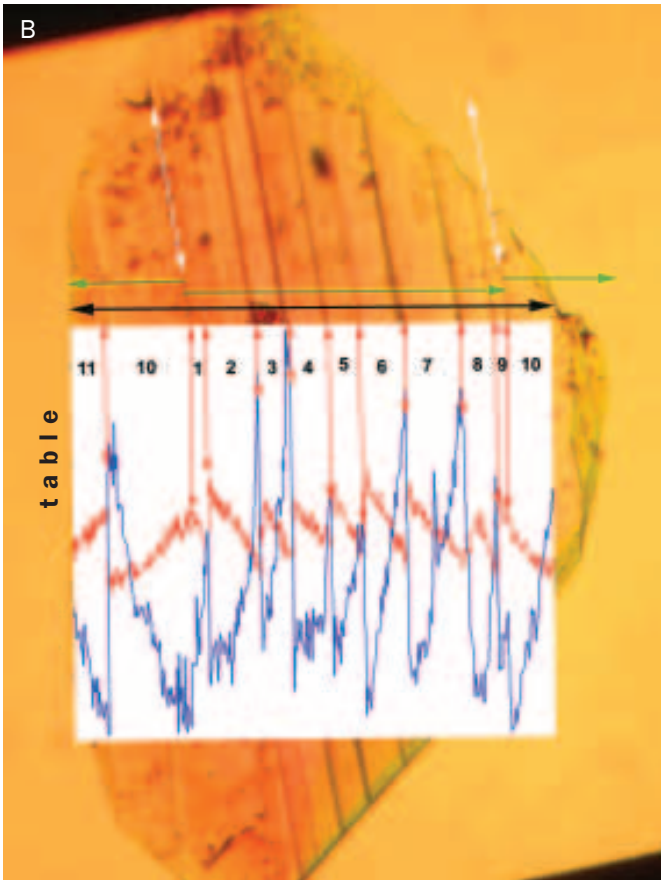

Table V: Colour and pleochroism in an oriented cube of synthetic alexandrite grown by Creative Crystals Inc.[1]

Direction of view	Light source	Colour to the unaided eye	Pleochroism		
			X	Y	Z
View ‖ a	daylight D_{65}	intense yellow green	–	yellow green	bluish green
	incandescent light A	greyish purplish red	–	orange	bluish green
View ‖ b	daylight D_{65}	blue green	blue violet	–	bluish green
	incandescent light A	violet purple	red purple	–	bluish green
View ‖ c	daylight D_{65}	light greenish yellow	blue violet	yellow green	–
	incandescent light A	red	red purple	orange	–

[1] Orientation: a 4.42, b 9.33, c 5.47; X ‖ a, Y ‖ b, Z ‖ c
lengths of the edges of the cube 5.9 × 5.8 × 5.8 mm

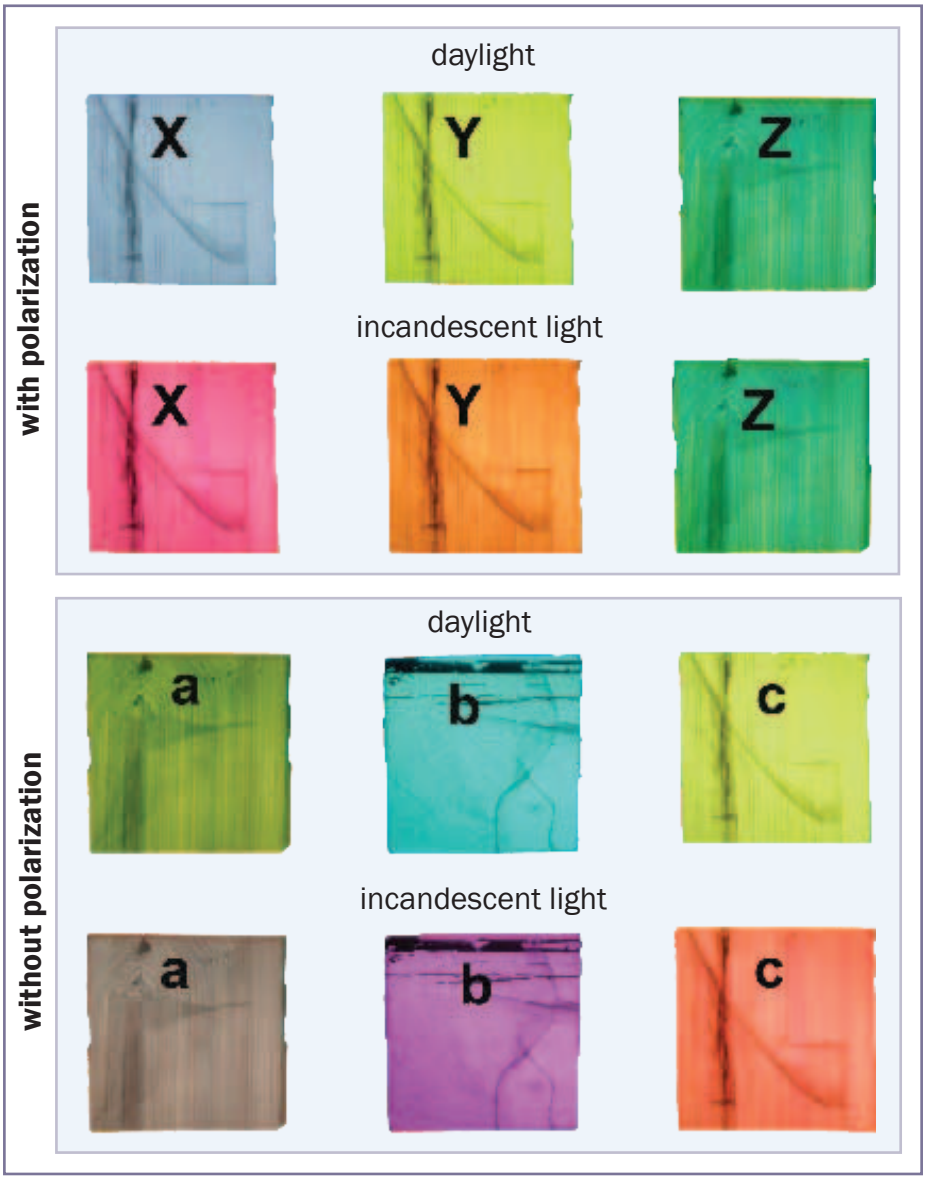

green lines in *Figure 36B*).

d) A stone was faceted from the final alexandrite crystal with a table cut somewhat oblique to the orientation of the seed.

Consequences of the applied growth technology

The synthetic alexandrites produced by Creative Crystals Inc. were grown in numerous successive growth cycles. In each growth period, the platinum crucible with solvent and seed crystals was continuously cooled within a period of about one week. This growth method is responsible for the three dimensional layered structure of the final product with each layer representing one individual growth cycle. Assuming a growth period of one week for one layer, the growth rate is about 0.03 – 0.04 mm per day.

The variation of growth conditions within each growth cycle caused distinct chemical zoning of chromium and iron within each growth layer, which is responsible for the observed colour zoning. At the beginning of each growth layer relatively chromium-rich alexandrite crystallized and towards the end of each growth layer, the chromium contents decreased and colour became less intense.

As each growth boundary is also a boundary between alexandrite layers of different chemical composition, the layers have slightly different optical properties, such as refractive indices. The interference pattern observed commonly at twin boundaries of natural or synthetic alexandrites is also based on the different optical properties displayed by adjacent parts of the twin which are in different

Figure 37: Schematic representation of colour and pleochroism in a cube of synthetic alexandrite in daylight and incandescent light; for polarized light (above) the three components X ‖ a, Y ‖ b and Z ‖ c are visible to the unaided eye; in non-polarized light different views parallel to the a-, b- and c-axes are depicted; growth zoning associated with colour zoning is also visible in some orientations of the sample.

Oriented cube of 3.22 ct, length of the edges 5.9 × 5.8 × 5.8 mm. Photos and artwork by K. Schmetzer.

orientations on each side of the twin plane. In natural alexandrites, series of parallel growth planes are common. In rare stones, the strongest or most visible boundaries between parallel growth planes can show distinct interference patterns under crossed polarizers (Schmetzer, 2011, 2012). This kind of pattern is comparable with that commonly present at each of the growth boundaries of the synthetic alexandrites from Creative Crystals Inc. But the interference pattern in the synthetic alexandrites is caused by the different optical properties arising from different trace element contents rather than by different structural orientations.

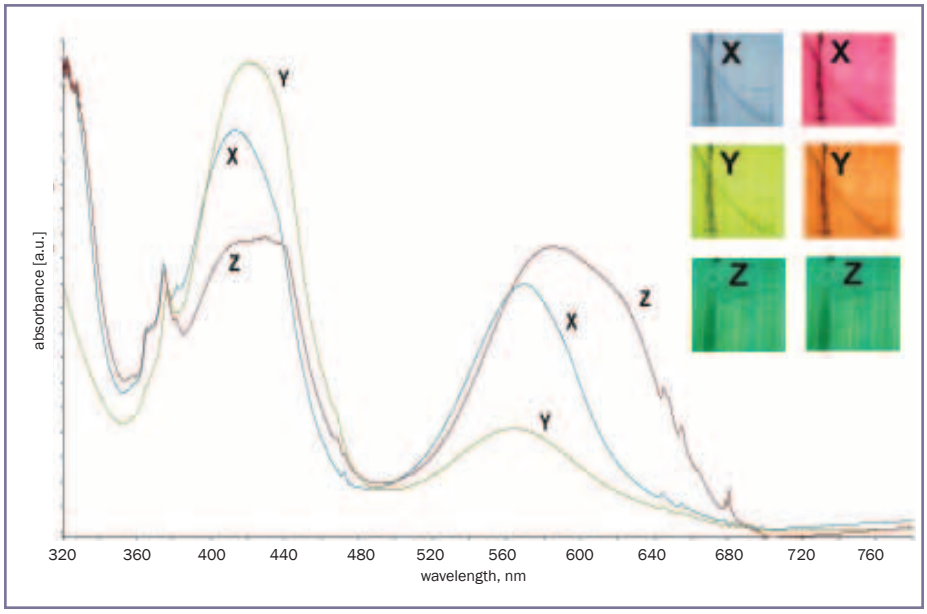

Figure 38: Absorption spectra of a synthetic alexandrite cube (see Figure 37*) for polarized light (with X || a, Y || b and Z || c); the colours in polarized light are also depicted for daylight (left column) and incandescent light (right column).*

Absorption spectroscopy in the visible and ultraviolet range and colour of the samples

For the evaluation of colour and pleochroism, an alexandrite cube was prepared, with an exact orientation of the faces perpendicular to the three crystallographic axes of the crystal (a, b, c). The various colours of the sample in daylight and incandescent light and in polarized and non-polarized light, are summarized in *Table V* and depicted in *Figure 37*. Absorption spectra of X, Y and Z in polarized light are given in *Figure 38*, and spectra recorded in non-polarized light along the a-, b- and c-axes are depicted in *Figure 39a*. Colorimetric parameters in the CIELAB colorimetric system were calculated from the non-polarized spectra and are plotted in the CIELAB colour circle in *Figure 39b*.

The absorption maxima recorded *(Table VI)* were assigned to trivalent chromium and iron, and are consistent with literature data (see, e.g., Farrell and Newnham, 1965; Bukin *et al.*, 1980). In polarized light, there is a distinct change of colour from daylight to incandescent light for X and Y, but an almost identical bluish green is observed in the Z direction for daylight and incandescent light. Using this distinct pleochroism, it would be possible to determine the approximate orientation of a rough crystal or of a

Table VI: Absorption peaks in the visible-range spectra of synthetic alexandrites grown by Creative Crystals Inc.

With polarization, absorption maxima and minima (in nm)

Polarization	X	Y	Z	Assignment
Maxima	570	564	586	Cr^{3+}
	–	–	440	Fe^{3+}
	–	–	430	Fe^{3+}
	414	421	420	Cr^{3+}
	381	381	381	Fe^{3+}
	375	377	375	Fe^{3+}
	365	364	365	Fe^{3+}
	–	–	356	Fe^{3+}
Minima	484	495	491	

Additional spin-forbidden chromium bands were observed at 680, 678, 655, 648, 645 and 472, 469, 467 nm.

Without polarization, absorption maxima and minima (in nm)

Orientation	a-axis	b-axis	c-axis	Assignment
Maxima	571	574	567	Cr^{3+}
	440	440 weak	–	Fe^{3+}
	430	430 weak	–	Fe^{3+}
	422	417	416	Cr^{3+}
	381	381	381	Fe^{3+}
	375	375	375	Fe^{3+}
	365	365	365	Fe^{3+}
	356	356	–	Fe^{3+}
Minima	494	488	490	

Additional spin-forbidden chromium bands were observed at 680, 678, 655, 648, 645 and 472, 469, 467 nm.

Flux-grown synthetic alexandrites from Creative Crystals Inc.

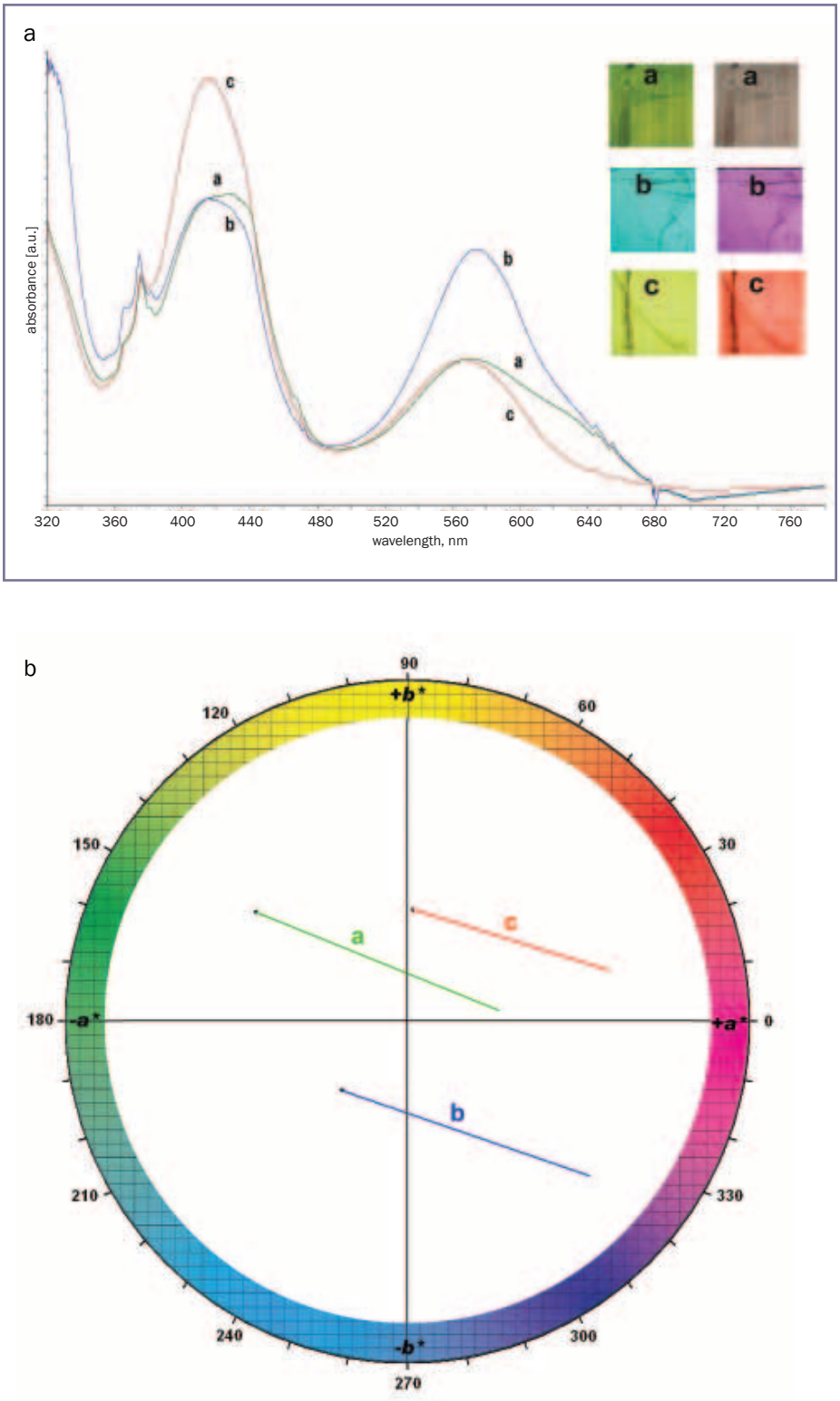

Figure 39: (a) Absorption spectra of a synthetic alexandrite cube (see Figure 37*) for non-polarized light in different views parallel to the a-, b- and c-axes, the colours in these directions are also depicted for daylight (left column) and incandescent light (right column); (b) colorimetric parameters are plotted for daylight and incandescent light in the CIELAB colour circle; they represent views parallel to the three crystallographic axes; the neutral point (white point) is in the centre of the a*b* coordinate system, the black circles represent the coordinates in daylight D_{65} and the ends of the differently coloured bars represent the coordinates in tungsten light A; the outer circle represents a chroma of 25. The pleochroism and typical colour change between daylight and incandescent light of the alexandrite for non-polarized light is consistent with the visual observation (see* Figure 37*). Colorimetric measurements by W. Balmer.*

faceted gemstone in the immersion microscope, especially by means of a commonly used tungsten bulb for incandescent illumination.

The two principal Cr^{3+} emissions of alexandrite are detected in some stones as 'negative' peaks in the absorption spectrum and, at the lower energy side (longer wavelength) of these peaks, additional luminescence bands may be present, also in the 'negative' direction; all other Cr^{3+} bands show a regular appearance *(Figures 38, 39a, 40a)*. This effect is caused by the use of a CCD-type Czerny-Turner spectrometer in combination with an integration sphere; such a setup permits the detection of all wavelengths at the same time in contrast to a traditional scanning spectrometer. In samples which can show strong luminescence, the light source used to record absorption spectra also excites fluorescence, which is detected at the same time. When the absorption dominates the emission, the peaks will point in the 'positive' direction while in the case of dominant emission, the peaks will point in the 'negative' direction.

As seen from *Figures 37* (lower half) and *39b* representing observations in non-polarized light, no 'ideal' orientation for the cutting of alexandrite exists. The most attractive intense green is seen in daylight in the direction along the a-axis, but the colour in incandescent light in this direction is not very attractive. In daylight, the colour along the b-axis seems to contain too much blue and the colour along the c-axis seems to contain too much yellow, although in incandescent light the colours along b or c are generally considered more 'attractive' than that seen along the a-axis. Therefore the search for the 'best' orientation of a rough sample for cutting to obtain the most attractive colours in both daylight and incandescent light is always a challenge.

Absorption spectra of different crystals recorded in directions perpendicular to the three seed orientations are presented in *Figure 40a*, and the colorimetric parameters calculated from absorption spectra for daylight and incandescent light are graphically represented in the

Flux-grown synthetic alexandrites from Creative Crystals Inc.

CIELAB colour circle in *Figure 40b*. The absorption minima in the visible range were determined at 487 nm for samples with **b** seed orientation, at 491 nm for samples with l seed orientation and at 495 for samples with **r** seed orientation. This indicates that the absorption minima show a clear shift for different seed orientations, which reflects the different colours of the samples.

The data obtained for crystals with seed orientation parallel to the **b** face (perpendicular to the b-axis) are comparable with the data obtained for the cube along the b-axis. In general trade opinion, the stones cut with this particular orientation of the table facet have 'too much blue' in daylight and 'too much violet' in incandescent light. Therefore, Creative Crystals Inc. stones for the trade were mostly cut with an orientation of the table facet inclined to the **b** (010) face.

For some of the samples with **r** seed orientation (see the upper example depicted in *Figure 40b*), the colours again may not be 'ideal', for in daylight there may be 'too much yellow' or in incandescent light, there may be 'too much red orange' and not enough blue. Therefore, most samples grown with r seed orientation have been cut with a table facet inclined to the **r** face (see, e.g. *Figure 34 a,b,c*). As seen for the samples with l seed orientation, their colours plotted in the CIELAB diagram represent, more or less, the most desired colours of alexandrite, green to bluish green in daylight and reddish purple to purple in incandescent light. This orientation is represented by a seed which is inclined to all three crystallographic axes. For practical application, this was also the best and most easily obtainable seed orientation for cutting purposes, i.e. for the best orientation of the table facet, which is inclined to all three crystal axes (D. Patterson, pers. comm., 2012).

However, we have to emphasize here that there are other factors which influence the colour of alexandrites in daylight and incandescent light. It has already been worked out, that — in addition to the orientation of the sample — the chemical composition, especially

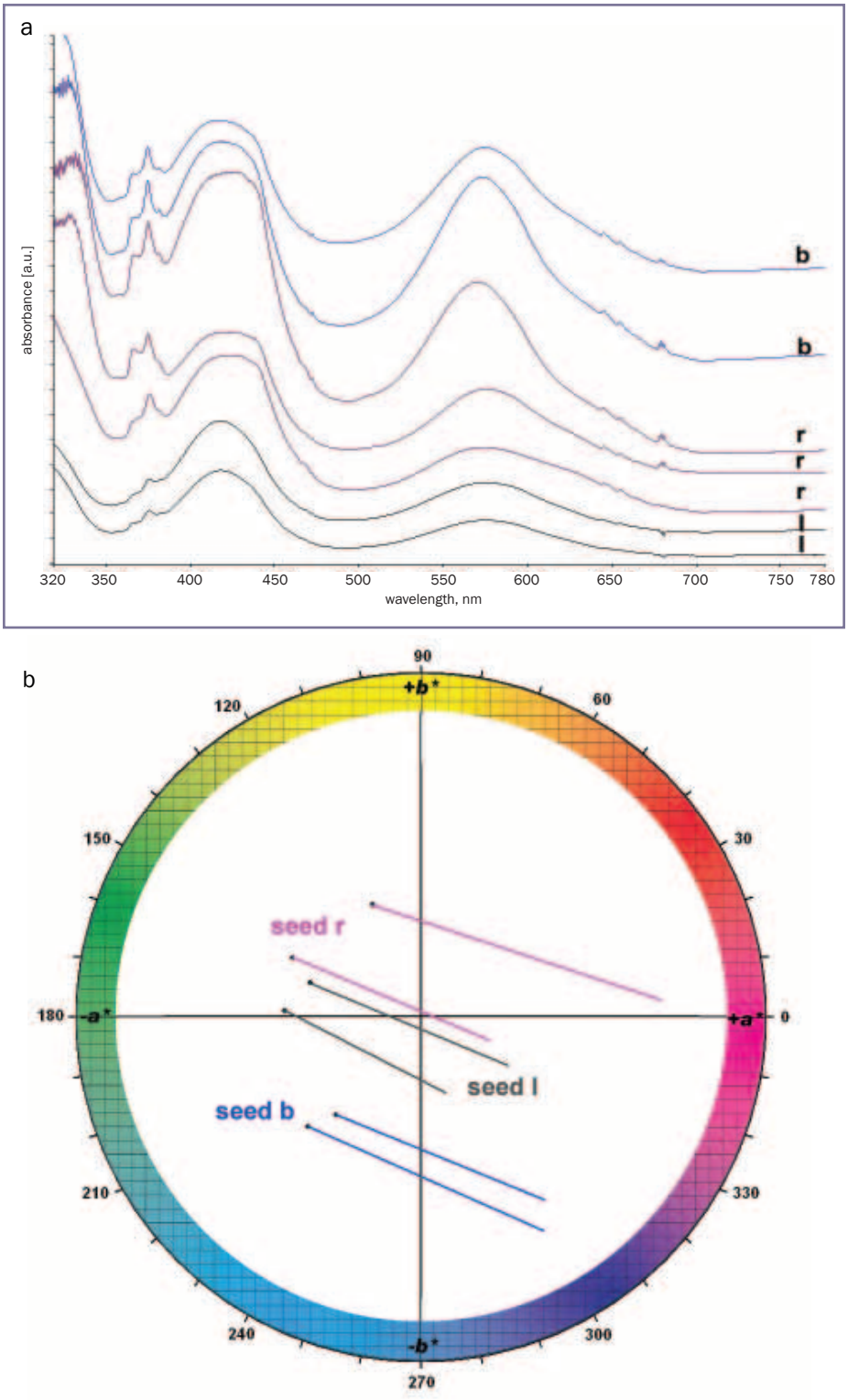

*Figure 40: (a) Absorption spectra of synthetic alexandrite crystals grown with different seed orientations for non-polarized light with the direction of the incident beam perpendicular to the seed plate; (b) colorimetric parameters are plotted for daylight and incandescent light in the CIELAB colour circle; they represent views perpendicular to the seed plate; the neutral point (white point) is in the centre of the a*b* coordinate system, the black circles represent the coordinates in daylight D_{65} and the ends of the differently coloured bars represent the coordinates in tungsten light A; the outer circle represents a chroma of 25. The dependency of colour and colour change on stone orientation is evident. The two samples with **l** seed orientation and one sample with **r** seed orientation show colours which are close to the desired 'ideal' coloration of alexandrite in daylight and incandescent light; the two samples with **b** seed orientation show 'too much blue', and the upper sample with **r** seed orientation shows 'too much yellow'. Colorimetric measurements by W. Balmer.*

the chromium content, plays an important role in determining the colour and colour change of a natural or synthetic alexandrite (Schmetzer and Bosshart, 2010; Schmetzer and Malsy, 2011). In addition, the length of the light path within a sample (influenced by cut and thickness) has also a strong influence on colour and colour change (Schmetzer *et al.*, 2012). Furthermore, in the cutting of alexandrite, the presence and/or variable concentration of inclusions, which causes variable transparency in different areas of the rough, must be taken into account to obtain the best stone.

Infrared spectroscopy

Infrared spectra were recorded for the oriented cube in the three directions parallel to the a-, b- and c-axes of the crystal. The spectra showed absorption bands with maxima at 3225, 2970 and 2655 cm^{-1} and shoulders at 2030 and 1995 cm^{-1} *(Figure 41)*. Although the spectra were recorded without polarization of the primary beam, the three bands at 3225, 2970 and 2655 cm^{-1} showed a clear polarization dependency. They were recorded in the spectra parallel to the b-axis (representing a combination of X and Z) and parallel to the c-axis (representing a combination of X and Y), but not in the spectrum parallel to the a-axis (representing a combination of Y and Z). This indicates a polarization of these lines parallel to X.

The data are consistent with infrared spectra published for Russian flux-grown chromium- and iron-bearing synthetic alexandrites, which showed small absorption bands in the same spectral range (Henn, 1992; Schmetzer *et al.*, 1996; Malsy and Armbruster, 2012). The different intensities of infrared absorption bands in natural and synthetic alexandrites measured in different orientations of the same gemstone were reported by Stockton and Kane (1988). The polarization dependency indicates structural OH-groups, as described in detail for polarized spectra of natural chrysoberyl (Bauerhansl and Beran, 1997). These OH-group absorption bands also showed a polarization in the X direction, but their absorption maxima were in somewhat different positions. For their stones, they proposed OH-dipoles parallel to the [100] direction, associated with Be vacancies, to account for the absorptions. This model might also apply for flux-grown synthetic alexandrite, but the shift of the band maxima is not yet understood in detail.

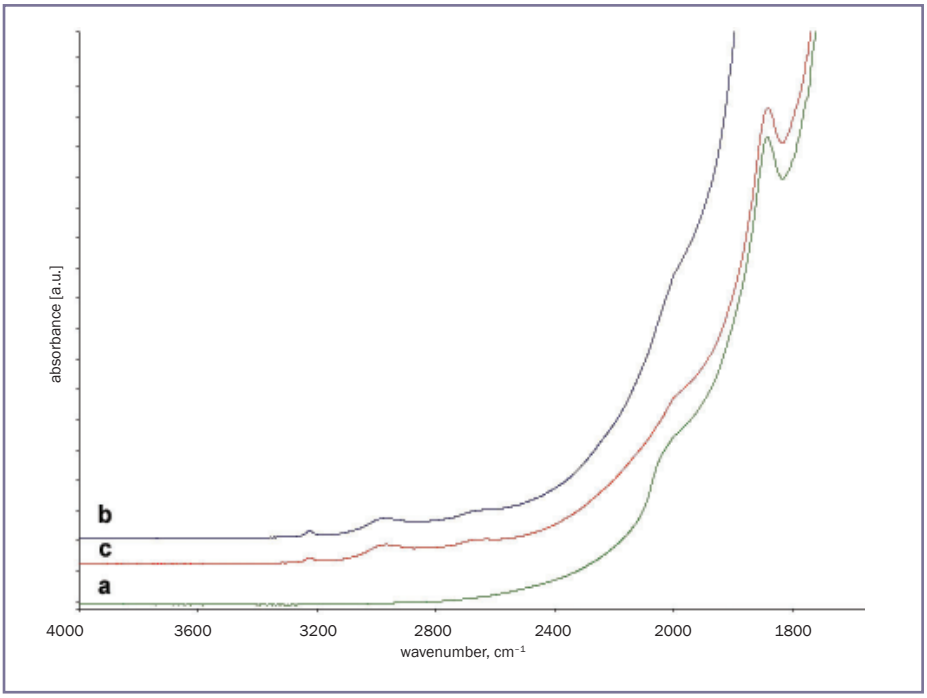

Figure 41: Infrared spectra of synthetic alexandrite cube in non-polarized light in views parallel to the a-, b- and c-axes of the crystal; the small absorption maxima near 3000 and 3200 cm^{-1} are present only in spectra representing views parallel to the b- and c-axes which indicates a polarization of these weak absorption bands parallel to X.

Comparison with Russian flux-grown alexandrites

Materials available on the market

Russian flux-grown alexandrite has been commercially available since the mid-1980s and has been described in detail in various mineralogical and gemmological papers (see, e.g., Trossarelli, 1986; Henn *et al.*, 1988; Henn, 1992, 2000; Schmetzer *et al.*, 1996). The samples were produced at the Institute of Geology and Geophysics, Novosibirsk, by a team around N.A. Novgorodtseva and G.V. Bukin from a bismuth- and molybdenum-bearing flux (Rodionov and Novgorodtseva, 1988; Bukin, 1993; Khranenko and Yurkin, 2000; A.Ya. Rodionov, pers. comm., 1988; G.V. Bukin, pers. comm., 1995; V.V. Gurov, pers. comm., 2011). In addition to the colour-causing trace elements, generally chromium and iron with some vanadium in some samples, these alexandrites are characterized by various contents of germanium (for details see Schmetzer *et al.*, 1996).

In a recent paper by Malsy and Armbruster (2012), three different types of Russian flux-grown alexandrite are mentioned. Two types labelled 'Tairus' and 'Bukin' (both types representing chromium- and iron-bearing alexandrites) show a similar chemical trace element pattern and relatively high concentrations of germanium. One might assume that the Tairus company, based in Novosibirsk, would have continued the production of the 'Bukin — Institute of Geology and Geophysics' type of synthetic alexandrite, but upon request, one author (KS) was informed that the Tairus company had never produced any iron- and chromium-bearing alexandrite by the flux method (V.V. Gurov, pers. comm., 2011, 2012). However, it was confirmed that Tairus is still selling stones produced at the Institute of Geology and Geophysics in Novosibirsk.

Flux-grown synthetic alexandrites from Creative Crystals Inc.

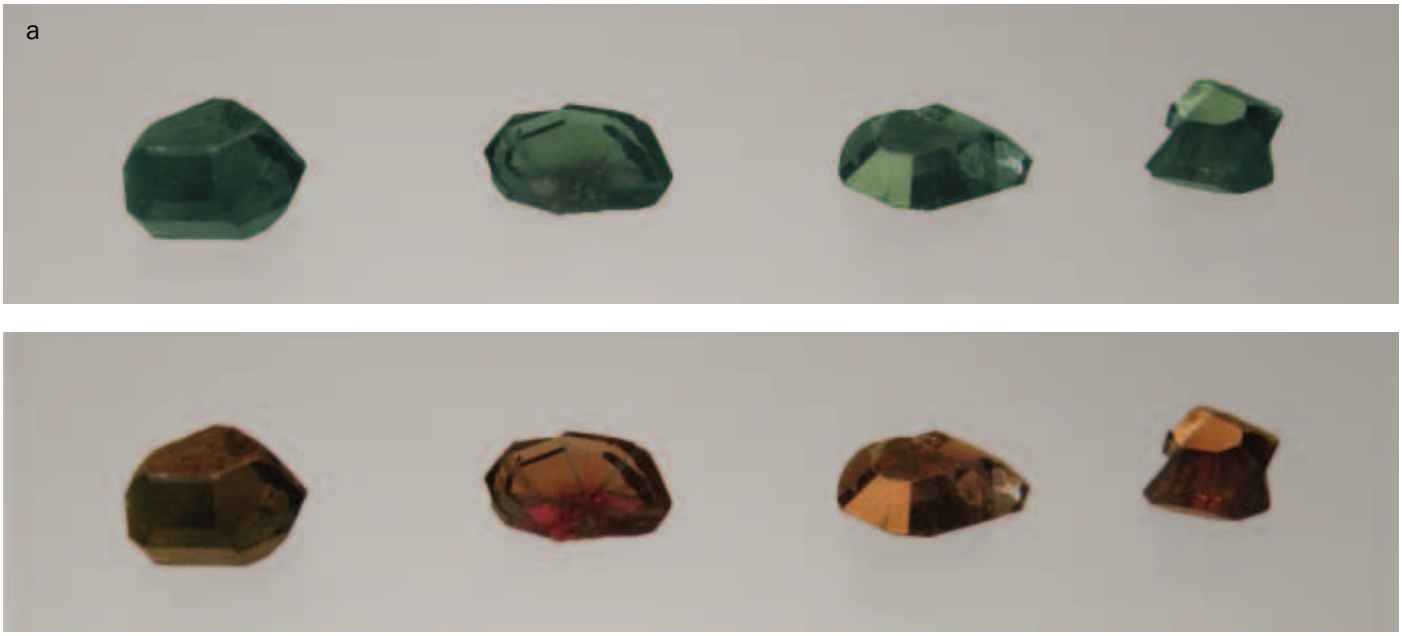

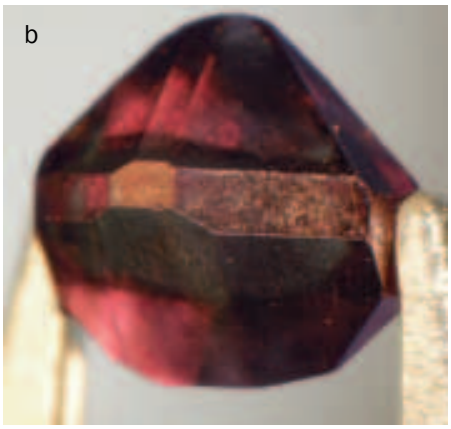

Figure 42: (a) Single crystal (left) and three cyclic twins (trillings) of flux-grown Russian synthetic alexandrites in daylight (above) and incandescent light (below); weight of samples from 5.47 to 2.45 ct; the single crystal on the left measures 11.5 × 7.5 mm.
(b) Single crystal flux-grown Russian synthetic alexandrite in incandescent light; weight of the sample 0.31 ct, size 3.9 × 3.7 mm; this sample is represented by Figure 43A*. Photos by K. Schmetzer.*

At present Tairus is producing and/or marketing synthetic alexandrites which are grown by the Czochralski technique and by a variant of the floating zone method described as "horizontally oriented crystallization (HOC)" (V.V. Gurov, pers. comm., 2011). Samples grown in Novosibirsk by the Czochralski technique were produced in iridium crucibles (see, e.g., Bukin *et al.*, 1981) which is consistent with the analytical data published by Malsy and Armbruster (2012) for the Czochralski-grown material assigned to Tairus. Alexandrites produced by the HOC method, on the other hand, are grown in boat-like containers of molybdenum (Gurov *et al.*, 2003; see also Schmetzer *et al.*, 2012).

A third type of 'flux-grown' Russian synthetic alexandrite, which did not contain significant amounts of germanium, was also attributed to Tairus by Malsy and Armbruster (2012). These chromium- and vanadium-bearing, iron-free samples contained traces of molybdenum. On enquiry by one author (KS) it was confirmed that the Tairus company had never produced any chromium- or chromium- and vanadium-bearing, iron-free alexandrites by the flux method and that the Tairus molybdenum-bearing stones are produced by the HOC technique (V.V. Gurov, pers. comm., 2012). Thus, it is likely that the chromium- and vanadium-bearing, iron- and germanium-free faceted Tairus material described by Malsy and Armbruster (2012) was produced by the HOC technique and is not flux-grown.

Growth technique and properties

The Russian alexandrite produced at the Institute of Geology and Geophysics, Novosibirsk, is grown in platinum crucibles in a reverse temperature gradient in which the nutrient is placed in the upper part of the crucible (dissolution zone) which is at a higher temperature than the base. The growth zone (crystallization zone) is in the lower part of the crucible. Small alexandrite crystals are formed by spontaneous nucleation at the bottom or close to the bottom of the crucible and grow continuously over several months. Most crystals grow in contact with the bottom of the crucible, and free-floating crystals are extremely rare (Rodionov and Novgorodtseva, 1988; Bukin, 1993; Schmetzer *et al.*, 1996; Khranenko and Yurkin, 2000). Although seeded growth is possible, with seeds placed at or attached to the bottom of the crucible (Bukin, 1993; Khranenko and Yurkin, 2000), no evidence of residual parts of seeds have been found so far in any sample examined by one author (KS).

Most crystals grown in contact with the bottom or with the wall of the crucible are twinned and have a somewhat dull and lustreless face, representing the contact plane of the crystal with the crucible. The highly reflecting crystal faces of the twins or trillings growing freely within the solvent show higher lustre *(Figure 42a)*. Only a few complete single crystals *(Figure 42b)* with no faces indicating contact with the crucible were found among 200 samples examined by one author in the study of 1995 and 1996 (Schmetzer *et al.*, 1996) and later. The morphologies of a single crystal and four

Flux-grown synthetic alexandrites from Creative Crystals Inc.

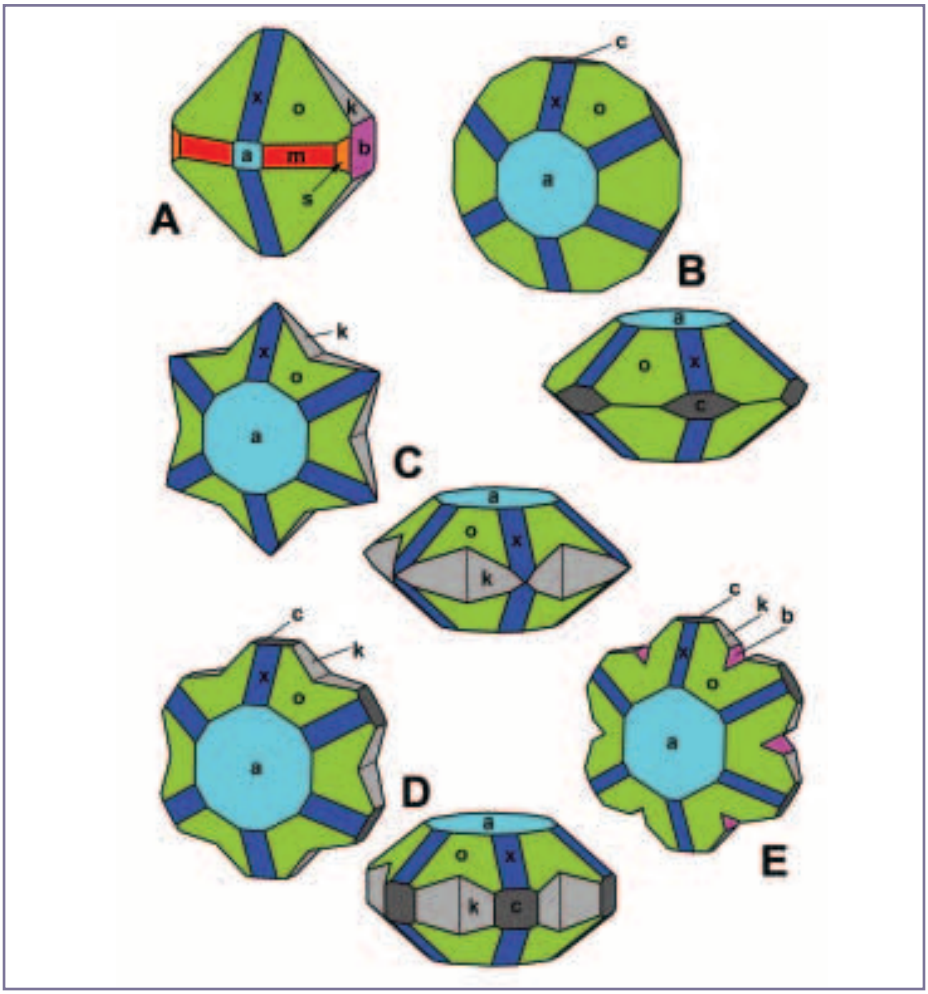

*Figure 43: Schematic drawings of a single crystal (A) and four cyclic twins (trillings, B to E) of flux-grown Russian synthetic alexandrites; three of the cyclic twins (B, C, D) are shown in views parallel to the a-axis (always upper left) and perpendicular to the c-axis, the other trilling (E) is shown parallel to the a-axis; single crystals (drawing A) and trillings with **b**-pinacoids (drawing E) are extremely rare. Crystal drawings and artwork by K. Schmetzer.*

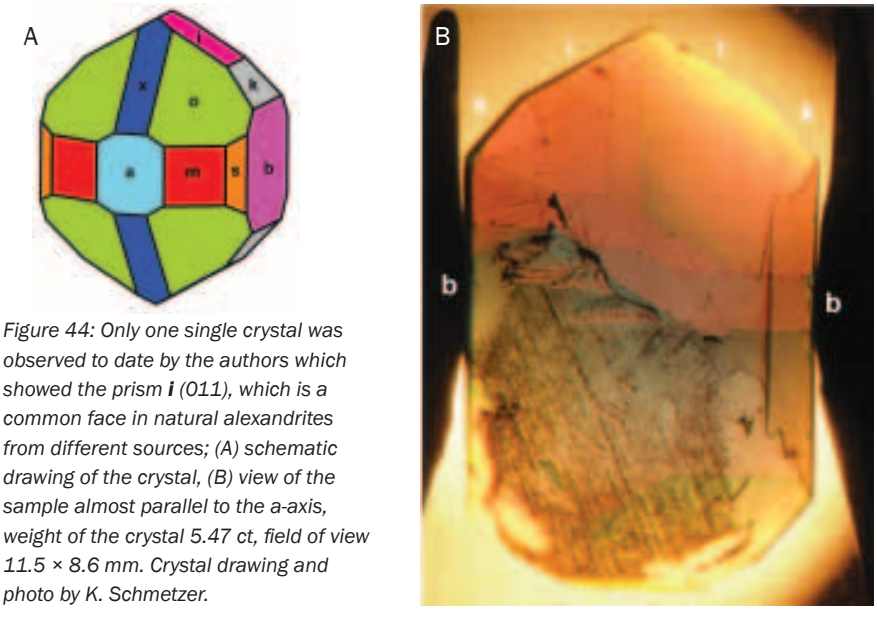

*Figure 44: Only one single crystal was observed to date by the authors which showed the prism **i** (011), which is a common face in natural alexandrites from different sources; (A) schematic drawing of the crystal, (B) view of the sample almost parallel to the a-axis, weight of the crystal 5.47 ct, field of view 11.5 × 8.6 mm. Crystal drawing and photo by K. Schmetzer.*

trillings are depicted in *Figure 43*. The various faces present in the single crystals and twins are the pinacoids **a** (100), **b** (010) and **c** (001), in combination with the five prism faces **m** (110), **s** (120), **x** (101), **i** (011) and **k** (021) and the dipyramid **o** (111). For all samples examined in the 1990s and for samples received from the trade in recent years, the two prism faces **s** and **i** were only observed in single crystals (*Figure 43*, sample A; Figure 44) and the pinacoid **b** is extremely rare in cyclic twins (see *Figure 43*, sample E).

The internal growth patterns of the samples closely reflect their external morphology *(Figures 42 a,b, 44A, 45)*. In the rough samples twins or trillings with re-entrant angles between different **k** prism faces are common *(Figure 46 A–C)*. This is the most characteristic pattern visible in a view parallel to the a-axis *(Figure 46 A,D)*. The most characteristic growth pattern in different views perpendicular to the a-axis are **a** pinacoids in combination with two **o** dipyramids *(Figure 46E)* or **a** pinacoids in combination with two **x** prism faces *(Figure 46F)*, occasionally also in combination with a **c** pinacoid.

As already mentioned, the Russian flux-grown material available in the trade contains significant amounts of germanium (up to 3.3 wt.% GeO_2) and traces of gallium and tin. Colour-causing transition metals are chromium (up to 4.6 wt.% Cr_2O_3) and iron (up to 1.6 wt.% Fe_2O_3), and some samples may contain up to 1.0 wt.% V_2O_3. Molybdenum- and bismuth-bearing compounds, from residual flux, have been detected, and a tungsten-bearing phase has also been found (Schmetzer *et al.*, 1996).

About 10 % of the samples examined in the 1990s (Schmetzer *et al.*, 1996), contained a pattern of colour zoning with an intensely dark core and a somewhat lighter rim. Between the core and rim, there was commonly a narrow zone with extremely high chromium content. These observations indicate, at least for these samples, crystal growth in several periods, with an addition of chromium to the nutrient between these periods.

Various forms of residual flux are present as inclusions in Russian flux-grown alexandrites. They range from isolated drops or dots to net-like patterns, 'feathers' or 'fingerprints'. Isolated particles of platinum originating from the surface of the crucible are present in some stones.

Discussion

To the best of our knowledge, this is the first detailed description of the synthetic alexandrites grown in the 1970s and early 1980s by Creative Crystals Inc. and correlates their properties with the applied growth technology. It is also the first account of flux-grown alexandrites (or other flux-grown gem materials), which were produced using a slow cooling technique in multiple successive growth cycles — in contrast to the Russian alexandrites which were grown in a furnace with a temperature gradient.

The main parameters influencing the final chemical and physical characteristics of the Creative Crystals Inc. gem material are:

a) orientation of the seed material
b) properties of the seed material (natural or synthetic, alexandrite or chrysoberyl)
c) concentration of colour-causing trace elements in the solvent at the beginning of each cooling phase and
d) varying concentrations of colour-causing trace elements during each cooling period of the solvent.

The orientation of the seed material and its properties (colourless or yellowish chrysoberyl or synthetic alexandrite) and the number of growth cycles performed to produce successive growth layers on both sides of the seed is responsible for the shape and habit of the final rough product. This indicates that strongly distorted crystals were grown from seeds with **r** and **l** orientation, but not from seeds cut parallel to the **b** pinacoid. The development of large **l** dipyramids — a face which is extremely rare in natural chrysoberyl and alexandrite — seems to be also a function of growth conditions, especially of the physical and chemical parameters of crystal growth (e.g. solvent composition, growth temperature). Colour and colour change of faceted stones are closely related to their trace element contents, to the thickness and cut of the stone, and especially to the orientation of the table facet to the crystal axes.

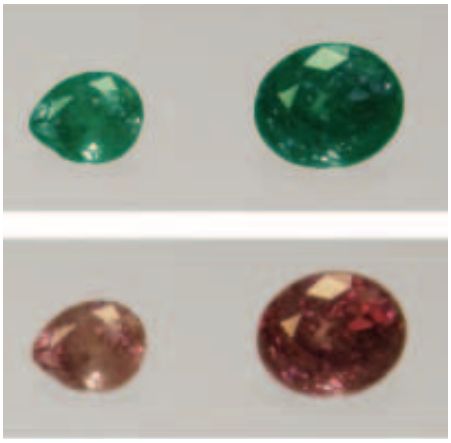

Figure 45: Faceted flux-grown Russian synthetic alexandrites in daylight (above) and incandescent light (below); weight of samples 0.43 and 1.08 ct; the oval sample on the right measures 6.3 × 5.3 mm. Photo by K. Schmetzer.

Chemical analyses (microprobe scans) clearly indicate strong variation of Cr and

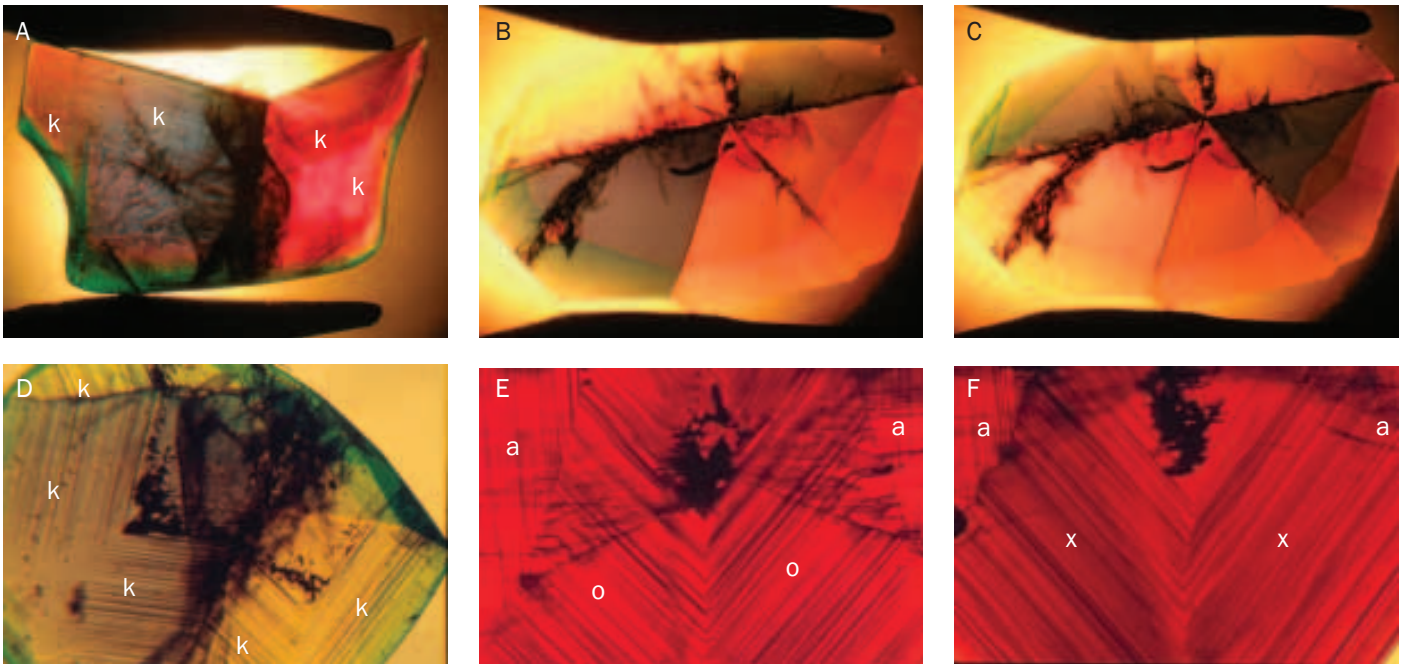

Figure 46: Microscopic features of Russian flux-grown synthetic alexandrites.
Twin (A) and trilling (B,C) in plane polarized light in views parallel to the a-axis; the pleochroism within the different parts of the samples is evident. The slightly curved lower surface of the twin (A) is the contact plane of the crystal with the crucible.

Immersion, field of view (A) 9.8 × 7.4 mm and (B,C) 10.5 × 7.9 mm.

Growth structures in faceted flux-grown Russian synthetic alexandrites (D,E,F) in different orientations; (D) growth zone [100], (E) growth zone [011], (F) growth zone [010], the faces of the different growth zones are labelled.

Immersion, field of view (D) 3.5 × 2.6 mm, (E,F) 4.5 × 3.4 mm. Photos by K. Schmetzer.

Fe contents within each growth layer. This variation is responsible for the colour zoning with an initial crystallization of intense colour followed continuously by less and less strongly-coloured alexandrite towards the outer margin of the growth layer. This production technology of multiple growth periods is also responsible for the abrupt changes of properties at the boundaries of the different growth layers, which explains both the layered growth zoning and the interference patterns visible at the growth boundaries.

In contrast, the Russian flux-grown material available on the market since the late 1980s was produced without seeds by spontaneous nucleation and crystal growth in a furnace in which the hotter nutrient at the top fed the growing crystals near the cooler base. Most crystals produced with this technique are twinned and show a slightly curved or almost plane face which is where there was contact with the bottom or wall of the crucible. Colour zoning is moderate and any layered or shell structure is absent.

Acknowledgements

The authors are grateful to Antoinette Matlins, Woodstock, VT, U.S.A., for her assistance in contacting people and locating research material available for loan for our study.

David Patterson, Geminex Corp., San Ramon, CA, U.S.A., former President of Creative Crystals Inc., submitted numerous faceted and rough samples from his private collection and provided valuable information regarding the growth process applied by the company for the production of synthetic alexandrites. Without his engagement to discuss our results, the work would not be so complete and conclusive. One alexandrite crystal was also kindly provided from the private collection of Kevin Patterson.

Further alexandrite crystals or faceted stones were kindly loaned by Stephen Avery, Lakewood, CO, U.S.A.; Cortney Balzan, Balzan Laboratories, San Francisco, CA, U.S.A.; Russell Feather, Smithsonian Institution, Washington DC, U.S.A.; Alan Hodgkinson, Portencross, Scotland, UK; Dr Michael Krzemnicki, SSEF, Swiss Gemmological Insitute, Basel, Switzerland; Dr Claudio Milisenda, Deutsche Gemmologische Gesellschaft, Idar-Oberstein, Germany; and Dr Terri Ottaway, Gemological Institue of America, Carlsbad, CA, U.S.A.

Thanks also go to Dr W. Balmer, Unterseen, Switzerland, who measured numerous rough and faceted alexandrites with his Zeiss MCS 311 colorimeter.

References

Bauerhansl, P., and Beran, A., 1997. Trace hydrogen in the olivine-type minerals chrysoberyl, Al_2BeO_4 and sinhalite, $MgAlBO_4$ – a polarized FTIR spectroscopic study. *Schweizerische Mineralogische und Petrographische Mitteilungen,* **77**, 131–6

Bonner, W.A., and Van Uitert, L.G.G., 1968. Growth of divalent metal aluminates. US Patent 3,370,963, assigned to Bell Telephone Laboratories, Incorporated, February 27, 1968

Bukin, G.V., 1993. Growth of crystals of beryllium oxides and silicates using fluxes. *Growth of Crystals*, **19**, 95–110

Bukin, G.V., Eliseev, A.V., Matrosov, V.N., Solntsev, V.P., Kharchenko, E.I., and Tsvetkov, E.G., 1980. The growth and examination of optical properties of gem alexandrite. In: Sidorenko, A.V. *et al.* (Eds). *Inhomogeneity of minerals and crystal growth*. Proceedings of the XI General Meeting of IMA, Novosibirsk 1978, published Moscow 1980, pp 317–28 (in Russian)

Bukin, G.V., Matrosov, V.N., Orekhova, V.P., Remigailo, Yu.L., Sevastyanov, B.K., Syomin, E.G., Solntsev, V.P., and Tsvetkov, E.G., 1981. Growth of alexandrite crystals and investigation of their properties. *Journal of Crystal Growth,* **52**, 537–41

Cline, C.F., and Patterson, D.A., 1975. Synthetic crystal and method of making same. US Patent 3,912,521, assigned to Creative Crystals Inc., October 14, 1975

Elwell, D., 1979. *Man-made gemstones*. Ellis Horwood Publishers, Chichester, England, 191 pp

Elwell, D., and Scheel, H.J., 1975. *Crystal growth from high-temperature solutions*. Academic Press, London, New York, San Francisco, 634 pp

Eppler, W.F., 1974. Synthetischer Alexandrit und synthetischer Opal. *Zeitschrift der Deutschen Gemmologischen Gesellschaft*, **23**(4), 286–93

Farrell, E.F., and Fang, J.H., 1964. Flux growth of chrysoberyl and alexandrite. *Journal of the American Ceramic Society,* **47**(6), 274–6

Farrell, E.F., Fang, J.H., and Newnham, R.E., 1963. Refinement of the chrysoberyl structure. *American Mineralogist,* **48**(7–8), 804–10

Farrell, E.F., and Newnham, R.E. 1965. Crystal-field spectra of chrysoberyl, alexandrite, peridot, and sinhalite. *American Mineralogist,* **50**(11–12), 1972–81

Gaal, R.A.P., 1976. Cathodoluminescence of gem materials. *Gems & Gemology,* **15**(8) 238–44

Goldschmidt, V., and Preiswerk, H., 1900. Chrysoberyllzwilling von Ceylon. *Zeitschrift für Krystallographie und Mineralogie,* **33**, 468–76

Gurov, V.V., Tsvetkov, E.G., and Kirdyashkin, A.G., 2003. Features of beryllium aluminate crystal growth by the method of horizontally oriented crystallization. *Journal of Crystal growth,* **256**, 361–7

Henn, U., 1992. Über die diagnostischen Merkmale von synthetischen Alexandriten aus der Gemeinschaft Unabhängiger Staaten (GUS). *Zeitschrift der Deutschen Gemmologischen Gesellschaft,* **41**(2/3), 85–93

Henn, U., 2000. Synthetische Alexandritdrillinge. *Zeitschrift der Deutschen Gemmologischen Gesellschaft,* **49**(1), 51–3

Henn, U., Malley, J., and Bank, H., 1988. Untersuchung eines synthetischen Alexandrits aus der UdSSR. *Zeitschrift der deutschen Gemmologischen Gesellschaft,* **37**(3/4), 85–8

Khranenko, G.G., and Yurkin, A.M., 2000. Controlled nucleation of chrysoberyl crystals in a flux system. *Inorganic Materials,* **36**(2), 171–2

Liddicoat, R.T., Jr., 1972. Synthetic alexandrite finally reaches the market. *Gems & Gemology,* **14**(4) 102–4

Malsy, A.-K., and Armbruster, T., 2012. Synthetic alexandrite — growth methods and their analytical fingerprints. *European Journal of Mineralogy,* **24**(1), 153–62

Nassau, K., 1980a. Synthetic gem materials in the 1980s. *Gems & Gemology,* **26**(1) 50–63

Nassau, K., 1980b. *Gems made by man*. Chilton Book Company, Radnor, Pennsylvania, USA, 364 pp

Pohl, A., 1989. Mineralogische Untersuchungen zur Charakterisierung und Unterscheidung natürlicher und synthetischer Alexandrite. Diplomarbeit, Universität Heidelberg, 140 pp (unpublished)

Rodionov, A.Ya., and Novgorodtseva, A.N., 1988. Crystallization of colored varieties of chrysoberyl by solution-melt and gas transport methods. *Tr. In-ta Geol. I Geofiz. SO AN SSSR,* **708**, 182–7 (in Russian)

Schmetzer, K., 2010. *Russian alexandrites*. Schweizerbart Science Publishers, Stuttgart, Germany, 141 pp

Schmetzer, K., 2011. Measurement and interpretation of growth patterns in chrysoberyl, including alexandrite. *Journal of Gemmology,* **32**(5-8), 129–44

Schmetzer, K., 2012. Natural alexandrites and chrysoberyls from Madagascar with irregular and regular growth patterns. *Australian Gemmologist,* **24**(10), 243–8

Schmetzer, K., Bernhardt, H.-J., Balmer, W.A., and Hainschwang, T., 2012. Synthetic alexandrites grown by the horizontally oriented crystallization (HOC) technique. *Journal of Gemmology* (submitted)

Schmetzer, K., and Bosshart, G., 2010. Colorimetric data of Russian alexandrite and yellowish green to green chrysoberyl. In: Schmetzer, K. *Russian alexandrites*. Schweizerbart Science Publishers, Stuttgart, pp 107–20

Schmetzer, K., and Malsy, A.-K., 2011. Alexandrite and colour-change chrysoberyl from the Lake Manyara alexandrite-emerald deposit in northern Tanzania. *Journal of Gemmology,* **32**(5-8) 179–209

Schmetzer, K., Peretti, A., Medenbach, O., and Bernhardt, H.-J., 1996. Russian flux-grown synthetic alexandrite. *Gems & Gemology,* **32**(3) 186–202

Stockton, C.M., and Kane, R.E., 1988. The distinction of natural from synthetic alexandrite by infrared spectroscopy. *Gems & Gemology,* **24**(1) 44–6

Trossarelli, C., 1986. Synthetic alexandrite from USSR. *La Gemmologia,* **11**(4), 6–22

The Authors

Dr Karl Schmetzer
D-85238 Petershausen, Germany
email: SchmetzerKarl@hotmail.com

Dr Heinz-Jürgen Bernhardt
ZEM, Institut für Geologie, Mineralogie und Geophysik, Ruhr-University, D-44780 Bochum, Germany
email: Heinz-Juergen.Bernhardt@rub.de

Thomas Hainschwang
GGTL Laboratories, Gemlab (Liechtenstein)/GemTechLab, FL 9496 Balzers, Liechtenstein/CH 1227 Geneva, Switzerland
email: thomas.hainschwang@ggtl-lab.org

Abstracts

Diamonds

The Vallerano diamond from ancient Rome: a scientific study.

A. Bedini, S. Ehrman, S. Nunziante, M. Pasini, I.A. Rapinesi and D. Sali. *Gems & Gemology,* **48**(1), 2012, 39–41.

Among the artefacts recovered from ancient Roman tombs at Vallerano during the 1990s was a gold ring set with an octahedral diamond crystal (approximately 0.15 ct). The ring can be linked to a young Syrian woman who died during the reign of Marcus Aurelius, making it the only Roman diamond jewel with a known background.

Examination of the mounted diamond's gemmological and spectroscopic properties was conducted at the National Roman Museum using portable instruments: a GIA Portalab equipped with a fibre optic light a binocular polarizing microscope; long- and shortwave UV lamps; and a Bruker Optics Alpha-R portable spectrometer. Infrared results point to a type Ia diamond with evidence of B aggregates and probable A aggregates. The diamond's internal features included a cluster of unidentified crystals. The diamond was inert to SW UV and fluoresced moderate blue to LW UV, exhibiting no phosphorescence to either.

Due to the fragile nature of the mounting, precautions were imposed for handling this historically valuable object. As a result, other observations are inconclusive and some questions remain unanswered. The ring's craftsmanship and simplicity of design, as well as the context in which it was found, provide insights into the burial practices and culture of the time period. E.A.S.

Diamonds can give moissanite results on testers.

A. Clark. *Gems & Jewellery,* **21**(1), 2012, 20.

A warning of the dangers of reliance on mechanical testing techniques by highlighting a case where a rare diamond type can fool even the most advanced combination tester. A.S.F.

Strain-induced birefringence in natural diamond: a review.

D. Howell. *Eur. J. Mineral.,* **24**, 2012, 575–85.

Birefringence in diamond is the result of strain modifying the isotropic properties of the ideal structure. The first to study this effect was Wertheim in the 1850s and between then and now there have been three major reviews of the topic by Lang (1967), Varshavsky (1968) and Orlov (1977). Howell considers five causes of strain-induced birefringence: Dislocations; Lattice parameter variations; Inclusions; Fractures; and Plastic deformation; and clearly describes the possible links between and combinations of these causes, at the same time putting them in the context of the three reviews mentioned above. Where Lang *(op. cit.)* categorized the different birefringent patterns in terms of their different causes, Orlov *(op. cit.)* differentiated the patterns themselves and Howell's study shows that Orlov's categories of 'stellate' and 'cruciform' patterns actually have the same cause. Birefringence patterns that are parallel to octahedral faces and relate to growth sequences are the result of variation in impurity contents across the layers. Birefringence in cross or star patterns is also due to impurity differences but between octahedral and cuboid sectors of mixed-habit diamonds. Laminations of birefringence that are parallel to octahedral planes but cut across growth layers are the result of slip on octahedral planes. A radial pattern of birefringence that is focused on a point indicates an inclusion. It is noted that the discussion of causes of birefringence will be applicable to synthetic diamonds grown at high pressures and temperatures but not necessarily to CVD diamonds which are grown in a different environment and can show very different birefringence patterns. The simplicity of imaging a diamond between crossed polarizers means that this technique can be a useful tool for learning about a diamond's history. R.R.H.

The magic circle.

A. Inns. *Gems & Jewellery,* **21**(1), 2012, 16–17.

A brief article attempting to explain a mysterious fluorescent circle seen in a diamond submitted to the American Gem Society (AGS) for testing. A.S.F.

Multiple core growth structure and nitrogen abundances of diamond crystals from Shandong and Liaoning kimberlite pipes, China.

T. Lu, H. Chen, Z. Qiu, J. Zhang, R. Wei, J. Ke, I. Sunagawa, R. Stern and T. Stachel. *Eur. J. Mineral.,* **24**, 2012, 651–6.

Diamond crystals from the Shandong and Liaoning kimberlites, China, display a distinct 'seed-like' multiple core growth structure with multi-stage growth history. Cathodoluminescence and DiamondView™ images revealed that the core portion of the diamonds is occupied by a 'seed-like' precipitated or smaller core which could be a resorbed early crystal formed by a cuboid growth mechanism. At the boundary between the core portion and the octahedral

Abstracts (continued)

layers, the nitrogen concentration drops abruptly to ~1 ppm from a few hundreds of ppm in the core portion, suggesting a fundamental change in geochemical growth environments in the mantle. This is associated with a switch in zoning trends in $\delta^{13}C$ from outward increasing to outward decreasing values, confirming that a change in growth conditions occurred. Authors' abstract

Distribution of OK1, N3 and NU1 defects in diamond crystals of different habits.

V.A. Nadolinny, O.P. Yuryeva, M.I. Rakhmanova, V.S. Shatsky, Y.N. Palyanov, I.N. Kupriyanov, D.A. Zedgenizov and A.L. Ragozin. *Eur. J. Mineral.,* **24**, 2012, 645–50.

Diamond crystals with low nitrogen contents from placer deposits and kimberlite pipes of Yakutia have been investigated using cathodoluminescence, photoluminescence, Fourier Transform infrared, electron spin resonance and electron microprobe techniques. Mica inclusions with high silicon and titanium contents are reported and nitrogen-titanium defect centres in the diamond structure are described. N-Ti centres cause peaks at 440.3 and 485 nm in the PL spectrum. Such centres are preferably developed in octahedral rather than cuboid sectors during diamond growth. R.R.H.

Gem news from Gary Roskin.

G. Roskin. *Gems & Jewellery,* **21**(3), 2012, 5–7.

The discovery and subsequent journey of the Argyle Jubilee Pink, a rare and exciting pink diamond discovered at Australia's Argyle mine. Weighing 12.76 ct, this extraordinary diamond was destined to take ten days to facet, and to become one of the finest faceted pinks in the world, but as is reported, events, and nature, conspired against this. A.S.F.

Plastic deformation of natural diamonds by twinning: evidence from X-ray diffraction studies.

S. V. Titkov, S. V. Krivovichev and N. I. Organova. *Min. Mag.,* **76**(1), 2012, 143–9.

A fragment of a pink-purple diamond crystal from the Internatsional'naya kimberlite in the Mir field, Siberia, was studied using single-crystal X-ray diffraction techniques. Then the fragment was broken to assess any changes in results arising from smaller sample size. Initial direct indexing of the diffraction pattern suggested a primitive hexagonal unit cell but further results and theoretical considerations indicated the presence of two diffraction patterns with cubic symmetry that are superposed. This is consistent with spinel law twinning along (111). The predominance of plastic deformation by dislocation slipping over mechanical twins is discussed in the context of the pressures and temperatures at which they take place. R.R.H.

Records of mantle metasomatism in the morphology of diamonds from the Slave craton.

Z. Zhang and Y. Fedortchouk. *Eur. J. Mineral.,* **24**, 2012, 619–32.

Octahedral and tetrahedral diamonds with {111} faces representing unresorbed, kimberlite-induced and mantle-derived resorption morphologies from the Ekati mine, Northwest Territories, Canada, were examined using cathodoluminescence imaging and Fourier Transform infrared spectroscopy. CL zoning patterns helped distinguish growth and resorption patterns and a 'classification tree' for recognition of different resorption styles is described. The diamonds are type IaA and IaB with 0-98% nitrogen in B defects and total N contents between 20 and 1697 ppm. There is a distinct correlation between the characters of mantle-derived resorption and the internal properties of the diamond crystals related to their history in the mantle. R.R.H.

Gems and Minerals

Tsavorite and other grossulars from Itrafo, Madagascar.

I. Adamo, V. Diella and F. Pezzotta. *Gems & Gemology,* **48**(3), 2012, 178–87.

Itrafo, in central Madagascar, has been a source of tsavorite and other grossular varieties since 2002. Production has been limited by the mountainous, remote location combined with security concerns due to bandits in the area. The material ranges from greenish brown to brownish/yellowish green to pure green and rarely exceeds 2–3 g. Eye-clean faceted stones of green colour rarely exceed 5 ct and only a small percentage of these are saturated enough to be classified as tsavorite. These are coloured mainly by vanadium and contain more iron than tsavorite from other localities such as Tanzania, Kenya, Pakistan and Gogogogo, Madagascar.

Twenty-two grossular samples were examined, including thirteen faceted stones ranging from 0.34–3.16 ct and nine rough specimens ranging from 0.07–0.50 g. Their colours ranged from greenish brown to green, including two tsavorites. For comparison, three samples of tsavorite from Tanzania and three from Gogogogo were also examined. The typical gemmological properties of grossular garnet were seen in all samples. The outstanding feature of these garnets is their iron content, Fe_2O_3>1 wt% (other localities generally do not exceed 0.30 wt%) and a small but significant andradite component (>3 mol%). The Itrafo tsavorites also had lower vanadium content than from other localities; the Fe_2O_3:V_2O_3 ratio in the former was always greater than 1 while the ratio in the latter was less than 1. Additionally, the chromium content of the Itrafo tsavorites was lower than Tanzanian and Kenyan samples, but similar to some Pakistani specimens. E.A.S.

Rough grading system for Zambian emeralds.

A. Banks. *Gems & Jewellery,* **21**(1), 2012, 14–15.

A new emerald grading system is discussed, implemented to help buyers understand the differences between the various qualities. Cuttability, colour, size and clarity are the basic factors, but within each there are numerous subdivisions which are briefly explained in this article. A.S.F.

Never smile at a crocodile.

M. Campbell Pedersen. *Gems & Jewellery,* **21**(1), 2012, 26–7.

The use of crocodile teeth in jewellery from Australia is discussed. A.S.F.

Copal vs. amber.

M. Campbell Pedersen and B. Williams. *Gems & Jewellery,* **20**(2), 2011, 20–4.

In a two-part study, the increasing difficulty in differentiating between

Abstracts (continued)

amber and copal is outlined, in light of the ever more complex treatments being undertaken. Tests range from simple observation and standard gemmological techniques, through to advanced lab testing by FTIR Raman, and crossed polarising filters. Of the treatments investigated, all can have the initial material (either amber or copal) determined by FTIR or Raman, through diagnostic peaks in the resultant spectra. A.S.F.

Cultured pearl farming and production in the Federated States of Micronesia.
L. E. Cartier, M.S. Krzemnicki and M. Ito. *Gems & Gemology,* **48**(2), 2012, 108–21.

A review is presented of the cultured pearl industry in the Federated States of Micronesia (FSM), including an evaluation of the viability of community-based farming projects and marketing opportunities for 'development pearls' and an examination of implications for FSM of recent developments in the global black cultured pearl industry. Oyster husbandry techniques and factors influencing pearl quality are discussed, along with the gemmological characteristics of the pearls.

Serious efforts to produce black cultured pearls in the FSM began about 25 years ago and utilize the *Pinctada margaritifera* oyster, cultivation of which was previously only practised in French Polynesia, the Cook Islands and Fiji. Farms on four islands in the state of Pohnpei (Pakin, Phonpei, Pingelap and Pweniou) are preparing for commercial pearl cultivation, with a total of 26,000 hatchery-reared oysters. These farms are projected to yield 6,500 cultured blister pearls and 2,000 loose bead-cultured pearls in 2012, with increasing production in the future. The cultured pearls show a range of colours; those with particularly distinct blue overtones are most prized and branded 'Micronesian Blue'. E.A.S.

Turquoise from Zhushan County, Hubei Province, China.
Q. Chen, Z. Yin, L. Qi and Y. Xiong. *Gems & Gemology,* **48**(3), 2012, 198–204.

Known since the late 1980s, turquoise deposits in Zhushan County in central China's Hubei Province are becoming a significant source of high quality material. These deposits form as lenses and fracture fillings within Cambrian-age slates and are projected to have significant potential for development. Eight rough and four polished untreated samples were studied, including their basic gemmological characteristics, as well as IR and UV-Vis-Nir spectral analysis. Most of these gemmological and spectral observations, including the presence of brownish-black veinlets/patches and irregular white blebs, were found to be similar to those noted in samples from elsewhere in Hubei Province. Chemical analysis revealed that the samples belong to the turquoise-chalcosiderite family. As it has a dense texture and uniform coloration (typically medium bluish green), the majority of Zhushan turquoise does not require treatment, though any lower-quality material usually undergoes polymer impregnation. E.A.S.

Composite malachite plates.
G. Choudhary. *Gems & Jewellery,* **20**(3), 2011, 3–5.

A report on a bonded malachite composite now being used to produce plates and decorative pieces. The composite can be detected using standard gemmological techniques, particularly the 10× lens. A.S.F.

Golden coral.
G. Choudhary. *Gems & Jewellery,* **21**(2), 2012, 12–13.

Details of a golden coral bead submitted for testing to the Gem Testing Laboratory of Jaipur, which showed evidence of both impregnation and surface polymer coating. A.S.F.

Inclusions in aquamarine from Ambatofotsikely, Madagascar.
F. Danet, M. Schoor, J.C. Boulliard, D. R. Neuville, O. Beyssac and V. Bourgoin. *Gems & Gemology,* **48**(3), 2012, 205–8.

Aquamarine with distinctive inclusions was found in the Ambatofotsikely area of central Madagascar in January 2012. Beryl from this deposit occurs as hexagonal prisms which are commonly highly fractured and of a moderate to strong greenish blue coloration. Only a very small amount of the aquamarine was suitable for faceting and several hundred stones weighing 1–35 ct have been cut. A gemmological examination was conducted of eight cut aquamarines (3047–13.59 ct) and nine rough samples (1.1–4.1 g) and Raman spectra of inclusions were collected. The inclusions consist of reddish-brown platelets of hematite along with black platelets, black needles and distinctive dark grey dendrites of ilmenite. Similar inclusions are known in beryl from Brazil, India, Mozambique and Sri Lanka, though this marks the first time dendritic ilmenite inclusions have been documented in aquamarine from Madagascar. E.A.S.

Surface features on gem crystal specimens.
A. de Goutière. *Gems & Jewellery,* **21**(1), 2012, 3–7.

Photomicrographs of various surface features on selected gem materials. highlighting the unique, and often overlooked, micro-world of rough crystals. A.S.F.

Sapphires from Thammannawa, Kataragama area, Sri Lanka.
P.G.R. Dharmaratne, H.M.R. Premasiri and D. Dillimuni. *Gems & Gemology,* **48**(2), 2012, 98–107.

The February 2012 discovery of commercial quantities of gem corundum near Kataragama in Southeastern Sri Lanka has revived gem mining activities in an area previously known only to contain hessonite garnet. The sapphires are hosted by weathered pegmatitic intrusions associated with mica layers which have yielded sharp-edged, well-formed crystals with a vitreous lustre that is unprecedented in Sri Lankan sapphires. These have transparent areas large enough to facet fine blue sapphires weighing more than 20 ct. The gemmological properties of 11 faceted sapphires and 22 crystals from the site are described. With the exception of two yellow crystals, all samples in the study were blue. Compared with other gem occurrences in Sri Lanka, this deposit seems to be unique in that only corundum has been found so far; other colours, star material and geuda sapphires have not been found. The blue crystals are a pure hue, unlike the violetish blue seen elsewhere in the country. A strong 450 nm absorption line was observed with both a prism and a diffraction spectroscope; this line is typically weak to moderate in other Sri Lankan blue sapphires. A weak red fluorescence was observed under longwave UV while they remained

Abstracts (continued)

inert to shortwave UV. Characteristic internal features include short and fine rutile needles concentrated in parallel layers, liquid-filled feathers and parallel arrangements of tabular negative crystals. E.A.S.

The origin of black coloration in onyx agate from Mali.
J. Götze, L. Nasdala, U. Kempe, E. Libowitzky, A. Rericha and T. Vennemann. *Min. Mag.,* **76**(1), 2012, 115–27.

Natural sharply-banded black and white onyx agate from a location near the city of Gao, about 850 km NE of Bamaku in Mali, has been investigated using optical and electron microscopy, micro-Raman X-ray diffraction, isotope analysis and electron spin resonance techniques to determine the cause(s) of colour. The black coloration is produced by disseminated grains, a few nm across, of graphite which may show a degree of disorder. The carbon isotope value ($\delta^{13}C$) of −31.1 is consistent with formation of the graphite by heating of kerogen or hydrothermal methane. The dark bands can contain up to 1.88 wt.% C and they are closely related to primary structural banding. R.R.H.

Mythbusting mineral.
K. Gregory. *Gems & Jewellery,* **20**(2), 2011, 6–7.

The procedure on how to approach the testing of an unknown stone, without resorting to laboratory techniques is described. By standard gemmological tests, the identity of a faceted pollucite was confirmed. A.S.F.

Bonny Scotland.
K. Gregory. *Gems & Jewellery,* **21**(2), 2012, 30–9.

A report of the Annual Conference of the Scottish Gemmological Association (SGA) held at the Queen's Hotel, Perth, in May 2012. Keynote speaker Professor Henry Hänni gave two presentations, the first reviewing pearl formation and the second discussing GemExpert, a consultancy business offering advice to those wishing to invest in gemstones. Other speakers included Maggie Campbell Pedersen, Professor Godfrey Fitton, Dr Elizabeth Goring, Dr Ulrich Henn, Richard Slater and Darko Sturman. A.S.F.

Gemstones.
L. Groat. *American Scientist,* **199**(2), 2012, 128–37.

An overview of several economically important gems whose value is also measured by their importance to geologists studying conditions deep in the Earth. Genesis, gemmological and geophysical significance, new research areas, as well as outstanding questions are considered for diamond, corundum, beryl, chrysoberyl, tanzanite, tsavorite, topaz, jadeite and nephrite. High-tech gem hunting is now possible given advances in understanding geological processes, along with the advent of newer technologies and publicly accessible satellite imaging. With increased availability of gems, scientists can continue to use them in their efforts to explore such questions as the origin of diamond's carbon, the genesis of the finest ruby and sapphire found in marble deposits, the unique nature of some emerald occurrences and other mysteries associated with the inner workings of the Earth. E.A.S.

Natural pearls and cultured pearls: a basic concept and its variations.
H. Hänni. *Australian Gemmologist,* **24**(11), 2012, 258–66.

A brief overview of current thinking on pearl formation in natural occurrences, as well as in molluscs used in pearl-culturing operations (freshwater and saltwater), with an emphasis on proper terminology. Explanations are accompanied by schematic diagrams, photographs and radiographs. In an experiment to demonstrate how any suitably sized inert object can be coated by nacre, Cambrian-age trilobites were used as nucleating material in *Pinctada maxima* oysters. After nine months, several pearls were produced, all with the underlying fossil morphology present. E.A.S.

Rötlicher Grossular aus Mexiko und Hydrogrossular aus Südafrika.
U. Henn and Th. Lind. *Gemmologie. Z. Dt. Gemmol. Ges.,* **61**(1–2), 2012, 3–12. 9 photographs, 3 tables, 6 graphs, bibl. German with English abstract.

Reddish manganese-bearing grossular garnets are found in Mexico and South Africa. The Mexican material has its raspberry-red colour concentrated in an outer rim with a darker, more andradite-rich core. The cuttable zone is opaque to translucent, as is also the material from South Africa, which is hydro-grossular and has lower RI and density than pure grossular garnet. E.S.

Fossils in amber.
M. Hügi. *Gems & Jewellery,* **21**(2), 2012, 41–5.

Various insects trapped within the time capsule that is amber are illustrated and discussed. A.S.F.

Gemstones from Vietnam: an update.
L.T. Huong, T. Hager, W. Hofmeister, C. Hauzenberger, D. Schwartz, P.V. Long, U. Wehmeister, N.N. Khoi and N. T. Nhung. *Gems & Gemology,* **48**(3), 2012, 158–75.

Vietnam's geological position along the margins of two cratons gives rise to a great diversity of gem materials. The most important gem localities consist of the marble-hosted ruby, sapphire and spinel deposits in the Northern provinces of Yen Bai (Luc Yen and Yen Binh districts) and Nghe An (Quy Chau and Quy Hop Districts). Basaltic volcanism accounts for peridot, zircon and blue, green and yellow sapphires found in the Central Highlands. In addition to its relatively young gem industry (30 years), cultured saltwater and freshwater pearl farming is on the rise as small scale and privately owned operations. Vietnam is also the leading source of extremely rare and expensive natural melo pearls which are recovered by fishermen from its coastal areas.

Using samples collected at mines from 2009 to 2012, updated gemmological data is provided for ruby, sapphire, spinel, tourmaline, peridot and garnet, and new chemical information is presented for spinel, tourmaline, peridot and garnet. Comparative charts condense observations for these selected species and localities: old and new mine corundum at Luc Yen; gem corundum from other localities in Vietnam (Nghe An, Quang Nam, Central Highlands and southern provinces); spinel from Luc Yen; tourmaline from Luc Yen; peridot from the Central Highlands; garnet from Luc Yen and Kon Tum. Brief descriptions, mining histories and present production of these gems are included, as well as for other less economically

Abstracts (continued)

important varieties such as aquamarine, yellow beryl (irradiated), topaz, quartz, zircon and green orthoclase. E.A.S.

Die historische Verwendung von Olivin — die Herkunft des Peridots in Barockschmuck.

J. Hyrsl. *Gemmologie. Z. Dt. Gemmol. Ges.,* **61**(1–2), 2012, 35–42. 7 photographs, 1 table, bibl. German with English abstract.

Gem-quality peridot is formed either in secondary veins in peridotites or found in ultrabasic xenoliths in basalts. Peridots of the first type were found on Zabargad island in the Red Sea where mining was active for about 100 years between the seventeenth and eighteenth centuries. Historical pieces from Prague, Vienna and Limburg were examined. E.S.

Spectral characteristics of natural-color saltwater cultured pearls from Pinctada maxima.

S. Karampelas. *Gems & Gemology*, **48**(3), 2012, 193–7.

Twenty-one saltwater cultured pearls (SWCPs) from *Pinctada maxima* in a variety of natural colours and ranging in size from 9.1–16.8 mm were studied using UV-Vis-NIR and PL spectroscopy to better understand colour mechanisms and to separate from other SWCPs. These pearls are marketed as 'South Sea' pearls and their body colours depend on the relative intensity of up to six absorptions, which are probably determined by various combinations of several pigments. Natural-colour SWCPs from ***Pinctada margaritifera*** and *Pteria sterna* show similar absorption and PL bands, but their UV-Vis-Nir spectra also show a 405 nm band that is not seen in those from *P. maxima*. An additional band at about 700 nm is known only from *P. margaritifera* SWCPs, while *P. sterna* SWCPs display more-intense PL bands and characteristic red fluorescence to longwave UV radiation. Subtle differences help with the identification of host molluscs and to separate from artificially coloured counterparts. The exact nature of the pigments responsible for the colour of SWCPs from *P. maxima* requires further research using destructive means. E.A.S.

Radioactive morganite.

H. Kitawaki, Y. Horikawa, K. Shozugawa and N. Nogawa. *Gems & Gemology,* **48**(1), 2012, 42–4.

Since its appearance in the Japanese market in May 2010, the Central Gem Laboratory in Tokyo has identified at least 10 cases of radioactive morganite with measurable levels found to be above the recommended exposure limit set by the International Commission on Radiological Protection. These were confirmed to be the result of treatment, rather than a naturally occurring phenomenon. In the present study, the radionuclides of two radioactive faceted morganites are analyzed in order to determine whether they had been artificially irradiated by a neutron source. Both sample 1 (49.18 ct) and sample 2 (39.40 ct) were of a strongly orangey-pink colour which seems to be typical of this material. Their gemmological properties and EDXRF spectroscopy results were consistent with beryl. Gamma-ray spectroscopy detected ^{134}Cs, ^{54}Mn and ^{65}Zn in sample 1 and ^{134}Cs and ^{54}Mn in sample 2. These radionuclides are activation products, confirmation that these morganites had been neutron irradiated. ^{134}Cs has a half-life of about two years; the radioactivity of these morganites should decay to a safe level within a period of several years since being treated. While it is common to use gamma rays to deepen the hue of morganite, it is unknown why these samples were irradiated with neutrons. E.A.S.

A secondary ion mass spectrometry (SIMS) re-evaluation of B and Li isotopic compositions of Cu-bearing elbaite from three global localities.

T. Ludwig, H.R. Marschall, P.A.E. Pogge von Strandmann, B.M. Shabaga, M. Fayek and F.C. Hawthorne. *Min. Mag.,* **75**(4), 2011, 2485–94.

Elbaites containing copper from the Batalha mine, Paraíba, Brazil, the Mavuco mine, Alto Ligonha, Mozambique, and an unlocated pegmatite in Nigeria were analysed for their boron and lithium isotope contents. The results were validated using standard tourmalines and appropriate NIST reference materials, and replace erroneous ratios previously published. Plots of Li and B isotope ratios of tourmalines from the three sources are significantly different and indicate the suitability of using these isotopes in combination as a provenance tool for 'Paraíba type' tourmaline. R.R.H.

Conditions for emerald formation at Davdar, China: fluid inclusion, trace element and stable isotope studies

D. Marshall, V. Pardieu, L. Loughrey, P. Jones and G. Xue. *Min. Mag.,* **76**(1), 2012, 213–26.

Emeralds of gem quality occur in quartz veins at Davdar in China near the border with Pakistan, Afghanistan and Tajikistan. Cr, V, Fe, Mg and Na contents were determined on a typical sample, which is zoned, using electron probe microanalysis, and using ICPMS to determine Be, Li and Ce. The results overlap those from emeralds from worldwide localities but are most similar to those from Panjshir, Afghanistan. Three-phase inclusions are present in the emerald and accompanying quartz and microthermometry on them indicates that the emerald formed between 325 and 375°C at pressures up to 160 MPa (1600 bars). Oxygen isotope work supports these values and hydrogen-deuterium values combined with the oxygen isotopes are shown to be a possible means of distinguishing Davdar emerald. R.R.H.

Einige Besonderheiten der Opale aus Athiopien.

C.C. Milisenda and U. Henn. *Gemmologie. Z. Dt. Gemmol. Ges.,* **61**(1–2), 2012, 43–54. 26 photographs, 2 diagrams, bibl. German with English abstract.

The article deals with opals from the Wollo Province in Ethiopia which came on the market in 2008 and are more stable than those from the Shewa district discovered in 1993. They are mostly translucent, milky white with a vivid play-of-colour consisting of all spectral colours.

They are hydrophane, i.e. they can absorb water and become more transparent when the play-of-colour can disappear. However, this process is reversible. Because of their porosity, opals are often treated with artificial resin to stabilize them or with smoke or sugar-acid to darken their colour. Important for the understanding of the opal genesis are inclusions of well preserved plant fossils. E.S.

Abstracts (continued)

Tiger's-eye revisited.
D. Morgan. *Gems & Jewellery,* **21**(3), 2012, 8–12.

A new way of looking at tiger's-eye and the processes involved in its formation are discussed. Instead of the usually accepted ideology of it being formed by a quartz replacement process, with crocidolite being replaced with quartz and creating the chatoyant effect, a system that was first suggested by Heaney and Fisher a decade earlier is detailed, where the quartz occurrence is a result of a crack-seal vein-filling process. This article considers the cause and effect of this process, and provides supporting evidence for this alternative theory. A.S.F.

The sapphires of Australia.
J. Ogden. *Gems & Jewellery,* **21**(2), 2012, 14–18.

A report of the author's visit to the sapphire mines located in the New South Wales and Queensland areas of Australia. These deposits yield a wide range of colours and clarities of crystal, with each locality seeming to offer different combinations and proliferations. The various scales of production in Australia require different levels of mechanization in sapphire mining, which is still relatively low-tech by modern standards. The author reviews his visits to various areas and the stones that have been found, and relates tales told by the miners. A.S.F.

Bicoloured quartz with unusual colour combination.
F. Payette. *Australian Gemmologist*, **24**(11), 2012, 272.

A 28.83 ct faceted gem measuring 21.08 × 17.41 × 10.50 mm was submitted for gemmological examination in late 2011 and revealed to be synthetic quartz. The most significant visual observation under magnification was that of chevron growth similar to that seen in hydrothermally grown synthetic beryl and synthetic amethyst. This is believed to be the first documented example of bicoloured blue/green synthetic quartz. E.A.S.

Essential features of the polytypic charoite-96 structure compared to charoite-90.
I.V. Rozhdestvenskaya, E. Mugnaioli, M. Czank, W. Depmeier, U. Kolb and S. Merlino. *Min. Mag.,* **75**(6), 2011, 2833–46.

After more than 50 years of attempts to determine the structure of charoite from the Murun massif, Yakutia, Sakha Republic, Siberia, Russia, scanning-transmission electron microscopy and electron diffraction techniques have yielded data to conclude that charoite occurs as four different polytypes which are commonly intergrown in nanocrystalline fibres. Automated diffraction tomography is described in the investigation of the charoite order-disorder family. Charoite-90 and charoite-96 are the two maximum-degree-of-order polytypes. R.R.H.

Oriented inclusions in alexandrite from the Lake Manyara deposit, Tanzania.
K. Schmetzer and H.J. Bernhardt. *Australian Gemmologist*, **24**(11), 2012, 267–71.

Under reflected light, regions of milky white are often observed in alexandrites from the Lake Manyara deposit in northern Tanzania. These are caused by two different types of oriented inclusions which are too small to be resolved using a gemmological microscope: needles or hollow channels oriented parallel to the crystallographic a-axis and inclusions on planes perpendicular to the a-axis. Photomicrographs of thin sections reveal the inclusions and their orientations; these are further interpreted in accompanying crystal drawings. E.A.S.

Treated ruby.
K Schmetzer, M. Krzemnicki and A. Hodgkinson. *Gems & Jewellery,* **21**(3), 2012, 14–17.

A new treatment for gem-quality corundum is reported. By using a proprietary treatment involving the use of lithium-based fluxes and heat, Ted Themelis treats rubies to improve their colour. This article focuses on a purplish-red ruby that was purchased by Alan Hodgkinson and subsequently underwent treatment by this process, showing the different stages that the stone experienced during it's transformation. A.S.F.

Natural alexandrite with an irregular growth pattern: a case study.
K. Schmetzer and A.-K. Malsy. *Journ. Gemmol. Assoc. of Hong Kong,* **32**, 2011, 1–10.

A 1.10 ct alexandrite with an unusual growth pattern of plane parallel growth faces and curved grain boundaries is compared with growth features typical of synthetic alexandrites grown by Seiko in Japan. Although there are similarities, evidence of the presence of OH groups from the infrared spectrum and contents of iron and vanadium that are higher than in Seiko stones indicate the stone under test to be natural, and possibly comparable with Madagascan alexandrites. R.R.H.

Ein Beitrag zum Thema Bernstein – Unterscheidung von Bernstein und Kopal sowie Erkennung von behandeltem grünen Bernstein.
K.Schollenbruch. *Gemmologie. Z. Dt. Gemmol. Ges.,* **61**(1–2), 2012, 13-34. 20 photographs, 1 table, 5 diagrams, bibl. German with English abstract.

A contribution to the topic amber — differentiation between amber and copal as well as determination of treated green amber.

The author gives a short history of amber and a table summarizing the different classical techniques of distinguishing between amber and copal, most of which are not very reliable and some are destructive, such as scratching, burning and dissolving. The best test seems to be by Fourier Transform infrared spectroscopy (FTIR). Green amber was introduced to the market a few years ago and can be produced from amber as well as copal. The classical differentiation tests fail to reveal the source of any particular sample as green amber is an artificially matured resin. Only laboratory methods like the FTIR can help.

E.S.

Granitic pegmatites as sources of colored gemstones.
W.B. Simmons, F. Pezzotta, J.E. Shigley and H. Berulen. *Elements,* **8**(4), 2012, 281–87.

Pegmatites are important sources of gemstones ranging from the rare and economically important species such as beryls and tourmaline to those which are abundant and less valuable such as quartz. Less-familiar 'collector' gems are produced as well, such as jeremejevite, brazilianite, danburite, petalite, euclase, pezzottaite and phenakite. Along with

Abstracts (continued)

the historic localities found in Brazil, Madagascar, Russia and the United States, important gem-bearing pegmatites have more recently been discovered in Congo, Mozambique, Namibia, Nigeria, Tanzania, Zambia, Afghanistan and Pakistan. These and other major gem-pegmatite localities are illustrated on a world geological map and summarized with their notable gem minerals in an accompanying table.

Gem-quality crystals are found in three settings: as crystals 'frozen' in massive quartz or feldspar in the core or core margin of a pegmatite (examples: beryl, variety aquamarine and tourmaline); as crystals in reaction zones surrounding pegmatites that intrude mafic rocks (examples: beryl, variety emerald, and chrysoberyl, variety alexandrite); as crystals in miarolitic cavities known as pockets (examples: beryl varieties aquamarine, heliodor and morganite; spessartine; spodumene, varieties kunzite and hiddenite; topaz; tourmaline, varieties indicolite, rubellite, verdelite, liddicoatite). Miarolitic cavities in some pegmatites have produced tons of gem crystals valued in excess of $50 million. Such spectacular occurrences are extremely rare and include: the Dunton pegmatite in Maine, USA; the Jonas pegmatite in Brazil; Antananarivo and Fianarantsoa regions in Madagascar; Volodark-Volynsky in the Ukraine; the Himalaya mine in California, USA; the Mount Mica pegmatite in Maine, USA.

An overview is given of the origin of gem-forming melts and subsequent formation of miarolitic cavities and gem-quality crystals. The three principal mechanisms discussed are (1) decompression in the ascending magma, or 'pressure quench', (2) fractional crystallization during isobaric solidification and (3) depletion of fluxing components by crystallization of minerals containing these elements, or 'chemical quench'. A model for pocket formation is described, concluding that while crystals growing from the margins of the pocket develop gemmy terminations, those growing entirely inside the pocket can be nearly flawless throughout. During final stages of pegmatite formation, damage to the crystals may result from pocket rupture, while changes in the growth environment may cause severe corrosion and alteration, making occurrences of gem-quality crystals extremely rare. E.A.S.

Emeralds from the Fazenda Bonfim region, Rio Grade do Norte, Brazil.
J.C. Zwaan, D.E. Jacob, T. Häger, M.T.O Cavalcanti and J. Kanis. *Gems & Gemology,* **48**(1), 2012, 2–17.

Since the 2006 discovery of the emerald deposit in the Fazenda Bonfim region of northeastern Brazil, exploration activities have produced a small amount of material from shallow pits and tunnels. These emeralds occur in association with small recrystallized pegmatite bodies and biotite schist. Though included crystals measuring several centimetres have been found, generally recovered transparent fragments and crystals average in size from 2–5 mm, yielding gems with a saturated bluish-green colour and a medium-light to medium tone.

Internal features consist of: partially-healed fissures with two-phase fluid inclusions (typically square, rectangular, or comma-like); hexagonally-shaped negative crystals forming CO_2-rich two-phase inclusions; partially decrepitated inclusions; parallel growth tubes; extremely fine unidentified fibre-like inclusions; homogeneous colour distribution and occasional moderate colour zoning parallel to the prism faces. Though uncommon, the following solid inclusions were observed: sodic plagioclase, platelets of phlogopite, thin flakes of hematite and clusters of minute grains of quartz. The emeralds' chemical composition is characterized by relatively high K; moderate Cr (the major chromophore), Fe and Mg; and low Na, V and Li. FTIR spectra show characteristics of alkalis, CO_2, and deuterated water.

The emeralds can be distinguished from those of other schist- and pegmatite-related commercial deposits based on these physical and chemical properties. Their higher Cs and lower Na contents separates them from the most closely matched emeralds of the Itabira District of Brazil. E.A.S.

Instruments and Techniques

Precision measurement of inter-facet angles on faceted gems using a goniometer.
A.H. Shen, W.A. Bassett, E.A. Skalwold, N.J. Fan and Y. Tao. *Gems & Gemology,* **48**(1), 2012, 32–8.

In this study, the authors examine the feasibility of using a well-established optical instrument to measure the angles of faceted diamonds to a very high precision, without relying on image analysis and computer algorithms. A Stoe & Rheinheimer two-circle reflecting goniometer (*circa* 1920) was used to measure inter-facet angles on five faceted diamonds that included round brilliants and fancy shapes. Historically, before the advent of X-ray diffraction techniques, this type of instrument was used by crystallographers to identify minerals by precision measurement of angles between crystal faces. This particular model was designed to handle large specimens; initially, to examine the newly discovered crystals of pink spodumene known as kunzite. Nearly 100 years later, this design innovation is what allowed the current investigators the space needed to accommodate their measurements of faceted gems.

Currently, non-contact optical scanners are important components for grading diamonds in gem laboratories. Such scanners are claimed to have a precision of ~0.1 degrees for facet angle measurements, compared to a precision of 0.034 degrees for the goniometer used in this study. Although time-consuming, goniometer measurements of facet angles are useful for highly precise applications such as producing reference stones, or 'master sets', or for independently calibrating optical scanners. Much like master sets used for colour-grading diamonds, these can be considered calibration standards for angle measurement. Another possible use of the goniometer is in the evaluation of facet quality, which was found to be evident during the measuring process. E.A.S.

Transmission X-ray diffraction as a new tool for diamond fluid inclusion studies.
E.M. Smith, M.G. Kopylova, L. Dubrovinsky, O. Navon, J. Ryder and E.L. Tomlinson. *Min. Mag.,* **75**(5), 2011, 2657–75.

Transmission X-ray diffraction using a high-brilliance diffractometer and a synchrotron were used to investigate fluid inclusions in fibrous diamonds from Mbuji-Mayi, Democratic Republic

Abstracts (continued)

of Congo; Wawa, Ontario, Canada; Panda kimberlite Ekati, NWT, Canada; and Jericho kimberlite, Nunavut, NWT, Canada. Daughter minerals identified include celadonite, dolomite and other carbonates, and sylvite and halite, the first positive identification of halite minerals in fibrous diamond. Further work is needed to understand detection limits of the method but it has potential as a useful complement to microprobe and infrared techniques. The authors comment that as fibrous diamond has a common nucleus and crystallographic orientation (i.e. it is not polycrystalline), the term 'monocrystalline diamond' should not be used to describe gem-quality diamond if one wishes to distinguish it from fibrous diamond. R.R.H.

Synthetics and Simulants

Recent advances in CVD synthetic diamond quality.
S. Eaton-Magaña and U.F.S. D'Haenens-Johansson. *Gems & Gemology,* **48**(2), 2012, 124–7.

The quality of synthetic diamonds produced by chemical vapour deposition (CVD) is currently very high due to improvements in gas-phase chemistry and growth parameters, the greater availability of high-purity HPHT synthetic diamond as a starting material, and the effective application of post-growth treatments. An overview of these developments is presented after a brief historical review of the CVD process. Spectroscopic measurements indicate that the purity of CVD synthetic diamonds is now comparable to or even higher than typical type IIa natural diamonds. It is predicted that CVD diamond sizes will continue to increase and the available colours will expand beyond colourless, pink and brown to include type IIb blue specimens doped with boron. E.A.S.

Aquamarine-coloured glass.
G. Millington. *Gems & Jewellery,* **21**(1), 2012, 32–4.

Details of a rough crystal submitted for testing as aquamarine which was identified as a form of devitrified glass. A.S.F.

Some days are stone.
G. Millington. *Gems & Jewellery,* **21**(3), 2012, 18–21.

A report on the necessity of microscopic examination of gemstones. Tell-tale inclusions in a selection of synthetic and imitation stones sent for testing were revealed under the microscope which had not been visible with 10x magnification. A.S.F.

Spherical cultured pearls: the early days.
J. Ogden. *Gems & Jewellery,* **21**(1), 2012, 28–30.

The author looks back at the history of cultured pearls, focusing on the spherical forms from their early development. through to 1921, highlighting the effect their introduction had on the market, and the early attempts to differentiate them. The different reactions of various markets are discussed and how pricing changed.
. A.S.F.

Faith in opals.
J. Ogden. *Gems & Jewellery,* **21**(3), 2012, 41.

The author visits Len Cram who carries out opal research in a shed at Australia's Lightning Ridge. He has devised a process to produce opal which he claims proves that it can be former faster than originally thought. A.S.F.

Synthetic star alexandrite.
K Schmetzer and A. Hodgkinson. *Gems & Jewellery,* **20**(3), 2011, 9–11.

A review of two synthetic alexandrite cabochons, both of which show asterism to varying degrees. The history of the production of synthetic alexandrite (Kyocera and Sumitomi) is covered briefly, before the determination of the crystallographic orientation of the inclusions responsible for the asterism is explained in depth with the accompaniment of diagrams. Comparison of this orientation with that of natural star alexandrite reveals differences that may aid identification of the production origin of any stone. A.S.F.

Characterization of colorless coated cubic zirconia (Diamantine).
J.E. Shigley, A. Gilbertson and S. Eaton-Magaña. *Gems & Gemology,* **48**(1), 2012, 18–30.

One type of coated cubic zirconia (CZ) marketed as 'Diamantine' by California-based Serenity Technologies was analyzed to determine the nature of the coating, including its durability. No differences were found between the gemmological properties of Diamantine and those of uncoated CZ. Both are easily distinguished from diamond on the basis of thermal conductivity, weight-to-diameter ratio and specific gravity.

Reported to be composed of nanocrystalline diamond, the 30–50 nm coating cannot be detected with a standard gemmological microscope or seen in polarized transmitted light at 1000× magnification. The only standard gemmological laboratory technique that could establish the presence of a coating was EDXRF spectroscopy, which detected Ti from the adhesion layer deposited on the CZ during the initial part of the coating process. While SEM imaging detected a coating consisting of nanocrystalline particles that may be diamond, it is unlikely that standard analytical methods and instruments used in advanced gemmological laboratories would be able to confirm their actual identity (due to the thinness of the layer, Raman spectroscopy could not detect whether diamond was present as indicated by a peak at 1332 cm^{-1}).

The value of the coating was questioned when testing results concluded that the coating does not add to the long-time durability of the CZ and that it appears not to be stable to normal wear and simple cleaning (such as with a polishing cloth, with or without alcohol).

Serenity is reportedly planning to release a new version of Diamantine, along with a testing device that can detect the coating. Questions remain regarding the responsibility at various levels of the gem industry for disclosure of different types of coatings on gems. As increased numbers of gems are treated with sophisticated coatings, techniques used at gemmological laboratories may have to be refined in order to detect them. These include SEM imaging, Nomarski differential interference contrast microscopy and ellipsometry techniques. E.A.S.

Abstracts (continued)

Nano-polycrystalline diamond sphere: a gemologist's perspective.
E.A. Skalwold. *Gems & Gemology,* **48**(2), 2012, 128–31.

A completely transparent 5.09 mm sphere fashioned from a relatively new type of synthetic diamond is described in regards to its unique characteristics and the technological process which created it. Nano-polycrystalline diamond (NPD) is compared to single crystal and polycrystalline varieties of both natural and synthetic diamond. NPD is composed of a tightly bonded mixture of 10–20 nm equigranular crystallites and 30–100 nm lamellar crystalline structures formed during a sintering process which converts high-purity graphite directly into synthetic diamond. NPD is harder and tougher than either natural or synthetic diamond and as a result, requires lasers to fashion. It resists breakage and has no particular cleavage direction; this in addition to its high transparency makes it extremely valuable to industry and research applications, as well as making it an interesting potential new gem material.

Author's abstract

Characterization of a synthetic nano-polycrystalline diamond gemstone.
E.A. Skalwold, N. Renfro, J.E. Shigley and C.M. Breeding. *Gems & Gemology,* **48**(3), 2012, 188–92.

A potential new synthetic gem material in the form of a faceted 0.88 ct brownish-yellow nano-polycrystalline diamond (NPD) has undergone a full gemmological examination for the first time. In addition to a chart summarizing its basic gemmological properties, photomicrographs illustrate its internal scene and its tatami-like strain pattern. A Presidium diamond tester registered positive for diamond, while a DTC DiamondSure™ screening device referred the sample for further testing. Deep-ultraviolet (~230 nm excitation) fluorescence imaging using the DTC DiamondView™ revealed an unevenly distributed, web-like orangey-red luminescence. Detailed spectroscopic analysis showed absorption spectra which were distinct from those of natural diamond.

The key identifying features include a hazy, roiled appearance (similar to that seen in hessonite garnet) and distinctive mid-IR, visible-range, and photoluminescence spectra. The authors stress that this sample, which was fashioned from early production, is only one example from a rapidly improving technology. Visual observations do not necessarily apply to all NPD specimens, particularly newer production, and therefore the advanced instrumentation of a gemmological laboratory is needed to confirm its identity. While NPD has been developed primarily for high-tech applications that require superior hardness and toughness, this faceted NPD sample illustrates its potential as a gemstone.

E.A.S.

CVD synthetic diamonds from Gemesis Corp.
W. Wang, U.F.S. D'Haenens-Johansson, P. Johnson, K.S. Moe, E. Emerson, M.E. Newton and T.M. Moses. *Gems & Gemology,* **48**(2), 2012, 80–97.

The gemmological characteristics and spectroscopic features are examined in Gemesis Corp's latest generation of chemical vapour deposition (CVD) single crystal diamonds. The 16 specimens in this study ranged in size from 0.24–0.90 ct and all but the largest were cut as round brilliants. Three were graded as colourless (F colour) and 12 as near-colourless and one was faintly coloured (L colour). Four diamonds received VS clarity grades while 12 had clarity grades between IF and VVS, marking the first time GIA has given an IF grade to a CVD synthetic diamond. Unlike other CVD diamonds, no dislocation-related graining was observed in these samples. Irregular, linear or sometimes 'tatami' birefringence patterns were observed between crossed polarizers, but were relatively weak in comparison with those observed in previously studied CVD samples.

Unlike the orange-red fluorescence commonly associated with CVD diamonds, these samples displayed weak green fluorescence under shortwave UV and six samples had this same reaction to longwave UV (the remainder were inert). The high-intensity ultra-short UV wavelength of the DTC DiamondView™ (225 nm radiation) revealed green or blue fluorescence along with growth striations having a green fluorescence of varying intensities. Evenly distributed blue phosphorescence was also observed in the DiamondView™, stronger in the blue fluorescing samples than in those which had fluoresced green. The samples displayed relatively featureless absorption spectra in the infrared region, unlike those reported for CVD synthetics from other sources.

Separating these new CVD synthetic diamonds from natural diamonds is becoming increasingly difficult using conventional gemmological procedures, and may not be possible without advanced instrumentation. PL spectroscopy at low temperature and UV fluorescence imaging are critical in distinguishing these synthetics from type IIa counterparts, such as natural, natural but HPHT treated, and from HPHT-grown synthetics. While post-growth treatment improves colour and possibly clarity, it appears that the striated growth pattern observed in the DiamondView™ is not affected by it and so remains the most important, if not the only visual identification feature. E.A.S.

Abstractors

A.S. Fellows – A.S.F. R.R. Harding – R.R.H. E.A. Skalwold – E.A.S. E. Stern – E.S.

Book reviews

Amethyst — Uncommon Vintage. H.A. Gilg, S. Liebetrau, G.A. Staebler and T. Wilson (Eds), 2012. Lithographie Ltd., Denver, 128 pages. ISBN 978-0-9836323-2-0. (US$40)

No. 16 in Lithographie's monograph series is so visually luscious one's mouth actually begins to water as page-after-page of exquisite purple-hued imagery greets the eye. This long anticipated volume brings together a diverse group of authors and photographers whose passion for this most highly-prized variety of quartz is self-evident in each of their contributions. Most appropriately, the volume opens and closes with the conjoined pens of the royal sovereigns of quartz, Si and Ann Frazier, as they offer first a historical overview and then a comprehensive glossary of terms related to amethyst. What comes in between leaves few mysteries untouched. Mineral collectors and gem enthusiasts of all levels will appreciate not only the aesthetic presentation, but also the level of detail contained in this volume, one which will surely become a standard reference on amethyst for years to come.

For our gemmological community, *Amethyst — Uncommon Vintage* offers an unparalleled resource for this classic gem. Jewellers, gemmologists, appraisers, coloured stone dealers, lapidaries, researchers and students will find that this volume provides a firm background for any pursuits related to amethyst and even quartz in general. While the overall visual presentation (dominated as it is by examples of amethyst in all its diverse natural forms) may seem to favour the collector of cabinet specimens rather than the lapidary arts, aficionados of the latter will not be disappointed. From Gerd Dreher's amethystine mouse — seemingly ready to bolt off the page with a swish of its golden tail — to a second-century intaglio featuring the binding of Herakles by Eros, the editors' carefully chosen photos of faceted stones, carvings and historic metal arts integrate with those of intact specimens, localities and other contextual scenes in an artful fashion that is both educational and compelling.

In addition to the Frazier's chapters, readers are treated to a concise lesson on the geological origins of amethyst by Dr H. Albert Gilg, followed by an overview by author Daniel Kile of its mineralogy, crystallography and optical properties, including that of ametrine. These two chapters very successfully convey relatively complex topics in a readable, easily understood, and most of all, enjoyable fashion — qualities which permeate the entire publication. They set the groundwork for the remaining chapters which focus on specific localities and types (see chapter listing below). Thereafter, the reader journeys around the world via authoritative text and visually stunning portraits as authors delve deeper into unique occurrences, morphologies, histories and personal stories surrounding amethyst. In closing, an extensive 'Literature and Cited Works' listing provides readers with added references to seek out on their own, while further validating its own place in one's gemmological library.

Arguably, the most valuable aspect of this tome for the gem community is the appreciation it brings for the natural crystal, perhaps for the first time. Comprehending amethyst's complexities broadens our understanding of it as a fashioned gem, a valuable asset whether faced with an unknown, educating a client or contemplating a bit of rough to buy or to facet. With its fine quality colour-rendition and printing, one would be hard-pressed to find any fault with this publication which packs so much information into just 128 pages.

Amethyst — Uncommon Vintage is destined to become a collector's item, just as have now hard-to-find previous titles such as *Tourmaline, Emerald, and Gold*. With that in mind and at its very reasonable price, one might even consider purchasing two copies, preserving one as pristine as the day it came off the press while the other not only provides personal enjoyment, but also may be shared with colleagues, clients and students.

Contents:

E.A.Skalwold

Book reviews (continued)

Characterization of Diamonds Color-enhanced by Suncrest Diamonds USA. D. Simic and A. M. Zaitsev, 2012. Analytical Gemology and Jewelry Ltd, New York City, NY, U.S.A. 24 pp

In this booklet the authors describe studies they have carried out on 15 natural brown diamonds before and after they have been colour-enhanced by high-pressure, high-temperature (HPHT) treatment and, for diamonds with a final pink colour, subsequent irradiation and annealing. As a scientific investigation the work confirms results obtained by other researchers and adds some interesting new findings; however, for the purposes of differentiating naturally-coloured diamonds from diamonds with a treated colour the procedures described have some shortcomings, as described below.

The text is reasonably well written, and the authors have explained most of the technical terms in yellow-highlighted boxes. There are some typographical errors and the English is rather strange in places, although the meaning is usually clear. However, there are a couple of serious mistakes. On page 2, when discussing the 'Imperial Red' treated colour it is stated that "The NV^- and NV^0 colour centers strongly absorb light in the red spectral range and cause red coloration of diamond." It is because these centres do not absorb red light (wavelengths longer than 640 nm) that the diamonds appear red! In the box on page 6 the authors say that "Photoluminescence comprises light with wavelength shorter than that of the light used for illumination." In reality the photoluminescence occurs at longer wavelengths than the wavelength used for excitation (as is clear in the examples that the authors give).

Simic and Zaitsev point out that the HPHT treatment of diamonds is a fast growing business, and that there is a growing trade in undisclosed colour-enhanced diamonds. The company with whom they have collaborated (Suncrest Diamonds of Utah, U.S.A.) fully discloses the origin of colour of the processed diamonds, but the authors believe that the treated nature of these diamonds frequently remains undisclosed when they are being resold. The motivation for the present study was to develop new approaches for the identification of diamonds that have been colour-enhanced.

The study investigated 5 type IIa diamonds that became colourless after the HPHT treatment, 5 type IaA diamonds that became yellow and 5 type IaB diamonds that were processed at HPHT, then irradiated with high-energy electrons and annealed (probably at approximately 800°C) to produce pink diamonds. Fluorescence images of the 'yellow' and 'pink' diamonds were obtained before and after the treatments, using longwave ultraviolet excitation. The fluorescence intensities of the 'colourless' diamonds were very weak before and after treatment and images could not be obtained. The authors also used a homemade 'express spectrometer' which measures a low-resolution photoluminescence (PL) spectrum from a diamond at room temperature. They found that before treatment the maximum luminescence intensity was at approximately 510 to 520 nm, and that, after treatment the maximum moved to the range 440 to 490 nm.

The authors also used high-resolution photoluminescence studies with the diamonds cooled to liquid nitrogen temperature, with three different wavelengths for excitation (488, 514 and 532 nm). In addition they recorded some high resolution infrared spectra. For reasons that are not obvious they do not appear to have measured any absorption spectra in the ultraviolet, visible and near-infrared regions.

For diamonds that have experienced HPHT annealing only, the authors find that some infrared absorption features and some photoluminescence lines, that were present before the HPHT processing, were destroyed by that treatment. For the spectral features documented one can therefore conclude that if a diamond has any of these features then it has probably not been colour-enhanced. Similar conclusions have been reached in earlier studies.

The discussion about the presence of H4 photoluminescence in the treated pink diamonds is somewhat misleading. The authors report that "The H4 center is usually considered as an indication of untreated natural diamonds." However, this is not what is stated in the references they cite. That previous research showed that the H4 centre is destroyed by HPHT treatment, and so it is true that H4 centres will be absent in a diamond that has been subjected only to HPHT treatment. The converse is not true; it is well known that H4 absorption and luminescence can be produced by irradiation and annealing (at c. 800 °C) in a type IaB diamond. If that is the only treatment employed the end result can be a treated yellow diamond. If the diamond has first been subjected to HPHT treatment, as described by Simic and Zaitsev, the end result can be a treated pink diamond, but, of course, H4 centres will also be produced.

My major worry with this article arises from the claims that the authors make in the summary: "… fluorescence imaging may be useful as a quick and inexpensive test of pink and yellow diamonds. …we have demonstrated a photoluminescence 'express- spectrometer' which is capable of fast recording of PL spectra of any diamond including even nominally non-fluorescent type IIa diamonds. … Using this spectrometer we have confirmed that the position of PL maximum, under excitation in the near UV range, is a useful parameter for identification of HPHT treatment."

There are two problems in making far-ranging conclusions from this sort of investigation. The first is that — as with most 'before and after' studies — it is very time-consuming to make measurements on a large number of diamonds. Thus, while it is straightforward to see changes that have occurred for the few diamonds examined in detail, it is much more difficult deciding which diamond in a parcel of 1000 diamonds is the one that has been colour-enhanced. The second problem, which is certainly relevant in this study, is that the authors have not used any 'control samples'. They only examined brown diamonds that became colourless, yellow or pink after treatment; ideally they should have also examined colourless, yellow and pink diamonds that were known to have a natural colour. More than 30 years ago I was fortunate to have the opportunity to examine large batches of diamonds straight from the DTC sorting tables in London. Under a longwave ultraviolet lamp diamonds colour-graded as brown displayed a whole range of luminescence colours — blue, green, yellow, pink — whereas blue was the dominant luminescence colour for diamonds colour-graded as colourless. (For many diamonds from all batches the

Book reviews (continued)

luminescence was weak, or invisible by eye, for reasons that are well understood.) On the basis of those observations I believe it would be very risky to decide the colour origin of a diamond using only the 'express spectrometer' described in this article. The fluorescence imaging technique is also unhelpful when examining an unknown diamond because, if it had indeed been treated, there is no record of the luminescence image before the treatment was carried out.

Suncrest diamonds are producing a large number of pink diamonds using the three-stage process of HPHT treatment, irradiation with high-energy electrons and annealing at typically 800°C. This process produces nitrogen-vacancy centres which are responsible for the pink colour. An absorption spectrum in the UV, visible and near-infrared regions will clearly show the presence of the negative (NV^-) centre, together with many other absorption lines known to be produced by irradiation and annealing (see, for example, the article by W. Wang *et al.* (2005), *Gems & Gemology,* **41**(6–19). Simic and Zaitsev have not used absorption spectroscopy in this wavelength range, and their express spectrometer does not always yield unambiguous results for the pink specimens. As seen in their figure 10, for diamonds with a low nitrogen concentration, photoluminescence from the neutral NV^0 centre certainly provides clear evidence that the diamond is a treated pink, but for high-nitrogen diamonds it is difficult to see obvious PL from either the NV^- or NV^0 centres with their apparatus.

The major gem-testing laboratories believe that they can detect most colour-enhanced diamonds, but to do so (particularly with colourless and yellow diamonds) may require a whole gamut of spectroscopic measurements — absorption spectroscopy in the ultraviolet, visible and infrared spectral regions and high-resolution photoluminescence spectroscopy with the diamond cooled to liquid-nitrogen temperature, using a range of laser wavelengths for excitation. One can understand the authors' desire to develop quicker and cheaper methods for assessing coloured diamonds, but I am not confident that luminescence imaging and the express spectrometer will be sufficiently reliable on their own to determine whether an unknown diamond is naturally or artificially coloured. Nevertheless, anyone concerned with the detection of colour-enhanced diamonds will find this article an interesting read.

A.T. Collins

Proceedings of the Gemmological Association of Great Britain and Notices

Gem-A Conference 2012

The 2012 Gem-A Conference was held on Sunday 4 November at the Hotel Russell, Bloomsbury. Speakers included Dr Lore Kiefert, Thomas Hainschwang, Richard Hughes, Ron Ringsrud, Jerry Sisk, Joanna Whalley, Bear Williams and Dr Hanco Zwaan.

The day concluded with a dinner/dance held at The Russell.

Conference Events

A programme of events and workshops was arranged to coincide with the Conference. These started on Saturday 3 November with two half-day seminars held by Richard Drucker entitled 'Colour assessment of gemstones'.

On Monday 5 November two half-day seminars were held — 'Is it real? Identifying amber' with Maggie Campbell Pedersen and 'All things bright and beautiful: a history of gems and gem setting' with Dr Jack Ogden. The Graduation Ceremony and Presentation of Awards was held in the evening at Goldsmiths' Hall (see report opposite).

On Tuesday 6 November Alan Hart led a tour of the Mineral Gallery at the Natural History Museum, South Kensington, including the opportunity to view the Museum's new acquisitions. This was followed in the afternoon by a guided tour of the Crown Jewels at the Tower of London with David Thomas. The final event was Gem Central hosted by Amanda Good, at which attendees had the opportunity to test their gem dealing skills.

A full report of the Conference and events was published in the Winter 2012 issue of *Gems & Jewellery*.

Conference Sponsors and Supporters:

The Association is most grateful to the following for their support:

MAJOR SPONSORS

Fellows Auctioneers
www.fellows.co.uk

Gemfields
www.gemfields.co.uk

SPONSORS

Marcus McCallum FGA, London
www.marcusmccallum.com

Gemworld
www.gemguide.com

SUPPORTERS

T.H. March, Insurance Brokers
www.thmarch.co.uk

GemmoRaman
www.gemmoraman.com

National Association of Goldsmiths'
Institute of Registered Valuers
www.jewelleryvaluers.org

ASSOCIATE SUPPORTERS

Apsara
www.apsara.co.uk

Brink's Global Services
www.brinksglobal.com

British Jewellers' Association
www.bja.org.uk

We would also like to thank dg3 Diversified Global Graphics Group for sponsoring conference materials. Visit their website at www.dg3.com

Gem-A Graduation Ceremony and Presentation of Awards

On Monday 5 November 2012 the Graduation Ceremony and Presentation of Awards was held at Goldsmiths' Hall in the City of London. James Riley, Gem-A CEO, welcomed those present which included graduates from Canada, China, France, The Netherlands, New Zealand, Sweden and the U.S.A., as well as those from the U.K.

Gem-A President Harry Levy then introduced the guest speaker, the President of CIBJO Dr Gaetano Cavalieri, who presented the awards and gave the address.

Following the presentations to the graduates, four members were awarded Fellowship status in recognition of their high level of expertise and who had made a significant contribution to the field of gemmology for no less than ten years were presented with their Fellowship diplomas by Cally Oldershaw, Chairman of the Gem-A Board. They were Richard Drucker of Glenview, Illinois, U.S.A., Antoinette Matlins of Woodstock, Vermont, U.S.A., James Riley of Knutsford, Cheshire, and Bear Williams of Jefferson City, Missouri, U.S.A.

Above: Dr Gaetano Cavalieri giving his address.
Below: Graduates gather on the magnificent staircase at Goldsmiths' Hall.

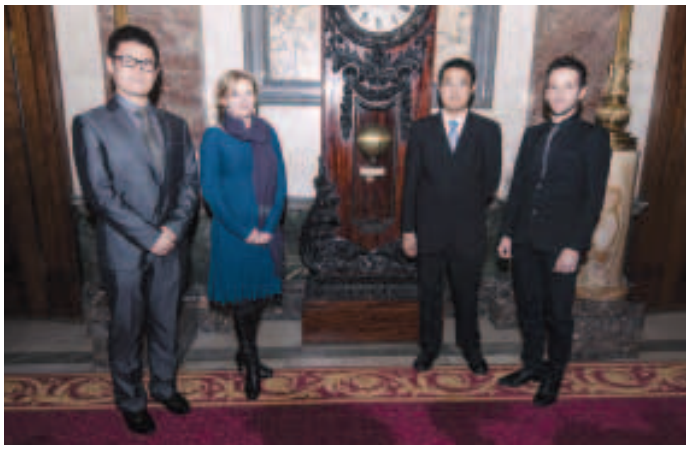

The prize winners (from left): Jiangli Tao, Beijing, China (Anderson-Bank Prize), Rona Bierrum, London (the Bruton Medal and the Deeks' Diamond Prize), Timothy Sheung Yin Li, Bradford, West Yorkshire (the Diamond Practical Prize) and Jonathan Tremblay, Bourth, France (the Christie's Prize for Gemmology).

It had also been agreed to grant Honorary Life Membership to three individuals who had worked tirelessly for the Association for many years. These were presented to Dr Tony Allnutt of Chislehurst, Kent, Peter Dwyer-Hickey of South Croydon, Surrey, and Dr Roger Harding of Devizes, Wiltshire. A new Vice President elected at the AGM held in July 2012, Professor Alan Collins, was presented with a certificate.

Dr Gaetano Cavalieri gave the address, congratulating the graduates on their great achievement.

The ceremony was followed by a reception for graduates and guests.

A report of the event was published in *Gems & Jewellery,* Winter 2012, **21**(4).

All photos courtesy of Photoshot.

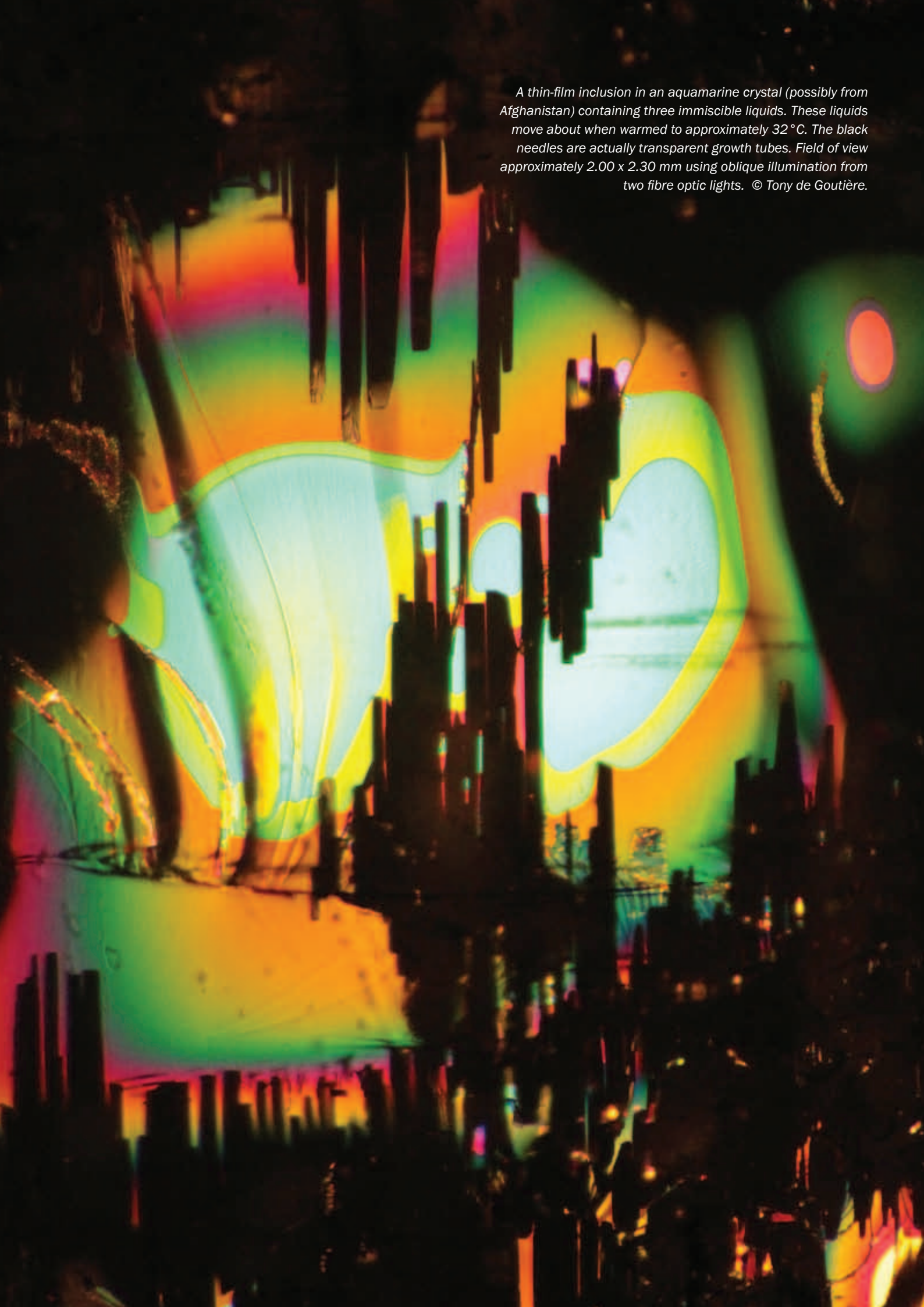

A thin-film inclusion in an aquamarine crystal (possibly from Afghanistan) containing three immiscible liquids. These liquids move about when warmed to approximately 32 °C. The black needles are actually transparent growth tubes. Field of view approximately 2.00 x 2.30 mm using oblique illumination from two fibre optic lights. © Tony de Goutière.

Gem-A Photographic Competition

2012 Competition winners

Overall winner and winner of Natural category

Tony de Goutière GG

Photomicrograph of a thin-film inclusion in an aquamarine crystal (see facing page)

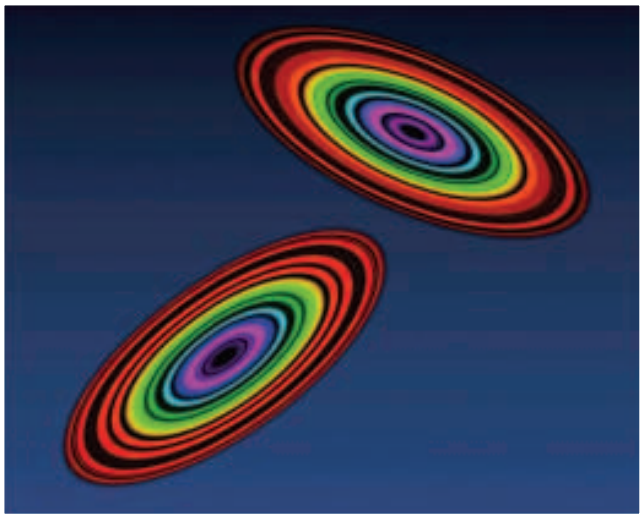

Winner of Treated category

John Harris FGA

'Close encounters.' Two spectra from the o-ray and e-ray of a Mogok zircon which have been altered to become an ellipse.

Winner of Melange category

Tay Thye Sun

The intense face of a miner making a last sales pitch, Tanzania.

The 2013 Competition is now open!

All Gem-A members are invited to participate. Once again there are four categories in which an image may be submitted:

1 **Natural**
Digital photograph (including photomicrography) with minimal post-production work (may include basic cropping, contrast and minor hue/saturation adjustments).

2 **Treated**
Digital photograph (including photomicrography) with significant post-production work (such as background manipulation, HDR, and contrast masking).

3 **Synthetic**
Computer-rendered 3D models of gemstones, crystals, crystal structures, images from microtomography, etc.

4 **Melange**
This category includes any gem-related image that doesn't fit in the above and may include such things as photos of a spectrum, a scanning electron microscope image, mining, cutting, etc.

The entries will be judged by an industry panel on the basis of gemmological interest, inspiration, artistic quality and, in the case of categories 2 and 3, computer skills and ingenuity. A prize will be awarded in each category and, depending on submissions and at the judges' discretion, an additional prize for the most humorous or unusual image might also be awarded. All prize winners will receive their image within a frameable mount. In addition there will be one overall winner who will receive a free Gem-A membership for the following year.

To enter

Please send a low resolution version of your photo to editor@gem-a.com. Entry forms and full details of the competition, including copyright information and Rules of Entry, can be accessed at www.gem-a.com/membership/photographic-competition.aspx or call Amandine on +44 (0)20 7404 3334.

Closing date: 28 June 2013

Winning entries will be announced at the Gem-A Conference 2013 and feature in *Gems & Jewellery*.

Gem-A Awards

Gem-A Examinations were held worldwide in January and June 2012. In the Examinations in Gemmology 311 students qualified in the Diploma Examination, including 16 with Distinction and 37 with Merit. In the Foundation in Gemmology Examination 381 qualified. In the Gem Diamond Examination 98 qualified, including 23 with Distinction and 15 with Merit.

Christie's Prize for Gemmology for the best candidate of the year in the Diploma Examination was awarded to **Jonathan Tremblay** of Bourth, France.

The **Anderson Bank Prize** for the best set of theory papers in the Diploma in Gemmology examination was awarded to **Jiangli Tao** of Beijing, P.R. China.

The **Read Practical Prize** for excellence in the Diploma Practical Examination was sponsored for 2012 by DeeDee Cunningham of Toronto, Canada. The Read Practical Prize was awarded to **Lauriane Forest** of Villeurbanne, France.

In the **Foundation Certificate in Gemmology** examination, the **Anderson Medal** for the candidate who submitted the best set of answers which, in the opinion of the Examiners, were of sufficiently high standard, and the **Hirsh Foundation Award** for the best candidate of the year, were awarded to **Andrea Blake** of Chevy Chase, Maryland, U.S.A..

In the **Gem Diamond Diploma** examination, the **Bruton Medal** for the best set of theory answer papers of the year and the **Deeks Diamond Prize** for the best candidate of the year, were awarded to **Rona Bierrum** of London.

The **Diamond Practical Prize** for excellence in the Diamond Practical Examination, is sponsored by Dominic Mok from AGIL, Hong Kong. The Diamond Practical Prize was awarded to **Timothy Sheung Yin Li** of Bradford, West Yorkshire.

The **Tully Medal** was not awarded.

The names of the successful candidates are listed below.

Examinations in Gemmology

Gemmology Diploma

Qualified with Distinction

Cheng Ping Shing, Kowloon, Hong Kong
Jin Bin, Zhuji, Zhejiang, P.R. China
Lally, Joanne Claire, Southampton, Hampshire
Li Dan, Beijing, P.R. China
Li Yuan, Beijing, P.R. China
Lin Ken, Wuhan, Hubei, P.R. China
Ma Autu, Xi'an, Shanxi, P.R. China
Ni Liang, Beijing, P.R. China
Nilsson, Paul G., Auckland, New Zealand
Porter, Rex, Hartley Whitney, Hampshire
Shi Miao, Beijing, P.R. China
Tereszczuk, Stasia, Berkhamsted, Hertfordshire
Tremblay, Jonathan, Bourth, France
Wu Xiaoting, Shandong, P.R. China
Zhou Haohao, Nantong, Jiangsu, P.R. China
Zhu Lin, Hebei, P.R. China

Qualified with Merit

Bai Xumeng, Beijing, P.R. China
Bierrum, Rona Ann Alison, London
Boisserand, Anne, Fréjus, France
Chen Xiao, Teda of Tianjin, P.R. China
Drouin, Claude, Loughborough, Leicestershire
Forest, Lauriane, Villeurbanne, France
Genet, Julie, Cagnes-sur-Mer, France
Huajie Jin, Hangzhou, P.R. China
Huang Xiaowan, Pan Yu District, P.R. China
Jiangli Tao, Glasgow,
Jie Liu, Guizhou, P.R. China
Lambert, Amelie Julia Sophie, London
Lei Ying, Beijing, P.R. China
Linlin Wang, London
Mack, Darling, Dollard-des-Ormeaux, Quebec, Canada
Mitchell, Shirley D., Windsor, Berkshire
Raoul, Julien, Élancourt, France
Rui Jia Zhang, Kunming, P.R. China

Sepper, Mariliis, Harjumaa, Estonia
Shuqiong Luo, Beijing, P.R. China
Si Tong Liu, Beijing, P.R. China
Sixun Yun, Ningxia, P.R. China
Van Colen, Louise, Tourgéville, France
Wang Jia, Jinzhou, P.R. China
Woodmansterne, Chloë Elinor, St. Albans, Hertfordshire
Wu Wenjun, Guangdong, P.R. China
Wyndham, Jessica, London
Xian Yu, Guangdong, P.R. China
Xiaona Zhang, Beijing, P.R. China
Xu Chun, Zhejiang, P.R. China
Young, Olivia, London
Yu Qingyuan, Guangzhou, P.R. China
Yuan Miao, Hangzhou, P.R. China
Yuan Ren, Beijing, P.R. China
Yumei Xia, Sichuan, P.R. China
Yutong Ma, Beijing, P.R. China
Zhang Jian, Beijing, P.R. China

Qualified
Ai Xia, Guilin, P.R. China
Andersson, Helene, Lannavaara, Sweden
Andre, Sandrine Marie, London
Armitage, Katherine Jane, Hove, East Sussex
Asplund, Jan Olof, Norrbotten, Sweden
Bai Meng, Xingan Meng, Inner Mongolia, P.R. China
Balasubramaniam, Subanthini, Birmingham, West Midlands
Bao Yi, Wuhan, Hubei, P.R. China
Bastidas, Emmanuel, Montmorency, France
Benistand, Angelique, La Chapelle-en-Vercors, France
Boele, Georgette, Almere, The Netherlands
Bombardier, Valerie, Candiac, Quebec, Canada
Branchard, Jean-Yves, Kamaryut Township, Yangon, Myanmar
Brianceau, Boris, Saint-Julien-des-Landes, France
Brom, Jean-Baptiste, London
Bruyère, Manon-Océane, L'Isle-sur-la-Sorgue, France
Buono, Pascal, Mont-Royal, Quebec, Canada
Burrows, Michael James, Kidderminster, Worcestershire
Cancé, Gregory, Montreal, Quebec, Canada
Cen Junxiao, Guangxi, P.R. China
Chan Shuk Lam, Kowloon, Hong Kong
Chan Chi Kin, Kowloon, Hong Kong
Chan Chui Wan, Annabel, Tsuen Wan, Hong Kong
Chan Miu Yee, New Territories, Hong Kong
Chan Wai Ling, New Territories, Hong Kong
Chandrasekera, Pali Kumari K., Nugegoda, Sri Lanka
Chang Cheng, New Taipei City, Taiwan, R.O. China
Chang Na, Qinghai, P.R. China
Chang YiMao, Shenzhen, Guangdong, P.R. China
Che Yandong, Hongshan, Chifeng, Inner Mongolia, P.R. China
Chen Hongyan, Hubei, P.R. China
Chen Kai, Guilin, P.R. China
Chen Tan, Guilin, P.R. China
Chen Ting, Jingzhou, Hubei, P.R. China
Chen Zejin, Beijing, P.R. China
Cheung Mei, Karen, New Territories, Hong Kong
Chiang Cheng-Hsien, New Taipei City, Taiwan, R.O. China
Chin Cheung, Beijing, P.R. China
Chow Po Ling, Sai Ying Pun, Hong Kong
Chu Yung-Huan, Taichung, Taiwan, R.O. China
Chu Zhongheng, Shangxi, P.R. China
Corton, Annabelle Rachael, Dubai, United Arab Emirates
David, Elysabeth, Bonn, Germany
Day, Kroy, Jimboomba, Queensland, Australia
De Vismes, Raphaele, Versailles, France
De Wit Sandstrom, Ida Marianne, Dalby, Sweden
Delor, Claude, Orléans, France
Di Geso, Alessandra Rosa, Kirkland, Quebec, Canada
Dingley, Stacey M., Dudley, West Midlands
Dong Yiting, Beijing, P.R. China
Duan Qi, Beijing, P.R. China
D'Ussel, Anne-Charlotte, Paris, France
Eastmond, Fiona M., Isleworth, Middlesex
Fayet, Timothée, Gland, Switzerland
Feng Liwei, Guilin, P.R. China
Forsner, Christina, Sodra Sandby, Sweden
Franchitti, Sarah Melle, Saint-Sébastien-de-Morsent, France
Fremy, Pierre, Bois-Colombes, France
Gao Minghao, Gan Su, P.R. China
Gao Rongxian, Guilin, P.R. China
Gautier, Isabelle Marie Nathalie Korenain, Bry-sur-Marne, France
Girard, Maxime, Agadir, Morocco
Goshanth, Namasivayam, Sabaragamuwa, Sri Lanka
Griffith, Julia Anna, Southampton, Hampshire
Gu Yian, Shanghai, P.R. China
Guo Jingqing, Fu Jian, P.R. China
Hameed, Aveen, Leicester
He Qing, Guilin, P.R. China
Ho Wing Sze, London
Hsiao Yu-Hsin, Taichung, Taiwan, R.O. China
Hu Huiyi, Guilin, P.R. China
Huang Chiao-Ying, Richmond, Greater London
Huang Haoming, Guilin, P.R. China
Huang Mulin, Changde, Hunan, P.R. China
Huang Wei, Guilin, P.R. China

Huang Yi, Jiang Xi, P.R. China
Hughes, Beata, Sutton Coldfield, West Midlands
Hunter, Sam, London
Ijima, Kaori, Saitama Pref., Japan
Jacques, Cecile, Toulon, France
Jangsawang, Nongnuch, Bangkok, Thailand
Janse, Leo, Zutphen, The Netherlands
Jaywardene, D.M. Dulip, Peradeniya, Sri Lanka
Jeffrey, Kip, Port Isaac, Cornwall
Ji Kaijie, Shanghai, P.R. China
Jiang Xue, Urumqi, Xinjiang, P.R. China
Jie Liu, Xinjiang, P.R. China
Johann, Deru, Villejuif, France
Jonsall, Lisa, Edsbyn, Sweden
Kang Chung-Jui, Tainan, Taiwan, R.O. China
Kang Ruinan, Jinzhong, Shanxi, P.R. China
Khalif Abdille, Abdifatah, Bangkok, Thailand
Knifeld, Stephanie Ann, Bournemouth, Dorset
Knochenhauer, Cecilia, Partille, Sweden
Kouya, Yuriko, Tokyo, Japan
Kunming Tay, Singapore
Lai Hongyan, Kunming, Yunnan, P.R. China
Lai May Wah, Sai Wan, Hong Kong
Lam Man Ngor, Cherrie, Pok Fu Lam, Hong Kong
Laszlo, Linda, Abu Dhabi, United Arab Emirates
Lau Yin Ling, Lecky, New Territories, Hong Kong
Lavoie, Martine, Montreal, Quebec, Canada
Lee Jin Sook, Gyeonggi-Do, South Korea
Lee Young Hee, Seoul, R.O. Korea
Lesouef, Julie, London
Leung Pui Sheung, Fennie, Welwyn Garden City, Hertfordshire
Leung Suet Lin, Kowloon, Hong Kong
Li Chenxi, Tan'An, Shandong, P.R. China
Li Cui, Shanghai, P.R. China
Li Qi, Qionghai City, Hainan, P.R. China
Li Qin, Beijing, P.R. China
Li Yanan, Guilin, P.R. China
Liang Kunlian, Guilin, P.R. China
Lin Bin, Guilin, P.R. China
Lin Guangkai, Beihai, Guangxi, P.R. China
Lin Ying, Changle, Fujian, P.R. China
Lindelow, Susanna, Malmö, Sweden
Liu Feng, Guangdong, P.R. China
Liu Jie, Beijing, P.R. China
Liu Lei, Hangshi, Hubei, P.R. China
Lu Liang, Shan Xi, P.R. China
Liu Lihong, Beijing, P.R. China
Liu Longyue, Beijing, P.R. China
Liu Lu, Jiang Su, P.R. China
Liu Lvqian, Guilin, P.R. China
Liu Qin, Beijing, P.R. China
Liu Yu, Wuhan City, Hubei, P.R. China
Liu Yunzhong, Beijing, P.R. China
Liu Zhexu, Tianjin, P.R. China
Ma Shui Chu, Kowloon, Hong Kong
Ma Sui Hung, Kowloon, Hong Kong
Ma Tingting, Beijing, P.R. China
McCallum, Neil Keith, Martinborough, New Zealand
Mak Yee Man, New Territories, Hong Kong
Manasse, Daniele, Rome, Italy
Marcus, Caroline, Oxford, Oxfordshire
Marier, Valerie, Acton Vale, Quebec, Canada
Meng Cheng, Beijing, P.R. China
Meunier, Delphine, Le Barcarès, France
Mingyu Yang, Shandong, P.R. China
Mo Xiangzhi, Hepu, Guangxi, P.R. China
Molina-Talavera, Jose, Malaga, Spain
Nadeeva, Katerina, London
Nay Hlaing Oo, Yangon, Myanmar
Naylor-Leyland, Jessica, London
Negus, Patricia, Durham, County Durham
Ni Wenjun, Guilin, P.R. China
Nie Ting, Zhong Xue, Hunan, P.R. China
Ostergaard, Marlon, Kings Beach, Queensland, Australia
Osterlund, Anders, Lulea, Sweden
Phillips, Jane, Hendra, Queensland, Australia
Phongsawat, Tichakorn, Chantaburi, Thailand
Poisson, Francis, Montreal, Quebec, Canada
Prickett, Sydney James, Huonville, Tasmania, Australia
Qiao Yuting, Xianyang, Shanxi, P.R. China
Qin Chao, Shanghai, P.R. China
Qin Minfeng, Guilin, P.R. China
Qin Yu Song, Jilin, P.R. China
Raybaut, Eric, Montreal, Quebec, Canada
Redmond, Sarah, Weybridge, Surrey
Roberts, Deborah, London
Robinson, Kate, West Didsbury, Berkshire
Robinson, Laura Jane, Dudley, West Midlands
Rossi, Célia, Montreal, Quebec, Canada
Ruofan Zhang, Tianjin, P.R. China
Russell, Lucy, Kidderminster, Worcestershire
Sanchez, Damian, Pontault-Combault, France
Sanders, Esmee Elice, Amsterdam, The Netherlands
She Songsong, Xucang, Henan, P.R. China
Shen Lingyun, Shanghai, P.R. China
Shen Mei, Taipei, Taiwan, R.O. China
Shih-Yu Wu, Taipei, Taiwan, R.O. China
Simon, Gowry, Wolverhampton, West Midlands
Sombatworapat, Supatra, Bangkok, Thailand
Song Lin, Guilin, P.R. China
Song Wen, Tianjin, P.R. China

Sonoda, Yasuko, Shizuoka Pref., Japan
Spofforth, Kristian David, London
Springe, Karl, Sveg, Sweden
Stenlund, Emelie Maria Christina, Strangnas, Sweden
Stevens, Sophie, London
Styles, Sophie Rashleigh, London
Surensoy, Zubeyde, London
Tan Xiaoyan, Shanghai, P.R. China
Tanaka, Atsuko, Tokyo, Japan
Tang Lingjing, Hunan, P.R. China
Tang Yik Hei, North Point, Hong Kong
Tian Xueyao, Shanghai, P.R. China
Tien-Lin Chang, New Taipei City, Taiwan, R.O. China
Tin Yin, Vicki, Kowloon, Hong Kong
Tong Ching Man Yucca, Kowloon, Hong Kong
Torndahl, Rebecca, Skanor, Sweden
Triantafillidis, Antonia, Montreal, Quebec, Canada
Ueda, Kenji, Osaka, Japan
Ullmer, Jacquelyn, Dayton, Ohio, U.S.A.
Van Der Wolf, Nicole A., Dublin, Ireland
Van Minsel, Eefje Eva, Austin, Texas, U.S.A.
Verdoorn-De Vrede, Veronica, Dordrecht, The Netherlands
Visvanathan, Sokkalingam, Singapore
Wang Bingzhen, Beijing, P.R. China
Wang Chong, Beijing, P.R. China
Wang Chunyang, Beijing, P.R. China
Wang Qingbo, Shanghai, P.R. China
Wang Qiyun, Guilin, P.R. China
Wang Weiwei, Shanghai, P.R. China
Wang Xiaojuan, Beijing, P.R. China
Wang Yan, Beijing, P.R. China
Wang Yue, Guangzhou, P.R. China
Wang Zhexin, Zhoushan, Zhejiang, P.R. China
Wen Shaomeng, Beijing, P.R. China
Westwood, Timothy, London
White, Lucy, Virginia Water, Surrey
Wijesekera, Maduni Champika, Kandy, Sri Lanka
Wilkinson, June, Wellingborough, Northamptonshire
Will, Diana Elizabeth, London
Withanage Perera, Tharanga Lahiru Priyawindanie, Piliyandala, Sri Lanka
Wong Shuk Ching, Hong Kong
Wong Ting, Kowloon, Hong Kong
Woodrow, Gillian, Wokingham, Berkshire
Wu Huijuan, Guilin, P.R. China
Wu Liangliang, Guangdong, P.R. China
Wu Tianyi, Beijing, P.R. China
Xiao Na, Changsha, Hunan, P.R. China
Xie Jie, Guilin, P.R. China
Xinfeng Gao, Shanghai, P.R. China
Xu Qian, Guilin, P.R. China
Xu Wei, Beijing, P.R. China
Xu Yang, Guilin, P.R. China
Ye Hongfeng, Beijing, P.R. China
Yang Mei, Beijing, P.R. China
Yao Mengting, Zhe Jiang, P.R. China
Yao Wei, Baotou, Inner Mongolia, P.R. China
Yi Zebang, Guilin, P.R. China
Yin Hanjie, Guilin, P.R. China
Yoshio, Kinoshita, Osaka, Japan
Yuan Lei, Yantai, Shandong, P. R. China
Yue Mingming, Baotou, Inner Mongolia, P.R. China
Yuen Lung Hon, New Territories, Hong Kong
Yuen Shui Ping, Central, Hong Kong
Yun-Wen Chou, Taipei, Taiwan, R.O. China
Zeng Weijing, Hubei, P.R. China
Zhan Yuxing, Yichang, Hubei, P.R. China
Zhang Congcong, Yucheng, Shandong, P.R. China
Zhang Rui, Xi'an, Shaanxi, P.R. China
Zhang WeiXiao, Beijing, P.R. China
Zhang Yaxi, Qinghai, P.R. China
Zhang Yiqun, Beijing, P.R. China
Zhang Yixin, Beijing, P.R. China
Zhang Yunting, Qingdao, Shandong, P.R. China
Zheng Kexiu, Leqing, Zhejiang, P.R. China
Zheng Xin, Shan Tou, Guangdong, P.R. China
Zheng Yifei, Shanghai, P.R. China
Zhengqing Yan, Shanghai, P.R. China
Zhou Mei, Guangxi, P.R. China
Zhou Min, Shijiazhuang, P.R. China
Zhou Nanbin, Beijing, P.R. China
Zhu Xiaoping, Shangrao, Jiangxi, P.R. China
Zhu Zeying, Shaoxing, Zhejiang, P.R. China

Foundation Certificate in Gemmology

Qualified

Amiel, Chantal, Aberdeen, Hong Kong
Ai Xia, Guangdong, P.R. China
Ailun Tao, Shanghai, P.R. China
Alessandri, Matthias, Ashgrove, Queensland, Australia
Alpert, Chloe, London
Altobelli, Martha, Austin, Texas, U.S.A.
Alvernhe, Paul, Nancy, France
An Xue Ying, Beijing, P.R. China
Apple, Jin Nanpeng, Montreal, Quebec, Canada
Armin, Leonie, Edinburgh
Assemmar, Soundouss, Montreal, Quebec, Canada
Astudillo, Victoria, Stockholm, Sweden
Au Cheuk Yin, New Territories, Hong Kong
Baduza-Sutton, Buyisa, Birmingham, West Midlands
Baker, Jan, Wellington Point, Queensland, Australia

Bastidas, Emmanuel, Montmorency, France
Beardmore, Lindsay Ann, Llandudno, Conwy
Bethmont, Lucie, Ozoir la Ferriere, France
Bevan, Lee, Auckland, New Zealand
Bierrum, Rona Ann Alison, London
Billot, Nathalie, Marseille, France
Bishop, Ellen D., Boughton, Chester
Blake, Andrea, Chevy Chase, Maryland, U.S.A.
Blandin, Marie-Azilis Corona, Ozoir-la-Ferrière, France
Blazewicz, Grazyna, London,
Bohlin, Anne Risstad, Stockholm, Sweden
Bouchard, Claudie, Terrebonne, Quebec, Canada
Bousouni, Maria Bousouni, Athens, Greece
Bouts, Antonia, Amsterdam, The Netherlands
Brown, Debra, Ellesmere Port, Cheshire
Bruyère, Manon-Océane, L'Isle-sur-la-Sorgue, France
Burden, Maxwell Jasper, Birmingham, West Midlands
Chan Chiu Shing, New Territories, Hong Kong
Chan Kuan-Lang, Roger Jan, New Taipei, Taiwan, R.O. China
Chan Ngai Man, Mendy, New Territories, Hong Kong
Chang Chun Kai, Taipei, Taiwan, R.O. China
Chant, Francesca, Barnham, West Sussex
Chatchaiyalerk, Supakanya, Bangkok, Thailand
Chen Dan Lu, Beijing, P.R. China
Chen Hsiu-Man, Chang Hua, Taiwan, R.O. China
Chen Ji Zhou, Beijing, P.R. China
Chen Kai, Fujian, P.R. China
Chen Tan, Zhejiang, P.R. China
Chen Yin-Chen, Taipei, Taiwan, R.O. China
Cheng-Hsien Chiang, Taipei City, Taiwan
Cheuk Wing Ng, Tiffany, London,
Chi Ching Tang, New Territories, Hong Kong
Chia Hui Cheng, Taipei City, Taiwan
Chi-Keong Chan, New Taipei City, Taiwan, R.O. China
Ching Man Ngan, Florence, New Territories, Hong Kong
Ching Obie Fong, New Territories, Hong Kong
Choi Lin Yu, New Territories, Hong Kong
Choukroun Loic, Lai Tsk Tsuen, Hong Kong
Chu Zhongheng, Shangxi, P.R. China
Chui Chun Hin, New Territories, Hong Kong
Chung Sik Lee, Chungbuk, Korea
Chun-Yu Lin, Yilan County, Taiwan, R.O. China
Coert, Edward James, Amsterdam, The Netherlands
Connolly, Margaret Gai, Sapphire, Queensland, Australia
Cotter, Sarah Ann, Bridge of Weir, Renfrewshire
Cowan, James, London,
Cribb, Stephen John, Muir of Ord, Ross-Shire
Dai Hui Ru, Beijing, P.R. China
Dai Yu-Ying, Taipei, Taiwan, R.O. China
De Laubier-Rhally, Armelle, London,
Dearing, Matthew, Illinios, U.S.A.
Deijen, Stephanie Elisabeth, Amsterdam, The Netherlands
Delor, Claude, Orléans, France
Devlin, Janet, Belfast, Northern Ireland
Dharmadasa, Etsushi, Aichi Prefecture, Japan
Di Pippo, Lucia, Saint-Léonard, Quebec, Canada
Difei Guo, Shanghai, P.R. China
Dimakias, Randrianarivony Cedric, Antananarivo, Madagascar
Dixon, Katie-Jean, Auckland, New Zealand
Dongmiao Peng, Shanghai, P.R. China
Dongyue Liu, Beijing, P.R. China
Duncan, Colleen, Westhill, Aberdeenshire
Durocher, Beatrice, Marseille, France
D'Ussel, Anne-Charlotte, Paris, France
Elliott, Beth, Ledgewood, New Jersey, U.S.A.
Esterhuysen, Stephanus, Viljoenskroon, South Africa
Eun Seok Choi, Daegu, Korea
Fan Yun, Beijing, P.R. China
Fangyi Zheng, Shanghai, P.R. China
Fanija, Panovska, Singapore,
Fayet, Timothée, Gland, Switzerland
Fazlali-Zadeh, Sonia, London
Feng Liwei, Zhejiang, P.R. China
Ferder, Edward, Lyndhurst, Hampshire
Franchitti, Sarah Melle, Saint-Sébastien-de-Morsent, France
Fredolin, Christophe, Jurancon, France
French, Lucy, London,
Fritz, Eric, Taylorsville, North Carolina, U.S.A.
Fung Cheung Yu, Daisy, New Territories, Hong Kong
Gao Rongxian, Guangxi, P.R. China
Gao Yan Zhen, Beijing, P.R. China
Gardner, Jillian B., Longniddry, East Lothian
Gauthier, Danielle, Laval, Quebec, Canada
Gautier, Isabelle Marie N. Koreman, Bry-sur-Marne, France
Gellini, Roberta, Nice, France
Genmeng Liang, Guangxi, P.R. China
Gibson, Antonia, Stockholm, Sweden
Girard, Maxime, Agadir, Morocco
Glenn, Alison, Chertsey, Surrey
Granic, Kata, Auckland, New Zealand
Guokai Xu, Guizhou, P.R. China
Haeringer, Manuelle, Marseille, France
Hammarqvist, Susanne, Stockholm, Sweden
Haogeng Xia, Guangdong, P.R. China
Haoxin Tian, Shangxi, P.R. China
Harris, Natalie, Merstham, Surrey
Hart-Jones, Jade, Winchelsea, East Sussex

Proceedings of the Gemmological Association of Great Britain and Notices

He Qing, Guangxi, P.R. China
Hein Thu Lwin, Yangon, Myanmar
Heitman, Cora, Knokke, Belgium
Hendra, Vanessa, Truro, Cornwall
Herold, Dorte, Zurich, Switzerland
Hersi, Ali Osman, Greenford, Middlesex
Higgo, Emma Grace, Hindhead, Surrey
Ho Sing Ming, Marie-Christine Melle, Montreal, Quebec, Canada
Ho Wai Fun, Margaret, Kowloon, Hong Kong
Homkhajorn, Hongrutai, Chantaburi, Thailand
Homkrajae, Artitaya, Bangkok, Thailand
Hong Ki Lam, New Territories, Hong Kong
Hsiao Ting Tai, Taoyuan Shien, Taiwan
Hu Huiyi, Guangxi, P.R. China
Huang Haoming, Guangxi, P.R. China
Huang Wei, Sichuan, P.R. China
Huang Xu Dong, Beijing, P.R. China
Huang Yu Ming, Beijing, P.R. China
Huayu Yang, Jiangsu, P.R. China
Hung Hoo, New Territories, Hong Kong
Huo Kai Jie, Beijing, P.R. China
Hurst, Samantha Louise, Wigan, Lancashire
Hyams, Elena, Redditch, Worcestershire
Ibison, Hannah, Kidlington, Oxford
Ieong Kam Fai, Kowloon, Hong Kong
Jan Yuh Hwang, Taipei City, Taiwan
Jendoubi, Faouzi, Paris, France
Jian Han, Shangxi, P.R. China
Jian Zhen Wu, London,
Jiang Jingyun, Shanghai, P.R. China
Jianhong Chen, Guangxi, P.R. China
Jie Gao, Birmingham, West Midlands
Jung Hyun Kim, Gyeonggi-Do, Korea
Ka Man Kwok, Ap Lei Chau, Hong Kong
Ka Wa Luk, Kowloon, Hong Kong
Ka Yan Lau, New Territories, Hong Kong
Kaikai Hua, Shenzhen, P.R. China
Kang Wei Rui, Beijing, P.R. China
Kankanamge, Rusiru Doraliyagoda, Mount Lavinia, Sri Lanka
Kariyawasam, Dilika, Nugegoda, Sri Lanka
Karunapala, Inoka, Kiribathkumbura, Sri Lanka
Kay Yee Wong, Tseung Kwano, Hong Kong
Keiko, Okonogi, Saitama Prefecture, Japan
Khalif Abdille, Abdifatah, Bangkok, Thailand
Kilaire, Nina, Birmingham, West Midlands
Kindley, Richard, Southend-on-Sea, Essex
Kingsford Smith, Suzanna Jane, Ho Chi Minh City, Vietnam
Kourbouzou, Athena, Athens, Greece
Ko-Wei Tsai, Tainan City, Taiwan, R.O. China
Kuo Wen-Yu, Taipei, Taiwan, R.O. China
Kyaw, Okkar, Yangon, Myanmar
Labonte, Julie A., St. John's, Newfoundland, Canada
Lam Sum To, Hung Hon, Hong Kong
Law, Ian, Crowthorne, Berkshire
Lawrie, David, Solihull, West Midlands
Leclerc, Thibault, Trélex, Switzerland
Lee Man Yee, Mandy, New Territories, Hong Kong
Lee Seul Jin, Daegu, Korea
Leedham, Laura, Oldbury, West Midlands
Lefebvre, Patrick, Luynes, France
Lejman, Travis, New York, U.S.A.
Lents, Joshua, New York, U.S.A.
Leung Ching Yee, Kowloon, Hong Kong
Leung Pui Sheung, Welwyn Garden City, Hertfordshire
Leung Ying, Evie, New Territories, Hong Kong
Li Cui, Shanghai, P.R. China
Li Man Kit, New Territories, Hong Kong
Li Xin, Beijing, P.R. China
Li Yanan, Guilin, P.R. China
Liang Kunlian, Guangxi, P.R. China
Lin Bin, Fujian, P.R. China
Lin Mei, Zhejiang, P.R. China
Lin Song, Shandong, P.R. China
Ling Yu, Beijing, P.R. China
Linlin Wang, London
Liu Lvqian, Guangdong, P.R. China
Liu Ting Jun, Beijing, P.R. China
Lo Yi-Ting, Taipei, Taiwan, R.O. China
Lu Bai Fei, Beijing, P.R. China
Lu Min-Ju, New Taipei, Taiwan, R.O. China
Ludlam, Louise Helen, Birmingham, West Midlands
Luo Wen Yan, Beijing, P.R. China
Lv Yi Jin, Beijing, P.R. China
Ma Yunlu, Beijing, P.R. China
Man Ching Fan, New Territories, Hong Kong
Man Man Chow, Shatin, Hong Kong
Man Wa Lau, Mongkok, Hong Kong
Mandinga, Andreia Gaivao, London,
Marshall, Angela, Cambridge
Matrone, Geraldine, Marseille, France
Matthews, Kate, Auchenblae, Aberdeenshire
Matur, Fabienne, Lambesc, France
Maxwell, Rachelle, London
Men, Oxana, Athens, Greece
Mendes, Isabella, Kidlington, Oxford
Meridoux, Marion, Saint-Gervais-les-Bains, France
Meyer, Marina, Baden-Württemberg, Germany
Mi Jun Cho, Seoul, Korea
Ming Zhang, Guangdong, P.R. China

Mingli Dang, Jiangsu, P.R. China
Mingyu Yang, Shanghai, P.R. China
Moussa, Farida, Yangon, Myanmar
Mowbray, Jennifer, Welburn, North Yorkshire
Murphy, Heather Marie, Bolton, Lancashire
Muyal, Jonathan Daniel, Bangkok, Thailand
Naguib, A. Aadil, Colombo, Sri Lanka
Ng Wing Ki, Joyce, Quarry Bay, Hong Kong
Ni Wenjun, Changzhou, P.R. China
Ning Ian Yip, New Territories, Hong Kong
Niu Xiaowei, Beijing, P.R. China
Norris, Edward Arthur Fynmore, London,
On Ying Choi, Kowloon, Hong Kong
Osterlund, Anders, Lulea, Sweden
Ouyang Huiping, Guangdong, P.R. China
Pak Hin Lau, New Territories, Hong Kong
Pang Huiting, Guilin, P.R. China
Parlavantza, Fotini, Athens, Greece
Pasquet, Emmanuel, Puteaux, France
Paulo, Jacob C. Esperanca, London
Pei-Ni Wo, London
Perez, James, Enfield, Middlesex
Peshall, Jessica, London
Pheulpin, Virginie, Geneva, Switzerland
Philp, Alexander W.L., Banchory, Aberdeenshire
Phongsawat, Tichakorn, Chantaburi, Thailand
Phyo-Kan-Nyunt, Hpone, Bangkok, Thailand
Piccini, Angelo, Genova, Italy
Ploetner, Meike, Colombo, Sri Lanka
Polhos, Katalin, London,
Portch, Amanda, Walli Creek, New South Wales, Australia
Qiang Zhong, Xinjiang, P.R. China
Qin Minfeng, Guangxi, P.R. China
Qu Meng, Beijing, P.R. China
Quinney, Holly F., Iles-des-Sœurs, Quebec, Canada
Raoul, Ando, Aubervilliers, France
Raoul, Julien, Élancourt, France
Rembeault, Benjamin, Montreal, Quebec, Canada
Riyao Gan, Guangxi, P.R. China
Robinson, Molly Pamela, Quenington, Gloucestershire
Roe, Sonia E., Walton-on-Thames, Surrey
Rong Luo, Central, Hong Kong
Rongy, Amandine, London
Rossi, Célia, Montreal, Quebec, Canada
Routledge, Susannah Jean, Buckhurst Hill, Essex
Ruiping Bian, Shanghai, P.R. China
Ryalls, Lucy, Birmingham, West Midlands
Saeseaw, Sudarat, Bangkok, Thailand
Sames, Jacob, Romford, Essex
San Fong Kwong, Cathy, Kowloon, Hong Kong
Sanchez, Damian, Pontault-Combault, France
Sandoval-Williams, Cuauhtemoc, Fribourg, Switzerland
Sau Man So, Bernadette, Sai Ying Poon, Hong Kong
Saw Kabaw Thaw Kino, Yangon, Myanmar
Sayers, Natalia, Pinner, Middlesex
Scanlon, Peter Andrew, Cavan, County Cavan, Ireland
Schreckenberg, Astrid Bosshard, Zurich, Switzerland
Seaman, Laura, Rugby, Warwickshire
See Sze Cheng, Cissy, Sai Kung, Hong Kong
Shekarriz, Toktam, Hampstead, Quebec, Canada
Sheung Si Lai, Wan Chai, Hong Kong
Sheung Yin Li, Timothy, Bradford, West Yorkshire
Shi Haicheng, Guilin, P.R. China
Shih-Yu Wu, Taipei City, Taiwan
Shilin Wu, Guangdong, P.R. China
Shou Shan Shan, Beijing, P.R. China
Siffelet, Guillaume, Olivet, France
Siritheerakul, Piradee, Bangkok, Thailand
Siu Kwai Ng, New Territories, Hong Kong
Skinner, Jasmine, Redhill, Surrey
Steele, Sarah Caldwell, Whitby, North Yorkshire
Street, Neil, Wilton, Connecticut, U.S.A.
Stucchi, Luisa M., Edinburgh, Midlothian
Styles, Sophie, London
Sui Chun Chan, Kowloon, Hong Kong
Sum Wing Fong, Serena, Tai Koo Shing, Hong Kong
Sun Jing Xuan, Beijing, P.R. China
Suthiyuth, Ratima, Bangkok, Thailand
Swift, Leila, London
Sze Man Wa, Winnie, Yau Tong, Hong Kong
Tacconi, Arianna, Rome, Italy
Tae Ho Kang, Gangwon-Do, Korea
Tahirisoa, Randrianarison, Antananarivo, Madagascar
Tak Fai Lee, Kowloon, Hong Kong
Takahiro, Yoda, Tokyo, Japan
Tang Yali, Beijing, P.R. China
Tavberidze, Sophia, London
Thompson, Noah, Chiddingfold, Surrey
Tian Jia Lu, Shanghai, P.R. China
Tien-Lin Chang, Taipei City, Taiwan
Tjioe, Ay Djoen, Montreal, Quebec, Canada
Toh Ping Fung, New Territories, Hong Kong
Tortolano, Alexis, Stirling,
Tremblay, Jonathan, Bourth, France
Tsalis, Nicholas, Wellington, New Zealand
Tsang Yeung Tat, Tai Po, Hong Kong
Van Colen, Louise, Tourgéville, France
van Gulik, Barbara Sophie, Edam, The Netherlands
Venturelli, Adelmo, Morges, Switzerland
Wai Ming Wong, Lantau Island, Hong Kong
Wai Tan Cheng, New Territories, Hong Kong

Wai Ying Chau, Tshen Wan, Hong Kong
Walker, Megan, Edinburgh,
Wang Cheng, Beijing, P.R. China
Wang Dong Qiu, Beijing, P.R. China
Wang Qiyun, Shanghai, P.R. China
Wang Si Jia, Beijing, P.R. China
Wang Zi, Beijing, P.R. China
Wei Zhou, Basel, Switzerland
Wen-Chi Chen, Taichung, Taiwan, R.O. China
Wenxi Huang, Shanghai, P.R. China
Wilkinson, Damien, Singapore
Win Than, Yangon, Myanmar
Wing Nga Wong, Quarry Bay, Hong Kong
Wing Yan Chan, Shatin, Hong Kong
Wingfield, Isabel, Birmingham, West Midlands
Winters, Melanie Ann, Christchurch, New Zealand
Wong, Flora, Hong Kong
Wong, Vannessa, Kowloon, Hong Kong
Wong Chi Yui, New Territories, Hong Kong
Wong Ka Yung, Kowloon, Hong Kong
Wong Tak Fook, New Territories, Hong Kong
Wong Ying Ha, New Territories, Hong Kong
Woodmansterne, Chloë Elinor, St. Albans, Hertfordshire
Wu An Na, Beijing, P.R. China
Wu Boyu, Beijing, P.R. China
Wu Huey-Ping, Taipei, Taiwan, R.O. China
Wu Yee Lee, New Territories, Hong Kong
Wut Sheung Ming, Aberdeen, Hong Kong
Xiao Ping-Wang, Shanghai, P.R. China
Xiaofei Tong, Shanghai, P.R. China
Xie Jie, Jiangsu, P.R. China
Xie Min, Guilin, P.R. China
Xinfeng Gao, Shanghai, P.R. China
Xu Qian, Anhui, P.R. China
Yan Chi Kit, Nicholas, New Territories, Hong Kong
Yang, Roseline, Taipei, Taiwan, R.O. China
Yang Fei, Beijing, P.R. China
Yang Xiao Wen, Beijing, P.R. China
Yanting Sun, Shanghai, P.R. China
Yat Yeung Tsang, New Territories, Hong Kong
Ye Fang Qi, Beijing, P.R. China
Yeung Hoi Fan, New Territories, Hong Kong
Yi Zebang, Guangxi, P.R. China
Yin Bei, Shanghai, P.R. China
Yin Hanjie, Hunan, P.R. China
Yin Moe Tint, Yangon, Myanmar
Ying, Richard A., Ap Lei Chau, Hong Kong
Yiu King San, New Territories, Hong Kong
Young Mi Yoon, Jeollanam-Do, Korea
Yu Kin Shing, New Territories, Hong Kong
Yu Yu Naing, Yangon, Myanmar
Yuanjun Lu, Shanghai, P.R. China
Yuanying, Birmingham, West Midlands
Yue Wang, Shangxi, P.R. China
Yun-Fei Hsieh, New Taipei City, Taiwan, R.O. China
Yun-Wen Chou, Taipei City, Taiwan
Yu-Shin Peng, Taichung, Taiwan, R.O. China
Zeligman, Juriel, Laren, The Netherlands
Zhang Yi Chi, Beijing, P.R. China
Zhang Yiqi, Guilin, P.R. China
Zhang Yu Sheng, Beijing, P.R. China
Zhao Xiaohuan, Beijing, P.R. China
Zhao Yang, Shanghai, P.R. China
Zheng, Bowen, Beijing, P.R. China
Zhengqing Yan, Shanghai, P.R. China
Zhong Rui, Beijing, P.R. China
Zhu Lan Ling, Beijing, P.R. China
Zi-Ning Huang, Birmingham, West Midlands
Zins, Bertrand, Cadiere d'azur, France

Gem Diamond Diploma examination

Qualified with Distinction
Barbour, Alexandra Frances, Litton Cheney, Dorset
Bierrum, Rona Ann Alison, London
Birks, Cherie-Ann, London
Campbell-Jones, Amy V., Sheffield, South Yorkshire
Chan Mei Ying, New Territories, Hong Kong
Cheng Ka Yan, Kowloon, Hong Kong
Dickson, Julia Amy Victoria, London
du Plessis, Sarel P., Kingston-upon-Thames, Surrey
Fitzgerald, Alison, Sevenoaks, Kent
Hart, Alan, Beckenham, Kent
Hui Cheuk Fan, New Territories, Hong Kong
Kocak, Sim, London
Leung Ka Yee, Ainsley, New Territories, Hong Kong
Li Sheung Yin, Timothy, Bradford, West Yorkshire
Mogridge, Emma Denise, Birmingham, West Midlands
Ng Wing Ki, Joyce, Quarry Bay, Hong Kong
Peart, Jyoti, London
Peshall, Jessica Monica Eyre, West Kensington, London
Reading, Charlotte Marie, Nuneaton, Warwickshire
Voulgaridis, Konstantinos, London
Wang Linlin, London
Woodmansterne, Chloë Elinor, St Albans, Hertfordshire
Wu Ming Tak, Quarry Bay, Hong Kong

Qualified with Merit
Birch, Ritsuko, Shrewsbury, Shropshire
Chang Jing, Zhangjiakou, Hebei, P.R. China
Harb, Rawan Jalal, London
Holland, Kate Joy, Edinburgh,
Hou Hong Xi, Zhejiang, P.R. China
Matthews, Emma, Sunninghill, Berkshire
Ning Wentao, Beijing, P.R. China
Patel, Hiren, London
Piao Guicheng, Beijing, P.R. China
Platis, Alexandros, Nafpaktos, Greece
Santilal, Shahil, Gants Hill, Essex
Sawyer, Nicola Hester, Keynsham, Somerset
Sojka, Marta, London
Wong Yee Man, Quarry Bay, Hong Kong
Wong Yu Ting, Tai Po, Hong Kong

Qualified
Agnihotri, Riya, Twickenham, Middlesex
Avraam, Zoey Anastasia, Bush Hill Park, Middlesex
Bailey, Anneabell, Althorne, Essex
Balasubramaniam, Subanthini, Birmingham, West Midlands
Bane, Jonathan William, Sheffield, South Yorkshire
Beardmore, Lindsay Ann, Llandudno, Conwy
Belgrave, Liga, Richmond, Surrey
Chan Wing Shan, Kowloon, Hong Kong
Chen Meizhen, Central, Hong Kong
Cheung Hiu Yan, Brenda, Tsuen Wan, Hong Kong
Cheung Kui Wang, Shau Kei Wan, Hong Kong
Choi Yiu Hung, Kowloon, Hong Kong
Costanzo, Alessandra, Rahoon, County Galway, Republic of Ireland
Ding Jing, Akesu, Xinjiang, P.R. China
Dingley, Stacey Marie, Worcester, Worcestershire
Ellis, Jodie, Huddersfield, West Yorkshire
Gao Boqiu, Beijing, P.R. of China
Hu Jiesheng, Shanghai, P.R. China
Huang Fei, Beijing, P.R. of China
Hung Hoo, New Territories, Hong Kong
Imre, Alexandra, London
Jiang Wenhao, Beijing, P.R. China
Jiao Daohua, Hanzhong, Shanxi, P.R. China
Karimzadeh, Leyla, London
Kirkham, Sally Louise, Birmingham, West Midlands
Ko, Roxana, Tseung Kwan O, Hong Kong
Kuropatwa, Olivia Grace, Malmesbury, Wiltshire
Kwan Sin Yi, New Territories, Hong Kong
Lai Yih-Hwey, Taoyuan, Taiwan, R.O. China
Lam Shuk Yin, New Territories, Hong Kong
Lavy, Stephanie, London
Lawrie, David, Knowle, West Midlands
Leung Pui Sheung, Fennie, Welwyn Garden City, Hertfordshire
Leung Teng Chu, Quarry Bay, Hong Kong
Leung Wing Yee, East Finchley, London
Leung Yin Chun, Jeannie, Kowloon, Hong Kong
Li Tsui Ping, Kowloon, Hong Kong
Liu Yingchen, Beijing, P.R. China
Liu-Murphy, Vanessa Jing, Oldbury, West Midlands
Lu Fang, Wuhan, Hubei, P.R. China
Lu Yini, Beijing, P.R. of China
Mughal, Nazia, Hayes, Middlesex
Or Ting Ting, Tammy, Causeway Bay, Hong Kong
Pang, Virginia, New Territories, Hong Kong
Pang Lai Suen, Kowloon, Hong Kong
Parry, Tessa Pryce, Wantage, Oxfordshire
Sayers, Natalia, Pinner, Middlesex
Sheung Si Lai, Wan Chai, Hong Kong
Sun Miao, Beijing, P.R. China
Tsang Man, Judy, Siu Sai Wan, Hong Kong
von Schantz, Casimir, Helsinki, Finland
Wang Shanshan, Yujiashan, Hubei, P.R. China
Wilson, Maria Dorothea, Rugby, Warwickshire
Wong Lai Wah, Kowloon, Hong Kong
Wong Ling Sum, Olivia, New Territories, Hong Kong
Wu Jiayi, Beijing, P.R. China
Yung Hoi Yan, Central, Hong Kong
Zhang Danqiong, Taiyuan, P.R. China
Zhang Jinmengting, Shandong, P.R. China
Zhang Yuhong, Beijing, P.R. of China

Events

The Gem-A Midlands Branch celebrated its Diamond Anniversary during the weekend 1 and 2 December 2012, with a Celebration Dinner and a one-day conference held at the Menzies Strathallan Hotel, Birmingham. Speakers included David Callaghan, Professor Alan Collins, Davina Dryland, Alan Hodgkinson, Evelyne Stern and Stephen Whittaker.

During the dinner Gem-A CEO James Riley presented Gwyn Green with an Honorary Life Membership in recognition of her commitment to the branch and her tireless work to promote gemmological education. David Callaghan, who had been elected a Vice President at the 2012 AGM, was presented with a certificate.

The conference was preceded on 30 November by a lecture by John Benjamin held at Fellows & Sons Auctioneers, Birmingham.

Proceedings of the Gemmological Association of Great Britain and Notices

Annual General Meeting

The Annual General Meeting was held on Wednesday 11 July 2012 at the Imperial Hotel, London WC1. The meeting was chaired by Cally Oldershaw, the Chairman of the Council. The Annual Report and Accounts were approved. Harry Levy was elected President for the period 2012–2014, and David Callaghan and Professor Alan Collins were elected as Vice Presidents. Steve Collins, Richard Slater and Jason Williams (who had been appointed by the Council since the 2011 Annual General Meeting) were re-elected, and Mary Burland, Professor Andy Rankin and Miranda Wells were elected to serve on the Council.

It was agreed that the Membership Liaison Committee be dissolved and that Articles 52 to 54 inclusive of the Memorandum and Articles of Association should be deleted.

Hazlems Fenton were re-appointed as auditors for the year.

The AGM was followed by a talk by Dr Emmanuel Fritsch entitled 'Ethiopian opals'.

Membership

During 2012, the Council approved the election to Membership of the following:

Fellowship and Diamond Membership (FGA DGA)

Asplund, Jan Olof, Stanmore, Middlesex
Balasubramaniam, Subanthini, Birmingham, West Midlands
Beale, Sioned, Lapworth, Warwickshire
Bierrum, Rona Ann Alison, London
Cheung Siu Lui, Sharon, New Territories, Hong Kong
Chung Tsz Bun, Kowloon, Hong Kong
Dingley, Stacey M., Dudley, West Midlands
Leung Pui Sheung, Fennie, Welwyn Garden City, Hertfordshire
Lo, Sunny, Kowloon, Hong Kong
Pietsch, Johanna, Stockholm, Sweden
Tao Jiangli, Glasgow

Fellowship (FGA)

Al-Saif, Manar, Stavanger, Norway
Andersson, Helene, Lannavaara, Sweden
Andre, Sandrine Marie, London
Astrom, Mikko, Vantaa, Finland
Barrows, Michael James, Kidderminster, Worcestershire
Chan Chui Wan, Annabel, Tsuen Wan, Hong Kong
Chan Chi Kin, Kowloon, Hong Kong
Corton, Annabelle Rachael, Dubai, United Arab Emirates
Daufresne, Marie, Antananarivo, Madagascar
Day, Kroy, Jimboomba, Queensland, Australia
Di Geso, Alessandra Rosa, Kirkland, Quebec, Canada
Gaonkar, Mahesh, Mumbai, India
Graff, Elliott, London
Grounds, Camilla Sara, London
Janse, Leo, Zutphen, The Netherlands
Jonsall, Lisa, Edsbyn, Sweden
Laszlo, Linda, Abu Dhabi, United Arab Emirates
Lee Lai Chun, Loletta, Hong Kong
Lu Jun, Yunnan, P.R. China
Marcus, Caroline R., Oxford
Marier, Valerie, Acton Vale, Quebec, Canada
Ngai Yip, Hong Kong
Orsini, Paolo, Alessandria, Italy
Osterlund, Anders, Lulea, Sweden
Phillips, Jane, Hendra, Queensland, Australia
Picard, Chloe, Vessy, Switzerland
Prickett, Sydney James, Huonville, Tasmania, Australia
Roberts, Deborah, London
Robinson, Laura Jane, Dudley, West Midlands
Russell, Lucy, Kidderminster, Worcestershire
Smither, Susi, London
Springe, Karl, Lannavaara, Sweden
Surensoy, Zubeyde, London
Thomas, Craig Arthur, Santon, Gauteng, South Africa
Timms, Ashley, Indooropily, Queensland, Australia
Ullmer, Jacquelyn, Dayton, Ohio, U.S.A.
Weir-De La Rochefoucauld, Juliet, Les Alluets-le-Roi, France
Weisenburn, Maria Johanna, Voorburg, The Netherlands
White, Lucy, Virginia Water, Surrey
Will, Diana Elizabeth, London
Willmott, Karra Jane, Croydon, Surrey
Wyndham, Jessica, London
Zhang Yu, Beijing, P.R. China

Diamond Membership (DGA)

Belgrave, Liga, Richmond, Surrey
Birch, Ritsuko, Shrewsbury, Shropshire
Dowding, Lucy Jane, St. Andrews, Fife
Holland, Katherine Joy, Edinburgh
Kocak, Sim, London
Lavy, Stephanie, London
Lawrie, David, Knowle, West Midlands
Li Sheung Yin, Timothy, Bradford, West Yorkshire
Liu-Murphy, Vanessa Jing, Oldbury, West Midlands
Patel, Hiren, London
Sawyer, Nicola, Keynsham, Somerset
Shi Su, Beijing, P.R. China

Associate Members

Barclay-Michaels, Allison, London
Chu, Dai, London
Clarkson, Deborah, Marlborough, Wiltshire
Collen, Mark, Tilford, Surrey

Gifts and Donations to the Association

The Association is most grateful to the following for their gifts and donations for research and teaching purposes:

Senarath B. Basnayake MSc FGA, Kandy, Sri Lanka, for a 3.46 ct parti-coloured yellow and blue faceted sapphire.

Patrick Coughlin, Yellow Emerald Mining Company LLC, St Clair, Missouri, U.S.A., for a selection of rough and cut 'yellow emeralds'.

Luc Genot FGA, Brussels, Belgium, for a can of jade lustre spray, a necklace of imitation chalcedony beads, and pieces of polished quartz with orpiment, dragon's blood jasper, azurite from China and jasper framed in marble.

Jie Han FGA, Beijing, P.R. China, for a copy of *The Golden Collections Jade Book*.

Emma Higgo, Hindhead, Surrey, for a copy of *The Diamond Compendium* by DeeDee Cunningham.

Richard W. Hughes FGA, Bangkok, Thailand, for a copy of *The Book of Ruby & Sapphire* from an unpublished manuscript by J.F. Halford-Watkins 1936, edited by Richard Hughes.

Akira Ito, Tokyo, Japan, for the books *Jewellery series 2: Design & Making* and a Japanese translation copy of *Gemstones of the World*.

Robert James FGA, San Antonio, Texas, U.S.A., for the World Gem Society book *2012 Guide to Tucson Treated & Created Gems*.

Kyalo Kiilu DGA, Coventry, West Midlands, for a selection of rough zoisite, iolite, apatite and ruby from East Africa.

Gary E. Megel, Fort Lauderdale, Florida, U.S.A., for a selection of faceted gemstones.

Damian Miles, Okehampton, Devon, for six faceted synthetic forsterites.

Elise A. Skalwold FGA, Ithaca, New York, U.S.A., for a copy of *The Edward Arthur Metzger Gem Collection* by W.A. Bassett and E.A. Skalwold.

David Weinberg, Bangkok, Thailand, for a selection of faceted gemstones including zircon, quartz and topaz.

Benjamin Zucker, New York, U.S.A., for a copy of *The Portrait Diamonds*.

Monetary donations were gratefully received from:

Petra C. Bardehle FGA, Holzhausen, Germany
Anthony de Goutiere GG, Victoria, British Columbia, Canada
Vincenzo De Michele, Milan, Italy
Ng Mei Hang DGA, Hong Kong
Raffi Katz, Watford, Hertfordshire
Kiyokatsu Koike FGA, Toride, Japan
Torbjorn Lindwall FGA DGA, Lannavaara, Sweden
Yuko Sekiguchi FGA, Saitama-Ken, Japan
Moe Moe Shwe FGA, Singapore
Paul L. Siegel FGA, Rocky Point, New York, U.S.A.
Susan M. Stocklmayer FGA, Perth, Western Australia
U Myint Tun FGA, Lulea, Sweden
Miranda Wells FGA DGA, Ironbridge, Shropshire

Bequest

The Association received a bequest from the estate of the late Professor Robert Howie for the sum of £3000. Professor Howie, who died on 10 March 2012, was a past President of the Association. An obituary is given on pages 110-111.

The Council of the Association is most grateful to Professor Howie for his bequest.

Davies, Anthony, Maidstone, Kent
De Marsac, Andre Emile, Beaconsfield, Buckinghamshire
Di Gregorio, Giuseppe, Spadafora, Messina, Italy
Drucker, Richard, Glenview, Illinois, U.S.A.
Elliott, Avril, Edinburgh
Farmer, Jane, London
Fitzner, Manuela, Malmö, Sweden
Friling, Beate, Berlin, Germany
Green, Beata, Radlett, Hertfordshire
Harris, Ruth, Borehamwood, Hertfordshire
Herold, Dorte, Zurich, Switzerland
Hersi, Ali Osman, Greenford, Middlesex
Hu, Ayahi Suda, London
Jung Che Kwan, Brenda, London

Karia, Raj, London
Lahner, Alen Mario, Vienna, Austria
Lawrence, Roger Vernon, Swythamley, Cheshire
Lecatsas, Maria, Hollywell, Queensland, Australia
Massingham, Olivia, Durley, Hampshire
McLauchlan, Kate, London
Ming Pik Sau, Caroline, Burnaby, British Columbia, Canada
Moore, Harriette, Newbury, Berkshire
Morton, Helen Skye Fugaccia, Aberdeen
Nichols, Caroline, Carmarthen
Noone, Mark, Cork City, Republic of Ireland
Perez, James, Enfield, Middlesex
Ryder, Adrian, Galway, Republic of Ireland
Saleem, Melanie, Manchester, Greater Manchester
Smith, Adam, Bleasby, Nottinghamshire
Springham, Melvin, Spandeau, Germany
Twist, Dewar, Saint-Congard, France
Vincent, Christopher, Bishops Stortford, Hertfordshire
Warren, Sharron, London
Wassell, Philip, Birmingham, West Midlands
Williams, Bear, Jefferson City, Missouri
Wright, Abby, New Plymouth, New Zealand
Yates, Elspeth, Aberdeen

Gold Corporate Membership

Ogden of Harrogate, Harrogate, North Yorkshire
Ian Quartermaine Ltd, Worcester
Rivoli Jewellers, St Helier, Jersey

Corporate Membership

Fish Brothers, London
Nimmi Blu Designs Ltd, Wimbledon, London
Trent Diamonds Ltd, West Bridgford, Nottinghamshire
William & Son, London

Transfers

Fellowship to Fellowship and Diamond Membership (FGA DGA)

Bane, Jonathan, London
Campbell-Jones, Amy Victoria, Galway, Republic of Ireland
Costanzo, Alessandra, Rugby, Warwickshire
Hart, Alan, London
Karimzadeh, Leyla, Birmingham, West Midlands
Kirkham, Sally, Helsinki, Finland
Mogridge, Emma Denise, Birmingham, West Midlands
Von Schantz, Casimir, Sheffield, South Yorkshire
Voulgaridis, Konstantinos, Sheffield, South Yorkshire
Wilson, Maria Dorothea, London

Diamond Membership to Fellowship and Diamond Membership (FGA DGA)

Goshanth, Namasivayam, Sabaragamuwa, Sri Lanka
Griffith, Julia Anna, Southampton, Hampshire
Manasse, Daniele, Rome, Italy
Mitchell, Shirley D., Windsor, Berkshire
Visvanathan, Sokkalingam, Singapore

Associate Membership to Fellowship (FGA)

Armitage, Katherine Jane, Hove, East Sussex
Boele, Georgette, Almere, The Netherlands
Brianceau, Boris, Saint-Julien-des-Landes, France
Chang Cheng, New Taipei City, Taiwan, R.O. China
Knifeld, Stephanie Ann, Queens Park, Bournemouth, Dorset
Lally, Joanne Claire, Southampton, Hampshire
McCallum, Neil Keith, Martinborough, New Zealand
Molina-Talavera, Jose, Malaga, Spain
Nilsson, Paul Graham, Auckland, New Zealand
Shen Mei, Taipei, Taiwan, R.O. China
Sonoda, Yasuko, Shizuoka Pref., Japan
Tereszczuk, Stasia-Mae, Berkhamsted, Hertfordshire
Torndahl, Rebecca, Skanor, Sweden
Van Der Wolf, Nicole A., Dublin, Republic of Ireland
Wilkinson, June, Wellingborough, Northamptonshire
Woodrow, Gillian, Wokingham, Berkshire

Subscriptions 2013

The membership subscriptions for 2013 are £100, with a £10 discount for those paying by direct debit (UK bank accounts only) .

Obituary

Nancy J. Baker BHSc GG FGA (D.1972), Kingston, Ontario, Canada, died on 21 July 2012.

Thor A. Johne FGA (D.1962, with Distinction), Oslo, Norway, died in August 2012. Thor was a Gem-A examiner for many years, dealing specifically with Norwegian translations.

Gwilym M. Jones FGA DGA (D.1980 with Distinction), Gilwern, Abergavenny, died in 2012.

James A. Houseago FGA DGA (D.1981), Lowestoft, Suffolk, died in 2012.

Keith Wallis FGA (D.1977), Surbiton, Surrey, died on 19 September 2012. An obituary was published in *Gems & Jewellery*, Winter 2012.

Professor Robert Andrew Howie

4 June 1923 – 10 March 2012

Bob Howie was born on 4 June 1923 in Olney, north Buckinghamshire in England and grew up on a nearby farm. His parents were Scottish and his father had moved south from Ayrshire after the First World War. He was educated at Bedford School and in 1941, at the age of 18, Bob cycled over to the nearby Cardington air base to volunteer. He joined up and was sent to Edinburgh and specialized in meteorology. His years in the RAF were eventful, and dangerous; he sailed across the Atlantic with U-boats lurking, flew aerobatics in a Tiger Moth aircraft in Saskatchewan and narrowly escaped death when a Halifax bomber that was attempting to take off brushed the top of the hut he was in and crashed into the sea. He was posted to Gibraltar where he contracted polio. He was bed ridden for a year and was left permanently disabled.

Bob was invalided out of the air force and went to Trinity College, Cambridge, where he read Natural Sciences: Chemistry, Geology and Mineralogy. He graduated in 1950 and then completed his doctorate at Cambridge with S.R. Nockolds on Indian charnockites. Despite limited analytical facilities, Bob demonstrated remarkable tenacity and perseverance in his research, completing large numbers of rock and laboriously separated mineral analyses. The origin of charnockites was, at the time, a source of geological controversy (were they igneous or metamorphic?) and Bob was able to demonstrate their igneous origin.

In 1953 Bob was appointed to a lectureship in Manchester. It was here that he started his collaboration with W.A. Deer (then Head of Department in Manchester) and Jack Zussman. This collaboration (and friendship) lasted the remainder of his life and resulted in the publication of the five-volume *Rock-forming Minerals* series. This monumental work is the bedrock of modern mineralogy and established the national and international reputation and acclaim for the authors. DHZ is a work of outstanding scholarship and has remained the most widely used mineralogical reference book; it has sold more than 125,000 copies worldwide. Bob made a massive contribution to the work which is still being revised and updated, together with the student version which is about to enter its third edition.

In 1962 Bob was appointed Reader, and later Professor, at King's College, London, and he remained there until the merger of the King's, Bedford and Chelsea Departments into the Department at Royal Holloway in 1986. Bob was appointed Lyell Professor of Geology at King's College and he brought this post to Royal Holloway with the departmental merger.

When appointed to King's he had been warned by the then Head of Department (the distinguished sedimentologist J.H. Taylor) about the 'traditionalist' attitudes of the College hierarchy. On appointment he was asked if, in view of his disability, was there anything specific he needed. Bob asked only for permission to park his car in the very limited King's car park as commuting would be difficult. The College agreed but the College Secretary (who ran everything) asked him how many days a week did he need to park? Bob said "everyday" to which the College Secretary exclaimed in horror: "You cannot come in every day — why can't you work at home like everybody else." Bob told him he could not do chemical analysis at home — it ruined the dining room carpet.

At King's, the extent and scope of Bob's contribution was recognized. He continued to publish his research output on mineralogical assemblages and also revised the *Rock-forming Minerals* with his co-authors (it became an eleven

volume work). It was in 1963 that S.O. Agrell and colleagues found three new minerals in the metamorphic rocks of the Franciscan in California. Appropriately they were named deerite, howieite and zussmanite.

He was awarded a DSc by Cambridge University in 1974, the Murchison medal by the Geological Society in 1976, the Distinguished Public Service Award of the Mineralogical Society of America in 1999 and a DSc by the University of Derby in 2009. He was an Honorary Fellow and President (1996–2000) of the Gemmological Association of Great Britain, and Vice-President (1973–1975) and member of council of the Geological Society. In addition, he was very active in University of London politics from the 1970s until near his retirement, acting as Dean of Science from 1979 to 1983 and as chairman of Academic Council from 1983 to 1986. He was a member of the University of London Senate 1974–78 and 1980–90 and member of the University Court 1984–89. His contribution was much respected – his steadfast integrity and 'what you see and hear is what you get' approach in his dealings with academics was a welcome change in the murky waters of academic politics. Many senior academics (and others) will also have abiding memories of his offers of "a lift up to Senate House". A lift in Bob's car was a never-to-be- forgotten-'Alton Towers'-type experience; Bob had learned to fly before he drove a car, and it showed.

Bob also made a substantive contribution towards the establishment of the new department at Royal Holloway. The merger of the three small Geology Departments from King's, Bedford and Chelsea into the department at Royal Holloway was fraught with difficulty and faced considerable opposition. This was especially so at King's where the College was reluctant to give up anything but unwilling to provide real support to a new enlarged Geology Department. Although Bob had spent so much of his time at King's and was a loyal supporter of the College, he recognized that the merger was the best option. King's College had a great reputation but for Geology it was out of touch and out of money. At King's and within the University, Bob guided the merger through many difficult times and his contribution was appreciated. He also succeeded in maintaining great respect from the senior management at King's and was appointed a Fellow of King's College. To his colleagues, Bob was a loyal and much respected academic. He brought to the Royal Holloway Department a national and international reputation.

Despite his scientific eminence, Bob could also establish a great rapport with undergraduate and post-graduate students. His field trips to Skye were memorable experiences for generations of students. Not deterred by his disability, and complete with raincoat tied up with string, Bob would use his detailed knowledge of well chosen outcrops to generate real enthusiasm for mineralogy in the field. His lecture on gemstones was a firm favourite of student societies. This lecture traditionally ended with Bob asking the students if they had heard that evening's news — and then producing a very convincing gem-encrusted royal crown. More seriously, his awareness of the mineralogical foundation of gemmology and his nurturing of the understanding of this link underpinned his contributions as an Associate Editor of *The Journal of Gemmology* and in providing numerous highly readable abstracts both for this publication and for *Gems & Gemology*.

Bob was the most independent of men but benefitted greatly, especially in his later years, from the support of his sons Robin and Timothy and their families.

The contribution that Bob Howie made to the Mineralogical Society was immense and possibly the achievement of which he was most proud. He joined the Society in 1950, served on the Council from 1958–61 and 1963 onwards. He was General Secretary in 1965, was Vice President on three occasions and President in 1978–80. He served as Book Reviews editor for *Mineralogical Magazine* from 1980 and was a Managing Trustee from 1977 to 1987. At each meeting of Council, Bob 'stamped' the attendance sheet with the rubber support at the bottom of his walking stick. Even though in later years, he had a four-hour drive to get to London-based Council meetings, Bob was always first to arrive, complete with his plasticbag 'briefcase' containing a book or two in need of review (many fellow Council members were persuaded to swap one of his books for a review), the latest batch of *MinAbs* proofs to fill any spare time and a packed lunch. Bob edited *Mineralogical Abstracts* from 1966 onwards and continued to contribute some 1600 abstracts every year, a simply phenomenal volume of work. Although he officially retired aged 67, his contribution to *MinAbs* and the Society continued undiminished. Though he began in the time of paper and red ink, Bob embraced new technology, and oversaw the transition of his beloved *Mineralogical Abstracts* from paper, first to CD *(MinSource)* and later to an online version *(MinAbs Online)*. Throughout his academic life he remained a great servant of the Society and this was recognized in 1994 with the unique honour of his election as an Honorary Life Fellow of the Mineralogical Society.

Nick Walsh
Mineralogical Society
(Reproduced with permission)

Professor Dr Ichiro Sunagawa

27 August 1924 – 20 December 2012

It is with deep sadness that we record the death of Professor Ichiro Sunagawa, who died from pneumonia on 20 December 2012. He was born in Hamamatsu although his family 'clan' had long lived in the village which gave rise to the family name — Sunagawa-machi (now renamed Kashiwa-cho, situated in the city of Tachikawa, west of Tokyo). Professor Sunagawa was educated at Tohoku Imperial University, gaining a BSc in mineralogy and then joined the Japanese Geological Survey in 1948 as a researcher. In 1957 he was awarded a PhD by Hokkaido University for his thesis 'Morphological variations in pyrite'. Still working for the Geological Survey, he was granted time at Royal Holloway College, University of London, from 1957 to 1960 to conduct a study of the surface structures of hematite and silicon carbide. In 1963 he was awarded the Geological Society of Japan prize for 'Study on the surface structures of crystals' based on this work.

In August 1971 he was appointed Professor of Tohoku University in charge of the Department of Minerals and remained in post until March 1988 when he was awarded the title Professor Emeritus.

His research activities continued unabated, and in March 1991 he was head of the Organizing Committee of the 9th International Conference in Crystal Growth for its meeting in Japan. Also in 1991 he became Principal of the Yamanashi Institute of Gemmology and Jewellery Arts and served until his retirement in 2005.

In endeavouring to understand the kinetic processes taking place at atomic and molecular levels, he researched their effects on crystalline form, homogeneity, integrity and aggregation from simple systems to those as complex as those in the organic world. He then applied the basic theories and insights obtained to problems in gemmology and mineral exploration. As such, he played the role of a pioneer, developing the new discipline of crystal growth studies, and helping found the Japan Association for Crystal Growth.

Professor Sunagawa also founded the Gemmological Association of Japan and, from 1991 to the present, served as an Examiner for The Gemmological Association of Great Britain and was an Associate Editor of *The Journal of Gemmology* — he was a major influence in establishing the high standard of gemmology in Japan through support for education and the spread of local qualifications and the

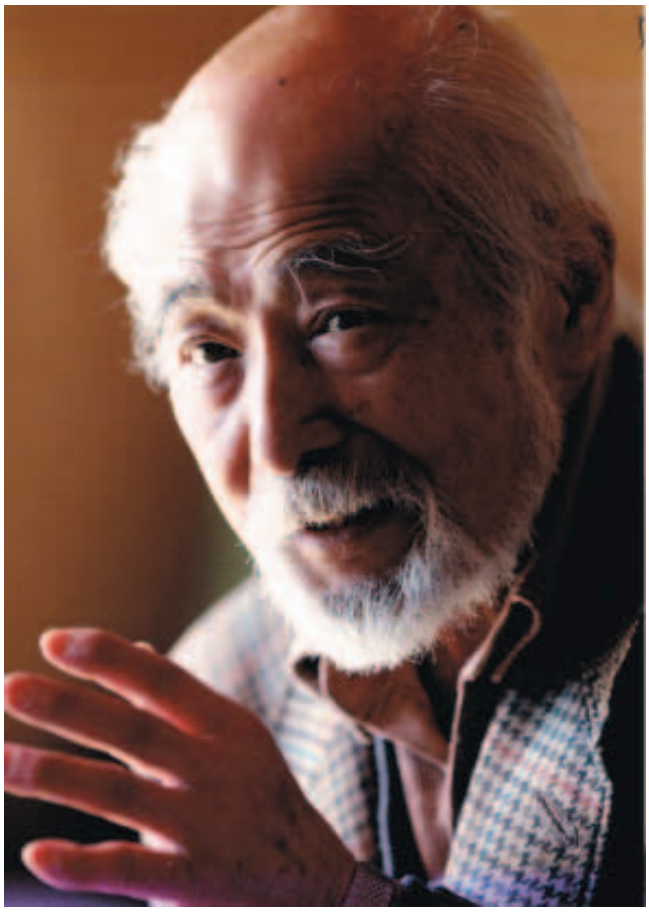

FGA. His international honorary awards include a doctorate from the University of Marseilles, France (for research on crystal growth mechanisms in minerals) in 1982, and Foreign Member of the Bulgarian Academy of Sciences in 1989, and he also held membership of the Russian Mineralogical Society, the Bulgarian Geological Society, the Mineralogical Society of Great Britain and Ireland, and the Korean Society of Crystal Growth; he was a member with honour of the Mineralogical Society of Japan.

He loved minerals from his schooldays until the end of his life and shared this love with his many international friends.

Farewell Professor Sunagawa, you will be sadly missed.

Takeshi Miyata
Tokyo, Japan

Gem-A Gemmology and Diamond Courses

Achieve your potential

A strong knowledge of gemstones and diamonds will increase customer confidence and boost your sales. Gain that knowledge by studying with the world's longest established educator in gemmology. Graduates may apply for election to Fellowship or Diamond membership of the Association enabling them to use the initials FGA or DGA after their name.

Open Distance Learning*

Gemmology Foundation ODL
11 March 2013 to January 2014
Fee: £1,820 (or £2,150 including three-day UK lab class)

Gemmology Diploma ODL
18 March 2013 to January 2014
Fee: £2,050 (or £2,650 including five-day UK lab class)

Diamond Diploma ODL
18 March 2013 to January 2014
Fee: £2,100 (including five-day UK lab class)

Blended Learning Course*

Combined Gemmology Foundation and Diploma
Online — Commencing 1 May 2013
Daytime on-site (London) class days — Tuesday, Wednesday and Thursday, 27 August 2013 to January 2014
Fee: £6,950

* Access to a computer with an internet connection is essential.

Full details at www.gem-a.com/education.aspx or call +44 (0)20 7404 3334
email education@gem-a.com

Understanding gems

Gem-A
THE GEMMOLOGICAL ASSOCIATION OF GREAT BRITAIN

27 Greville Street (Saffron Hill entrance), London EC1N 8TN
tel: +44 (0)20 7404 3334 fax: +44 (0)20 7404 8843
email: information@gem-a.com
UK Registered Charity No. 1109555

The Journal of
Gemmology
2012 / Volume 33 / Nos. 1–4

Contents

Cover Picture: The modern language of colour — spectra of different varieties of iron-bearing quartz. (See Review of some current coloured quartz varieties by U. Henn and R. Schultz-Güttler pages 29 to 43.)

The Gemmological Association of Great Britain

27 Greville Street, London EC1N 8TN, UK
T: +44 (0)20 7404 3334 **F**: +44 (0)20 7404 8843
E: information@gem-a.com **W**: www.gem-a.com

Printed by DG3 (Europe) Ltd
ISSN: 1355-4565